University of Minnesota
St. Anthony Falls Hydraulic Laboratory

Project Report No. 306

DEPOSITING AND ERODING SEDIMENT-DRIVEN FLOWS: TURBIDITY CURRENTS

by

Marcelo H. Garcia

Sponsored by

National Science Foundation
Washington, D. C.
Grant No. NSF/EAR-8517747

April 1990
Minneapolis, Minnesota

ABSTRACT

Laboratory experiments were conducted to observe the behavior of turbidity currents in the vicinity of the slope break between a submarine canyon and its associated depositional fan.

Sediment–laden and saline hydraulic jumps were produced. The vertical structure of the currents was found to depend on flow regime. Velocity and sediment concentration profiles showed a good degree of similarity as the current evolved in the downslope direction. The grain size of the suspended sediment did not affect the vertical velocity distribution in weakly depositional flows. Grain size showed a clear tendency to decrease vertically. Smaller grains were more uniformly distributed vertically. The saline and turbid hydraulic jumps showed similar characteristics. The amount of water entrained by the flows while going through a jump was small. The change in flow regime caused a marked reduction of the bed shear stress downstream of the jump. The thickness of the deposit left immediately downstream of the jump increased as the ratio of the bed shear velocity downstream of the jump to the particle fall velocity decreased.

A clear correlation between turbidite thickness and grain size was observed. The thickness of the turbidites was seen to decrease roughly exponentially with distance. Any increase in the thickness of the deposits near a canyon–fan transition will not be due to the break in slope itself but rather due to the hydraulic jump induced by the break.

It was observed that a fine–grained turbidity current of sufficient strength can entrain substantial amounts of bed sediment into suspension. The rate of sediment entrainment showed a clear tendency to increase with current velocity. Prominent bedforms developed during the experiments. The bedforms were found to have an important effect on boundary shear stress. The effect of the bedforms was removed successfully by modifying the technique of Nelson and Smith (1989) for open channel flows.

Two formulations to evaluate sediment entrainment rates were obtained using data from equilibrium open channel suspensions, one for well–sorted sediment and the other for poorly–sorted sediment.

An integral model for steady, spatially developing turbidity currents driven by poorly–sorted sediment was developed and used as a basis for the analysis of the experimental results.

Acknowledgement

This research was sponsored by the National Science Foundation under grant No. NSF/EAR–8517747.

The author is grateful to Professor Gary Parker for his constant guidance and support.

This report was submitted to the University of Minnesota Graduate School on December 1989, as a thesis in partial fulfillment of the requirements for the degree of Doctor of Philosophy.

TABLE OF CONTENTS

	Page No.
ABSTRACT	i
ACKNOWLEDGEMENTS	ii
LIST OF FIGURES	vi
LIST OF TABLES	xii
LIST OF SYMBOLS	xiii
CHAPTER 1 – INTRODUCTION	
1.1 Sediment–Driven Flows: Turbidity Currents	1
1.2 Geological Implications of Turbidity Flows	4
1.3 Engineering Significance of Turbidity Flows	4
1.4 Field Observations of Turbidity Flows	6
1.5 Previous Analytical and Experimental Work	12
1.5.1 Analytical Studies	12
1.5.2 Experimental Studies	13
1.6 Present Study	15
1.6.1 Motivation	15
1.6.2 Objectives	17
CHAPTER 2 – THEORETICAL BACKGROUND	
2.1 Governing Equations for a Dilute Suspension	18
2.2 Vertically Integrated Balance Equations	20
2.3 Similarity Assumption and Slab Approximation	22
2.4 Closure for Theoretical Model	23
2.5 Spatial Development of Turbidity Currents	25
2.6 Supercritical and Subcritical Flows	27
2.7 Internal Hydraulic Jump	27
2.8 Bed Variation due to Sediment Erosion and Deposition	30
CHAPTER 3 – EXPERIMENTAL APPARATUS AND PROCEDURE	
3.1 The Flume	31
3.2 Measuring Instrumentation	33
3.2.1 Flow Velocity Measurements	33
3.2.2 Suspended Sediment Concentration Measurements	33
3.2.2.1 Well–Sorted Sediment	33
3.2.2.2 Poorly–Sorted Sediment	33
3.2.3 Salinity–Density Measurements	36

Page No.

3.3 Instrumentation Set–up and Data Collection 36
3.4 Particle Size Analyzer 40
3.5 Sediment Materials 40
3.6 Experimental Procedure: Conservative Saline Currents 43
3.6.1 Dense Fluid and Flume Preparation 43
3.6.2 Preparation of Measuring Instruments 43
3.6.3 The Run 44
3.7 Experimental Procedure: Turbidity Currents 45
3.7.1 Currents Driven by Well–Sorted Sediment 45
3.7.2 Currents Driven by Poorly–Sorted Sediment 45
3.8 Experimental Procedure: Eroding Saline Currents 46

CHAPTER 4 –
EXPERIMENTAL RESULTS: CONSERVATIVE SALINE CURRENTS

4.1 Purpose of the Experiments 48
4.2 Overview of the Experiments 48
4.3 Flow Measurements 49
4.4 Layer–Averaged Flow Parameters 52
4.5 Spatial Development of the Underflows 52
4.6 Characteristics of the Hydraulic Jumps 54
4.7 Variation of Bed Shear Stress 59
4.8 Similarity of Profiles and Other Characteristics 59
4.9 Conclusions 66

CHAPTER 5 –
EXPERIMENTAL RESULTS: DEPOSITIONAL TURBIDITY CURRENTS

5.1 Currents Driven by Well–Sorted Sediment 68
5.1.1 Purpose of the Experiments 68
5.1.2 Overview of the Experiments 68
5.1.3 Flow Measurements 70
5.1.4 Spatial Development of the Currents 70
5.1.5 Characteristics of the Hydraulic Jumps 74
5.1.6 Vertical Structure of the Currents 76
5.1.7 Turbidites Deposited from Suspension 76
5.1.8 Turbidites Deposited from Bedload 84
5.1.9 Discussion and Conclusions 85
5.2 Currents Driven by Poorly–Sorted Sediment 88
5.2.1 Purpose of the Experiments 88
5.2.2 Overview of the Experiments 88
5.2.3 Flow Characteristics 91
5.2.4 Vertical Sorting of Suspended Sediment 91
5.2.5 Variation of Turbidite Thickness and Grain Size 91
5.2.6 Similarity of Velocity and Sediment Profiles 98
5.2.7 Conclusions 106

CHAPTER 6
EXPERIMENTAL RESULTS: SEDIMENT–ENTRAINING CURRENTS

6.1 Purpose of the Experiments 108
6.2 Overview of the Experiments 108
6.3 Observations of Sediment Entrainment into Suspension 111
6.4 Evaluation of Sediment Entrainment 111
6.5 Determination of Bed Shear Stress 115
6.6 Characteristics of Bedforms 122
6.7 Removal of Bedform Effect 123
6.8 Conclusions 127

CHAPTER 7
SEDIMENT ENTRAINMENT FUNCTIONS

7.1 Introduction 130
7.2 Problem Formulation 130
7.3 Previous Functions 132
7.3.1 Einstein (1950) 132
7.3.2 Engelund and Fredsoe (1976) 134
7.3.3 Smith and McLean (1977) 134
7.3.4 Itakura and Kishi (1980) 135
7.3.5 Van Rijn (1984) 136
7.3.6 Celik and Rodi (1984) 136
7.3.7 Akiyama and Fukushima (1985) 137
7.4 Data Selection 137
7.5 Predictions versus Observations 138
7.6 Proposed Entrainment Function for Uniform Sediment 146
7.7 Entrainment Function for Non–Uniform Sediment 148
7.8 Comparison With Data From Sediment–Entraining Currents 158
7.9 Conclusions 161

CHAPTER 8 – SUMMARY AND CONCLUSIONS

8.1 Summary 164
8.2 Conclusions 164
8.2.1 Flow Characteristics 164
8.2.2 Hydraulic Jump 165
8.2.3 Sediment Deposits: Turbidites 166
8.2.4 Sediment Entrainment 166
8.2.5 Sediment Entrainment Functions 167
8.2.6 Modeling Considerations 167

REFERENCES 169

APPENDIX A A.1
APPENDIX B B.1

LIST OF FIGURES

FIGURE		PAGE
1.1	Plunge point of the sediment–laden Linth River into Lake Walensee, Switzerland. A turbidity current forms downstream (from Lambert et al., 1976).	2
1.2	Head of a turbidity current flowing downslope. The flow is driven by 100 μ crushed coal.	3
1.3	Modeled topography of Scripps and La Jolla Submarine Canyons (courtesy of Doug Inman, Scripps Institution of Oceanography).	5
1.4	Turbidity current flowing into a laboratory reservoir (from Bell, 1942).	7
1.5	Physical characteristics of Scripps Submarine Canyon (courtesy of Douglas Inman).	8
1.6	Man–made depositional fan at Silver Bay, Minnesota (from Normark and Dickson, 1976b).	11
1.7	Average slopes of submarine canyons and fans (from several sources).	16
2.1	Turbidity current flowing downslope through a quiescent body of water.	19
2.2	Transition from supercritical flow to subcritical flow through a hydraulic jump.	28
3.1	Schematic of the experimental facility.	32
3.2	Micropropeller and typical calibration curve.	34
3.3	Light probe and typical calibration curve.	35
3.4	Rake of siphons used to sample poorly–sorted suspended sediment.	37
3.5	Typical calibration curve for light probe with blue dye.	38
3.6	Schematic of instrumentation set–up.	39

Page No.

3.7 Typical sediment size distributions. 41

3.8 Schematic of the flume with an erodible bed region. 47

4.1 Density current front. The flow is from left to right. 50

4.2 Typical velocity and fractional density profiles at two different locations, one upstream (x = 200 cm) and the other downstream (x = 900) of the break in slope (x = 500 cm). 51

4.3 Plot of buoyancy discharge ϕ versus layer–averaged velocity U along the sloping bed region. 53

4.4 Variation of current thickness along the sloping bed region. 55

4.5 Water entrainment coefficient e_w as a function of the bulk Richardson number R_i. The line is that of equation (2.28) (from Garcia, 1985). 56

4.6 Typical observations for a saline current (run SAL11). 57

4.7 Flow visualization of internal hydraulic jump. 60

4.8 Variation of bed shear velocity along the centerline of the flume. 61

4.9 Similarity collapse of velocity profiles for supercritical and subcritical flows. 62

4.10 Similarity collapse of excess fractional density profiles for supercritical and subcritical flows. 63

4.11 Shape factors for supercritical and subcritical flows. 65

5.1 Observations for a turbidity current driven by 4 μ sediment (run NOVA3). 71

5.2 Velocity profiles before and after the jump, for a saline current (SAL29) and a turbidity current driven by 4 μ sediment (NOVA7). Both currents have the same inlet conditions. 72

5.3 Observations for a turbidity current driven by 9 μ sediment (run DAPER2). 73

		Page No.
5.4	Thickness ratio h_2/h_1 versus the pre–jump Richardson number R_{i_1}. The line is that given by the relationship for non–entraining jumps (2.47).	75
5.5	Similarity collapse of velocity profiles for currents driven by 4 μ sediment.	77
5.6	Similarity collapse of sediment concentration profiles for currents driven 4 μ sediment.	78
5.7	Similarity collapse of velocity profiles for currents driven by 9 μ sediment.	79
5.8	Similarity collapse of sediment concentration profiles for currents driven by 9 μ sediment.	80
5.9	Similarity collapse of velocity and sediment concentration profiles for currents driven by 30 μ sediment.	81
5.10	Definition diagram for characteristic current parameters.	82
5.11	Depositional patterns produced by currents driven by different materials. The break in slope is 5 m from the inlet.	83
5.12	Deposit of plastic particles right after the hydraulic jump undergone by a saline current. The flow is from left to right.	86
5.13	Typical size distribution of the sediment used in the experiments.	89
5.14	Observations made for a typical current at two stations along the sloping region and two stations along the horizontal region (run DEPO3).	92
5.15	Size distribution of suspended sediment samples taken at different locations above the bed. The size distribution of the suspended sediment at the inlet (base) is also included. The data correspond to the measurements taken at 400 cm from the inlet during run DEPO3.	93
5.16	Vertical concentration profiles for different grain sizes. Data from run DEPO3 at x = 400 cm.	94

Page No.

5.17 Depositional patterns produced by currents driven by poorly–sorted sediment. 95

5.18 Variation of turbidite median grain size D_{50} with distance from the inlet. 96

5.19 Grain size distribution in turbidites along the model canyon (x = 250 and 450 cm) and the model fan (x = 650 and 950 cm). Data from run DEPO2. 97

5.20 Similarity collapse of velocity profiles measured along the supercritical region of the flows (top) and along the subcritical region of the flows (bottom). 99

5.21 Normalized sediment concentration profiles for different grain sizes. Data from run DEPO3 at x = 400 cm. 100

5.22 Similarity collapse of concentration profiles for different grain sizes. Data from measurements taken at x = 400 cm during runs DEPO1, DEPO3, and MIX3. 102

5.23 Plot of z_{ci}/h versus the corresponding values of $\delta_i = D_i/D_{sg}$. Data from sediment concentration profiles measured at x = 400 cm. 103

5.24 Plot of c_{b_i}/C_i versus the corresponding values of $\delta_i = D_i/D_{sg}$. Data from sediment concentration profiles measured at x = 400 cm. 104

5.25 Values of the shape factors α_i and β_i as a function of $\delta_i = D_i/D_{sg}$. 105

6.1 Flow configuration considered in the experiments. 109

6.2 Volumetric sediment transport rate UCh at the farthest downstream measuring station versus saline current buoyancy discharge Φ_0. 112

6.3 Velocity and sediment (coal) concentration profiles along the centerline of the erodible bed region. Data from run C1. 113

6.4 Near–bed concentration along the centerline of the erodible bed region. The horizontal distance x is measured from the inlet. 114

Page No.

6.5 Sediment entrainment coefficient E_s as a function of the current velocity U just upstream of the erodible region. 116

6.6 Skin friction coefficient C_D' versus current Reynolds number $R_e = Uh/\nu$. Data from fixed bed region. The line is that of equation (6.11). 120

6.7 Sediment entrainment coefficient E_s versus dimensionless skin friction velocity u_*'/v_s. 121

6.8 Top view of two–dimensional bedforms originated by the passage of a density current. The flow was from right to left. 124

6.9 Characteristic dimensions of a typical bedform. The flow was from left to right. 125

6.10 Comparison of skin friction coefficients predicted with the empirical relationship (6.11) versus those predicted with the modified Nelson–Smith formulation (6.20). 128

7.1 Definition diagram for open channel flow over an erodible bed. 131

7.2 Plot of different formulations for near–bed reference suspended sediment concentration. 133

7.3 Comparison of predicted and observed values using Einstein's relationship. 140

7.4a,b Comparison of predicted and observed values using Engelund–Fredsoe's (top) and Smith–McLean's (bottom) relationships. 141

7.5a,b Comparison of predicted and observed values using Itakura–Kishi's (top) and Van Rijn's (bottom) relationships. 143

7.6a,b Comparison of predicted and observed values using Celik–Rodi's (top) and Akiyama–Fukushima's (bottom) relationships. 145

Page No.

7.7 Plot of sediment entrainment coefficient E_s versus dimensionless skin shear velocity u_*'/v_s. 149

7.8 Plot of sediment entrainment coefficient E_s versus similarity variable Z_u for $0 < n < 1$. 150

7.9 Plot of entrainment relationship for uniform sediment (7.36) and the data used in the derivation. 151

7.10 Comparison of predicted and observed values of reference concentration using the present formulation (7.36). 152

7.11 Plot of entrainment coefficient E_{s_i} versus dimensionless skin friction u_*'/v_{s_i}. 155

7.12 Plot of entrainment coefficient E_{s_i} versus similarity variable Z_m with $m = 0.2$. The line is that of the proposed formulation for uniform sediment (7.36). 156

7.13 Plot of entrainment coefficient E_{s_i} versus similarity variable $Z_{eff} = \lambda Z_m$. 157

7.14 Comparison of observations versus predictions using the formulation for non–uniform sediment (7.42) and data from the Niobrara River. 159

7.15 Plot of sediment entrainment rates produced by density currents and the relationship obtained for open channel flows (7.36). 160

7.16 Plot of f_o as a function of particle Reynolds number R_p. 162

LIST OF TABLES

TABLE		Page No.
1.1	Characteristics of turbidity currents in the ocean.	9
3.1	Characteristics of sediment materials.	42
4.1	Inlet conditions of selected experiments.	49
4.2	Characteristics of saline hydraulic jumps	58
5.1	Inlet conditions and other characteristics of the experiments.	69
5.2	Characteristics of turbid hydraulic jumps.	74
5.3	Characteristics of supercritical flow profiles.	84
5.4	Sediment size ranges.	90
5.5	Inlet conditions and other characteristics of the experiments.	90
6.1	Experimental conditions.	110
6.2	Parameters in the erodible bed region.	118
6.3	Parameters in the fixed bed region.	122
6.4	Bedform characteristics.	126
6.5	Comparison of skin friction coefficients.	127
7.1	Performance of various formulae.	146
7.2	Characteristics of bed sediment.	153

LIST OF SYMBOLS

ROMAN SYMBOLS

A Constant ($= 1.3 \cdot 10^{-7}$).

A_d Mean absolute deviation of the ratio c_{aep}/c_{aeo}.

b Reference level placed at $z = 0.05$ h.

b_1, b_2 Parameters defined by $b_1 = \log(M_e)$ and $b_2 = \log(A_d)$.

C Layer–averaged volumetric concentration of well–sorted sediment.

C_0 Value of C at the inlet.

C_i Layer–averaged volumetric concentration of sediment in the ith size range.

C_{i0} Value of C_i at the inlet.

$\mathbf{C}$ Sum of the layer–averaged concentrations corresponding to each sediment size range, i.e. $\Sigma\, C_i$.

$\mathbf{C_0}$ Value of $\mathbf{C}$ at the inlet.

C_m Mean transport concentration for open–channel flows, i.e. suspended sediment flux divided by volume flux.

c Local volumetric concentration of well–sorted sediment, averaged over turbulence.

c_i Local volumetric concentration of sediment in the ith size range, averaged over turbulence.

c_i' fluctuating volumetric concentration of sediment in the ith size range.

$\mathbf{c}$ sum of the local volumetric concentrations corresponding to each sediment size range, i.e. $\Sigma\, c_i$.

c_a Near–bed volumetric sediment concentration for open–channel flows, taken at z = 0.05 H.

c_{a_i} Near–bed volumetric concentration of sediment in the ith size range.

c_{ae},c_{ae_i} Equilibrium values of c_a and c_{a_i}, respectively.

$\mathbf{c_{ae}}$ Computed value of c_{ae} at a refence level "a".

c_{aeo},c_{aep} Observed and predicted values of c_{ae}, respectively.

c_b Near–bed volumetric sediment concentration for turbidity currents, taken at z = 0.05 h.

c_{b_i} Near–bed volumetric concentration of sediment in the ith size range.

C_D Bed friction coefficient.

C_D' Skin friction coefficient.

C_D'' Bedform drag coefficient.

C_f Bedform drag coefficient in Nelson–Smith formulation.

C' Chezy coefficient.

D Sediment diameter.

D_i Diameter of the sediment in the ith size range.

D_r,D_{r-1} Sediment diameter of upper and lower limit for a given size range.

D_s Mean sediment diameter.

D_{sg} Geometric mean size.

$\mathbf{D_{sg}}$ Geometric mean size of suspended sediment.

D_{50} Median grain size.

D_* Dimensionless sediment diameter.

E_s Sediment entrainment coefficient.

E_{s_i} Sediment entrainment coefficient for the material in the ith size range.

$E^o_{s_i}$ Sediment entrainment coefficient for the material in the ith size range based on the amount available of this sediment size in the bed, i.e. $p_i E_{s_i}$.

e_w Water entrainment coefficient.

F Froude number.

F_* Limit Froude number dividing downstream–migrating antidunes from upstream–migrating antidunes.

F_a Near–bed volumetric upward normal Reynolds flux of sediment.

F_{b_i} Near–bed volumetric upward normal Reynolds flux of sediment in the ith size range.

F_i Volumetric upward normal Reynolds flux of sediment in the ith size range.

f_i Fraction of material in the ith size range.

f_o Similarity function for sediment concentration profiles.

f_o Similarity function for particle Reynolds number.

g Gravitational acceleration.

g_o Shape function.

g_* Shape function.

H Flow depth in an open channel.

h Turbidity current thickness.

h_0 Value of h at the inlet.

h_1, h_2 Value of h before and after a hydraulic jump, respectively.

k Bedform wavenumber.

k_o Constant (=1.14).

k_s Equivalent bed roughness.

$k_{i\ i=1,4}$ Constants with values of 0.008, 0.14, 0.143, and 2.0, respectively.

ℓ Longitudinal distance covered by a particle during the depositional process.

ℓ_b Bedform wavelength.

M_e Mean value of the ratio c_{aep}/c_{aeo}.

m Power in sediment entrainment function for non–uniform sediment.

n Power in sediment entrainment function for uniform sediment.

p Local mean pressure due to the weight of the suspended sediment.

p_i Fraction of bed material in the ith size range.

Q_o Mixing–tank flow discharge.

Q_m Manifold flow rate.

q Flow rate per unit width.

q_0 Value of q at the inlet.

q_b Volumetric bedload discharge per unit width.

q_s Volumetric suspended sediment discharge per unit width.

q_{s_i} Volumetric suspended sediment discharge for the ith size range.

q_1, q_2 Values of q before and after a hydraulic jump, respectively.

R Submerged specific gravity of the sediment.

R_b Hydraulic radius with respect to the bed.

R_b' Hydraulic radius with respect to the grains.

R_e Reynolds number.

R_{e_0} Value of R_e at the inlet.

R_i Gradient Richardson number.

R_i Richardson number.

R_{i_0} Value of R_i at the inlet.

R_{ic} Critical Richardson number.

R_{in} Normal Richardson number.

R_p Particle Reynolds number.

R_{p_i} Particle Reynolds number for sediment with a grain size D_i.

r_o Ratio of near–bed concentration to layer–averaged concentration for uniform sediment.

r_{o_i} Ratio of near–bed concentration to layer–averaged concentration for sediment in the ith size range.

S Bed slope.

S_o Normalized excess shear stress.

s Submerged specific gravity of the sediment.

T_{in} Temperature of the dense fluid emanating from the inlet.

T_{fl} Temperature of the uncontaminated water in the flume.

t Time.

t_o Characteristic depositional time.

U Layer–averaged velocity in the x–direction.

U_a Average layer–averaged velocity.

U_r Reference velocity.

u Local velocity in the x–direction, averaged over turbulence.

u' Fluctuating component of the velocity in the x–direction.

u_m Maximum velocity in the x–direction along a given vertical.

u_* Bed shear velocity.

u_{*_c} Critical bed shear velocity associated with the initiation of motion.

u_*' Skin (grain) shear velocity.

u_*'' Bedform shear velocity.

v_s Sediment fall velocity.

v_{s_i} Fall velocity of sediment in the ith size range.

w Local velocity in the z–direction, averaged over turbulence.

w' Fluctuating component of the local velocity in the z–direction.

w_e Water entrainment velocity.

w_ω Fictitious velocity.

W_* Dimensionless sediment fall velocity.

x Longitudinal down–channel axis.

$\mathbf{x}$ Correction factor for viscous effects.

Z_u Similarity variable for uniform sediment.

Z_m Similarity variable for non–uniform sediment.

Z_{eff} Effective similarity variable.

z Vertical axis, normal to the bed.

z_b Bed elevation.

z_o Zero–velocity level.

z_c Distance above the bed at which $c = 0.5\ c_b$.

z_{ci} Distance above the bed at which $c_i = 0.5\ c_{b_i}$.

z_m Distance above the bed to the point of maximum velocity.

z_n Distance above the bed at which $u = 0.5\ u_m$.

GREEK SYMBOLS

α_i Shape factor for sediment in the ith size range.

α_o Constant (= 26.3).

α_O Shape factor for saline currents

β_i Shape factor for sediment in the ith size range.

γ_o Constant ($= 2.4 \cdot 10^{-3}$).

δ Excess fractional density due to salt.

δ_i Normalized grain size

Δ Layer–averaged excess fractional density due to salt.

Δ_b Bedform height.

ΔB Buoyancy scale.

ΔV Velocity scale.

η Normalized vertical coordinate.

θ Dimensionless bed shear stress.

θ_c Dimensionless critical bed shear stress.

θ' Dimensionless skin (grain) shear stress.

κ Von Karman's constant (= 0.4).

λ Bed porosity (Chapter 2).

λ,λ Stretching factor (Chapter 7).

λ_o Reference value of λ.

ν Kinematic viscosity of uncontaminated water.

ξ_u Shape function for velocity.

ξ_{ci} Shape function for concentration of sediment in the ith size range.

ρ Density of uncontaminated water.

ρ_s Sediment density.

σ_ϕ Standard deviation on the ϕ scale.

$\sigma_{\phi o}$ Reference value of $\sigma_{\phi o}$.

σ_{sg} Geometric standard deviation.

τ Reynolds stress.

τ_b Bed shear stress.

τ_b' Bed shear stress due to grain (skin) friction.

τ_b'' Bed shear stress due to the form drag associated with bedforms.

ϕ Scale for sediment size.

$\overline{\phi}$ Mean value of ϕ.

ϕ_i Value of ϕ corresponding to D_i.

Ψ Volumetric sediment discharge per unit width.

Φ Buoyancy discharge per unit width.

Φ_0 Value of Φ at the inlet.

Φ_a Average buoyancy discharge.

Φ_s Buoyancy discharge due to suspended sediment.

ψ_i Volumetric sediment discharge of material in the ith size range per unit width.

ψ_{e_i} Equilibrium value of the sediment discharge of material in the ith size range.

θ Dimensionless bedload transport rate.

CHAPTER 1. INTRODUCTION

1.1 Sediment–Driven Flows: Turbidity Currents

Turbidity currents are currents of water laden with sediment that move downslope in otherwise still bodies of water. Their driving force is obtained from the sediment, which renders the flowing turbid water heavier than the clear water above. A turbidity current initiated by a sediment–laden river flowing into a lake is illustrated in Figure 1.1 (Lambert et al., 1976).

Turbidity currents occur in the ocean (Inman et al., 1976), lakes (Weirich, 1984), and reservoirs (Chikita, 1989). They may be caused by the direct inflow of turbid water, as shown in Figure 1.1, by wave action (Shepard et al., 1974), by subaqueous slumps induced by seismic or other disturbances (Dengler et al., 1984; El–Robrini et al., 1985; Lambert and Giovanoli, 1987), by dumping of mining tailings (Normark and Dickson, 1976a; Hay et al., 1982), or by dredging operations (Estourgie, 1988).

Two types of turbidity currents can be distinguished: the discontinuous or surge–like currents and the continuous or plume–like currents. Discontinuous currents are usually generated by instantaneous sources of suspended sediment and therefore are events of limited time duration. The turbidity current generated by an earthquake at the Grand Banks of Newfoundland in 1929 (Heezen and Ewing, 1952), is a good example of a discontinuous current. On the other hand, continuous currents are produced by steady sources of suspended sediment and can last for hours and even days. The sediment–driven plume shown in Figure 1.1 evolves into a continuous turbidity current downstream from the point where it plunges.

Turbidity currents are characterized by a well defined front or "head", followed by a thinner layer known as the "body" of the current (Figure 1.2). Continuous turbidity flows are characterized by a body which is several times the length of the head, while in the case of pulse–like or discontinuous currents the body reduces to a short "tail".

Turbidity currents are members of a larger class of stratified flows known as gravity or density currents (Simpson, 1982). A simple density current is driven by density differences produced by salinity or temperature. Salt and heat are conservative contaminants; they may be advected or diffused, but their total amount in the flow is conserved. By contrast, sediment is in general a non–conservative contaminant; sediment can be entrained from, or deposited on, the bed, thus changing the total amount of sediment in suspension.

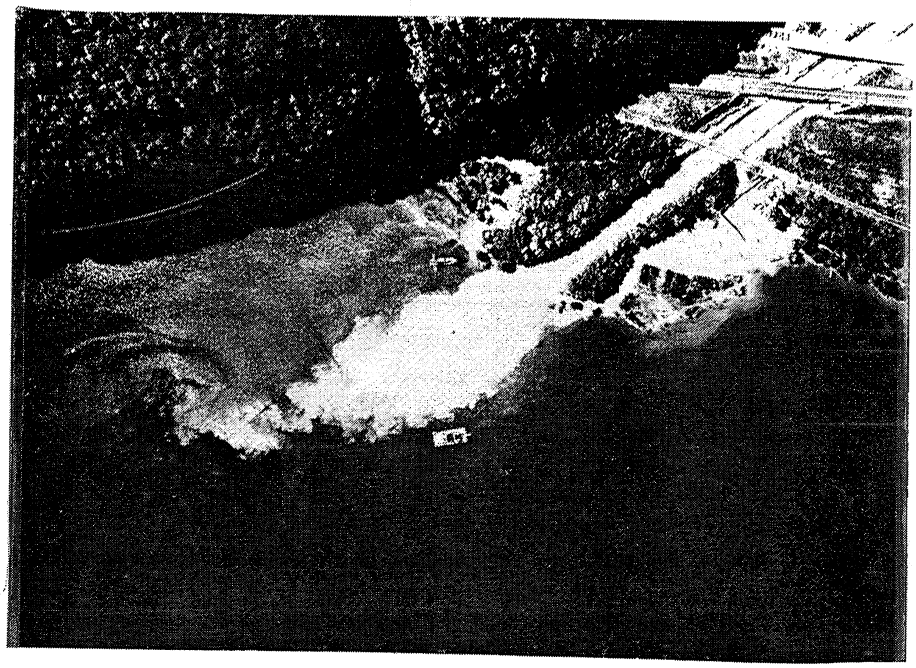

Fig. 1.1 Plunge point of the sediment–laden Linth River into Lake Walensee. A turbidity current forms downstream (from Lambert et al., 1976).

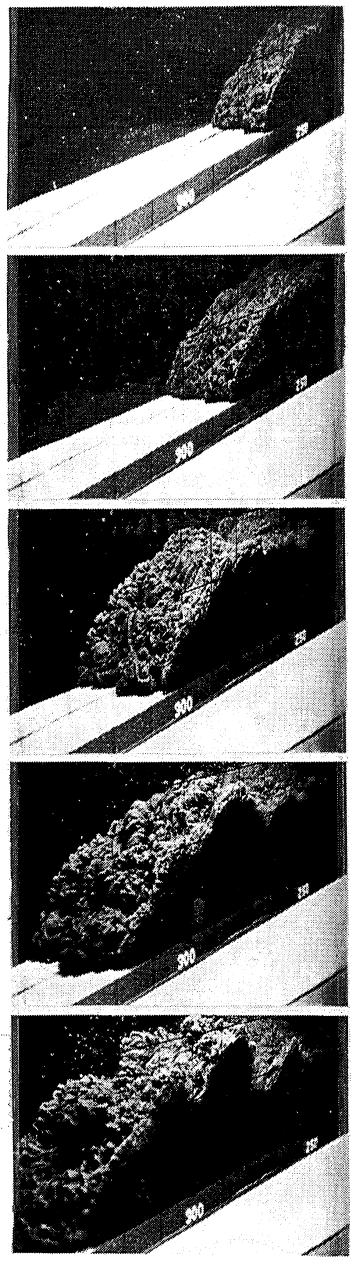

Fig. 1.2 Head of a turbidity current flowing downslope. The current is driven by 100 μ crushed coal.

A turbidity current must generate enough turbulence to hold its sediment in suspension. If it is not able to do so, the sediment deposits and the current dies. This suggests that continuous and discontinuous currents can be subdivided into depositing and eroding types, depending on which one of the mechanisms, deposition or erosion, dominates.

The extra degree of freedom, i.e. sediment entrainment and deposition, is what makes turbidity currents far more interesting than their simpler cousins, the conservative currents. Under certain conditions, a turbidity current might erode its bed, pick up sediment, become heavier, accelerate, and pick up even more sediment, increasing its driving force in a self–reinforcing cycle.

1.2 Geological Implications of Turbidity Flows

Turbidity currents constitute a major mechanism for the transport of fluvial, littoral, and shelf sediments into deeper waters. These flows are considered to be responsible for the scouring of many, but not all, submarine canyons, which are often of massive proportions (Shepard and Dill, 1966). They may be eroded directly into deltaic deposits in the form of a delta–front trough, or into the continental shelf as in the case of Scripps and La Jolla submarine canyons (Figure 1.3). Only flows of substantial velocity could accomplish this excavation. The conditions under which the generation of such swift, canyon–scouring currents becomes possible, have intrigued marine geologists and oceanographers for many years (Menard, 1964).

Below the mouths of most canyons, turbidity currents form vast depositional fans which have many of the features of alluvial fans (Bouma et al., 1985). The sedimentary deposits created by turbidity currents, known as turbidites (Bouma, 1962), are a major constituent of the geological record (Pettijohn et al., 1987). Turbidite formation has a direct impact on the morphology and facies of submarine fans (Walker, 1980). Since submarine fans can constitute major hydrocarbon reservoirs (Shanmugam and Moiola, 1985), they have become one of the most studied depositional systems. As pointed out by Normark et al. (1983/84), there is a lack of common ground between models for modern and ancient turbidite deposits. In order to understand the mechanism of turbidite formation, it is necessary to develop a satisfactory model of turbidity currents which can relate the nature of this flows to the deposits.

1.3 Engineering Significance of Turbidity Flows

Probably the most important impact of turbidity currents in ocean engineering practice is on the reliability of structures (Seymour, 1986). Heezen and Ewing (1952) re–examined the data from the Grand Banks earthquake of 1929 and based on the timing of the breaks in a large number of transoceanic telegraph cables, they deduced that the failures had been most likely produced by a turbidity current generated by the earthquake. More recently, similar cable failures due to the action of turbidity flows have been reported in Hawaii (Dengler et al., 1984) and Algeria (El–Robrini et al., 1985). It is clear from these observations that

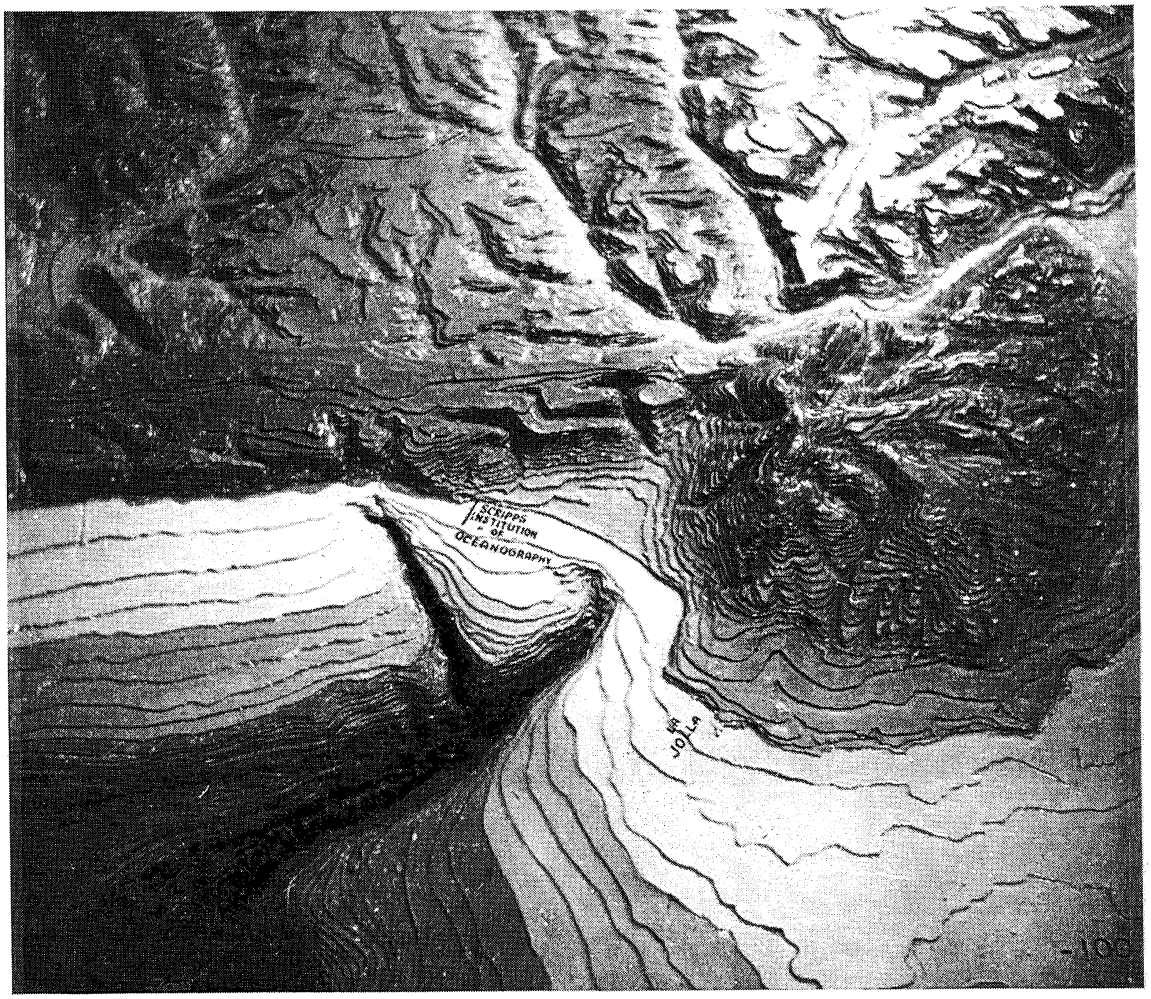

Fig. 1.3 Modeled Topography of Scripps and La Jolla submarine canyons (courtesy of Doug Inman, Scripps Institution of Oceanography).

swift currents are capable of both producing large drag forces and also undermining foundational supports for cables and pipelines. For example, a proposed ocean thermal energy conversion plant is to be located off the coast of Oahu, Hawaii (Niedoroda et al., 1985). An intake pipe with a diameter of about 10 m is to be built on steep slopes in deep water. The evidence for turbidity currents having speeds of up to 2 m/s on this area (Dengler et al., 1984) suggests that the design of the foundation for this intake pipe will be a challenging engineering problem.

Another important engineering aspect of turbidity currents has to do with the impact these flows have on the water quality and sedimentation in lakes and reservoirs (Hakanson and Jansson, 1983; Bruk, 1985). Turbidity flows were observed in lakes and man–made reservoirs long before their occurrence in the ocean became apparent (Forel, 1885; Grover and Howard, 1938). A continuous turbidity current flowing into a laboratory reservoir is shown in Figure 1.4 (Bell, 1942). This situation usually occurs during flood periods when rivers carry a large amount of sediment in suspension (Graf, 1983). In China, where the suspended load in most rivers is very large, the venting of turbidity currents through bottom outlets to reduce the siltation of reservoirs has become common practice (Fan, 1985). Even though the bed slopes of lakes and reservoirs are orders of magnitude smaller than those in the ocean, turbidity currents are still capable of traveling very long distances without loosing their identities, e.g. more than 100 km in Lake Mead (Howard, 1953).

The ability of turbidity currents to transport sediment has also been put to use for the disposal of mining tailings (Normark and Dickson, 1976a) and ash from power station boilers (Jenkins, 1970). Environmental concern has reduced waste disposal into lakes, but in the ocean, the dumping of mining tailings continues (Hay, 1987a,b).

1.4 Field Observations of Turbidity Flows

Only a few direct observations of turbidity currents in the field have been made. Field measurements are rendered difficult by the need to work underwater, the substantial equipment requirements, and the tendency for swift currents to destroy the measuring apparatus (Inman et al., 1976). Most of the field work has been related to continuous turbidity currents. The reason for this is that the occurrence of discontinuous or surge–like currents is difficult to predict and thus more complicated to monitor.

Table 1.1 summarizes the major field studies in the ocean to date. The first comprehensive observations of turbidity currents were made as part of a long–range program at Scripps Institution of Oceanography. In a landmark contribution, Inman et al. (1976) explained the development of sustained sand–driven turbidity currents in Scripps submarine canyon (Figure 1.5). Sand is supplied to the head of the canyon by littoral drift. During storms, a pattern of edge waves is set up along the shore, with an antinode at the head of the canyon. The waves action serves to stir up sand at the head and to induce a weak, oscillating down–canyon flow. The sediment–laden water starts to move downslope due to the action of gravity

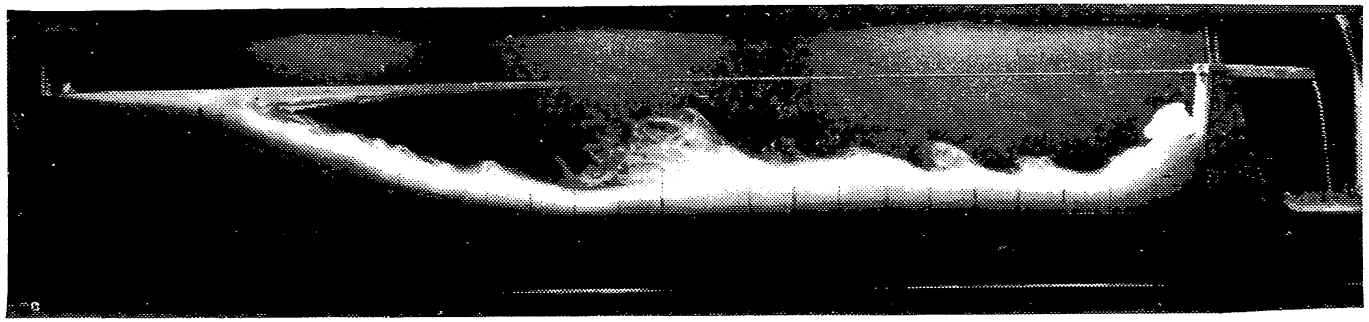

Fig. 1.4 Continuous turbidity current flowing into a laboratory reservoir (after Bell, 1942).

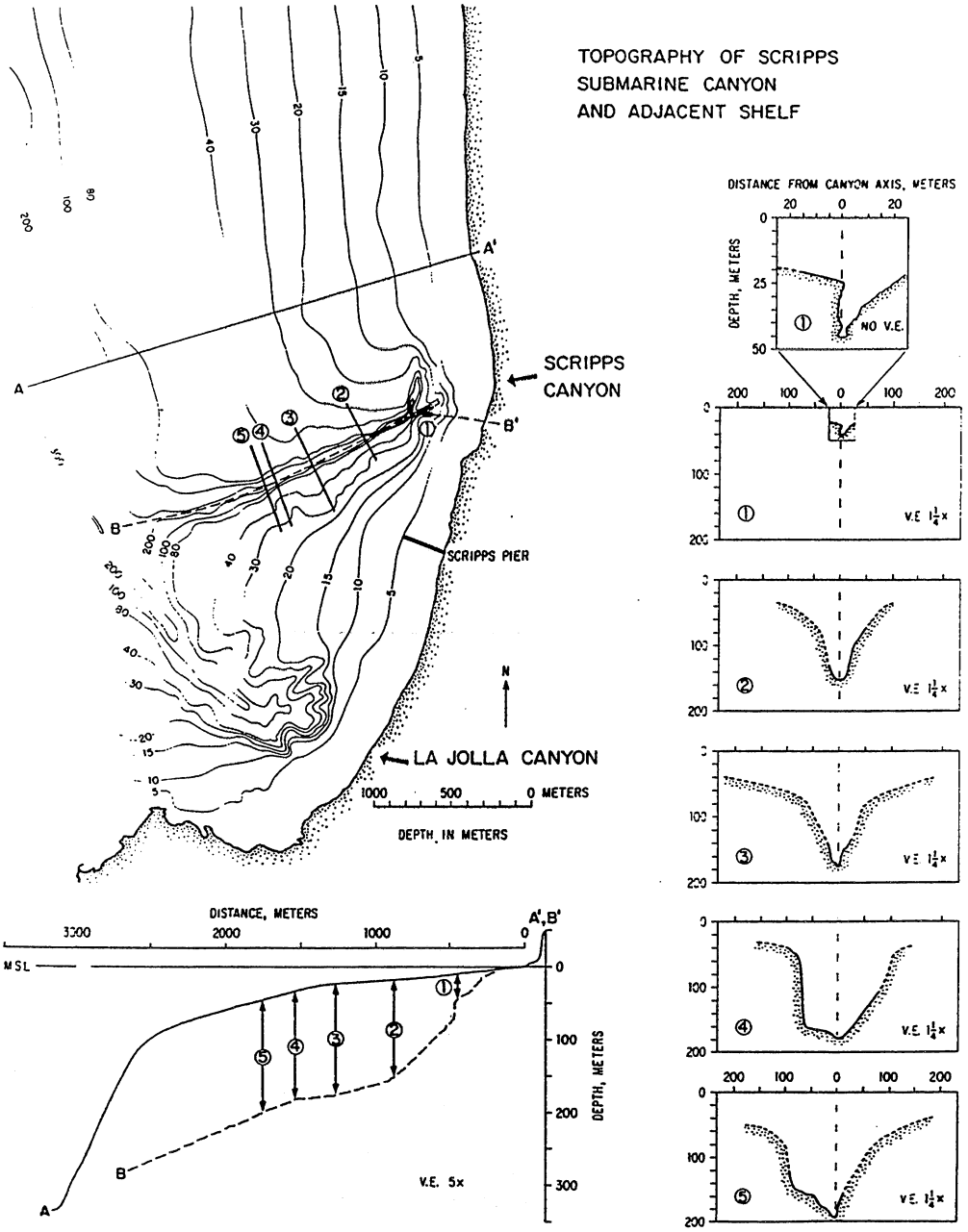

Fig. 1.5 Physical characteristics of Scripps Submarine Canyon (courtesy of Doug Inman).

TABLE 1.1 CHARACTERISTICS OF TURBIDITY CURRENTS IN THE OCEAN

Site	Mean Bottom Slope	Sediment Size (mm)	Flow Speed (m/s)	Flow Thickness (m)	Flow Duration (hr)	Observer
Scripps Canyon	0.08	0.15	1.90	< 5.0	2.50	Inman et al. (1976)
Rupert Inlet	0.04 0.04	0.03 0.03	0.30–1.20 0.20–0.60	2.0–5.0 15.0	< 1.0 ?	Hay (1987)
Bute Inlet	0.01	0.30	0.15	> 4.0	2.5	Prior et al. (1987)
Salt River Canyon	0.10 0.10	0.30–0.60 0.30–0.60	0.45–0.80 1.50–2.40	> 2.0 > 2.0	0.25–2.0 0.10	Wood et al. (1984)
Oahu Hawaii	0.09	0.20	3.00	?	0.50	Dengler et al. (1984)

on the suspended sand in discontinuous pulses. If the storm is of sufficient duration, the discontinuous pulses evolve into a strong, down–canyon current that continues to flow until it depletes the sand supply at the canyon head. This current is often strong enough to destroy the equipment installed to monitor it. Inman et al. (1976) report the measurement of nine such currents. They note the following:

> "On 24 November 1968 a sustained current of 190 cm/s was measured for 2–1/2 hours before losing the sensors. In all cases, instruments placed at site 1 (depth 44 m) were lost following the initiation of sustained downcanyon flows. The flows always begin with up– and down–canyon events or pulses that progressively become stronger in the down–canyon direction."

More recently, Hay et al. (1982) and Hay (1987a,b) used the Rayleigh scattering mechanism as a technique to avoid the loss or damage of conventional instrumentation. They obtained acoustic backscatter images to estimate the thickness and the excess density of both surge–like and continuous currents. The field experiments were conducted at Rupert Inlet, British Columbia, which serves as a receiving basin for tailings discharged by Island Copper Mine.

Prior et al. (1987) observed intense turbidity current activity in another British Columbia fjord. A year–long monitoring program was conducted within an elongated channel–fan system at Bute Inlet, which is supplied at its head by the Homathko and Southgate rivers. Measurements of bottom velocities and sediment collected in traps, as well as damage to

moorings and equipment, captured the signatures of frequent, energetic events. Maximum velocities were estimated to be about 3 m/s, while flow thicknesses were on the order of 30 m or more. Coarse sand was lifted 6 to 7.5 m above the sea floor. The turbidity currents travelled as far as 50 km over bottom slopes of less than two percent.

Wood et al. (1984) obtained continuous measurements of current velocities in the head of Salt river submarine canyon, St. Croix, U.S. Virgin Islands, during a six day period following the passage of hurricane Klaus. They were able to observe an intense down–canyon flow event that persisted for approximately thirty hours. Average down–canyon current speeds during this event ranged from 45 to 80 cm/s. High velocity pulses, ranging from 1.5 to 2.4 m/s, occurred at irregular intervals. These high velocity pulses were associated with extremely large suspended sediment concentrations that reduced visibility conditions to zero. Large bed forms were seen to migrate downslope at rates estimated to be on the order of meters per hour.

Indirect measurements of turbidity current speeds have recently been obtained by Dengler et al. (1984). Off southeast Oahu, Hawaii, an array of current sensors recorded four successive episodes of downslope displacement associated with high speed near bottom currents of up to 2 m/s. These episodes coincided with the maximum storm effects of hurricane Iwa, suggesting that the turbidity current events were caused by a succession of slope failures.

There have been also a number of observations of turbidity currents in lakes and reservoirs. It is easier to deploy sensors in these water bodies than in the ocean, and the occurrence of turbidity flow events can, in most cases, be determined beforehand.

Normark and Dickson (1976a) observed turbidity currents produced by the discharge of taconite tailings into Lake Superior at Silver Bay, Minnesota. The sublacustrine fan formed by the currents covers an area of approximately 20 km^2 and extends to a water depth of 285 m (Normark and Dickson, 1976b). The geometry, morphology, and sediment distribution on this small, man–made fan fit the characteristics of submarine fans remarkably well (Figure 1.6).

Lambert et al. (1976) and Lambert (1982) measured the speed and direction of turbidity currents induced by two sediment–laden rivers flowing into Lake Walensee (Figure 1.1) and by the Rhine river flowing into Lake Constance, Switzerland. More recently, Lambert and Giovanoli (1987) observed channelized turbidity currents in Lake Geneva. During 72 days of current measurements, several river–induced turbidity currents having velocities larger than 30 cm/s were recorded in the subaqueous canyon of the Rhone delta. The observed peak velocity was 90 cm/s. The detachment of instruments from their anchors was attributed to a major subaqueous slide that took place just after the peak discharge of the Rhone river.

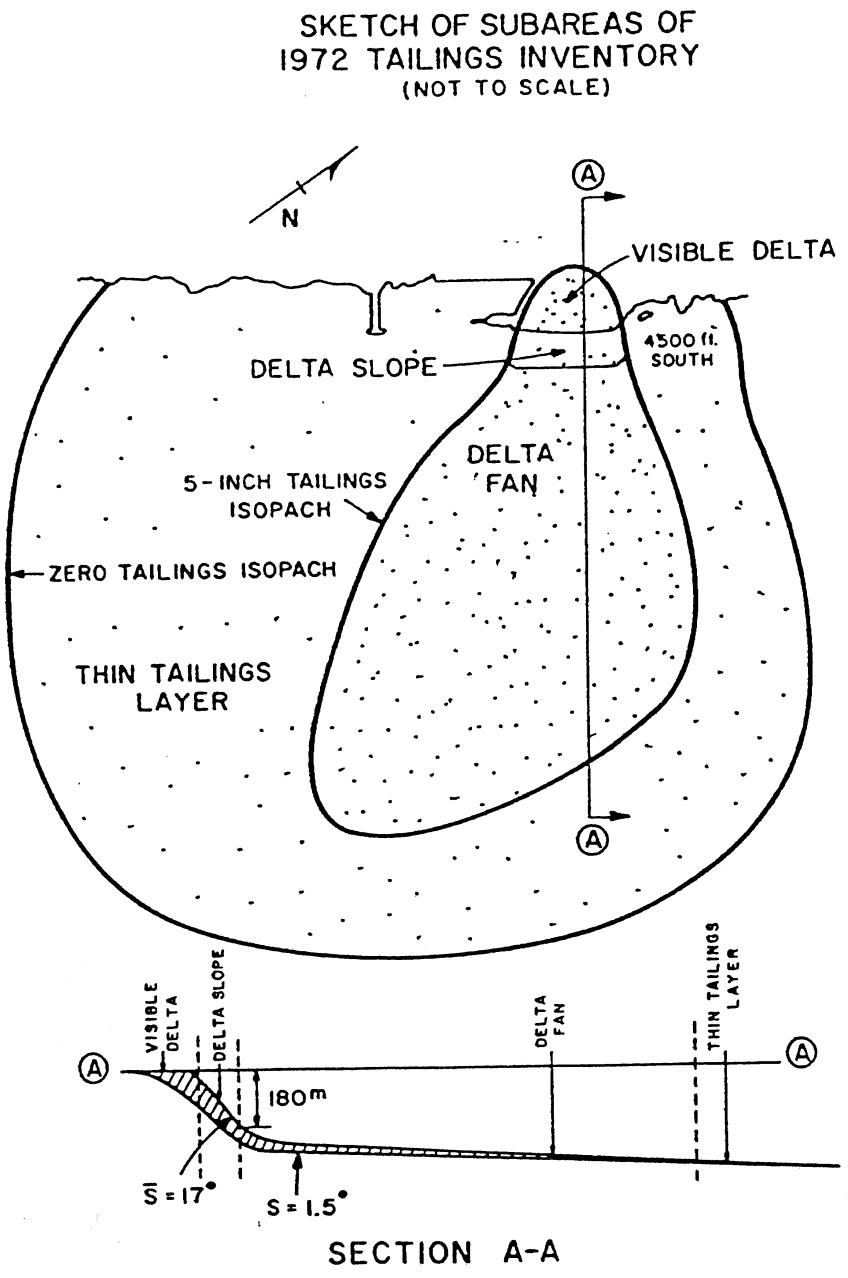

Fig. 1.6 Man–made depositional fan at Silver Bay, Minnesota (from Normark and Dickson, 1976b).

Weirich (1984, 1986) has used a three–dimensional sensor network to monitor the occurrence and development of turbidity currents in a Canadian glacial lake. Weirich was able to collect detailed information on surge events having velocities of 1.1 m/s and continuous currents exceeding 90 cm/s.

Chikita (1980, 1989) has conducted an extensive program of measurements at Katsurazawa Reservoir, Sapporo, Japan, producing detailed information about the vertical structure of turbidity currents. Velocity, temperature, and sediment concentration profiles were measured at a number of locations within the reservoir. The flow measurements were complemented with grain size distributions of both suspended and bottom sediment samples.

1.5 Previous Analytical and Experimental Work

1.5.1 Analytical Studies

Many attempts have been made to delineate the equations of motion for turbidity currents. Hinze (1960), Plapp and Mitchell (1960), Johnson (1962), and Chu et al. (1979) provide detailed analytical treatments. A characteristic of all of these studies is the difficulty in formulating the process of simultaneous entrainment of sediment from, and deposition onto, the bed. More recent treatments incorporate the possibility of erosion and deposition, thus advancing beyond the formulation for conservative density currents presented in the landmark paper of Ellison and Turner (1959).

Pantin (1979) made a very important step forward by obtaining the first description of a turbidity current that could either deposit or erode. He used a phase–plane analysis to show how a small disturbance can evolve into a sustained turbidity flow.

Parker (1982) formulated a model similar to that of Pantin. He proposed that under certain circumstances, turbidity currents may "ignite" or self–accelerate to high velocities by means of sediment entrainment from the bed. Parker used his model to explain the generation of currents swift enough to scour submarine canyons.

Pallesen (1983) tried to delineate the conditions needed for erosion and deposition using concepts developed by Pedersen (1977) for conservative density currents and obtained a modified Bagnold autosuspension criterion (Bagnold, 1962).

Stow and Bowen (1980) developed a model for the transport and sorting of fine–grained sediment by muddy turbidity currents. Later, Bowen et al. (1984) used a similar approach to model turbidity currents in Navy Submarine Fan.

Siegenthaler and Buhler (1985) and Buhler and Siegenthaler (1986) were able to obtain a description of turbidity currents and their deposits on inclined boundaries. Siegenthaler and Buhler (1986) also proposed a method to reconstruct the characteristics of surge–like turbidity currents based on hydromechanical parameters of the sediment deposit.

The models of Pantin (1979) and Parker (1982) were formulated for the rather unrealistic case of currents that are constant in space but developing in time. Parker, Fukushima, and Pantin (1986) extended the model to continuous currents that develop spatially. They used it to predict the generation of self–accelerating currents in Scripps submarine canyon (Fukushima et al., 1985), using information obtained by Inman et al. (1976).

Akiyama and Stefan (1985) extended Ellison and Turner's model for spatially developing conservative currents to account for sediment erosion and deposition. They found that turbidity currents can be accelerating–erosive, decelerating–erosive, or decelerating–depositive, depending on the initial flow conditions, bed slope, water temperature, and sediment characteristics. Recently, Akiyama and Stefan (1988) extended their model to simulate eroding and depositing turbidity currents in a slightly diverging channel.

Hay (1987b) developed a model for continuous turbidity currents which accounts for the effect of channel curvature and overspill, and used it to provide estimates of tailings transport and deposition at Rupert Inlet, British Columbia.

The majority of the theoretical models for turbidity currents are of the integral or depth–averaged type, i.e. the equations of motion are integrated in the vertical direction. Recently, Stacey and Bowen (1988a,b) developed a numerical model for unsteady, spatially uniform turbidity currents using a mixing–length model for turbulence. This constitutes the first attempt to compute the vertical structure of turbidity currents.

1.5.2 Experimental Studies

Most of the experimental work on gravity currents along inclined or horizontal boundaries has concentrated on conservative density currents (Ellison and Turner, 1959; Fietz and Wood, 1967; Wilkinson and Wood, 1971; Simpson and Britter, 1979), while sediment–driven flows have received less attention. The main reason for this, besides experimental convenience, is that conservative currents cover a wide range of geophysical phenomena, e.g. katabatic winds, dust storms, saltwater intrusions in estuaries, convective currents in lakes and reservoirs, and the flow of methane along the roof of mines (Turner, 1973).

Experimental studies by sedimentologists have emphasized depositing turbidity currents and associated turbidites (Kuenen and Migliorini, 1950; Middleton, 1967; Luthi, 1980, 1981). On the other hand, experimental studies conducted by hydraulic engineers concerned with problems associated with lakes and reservoirs have been devoted to currents driven by fine sediment that neither deposit nor erode (Stefan, 1973; Ashida and Egashira, 1975).

Among the earliest experimental studies is the work of Michon, Goddet, and Bonnefille (1955). They conducted experiments on continuous currents driven by fine sediment in two laboratory flumes and a field canal. Their main interest was in examining velocity, temperature, and sediment concentration profiles and evaluating the effect of roughness on the flow structure.

Middleton (1967) performed one the most complete studies on turbidite formation by discontinuous turbidity currents. By releasing suspensions of plastic beads, graded beds were formed. The experiments indicated that the structure of the deposits was quite different, depending on the concentration of the initial suspension. More recently, Middleton and Neal (1989) conducted similar experiments using both glass and plastic beads. They studied the effect of sediment concentration, grain size, and mixture volume on turbidite thickness.

Tesaker (1969) conducted experiments on continuous currents driven by clay. By adding different amounts of sand, the ability of the clay–driven currents to transport sand was tested. Due to the fact that the sand used was rather coarse, most of the flows were strongly depositional.

Luthi (1981) was interested in modeling the formation of deltas in lakes. He performed experiments on non–channelized turbidity currents and their deposits. Using a fairly large tank, Luthi was able to reproduce some of the characteristics (e.g. depositional lobes) of turbidites in submarine fans (Normark, 1970).

Siegenthaler and Buhler (1985) investigated continuous depositional turbidity currents in two laboratory flumes. Measurements of bulk flow properties, such as flow speed and thickness, and turbidite thicknesses were taken. The depositional currents were characterized by a dimensionless sedimentation number proportional to the rate at which buoyancy is lost; this number remained approximately constant during an experiment.

Garcia (1985) carried out experiments on continuous turbidity currents driven by uniform sediment. The objective of these experiments was to generate self–accelerating turbidity currents by allowing the currents to entrain sediment from the bed. Because of the limited length of the experimental channel (20 m), the phenomenon of self–acceleration was not clearly manifested during the experiments. Numerical predictions coupled with the experimental observations suggested that a channel a few hundred meters long would be necessary to reproduce the "accelerating" currents envisioned by Parker (1982), Fukushima et al. (1985), and Akiyama and Stefan (1986).

1.6 Present Study

1.6.1 Motivation

As illustrated in Figure 1.7, submarine canyons have very steep slopes which are, in general, much larger than those encountered in submarine fans. The slope discontinuity is indicative of a transition from an overall erosive environment upstream (Inman et al., 1976) to an overall depositional environment downstream (Normark, 1970). This transition appears to be driven, at least in part, by a change in flow regime of turbidity currents from high–velocity supercritical flow to low–velocity subcritical flow (Komar, 1971). Aspects of such a transition are illustrated for the case of a current flowing through a reservoir in Figure 1.4.

It is well known from studies of subaerial open–channel flow (Rajaratnam, 1967) and density flows (Turner, 1973) that this change in flow regime is accomplished via a hydraulic jump. A bulk Richardson number R_i describing the flow has a critical value R_{ic} near unity, such that the range $R_i < R_{ic}$ corresponds to the high–velocity regime upstream of the jump, and the range $R_i > R_{ic}$ corresponds to the low–velocity regime downstream.

The submerged hydraulic jump so hypothesized and the resultant sedimentary deposits have been the subject of considerable speculation. Menard (1964) argued that the development of levees bordering deep–sea channels was caused by the thickening of a turbidity current after a hydraulic jump. Van Andel and Komar (1969) posited the occurrence of hydraulic jumps in order to interpret the characteristics of sediment deposits in enclosed basins. Mutti (1977) suggested that turbidity currents going through a change in slope drop excess sand and form particular turbidites at the mouth of submarine channels. Ravenne and Beghin (1983) observed that certain characteristics in the sedimentary record of debris flows, e.g. strong local deposition, may indicate the location of a jump.

The hydraulic jump itself remains unobserved in the field, in part due to the depth at which it is inferred to occur (greater than 1000 m in the ocean). Likewise, the several experimental studies conducted to date on depositional turbidity currents have not included the change in slope necessary to induce a hydraulic jump.

Internal hydraulic jumps associated with stratification due to salt or temperature (as opposed to sediment) have been studied extensively (Yih and Guha, 1955; Wood, 1967; Wilkinson and Wood, 1971; Stefan and Hayakawa, 1972; Wood and Simpson, 1984; Baddour, 1987; Rajaratnam et al., 1988). These studies, along with several existing theories of eroding and depositing turbidity currents (Fukushima et al., 1985; Akiyama and Stefan, 1985; Parker et al., 1986), have motivated the work presented herein.

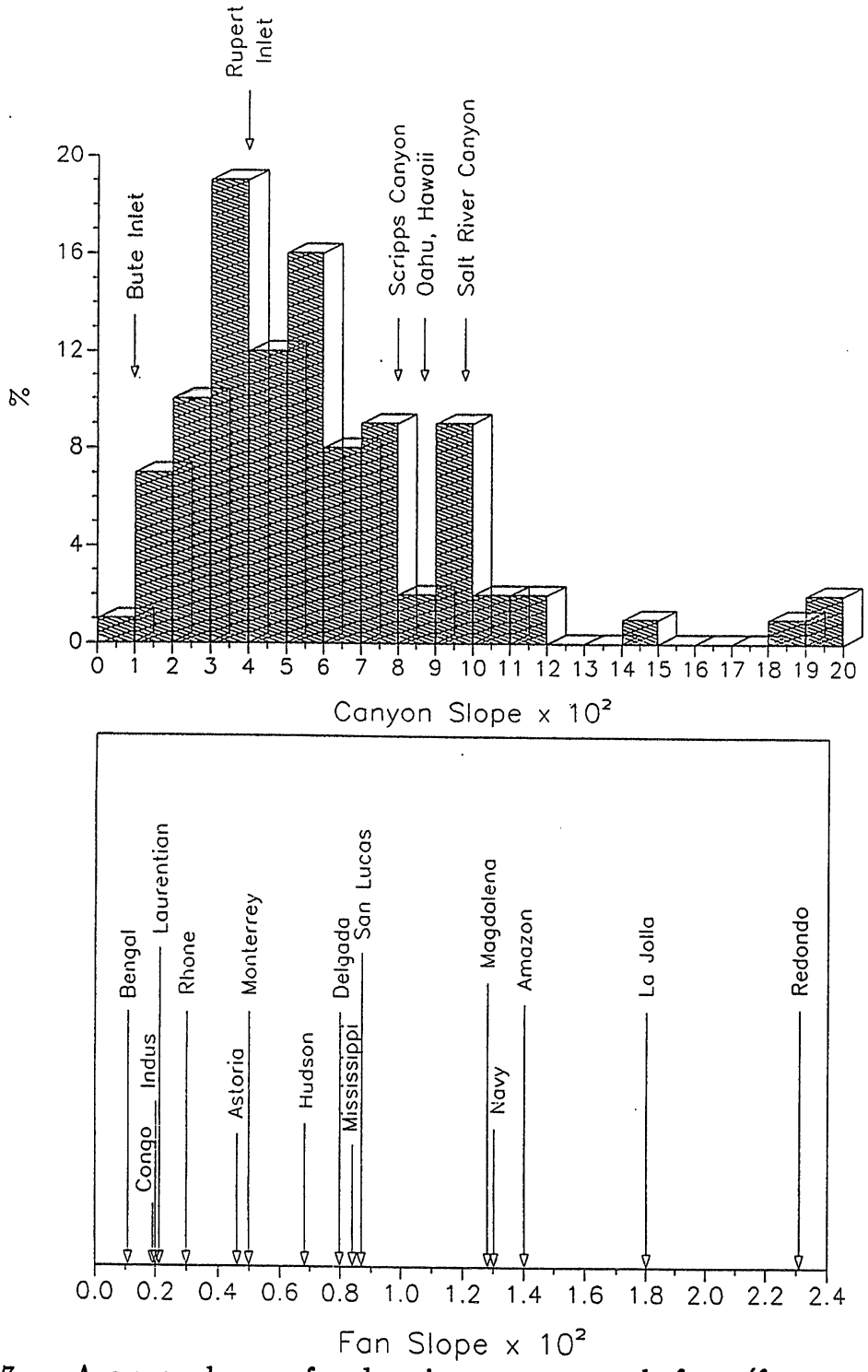

Fig. 1.7 Average slopes of submarine canyons and fans (from several sources).

1.6.2 Objectives

The objectives of this study were to examine the hydraulics, depositional characteristics, and erosive capabilities of turbidity currents in the proximity of a slope change. To accomplish this an experimental study was conducted. The experimental work aimed at investigating the following aspects:

i) the characteristics of continuous, saline and turbidity currents in different flow regimes (i.e. supercritical and subcritical),
ii) the degree of similarity between internal hydraulic jumps in underflows driven by salt and sediment,
iii) the role of the hydraulic jump in the mechanics of sediment deposition and flow dilution by water entrainment from above,
iv) the effect of sediment characteristics, such as sediment fall velocity and non–uniformity on the spatial pattern of deposition, turbidite thickness, and longitudinal and vertical sorting.
v) the conditions under which the slope discontinuity is clearly reflected in the depositional record, and
vi) the ability of currents driven by fine sediment to entrain bed sediment into suspension and carry it to deeper waters.

In Chapter 2, the equations of motion for a dilute suspension are presented and an integral model for turbidity currents driven by poorly–sorted sediment is developed.

In Chapter 3, the experimental apparatus and procedure are described.

In Chapter 4, the experimental results on conservative saline currents are presented.

In Chapter 5, the experimental results on depositional turbidity currents are presented.

In Chapter 6, the experimental results on sediment–entraining saline currents are presented.

In Chapter 7, several existing relationships for computing sediment entrainment rates in open channel flows are tested and two new formulations are obtained.

In Chapter 8, a summary and conclusions are presented.

CHAPTER 2. THEORETICAL BACKGROUND

2.1 Governing Equations for a Dilute Suspension

The situation described in Figure 2.1 is considered. A steady, continuous turbidity current is flowing downslope through a quiescent body of water, which is assumed to be infinitely deep and unstratified except for the turbidity current itself. The cross–section is taken to be rectangular, with a width many times longer than the underflow thickness, so that variations in the lateral direction can be neglected. The bed has a constant, small slope S and is covered with sediment; the x coordinate is directed downslope tangential to the bed, and the z coordinate is directed upward normal to the bed. The suspension is made up of a mixture having N size ranges, and is assumed to be sufficiently dilute so that collision between grains and hindered settling can be neglected. The submerged specific gravity of the sediment is denoted by $R = (\rho_s/\rho - 1)$, where ρ_s is the density of the sediment and ρ is the density of the clear water. The local components of the flow velocity, averaged over the turbulence are u(x,z) and w(x,z) in the x and z directions respectively; $c_i(x,z)$ denotes the local component of volumetric concentration of sediment in the ith size range, averaged over the turbulence; p(x,z) denotes the deviation of the pressure from its clear–water hydrostatic value, averaged over the turbulence. The fluctuating components (i.e. instantaneous minus average) of the velocity in the x and z directions are u′ and w′, respectively, and c_i' is the fluctuating volumetric concentration of sediment in the ith size range. The total volumetric concentration of suspended sediment at a given point, is given by $\mathbf{c} = \Sigma\, c_i$. The conditions $\mathbf{c} << 1$ and $Rc << 1$ are assumed to be satisfied everywhere within the flow, justifying the assumption of a kinematic viscosity ν equal to the value for clear water. The same assumptions also justify the use of the Boussinesq approximation; that is, density differences affect only body forces. The density of the suspension is thus taken to be equal to ρ everywhere, except when multiplied by the gravitational acceleration in which case is to be $\rho(1+Rc)$. Since the slope is taken to satisfy the condition $S << 1$, the components of the gravitational acceleration g in the x and z direction can be approximated as gS and –g respectively. It is assumed that within the turbidity current, the scalings $u >> w$ and $\partial/\partial z >> \partial/\partial x$ hold (i.e. the slender flow or boundary layer approximation). The turbidity current is assumed to be fully turbulent, with all viscous terms negligible. Under these constraints, the equations of motion averaged over the turbulence take the following form:

Mean fluid mass balance

$$\frac{\partial u}{\partial x} + \frac{\partial w}{\partial z} = 0 \qquad (2.1)$$

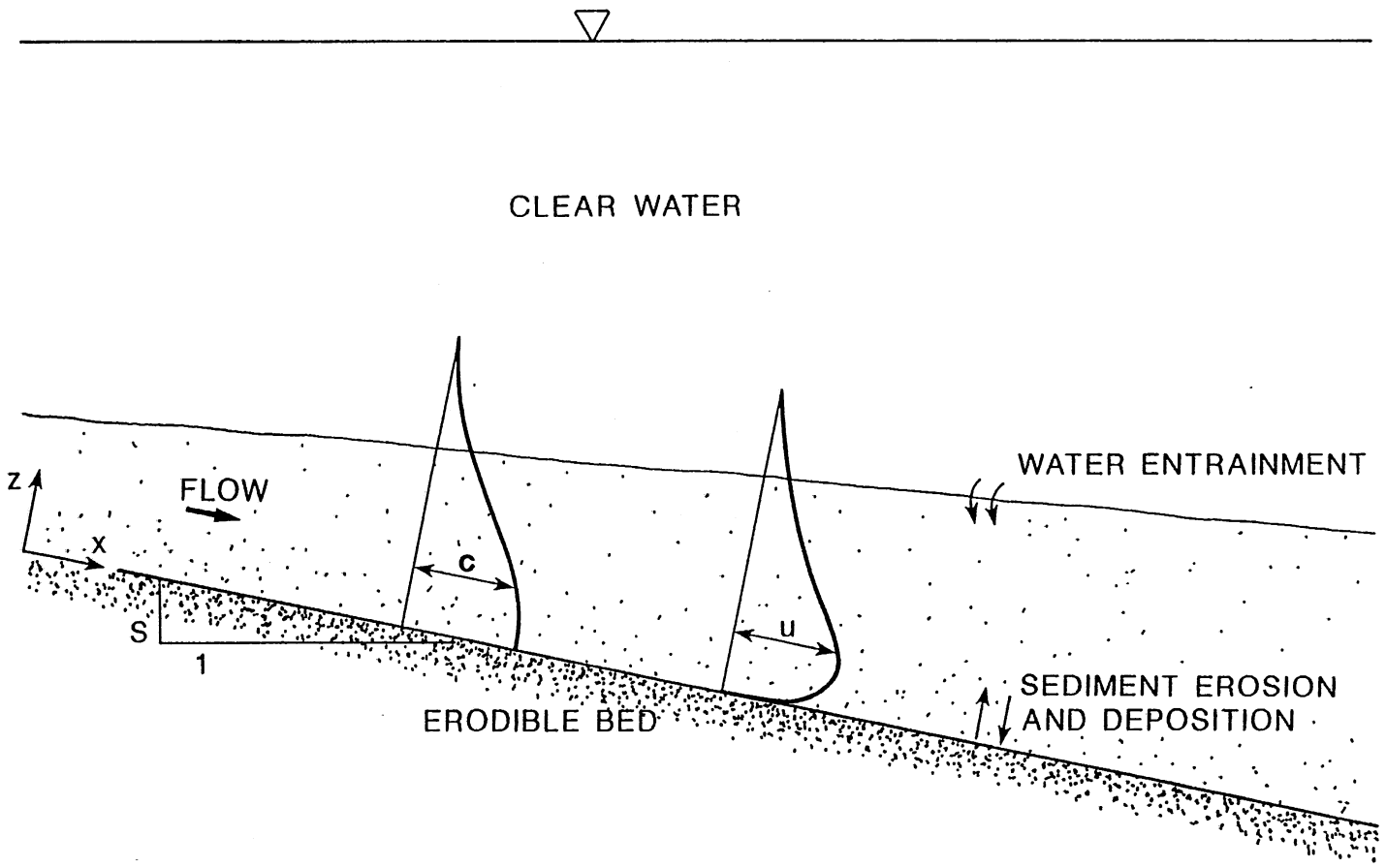

Fig. 2.1 Turbidity current flowing downslope through a quiescent body of water.

Mean momentum balance in the x and z directions

$$\frac{\partial u^2}{\partial x} + \frac{\partial uw}{\partial z} = - \frac{1}{\rho} \frac{\partial p}{\partial x} + g\ R\ c\ S + \frac{1}{\rho} \frac{\partial \tau}{\partial z} \tag{2.2}$$

$$0 = - \frac{1}{\rho} \frac{\partial p}{\partial z} - g\ R\ c \tag{2.3}$$

Mean sediment mass balance for the material in the ith size range

$$\frac{\partial u c_i}{\partial x} + \frac{\partial w c_i}{\partial z} = - \frac{\partial}{\partial z} (F_i - v_{s_i} c_i) \tag{2.4}$$

where $\tau = - \rho \overline{u'w'}$ is the Reynolds stress, $F_i = \overline{c_i'w'}$ is the Reynolds sediment flux, and v_{s_i} is the fall velocity of the sediment in the ith size range.

The upward component of the mean momentum balance (2.3) can be reduced to

$$p = \rho\ g\ R \int_z^\infty c\ dz \tag{2.5}$$

corresponding to the component of hydrostatic pressure due to the weight of the sediment. After taking the derivative of p with respect to x in (2.5), and upon substitution into (2.2), the downslope component of mean momentum balance reduces to

$$\frac{\partial u^2}{\partial x} + \frac{\partial uw}{\partial z} = - g\ R \frac{\partial}{\partial x} \int_z^\infty c\ dz + g\ R\ c\ S + \frac{1}{\rho} \frac{\partial \tau}{\partial z} \tag{2.6}$$

2.2 Vertically Integrated Balance Equations

For the geometry of Figure 2.1, equations (2.1), (2.4), and (2.6) can be integrated in the z direction to yield the following relations: mean momentum balance,

$$\frac{d}{dx} \int_0^\infty u^2\ dz = - g\ R \frac{d}{dx} \int_0^\infty \int_z^\infty c\ dz'dz + g\ R\ S \int_0^\infty c\ dz - u_*^2 \tag{2.7}$$

where $u_*^2 = \tau|_{z=b} / \rho = - \overline{u'w'}|_{z=b}$ denotes an approximation of the kinematic bed shear stress $\tau|_{z=0}$, u_* is the bed shear velocity, and $z = b$ denotes a level very close to the bed but outside any range where viscous effects are important. The parameter u_* denotes the bed shear velocity. The equation of mean fluid mass balance (2.1), integrates to yield

$$\frac{d}{dx}\int_0^{\infty} u\,dz + w_{\infty} = 0 \tag{2.8}$$

where w_{∞} is a fictitious velocity needed by the nature of the boundary layer approximation. For boundary layers of the type shown in Figure 2.1, it is common to set $w_{\infty} = \partial h/\partial t - w_e$, where the first term on the right represents the time rate of growth of the layer thickness h, and w_e is an entrainment velocity. For the steady current being considered herein $\partial h/\partial t = 0$, and equation (2.8) reduces to

$$\frac{d}{dx}\int_0^{\infty} u\,dz = w_e \tag{2.9}$$

The equation of mean sediment mass balance for the material in the ith size range (2.4) integrates to yield

$$\frac{d}{dx}\int_0^{\infty} u\,c_i\,dz = F_{b_i} - v_{s_i}\,c_{b_i} \tag{2.10}$$

where c_{b_i} denotes the near–bed concentration of the sediment in the ith size range, and $F_{b_i} = \overline{c_i' w'}|_{z=b}$ denotes the near–bed volumetric upward normal Reynolds flux of sediment in that size range, in both cases evaluated at a distance $z = b$ above the bed. The term F_{b_i} represents the rate of entrainment of sediment from the bed into the suspension by turbulence. A dimensionless entrainment rate $E^{\circ}_{s_i}$ can be defined such that $F_{b_i} = v_{s_i} E^{\circ}_{s_i}$, so that (2.10) takes the form

$$\frac{d}{dx}\int_0^{\infty} u\,c_i\,dz = v_{s_i}\,(E^{\circ}_{s_i} - c_{b_i}) \tag{2.11}$$

Thus $v_{s_i}(E^{\circ}_{s_i} - c_{b_i})$ denotes the difference between the erosion rate of sediment from the bed and the deposition rate of sediment on the bed. That is, it denotes the net rate of incorporation of bed sediment of the ith size range into the flow. The equation of sediment balance for a turbidity current driven by a mixture of sediment is obtained by summing (2.11) over all sizes;

$$\frac{d}{dx}\sum_{i=1}^{n}\int_0^{\infty} u\,c_i\,dz = \sum_{i=1}^{n} v_{s_i}\,(E^{\circ}_{s_i} - c_{b_i}) \tag{2.12}$$

2.3 Similarity Assumption and Slab Approximation

In order to allow for a tractable model, it is necessary to make some assumptions concerning the vertical structure of the flow. As it is done in most integral models, the assumption of similarity is introduced. The parameters u and c_i are assumed to maintain approximately similar profiles in the z–direction as the current develops in the downslope direction. That is, the following similarity laws are assumed to hold

$$\frac{u(x,z)}{U(x)} = \xi_u(\eta); \qquad \frac{c_i(x,z)}{C_i(x)} = \xi_{ci}(\eta,\delta_i) \qquad i=1...N \tag{2.13}$$

where

$$\eta = \frac{z}{h} \quad ; \quad \delta_i = \frac{D_i}{D_{sg}}$$

In the above equations, D_i denotes the mean diameter of the suspended sediment in the ith size range, and D_{sg} denotes a geometric mean size of the suspended sediment given by

$$\ln(D_{sg}) = \frac{\Sigma\, C_i \ln(D_i)}{\Sigma\, C_i} \tag{2.14}$$

The layer–averaged velocity U and volumetric concentration C_i, and also the layer thickness h, are defined via a set of moments (Ellison and Turner, 1959):

$$Uh = \int_0^\infty u\, dz \qquad \left[\int_0^\infty \xi_u\, d\eta = 1\right] \tag{2.15}$$

$$U^2h = \int_0^\infty u^2\, dz \qquad \left[\int_0^\infty \xi_u^2\, d\eta = 1\right] \tag{2.16}$$

$$UC_ih = \int_0^\infty u\, c_i\, dz \quad i=1...N \quad \left[\int_0^\infty \xi_u\, \xi_{ci}\, d\eta = 1\right] \tag{2.17}$$

The following relations are obtained with the aid of (2.13) ~ (2.17): The equation of fluid mass balance, (2.9) becomes;

$$\frac{dUh}{dx} = w_e \tag{2.18}$$

The equation of sediment mass balance, (2.12) integrates to;

$$\sum_{i=1}^{n} \frac{dUC_ih}{dx} = \sum_{i=1}^{n} v_{s_i} (E^\circ_{s_i} - c_{b_i}) \tag{2.19}$$

where c_{b_i} is evaluated at $z = b = 0.05\ h$ or $\eta = 0.05$. Equation of momentum balance, (2.7) becomes;

$$\frac{dU^2h}{dx} = g\ R\ (\Sigma\ \alpha_i\ C_i)\ h\ S - \frac{1}{2}\ g\ R\ \frac{d}{dx}((\Sigma\ \beta_i\ C_i)h^2) - u_*^2 \quad (2.20)$$

where α_i and β_i are shape factors defined as follows

$$\alpha_i = \int_0^\infty \xi_{ci}(\eta,\delta_i)\ d\eta \quad (2.21)$$

$$\beta_i = 2 \int_0^\infty \int_\eta^\infty \xi_{ci}(\eta,\delta_i)\ d\eta' d\eta \quad (2.22)$$

These order one shape factors will be evaluated later with the aid of the experimental data. A reasonable approximation, however, can be obtained by introducing the so–called "top hat" (Turner, 1973) or "slab" (Pantin, 1979) assumption, according to which the shape functions have one constant value inside the turbidity current, an another outside it. For a turbidity current moving under clear, still water, the assumption can be phrased as follows:

$$\xi_u(\eta) = \xi_{ci}(\eta,\delta_i) = \left\{ \begin{array}{ll} 1 & \text{for } 0 < \eta < 1 \\ 0 & \text{for } \eta > 1 \end{array} \right\} \quad (2.23)$$

With the aid of (2.23), equation (2.20) reduces to

$$\frac{dU^2h}{dx} = g\ R\ C\ h\ S - \frac{1}{2}\ g\ R\ \frac{d}{dx}(C\ h^2) - u_*^2 \quad (2.24)$$

where

$$C = \Sigma\ C_i \quad (2.25)$$

denotes the sum of the layer–averaged concentrations corresponding to each sediment size range.

2.4 Closure for Theoretical Model

The model derived for steady, continuous turbidity currents driven by a mixture of sediment consists of the equations of fluid mass, sediment mass, and momentum balance, i.e. (2.18), (2.19) and (2.24). This model is an extension of the three–equation models proposed by Fukushima et al. (1985), Akiyama and Stefan (1985), and Parker et al. (1986) to describe the development of turbidity currents driven by uniform sediment. The theoretical model proposed herein must be appropriately closed with

algebraic laws for w_e, u_*, E^o_{si}, and c_{bi}, as functions of U, C_i, and h. Although some of the parameters concerning the closure relationships will be obtained with the data gathered during the experiments, a tentative set of relationships is introduced at this point. The relation for water entrainment is taken to be

$$w_e = e_w U \tag{2.26}$$

where e_w is a water entrainment coefficient known to be a function of the bulk Richardson number R_i (Ellison and Turner, 1959), which is defined as

$$R_i = \frac{gRCh}{U^2} \tag{2.27}$$

There are a number of empirical relationships in the literature for $e_w(R_i)$. For example, the following expression

$$e_w = \frac{0.075}{(1+718\ R_i^{2.4})^{0.5}} \tag{2.28}$$

was obtained by Garcia (1985) using data for turbidity currents and conservative saline currents. According to (2.28), as R_i approaches zero, e_w approaches a value of 0.075, which is appropriate for non-stratified flows, and as R_i increases, e_w decreases rapidly.

It is customary to take the bed shear stress to be proportional to the square of the velocity (Turner, 1973), so that

$$u_*^2 = C_D\ U^2 \tag{2.29}$$

where C_D is a bed friction coefficient. In general, C_D can be expected to be a function of boundary layer parameters. The values of C_D for turbidity currents have been found to vary between 0.002 and 0.05 (Garcia, 1985); the lower values correspond to observations in reservoirs, and the higher values are associated with laboratory experiments. In principle, C_D can be taken to be constant for a given current in order to simplify the analysis.

The near-bed concentration c_{bi} can be related to the layer-averaged concentration C_i by a parameter r_{oi};

$$c_{bi} = r_{oi}\ C_i \tag{2.30}$$

where

$$r_{oi} = r_o \, g_o(\delta_i) \tag{2.31}$$

In (2.31), $r_o = c_b/C$ is a shape factor denoting the ratio between the near–bed concentration and the layer–averaged concentration for the case of uniform sediment (Parker, 1982), and $g_o(\delta_i)$ is a function that accounts for the non–uniformity of the sediment size. The experiments of Parker et al. (1987) indicate that r_o is almost a constant, equal to about 2.0, for a wide range of dimensionless shear velocities u_*/v_s. Information concerning the function $g_o(\delta_i)$ will be obtained later in the light of the experimental results.

The sediment entrainment coefficient $E^o_{s_i}$ can be evaluated as

$$E^o_{s_i} = p_i \, E_{s_i} \tag{2.32}$$

where p_i denotes the fraction of material in the ith size range present in the bed, and E_{s_i} is the entrainment coefficient for a bed fully covered by sediment in the ith size range. E_{s_i} is expected to be a function of the bed shear stress and the sediment characteristics. The characteristics of the entrainment function are treated later in more detail.

With the aid of (2.26), (2.29), (2.30), and (2.32), equations (2.18), (2.19), and (2.24), are reduced to

$$\frac{dUh}{dx} = e_w \, U \tag{2.33}$$

$$\sum_{i=1}^{n} \frac{dUC_i h}{dx} = \sum_{i=1}^{n} v_{s_i} \, (p_i \, E_{s_i} - r_{o_i} \, C_i) \tag{2.34}$$

$$\frac{dU^2 h}{dx} = g \, R \, C \, h \, S - \frac{1}{2} \, g \, R \, \frac{d}{dx}(C \, h^2) - C_D \, U^2 \tag{2.35}$$

2.5 Spatial Development of Turbidity Currents

The equations of motion (2.33), (2.34), and (2.35), can be cast in the following form

$$\frac{dh}{dx} = \frac{-R_i S + C_D + e_w \left[2 - \frac{R_i}{2}\right] + \frac{R_i}{2} \Sigma \, r_{o_i} \frac{v_{s\,i}}{U} \frac{\psi_i}{\psi} \left[\frac{\psi_{e_i}}{\psi_i} - 1\right]}{(1 - R_i)} \tag{2.36}$$

$$\frac{h}{U}\frac{dU}{dx} = e_w - \frac{dh}{dx} \tag{2.37}$$

$$\frac{h}{\psi}\frac{d\psi}{dx} = \Sigma\, r_{o_i}\frac{v_{s_i}}{U}\frac{\psi_i}{\psi}\left[\frac{\psi_{e_i}}{\psi_i} - 1\right] \tag{2.38}$$

where

$$\psi = \Sigma\, U\, C_i\, h = \Sigma\, \psi_i \tag{2.39}$$

is the volumetric sediment discharge per unit width of the turbidity current, and

$$\psi_{e_i} = \frac{p_i\, E_{s_i}\, U\, h}{r_{o_i}} \tag{2.40}$$

corresponds to the equilibrium value of the sediment discharge of material in the ith size range ψ_i, (i.e. the value at which erosion and deposition balance) for the existing values of flow velocity U and thickness h.

Equations (2.36), (2.37), and (2.38) may be called the "backwater" relations for turbidity currents, since they are equivalent to the equations describing slowly varying flows in open channels (Henderson, 1966). In fact, they provide a remarkable unification of a wide variety of flows. In their full form, they describe turbidity currents that spatially develop as they erode and deposit sediment. In the limit as v_{s_i}/U tends to zero, it is seen from equation (2.38) that the buoyancy transport $gR\psi$ becomes constant; equations (2.36) and (2.37) thus describe (for order one shape factors) the simple conservative density underflows of Ellison and Turner (1959). In this case, an equilibrium (normal) state exists, for which the Richardson number R_i and velocity U are constant, and the current thickness increases linearly with distance due to water entrainment.

If the product RC is set equal to unity in the definition of the Richardson number, and e_w and v_{s_i}/U are taken to vanish, equation (2.36) describes water surface profiles in open channel flows. In this case

$Ri = 1 / F^2$, where $F = U / \sqrt{gh}$ is the Froude number, and h is now the water depth. An equilibrium (normal) state exists, for which U, F, and h are all constant.

If Ri and v_{s_i}/U are allowed to vanish, the integral equations for the clear water wall jet are obtained (Rajaratnam, 1976). In this case, no constant equilibrium exists; U decreases, and h increases, in the downstream direction.

The set of equations (2.36)–(2.38) can also be used to model currents driven by density differences induced by both a conservative contaminant (e.g. temperature) and a non–conservative contaminant (e.g. sediment).

2.6 Supercritical and Subcritical Flows

The bulk Richardson number R_i (equation 2.27) is an important parameter governing the behavior of stratified, slender flows such as turbidity currents. This parameter has a critical value R_{ic} near unity, such that the range $R_i < R_{ic}$ corresponds to a high–velocity supercritical flow regime, and the range $R_i > R_{ic}$ corresponds to a low–velocity subcritical flow regime. In the supercritical regime, disturbances are unable to propagate upstream; thus supercritical flows are controlled from upstream. On the other hand, in the subcritical regime where disturbances are able to propagate in the upstream direction, flows are controlled from downstream. For subcritical flows, the entrainment of water from above becomes small and w_e can be taken to vanish (Turner, 1973).

In the ocean, turbidity currents are expected to be supercritical as they move downslope in submarine canyons, which are characteristically steep (Komar, 1971). Once such a current flows onto the submarine fan, it tends toward the subcritical regime due to the decline in slope.

To predict the development of supercritical currents, equations (2.36)–(2.38) can be integrated numerically starting at the canyon head and marching stepwise in the downslope direction. In the case of subcritical currents, the situation is far more complicated due to the fact that it is necessary to specify the flow parameters at some point located at the extremities of the fan or abyssal plain, from where the backwater relations can be integrated in the upstream direction. However, these boundary conditions are not known beforehand since they depend on how the current develops until reaching such a point.

2.7 Internal Hydraulic Jump

The change from supercritical flow to subcritical flow is accomplished via a hydraulic jump (Turner, 1973) as illustrated in Figure 2.2. Therein a turbidity current undergoes a hydraulic jump induced by a change in bed slope in the proximity of a canyon–fan transition. To simplify the analysis, the fan is assumed to be horizontal, bed friction in the jump region is neglected, and water entrainment from above due to the jump is considered negligible. Under these assumptions, fluid mass is conserved and (2.33) reduces to

$$q = Uh = \text{constant} \tag{2.41}$$

through the jump; here q is the flow discharge per unit width. Furthermore, it is assumed that the rate of sediment entrainment is equal to the rate of sediment deposition within the jump, thus sediment mass is conserved and (2.38) reduces to

$$\psi = \text{constant} \tag{2.42}$$

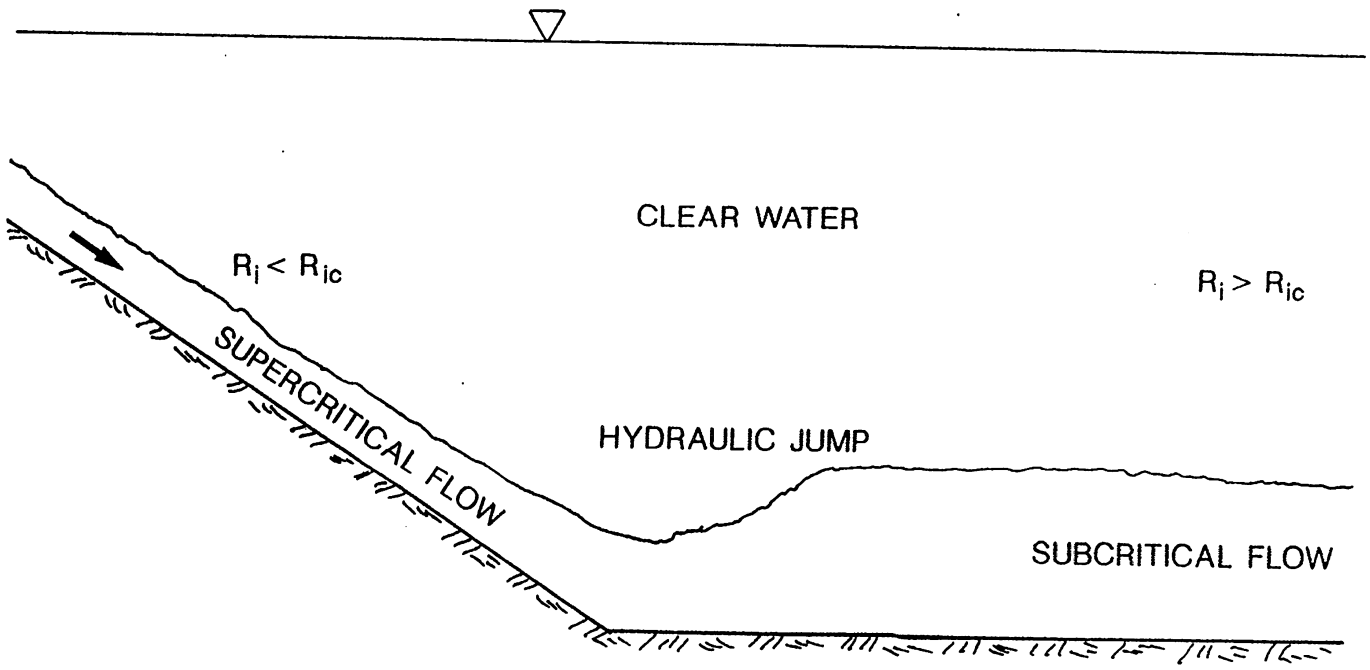

Fig. 2.2 Transition from supercritical flow to subcritical flow through a hydraulic jump.

Under these constraints, the sum of the momentum flux and the pressure force is conserved (Wilkinson and Wood, 1971; Stefan and Hayakawa, 1972), that is

$$\left| U^2 h + \beta \frac{1}{2} g R C h^2 \right|_1 = \left| U^2 h + \beta \frac{1}{2} g R C h^2 \right|_2 \qquad (2.43)$$

where the term in the left side represents the flow force evaluated at section 1 just before the jump, and the term in the right side is the flow force at section 2 just after the jump. The shape factor β can have different values on each side of the jump, but assuming that the "slab" approximation is valid for both supercritical and subcritical currents (i.e. $\beta_1 = \beta_2 = 1$), and using the following relationships

$$q = U_1 h_1 = U_2 h_2 \qquad (2.44)$$

$$\frac{R_{i_2}}{R_{i_1}} = \left[\frac{h_2}{h_1}\right]^3 \qquad (2.45)$$

obtained with the aid of (2.27), (2.41), and (2.42), equation (2.43) can be reduced to

$$\left[\frac{h_2}{h_1}\right]^3 - (1 + 2 R_{i_1}^{-1}) \left[\frac{h_2}{h_1}\right] + 2 R_{i_1}^{-1} = 0 \qquad (2.46)$$

In addition to the trivial solution $h_1 = h_2$, this equation has the following solution

$$\frac{h_2}{h_1} = \frac{1}{2} \left[\sqrt{1 + 8 R_{i_1}^{-1}} - 1\right] \qquad (2.47)$$

The above relation was originally obtained by Yih and Guha (1954), while studying hydraulic jumps in two–layer flows. For a known pre–jump Richardson number R_{i_1}, this equation gives the ratio of the sequent or conjugate current thickness h_2 to the initial current thickness h_1. It is important to realize that the current thickness h_2 is determined by the subcritical flow, which is regulated by some type of control acting further downstream. Therefore, if the control produces a current thickness h_2 which satisfies equation (2.47) then a jump will form; otherwise it will not. It should also be clear that the subcritical flow influences the location of the jump, which furthermore controls the length of the water–entraining supercritical flow upstream of the jump. This in turn influences downstream conditions. In laboratory experiments, the downstream boundary conditions are usually imposed by the experimenter (e.g. weir, sluice gate, outfall) due to the finite length of experimental facilities. In the ocean, where a current may travel several hundred kilometers without losing its identity, it is expected that the control of the flow will be through sediment deposition and bed friction.

2.8 Bed Variation due to Sediment Erosion and Deposition

The bed elevation of submarine canyons and fans where turbidity currents occur rather frequently can be expected to change over time due to sediment erosion and deposition. If the amount of sediment transported as bedload is neglected, the condition for conservation of sediment mass for a bed completely covered by sediment is given by

$$\frac{\partial z_b}{\partial t} + \frac{1}{1-\lambda}\frac{d\psi}{dx} = 0 \tag{2.48}$$

where z_b is the bed level, t is the time, λ is the bed porosity, x is the downstream distance, and ψ is the volumetric discharge of suspended sediment per unit width. With the help of (2.19) and (2.39), equation (2.48) reduces to

$$\frac{\partial z_b}{\partial t} = \frac{1}{1-\lambda}\sum_{i=1}^{n} v_{s_i}\,(c_{b_i} - E^{\circ}_{s_i}) \tag{2.49}$$

from which the following conditions can be discerned

for $c_{b_i} > E^{\circ}_{s_i}$ $\quad \frac{\partial z_b}{\partial t} > 0 \quad \Rightarrow$ aggrading bed

for $c_{b_i} < E^{\circ}_{s_i}$ $\quad \frac{\partial z_b}{\partial t} < 0 \quad \Rightarrow$ degrading bed

These conditions clearly indicate that in active submarine canyons, where erosion may often prevail over deposition, the bed of the canyon will degrade over time. On the other hand, in submarine fans where turbidity currents are often too weak to entrain sediment, sediment deposition will dominate and the fan surface will aggrade over time.

CHAPTER 3 EXPERIMENTAL APPARATUS AND PROCEDURE

3.1 The Flume

The experiments were conducted in the flume shown in Figure 3.1. The channel was 30 cm wide, 78 cm in depth, and 11.6 m in length. The slope transition was modeled in a simple one–dimensional configuration. A 5 m long inclined bed with a slope of 0.08 (4.6°) modeled the canyon and was adjoined to a 6.6 m long horizontal bed modeling the associated abyssal fan. The model canyon head, where the currents start to flow downslope, consisted of a submerged sluice gate.

The facility could be used to generate a sediment–driven current or a conservative saline current as desired. A mixing tank with a maximum capacity of 2000 liters was used to prepare the dense fluid, by either mixing sediment and water or by dissolving salt in water. After filling the experimental flume with uncontaminated tap water, the dense fluid was pumped up to a constant head tank, from where it was piped to the model canyon head (submerged sluice gate) with the help of a system of valves and a calibrated orifice flow meter. In this fashion, a saline or sediment–laden bottom current of known density could be delivered at a known rate.

The density difference between the underflow and the uncontaminated water above it acted to drive the current downslope. After traveling the length of the flume, the current emptied into an end tank. The level of the contaminated fluid in the end tank was kept below the channel bed by means of a bottom drain. This caused the downstream end of the channel to act as a submerged free overfall, preventing the reflection of the current from the end tank back upstream. Uncontaminated water was supplied to the end tank through a manifold placed at the surface to make up for the ambient water entrained by the underflow. An overflow weir served to maintain a constant water level in the flume. Proper operation of the flume and end tank allowed for the maintenance of sustained bottom currents for as long as one hour. In this way, it was possible to measure the flow in detail and to model the formation of rather thick turbidites in spite of the fact that only dilute suspensions were considered.

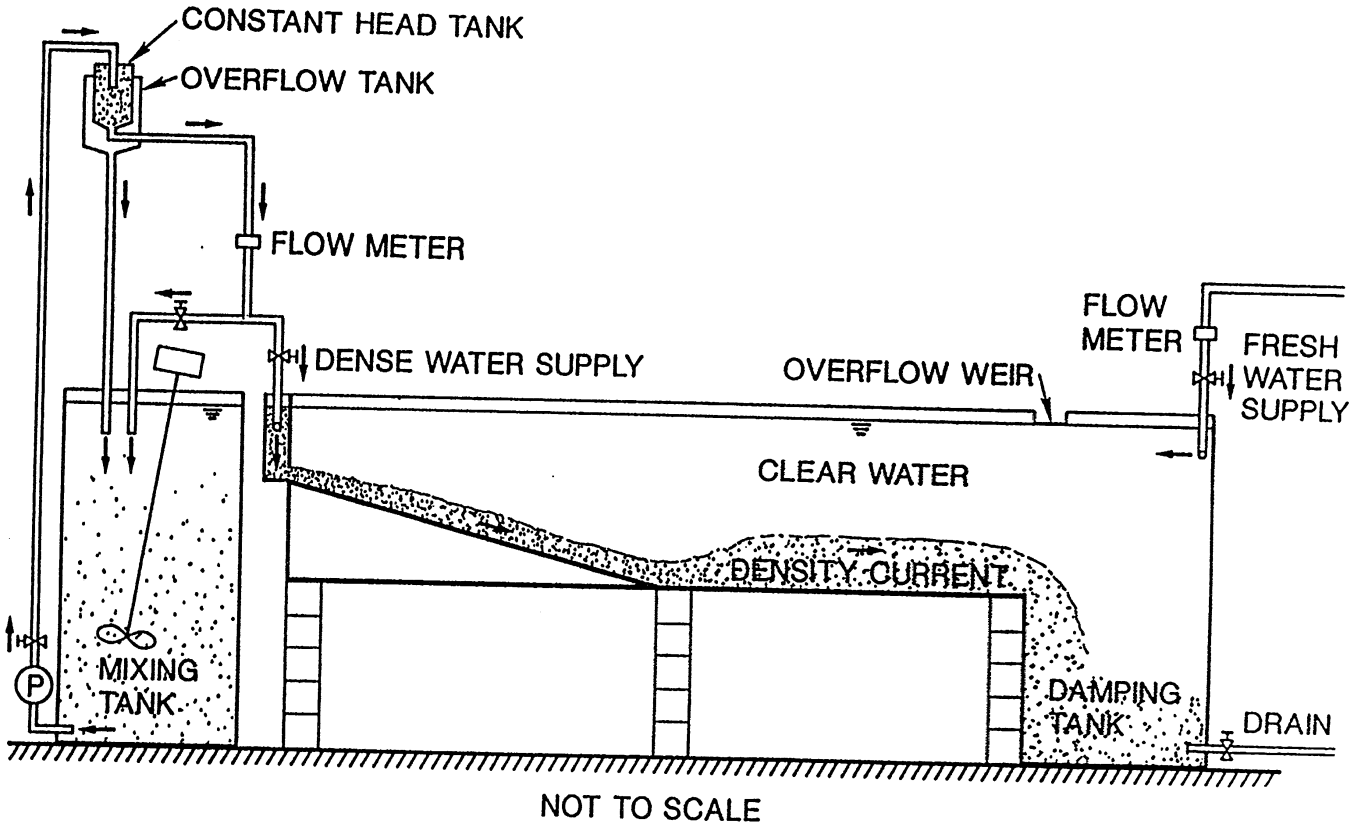

Fig. 3.1 Schematic of the experimental facility.

3.2 Measuring Instrumentation

3.2.1 Flow Velocity Measurements

The instrument used to measure flow velocities was a 3 mm diameter Shinozuka model SV–3 micropropeller, which has a measuring range of 2 cm/s to 100 cm/s and a reported accuracy of ± 10 % (Figure 3.2). This instrument operates by generating a periodic signal with a frequency which is proportional to the angular velocity of the rotating propeller. This angular velocity is in turn linearly related to the velocity of the moving fluid. The miniature current meter was periodically calibrated in a 12 m long towing tank which could produce constant speeds ranging from 1 cm/s to 25 cm/s. A typical calibration curve is shown in Figure 3.2. The micropropeller was mounted on a movable gage in order to measure flow velocities at different depths. Even though the current meter was originally designed for use in uncontaminated water, it was found that with proper care the miniature meter withstood the unfavorable conditions associated with saline or turbidity current experiments. Four different probes were used during the experimental study.

3.2.2 Suspended Sediment Concentration Measurements

3.2.2.1 Well–Sorted Sediment

To measure sediment concentrations of suspended sediment with uniform size, a Kenek model PM–206 optical light probe was used (Figure 3.3). The measuring range of the probe decreases with sediment size. The operating principle of this instrument is based on the attenuation of light due to the presence of suspended sediment. A photodetector determines the amount of light passing from a light source through a suspension and generates a signal proportional to the amount of light attenuated. Both the light receiver and the light source have a diameter of 2 mm, and the measuring gap between them is 10 mm long. By relating the light attenuation to the concentration of sediment in the suspension, instantaneous measurements of sediment concentration are obtained. This instrument was calibrated for use with the different types of sediment employed during the experiments. The calibration consisted of submerging the probe in a container with a suspension of known sediment concentration and recording the associated signal from the photodetector. In each calibration, the range of sediment concentrations between clear water and the maximum concentration expected in an experiment was covered. A typical calibration curve is shown in Figure 3.3. The probe was placed side by side with the micropropeller. In this way, the point gage holding both probes could be displaced vertically to obtain sediment concentrations and flow velocities at different locations within the flow.

3.2.2.2 Poorly–Sorted Sediment

Since the amount of light attenuation caused by a large sediment particle can be the same as that caused by a number of smaller particles, it was not possible to use the optical light probe to measure concentrations of poorly–sorted sediment. The more traditional method of measuring

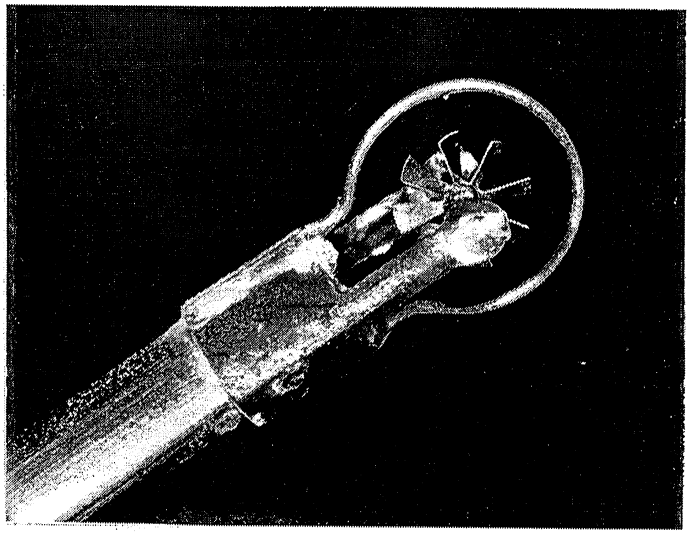

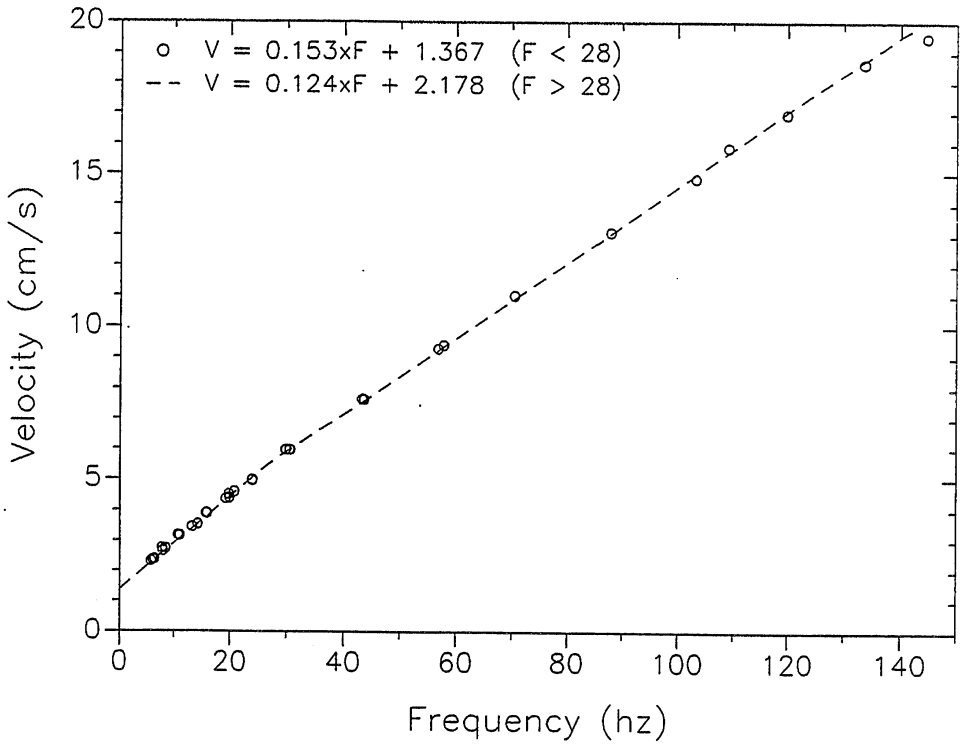

Fig. 3.2 Micropropeller and typical calibration curve.

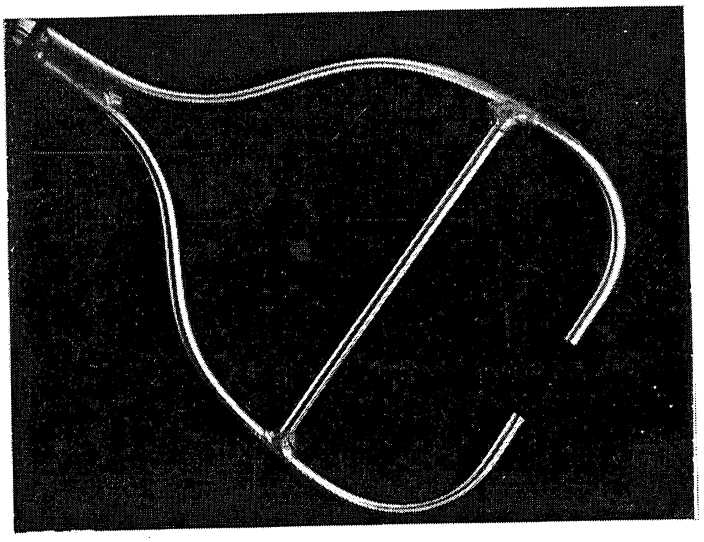

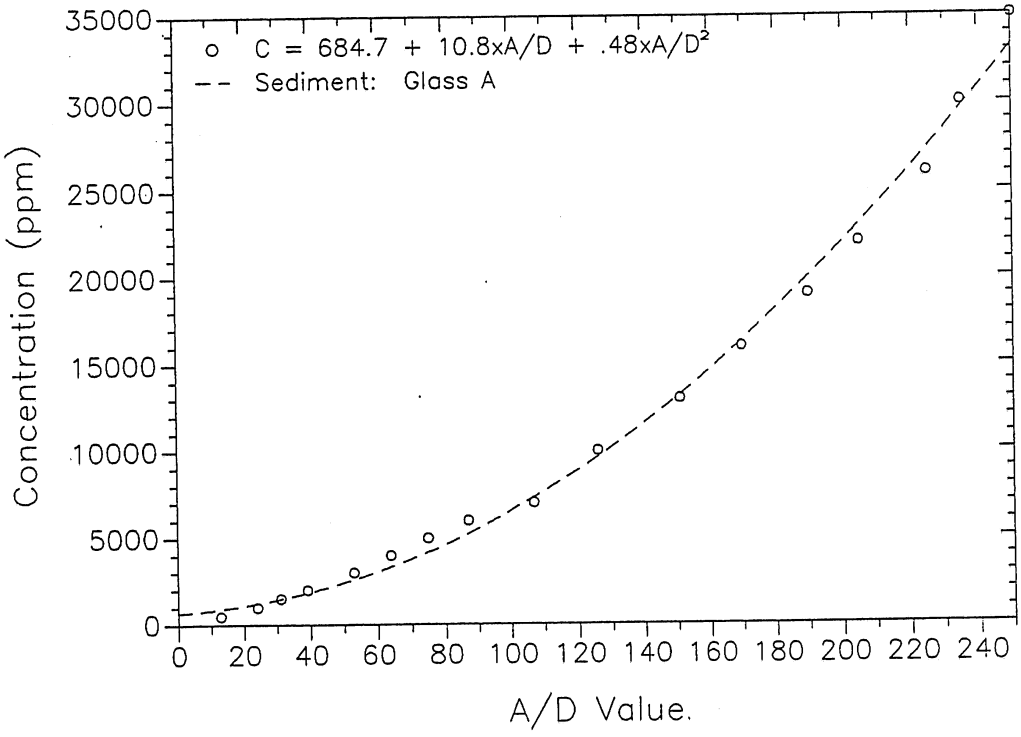

Fig. 3.3 Light probe and typical calibration curve.

sediment concentrations by means of siphons was employed instead. A rake of point samplers (Figure 3.4) was built for each measuring station taking into account the possible differences in flow thickness along the model canyon and fan. The samplers were made from 5 mm O.D. brass tubing. A streamlined shape was given to the tip of the samplers to minimize any perturbation of the flow. Each sampler was connected to a plastic hose allowing for sampling using a siphon arrangement. The samples were collected in 1000 ml glass beakers and were later analyzed to determine the averaged volumetric sediment concentration at each measuring point. Some of this samples were also used to determine the size distribution of the suspended sediment.

3.2.3 Salinity–Density Measurements

The optical light probe used to measure turbidity was also used to measure density differences due to salt content. This was done by introducing a certain amount of blue dye into the mixing tank during the preparation of the saline solution. A sample of the solution in the mixing tank was diluted to produce several reference samples of known dye and salt concentration. These samples were then used to calibrate the light probe (Figure 3.5). The density difference between the fluid in the mixing tank and the uncontaminated water in the flume was obtained by weighing samples having the same volume from both water bodies. The blue dye was used as a tracer during an experiment, and the measurements of dye concentration within a current were converted into values of excess fractional density.

3.3 Instrumentation Set–up and Data Collection

The point gage holding both the micropropeller and the light probe was mounted on a trolley (Figure 3.6). The trolley could be moved over rails which extended along the side of the flume, allowing for positioning of the instrumentation at any desired location within the model canyon and fan. Once the trolley was positioned at a measuring station along the centerline of the flume, the point gage could be moved up and down to measure velocity and sediment concentration (or excess density in the case of saline currents) profiles in the vertical direction. Additional trolleys were used to position the rakes of siphons during the experiments with poorly–sorted sediment.

The analog signals generated by the micropropeller and the light probe during an experiment were monitored by a microcomputer via an analog to digital converter card. In the case of the micropropeller, the analog signal was amplified before the conversion to take full advantage of the range of the A/D converter. The digitized signals were then used to calculate the mean flow properties of interest.

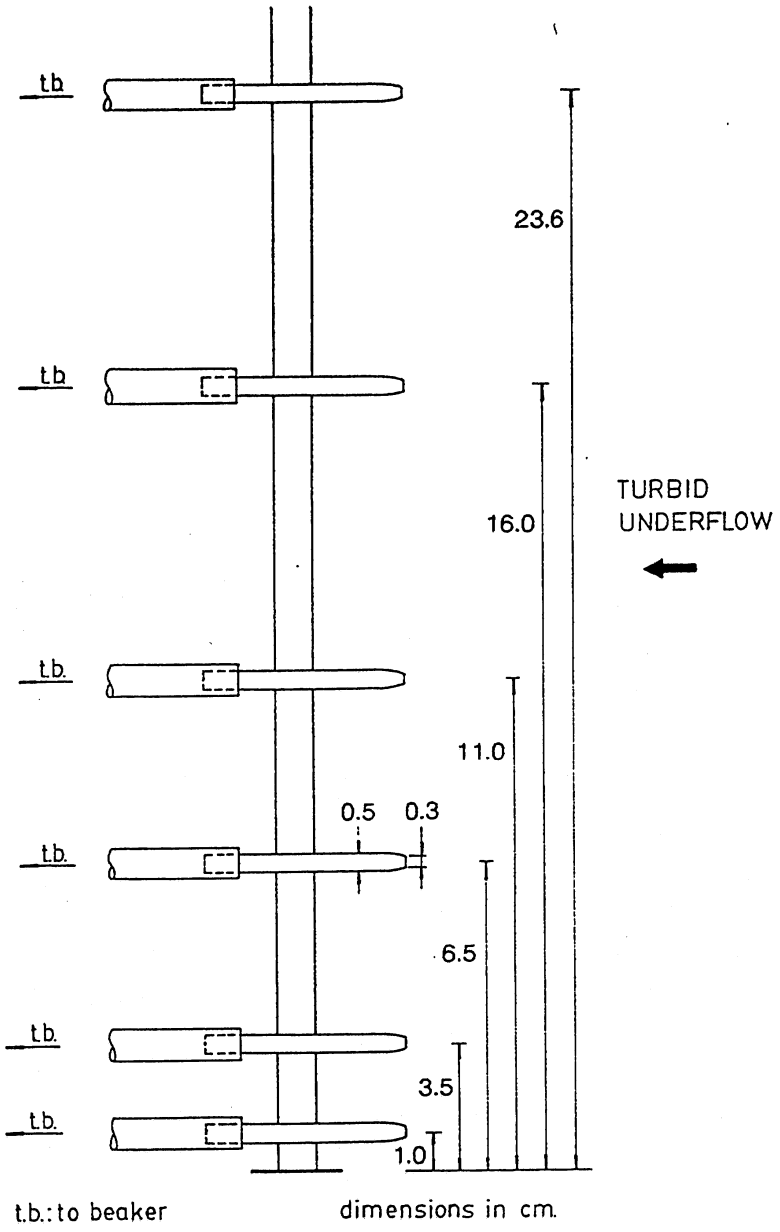

Fig. 3.4 Rake of siphons used to sample poorly–sorted suspended sediment.

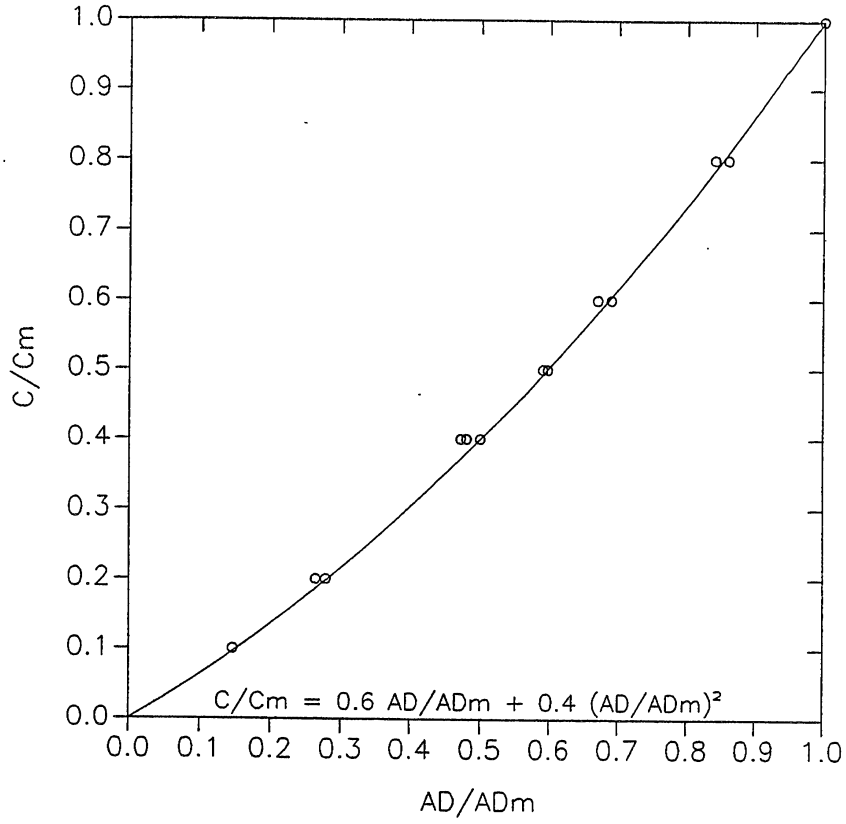

Fig. 3.5 Typical calibration curve for light probe with blue dye.

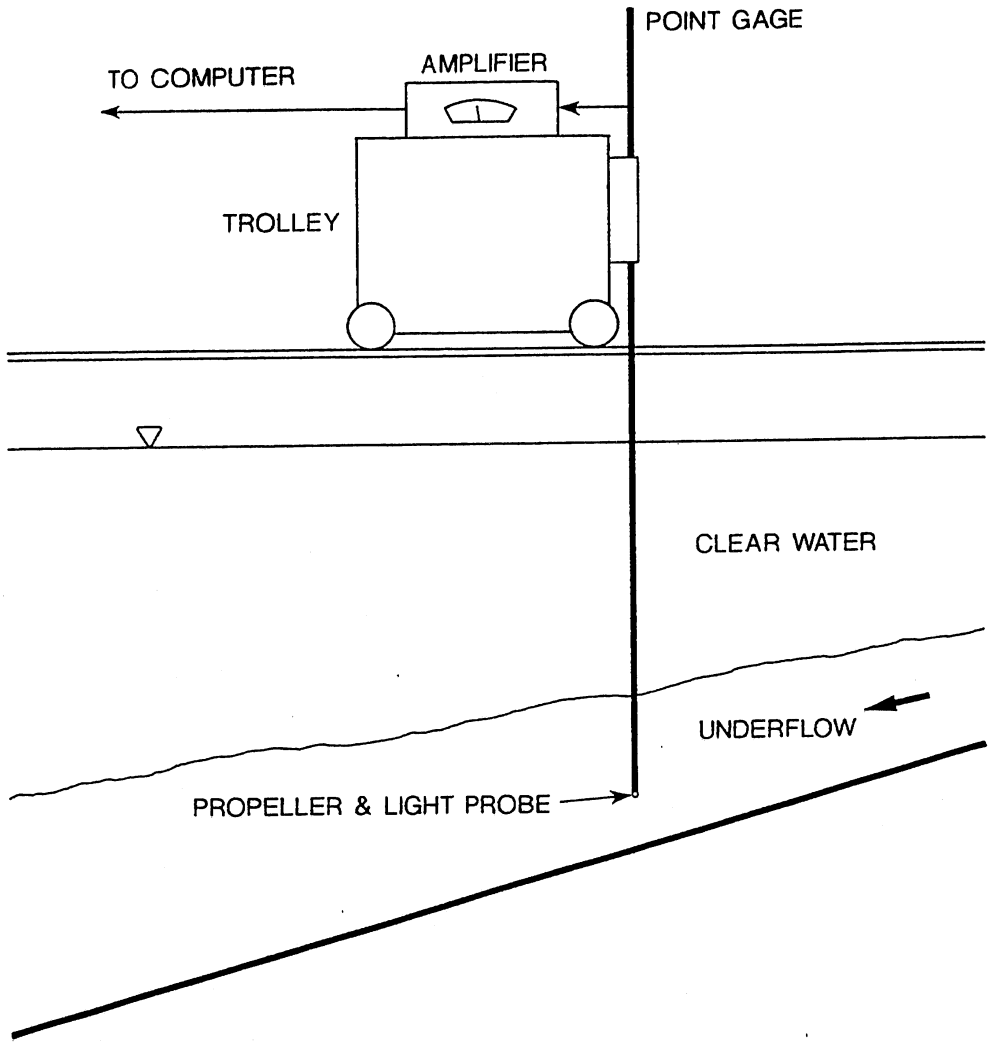

Fig. 3.6 Schematic of instrumentation set–up.

3.4 Particle Size Analyzer

To determine the size distribution of the different sediment materials employed during the experiments, a model TA II Coulter Counter was used (courtesy of Pillsbury Co.). This instrument determines the number and sizes of particles suspended in a conductive liquid by forcing the suspension to flow through a small aperture. Electrodes are immersed in the conductive fluid on both sides of the aperture. As a particle passes through the aperture, it changes the resistance between the electrodes. This produces an electric current pulse of short duration having a magnitude proportional to the particle volume. The series of pulses is electronically classified by size and counted. The Coulter Counter is calibrated by running a test with a suspension of glass spheres of known size. The size distribution obtained when analyzing a sediment sample with this instrument thus corresponds to that for spheres with same volume as the sediment particles. Probably the most outstanding feature of this instrument is its capability to provide size distributions for very small sediment samples (a few milligrams). By using different aperture sizes, the Coulter counter model TA II can be used to analyze particles with sizes varying from 0.4μ to 800μ.

3.5 Sediment Materials

A variety of sediment materials were used during the experimental study. To classify the different types of sediment, it is useful to introduce the ϕ scale for sediment size. This scale, which is commonly employed by sedimentologists, is defined as

$$D = 2^{-\phi} \tag{3.1}$$

where D is the diameter of the sediment in millimeters. In this scale, the smaller sediment diameters correspond to larger values of ϕ. A value of $\phi = 0$ corresponds to a coarse sand, while a value of $\phi = 9$ corresponds to a very fine silt. The mean value of ϕ is given by

$$\overline{\phi} = \Sigma\ \phi_i\ f_i = \Sigma - (\ln(D_i)/\ln(2))\ f_i \tag{3.2}$$

and the standard deviation on the ϕ scale is given by

$$\sigma_\phi^2 = \Sigma\ (\phi_i - \overline{\phi})^2\ f_i \tag{3.3}$$

where $\phi_i = -\ln(D_i)/\ln(2)$, D_i is the diameter of the sediment in the ith size range, and f_i is the fraction of material in that size range. For a completely uniform sediment $\sigma_\phi = 0$. The parameters $\overline{\phi}$ and σ_ϕ are related to the more familiar geometric mean size D_{sg} and its standard deviation σ_{sg}, by the following relations:

$$D_{sg} = 2^{-\overline{\phi}} \tag{3.2}$$

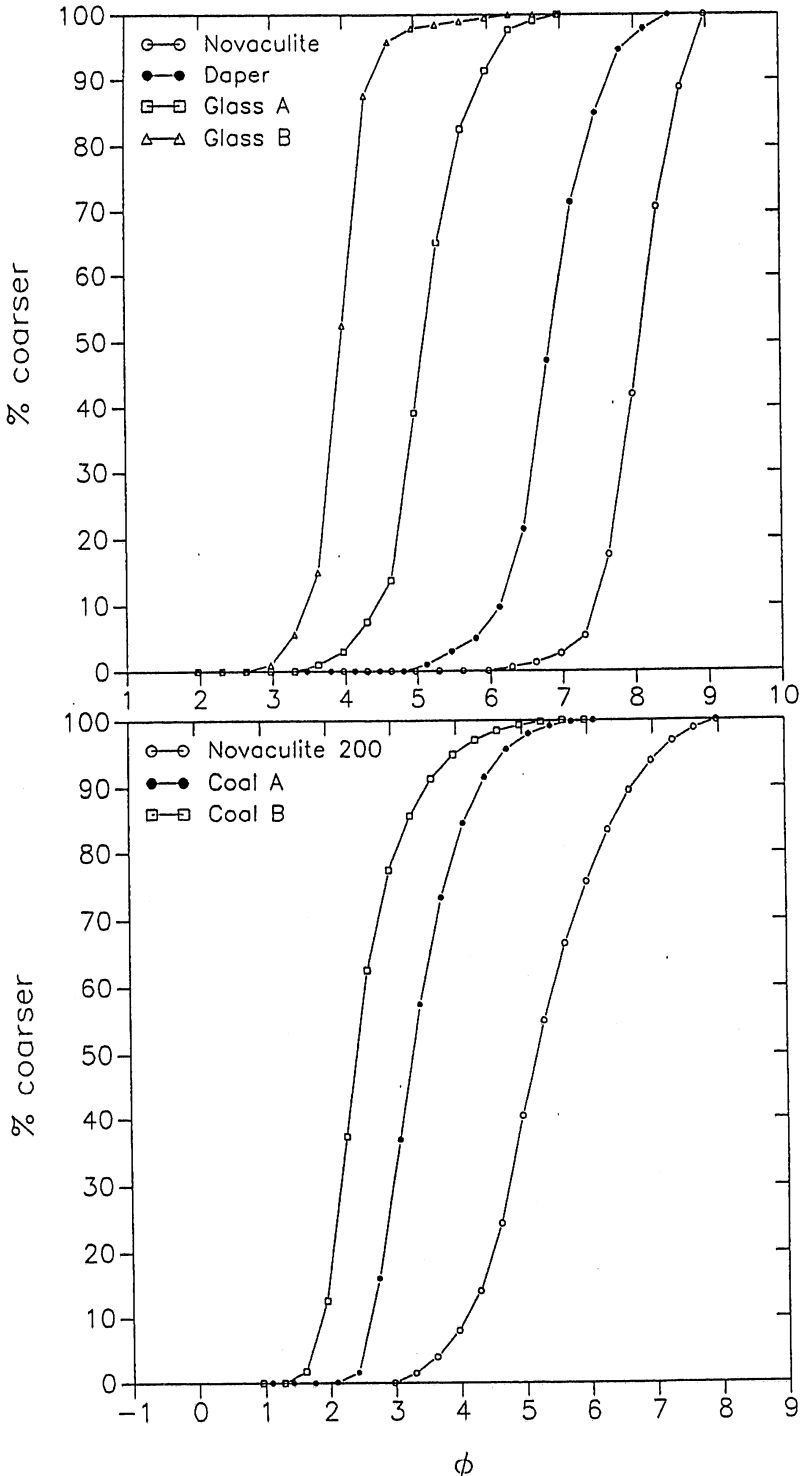

Fig. 3.7 Typical sediment size distributions.

$$\sigma_{sg} = 2^{\sigma_\phi} \tag{3.3}$$

In Figure 3.7, typical cumulative frequency curves for the different sediments employed to generate turbidity currents are shown. Three grades of silica and two grades of glass were used for the turbidity current experiments, while two grades of crushed coal were used for the sediment entrainment experiments. The characteristics of these sediments are summarized in Table 3.1.

TABLE 3.1 CHARACTERISTICS OF SEDIMENT MATERIALS

Material	$\overline{\phi}$	σ_ϕ	$D_{sg}(\mu)$	σ_{sg}	$R = \rho_s/\rho - 1$	v_s(cm/s)
Novaculite	8.05	0.47	4.0	1.38	1.65	0.002
Daper	6.80	0.63	9.0	1.55	1.65	0.008
Glass A	5.10	0.56	30.0	1.47	1.50	0.085
Glass B	3.95	0.37	65.0	1.29	1.50	0.350
Novaculite 200	5.21	1.00	27.0	2.00	1.65	0.060
Coal A	3.32	0.64	100.0	1.56	0.35	0.190
Coal B	2.47	0.66	180.0	1.51	0.35	0.620

note: sediment fall velocity v_s estimated at 20°C.

To estimate the fall velocity v_s associated with the different sediment materials, the empirical relation developed by Dietrich (1984) was used. This equation is given by

$$v_s = (g\ R\ \nu\ W_*)^{1/3} \tag{3.4}$$

where

$$\log(W_*) = -3.7617 + 1.92944 \log(D_*) - 0.09815 (\log(D_*))^2 - 0.00575 (\log(D_*))^3 + 0.00056 (\log(D_*))^4 \tag{3.5}$$

$$D_* = g\ R\ D_{sg}^3 / \nu^2 \tag{3.6}$$

Here g is the acceleration of gravity, R is the submerged specific gravity of the sediment, D_{sg} is the geometric mean size of the sediment, and ν is the kinematic viscosity of the water. The fall velocities estimated with (3.4) are included in Table 3.1.

3.6 Experimental Procedure: Conservative Saline Currents

3.6.1 Dense Fluid and Flume Preparation

Prior to each experiment, the mixing tank and the flume were cleaned and then filled with city water. After this, table salt was added to the mixing tank until the desired fluid density was achieved. Once the dense fluid was ready, it was recirculated with a pump through the constant head tank system. A calibrated orifice meter, a manometer, and a valve were then used to adjust the desired flow rate (Q_o). After preparing the dense fluid, but a few minutes before starting a run, the damping tank at the end of the flume was set by drawing water through the bottom drain. At the same time, water was supplied through the surface manifold so that the level of uncontaminated water in the flume remained constant. The amount of city water supplied by the manifold (Q_m) to the end tank was measured with a calibrated orifice meter; and it was usually set to be twice as large as the flow rate set up previously in the mixing tank ($Q_m = 2\ Q_o$) to account for the entrainment of uncontaminated water by the current.

Standard mercury thermometers were used to measure fluid temperatures in the mixing tank and in the flume. This was done to ensure that the only source of density difference was the salt (or sediment for the turbidity currents). A temperature difference of 1 $^{\circ}C$ gives a density difference on the order of 10^{-4} g/cm^3, which is only 1.5 % of the average density difference generated during the experiments. This estimate indicates that the difference in water temperatures would have to be fairly large to have any significant influence on the dynamics of the underflows.

3.6.2 Preparation of Measuring Instruments

After preparing the dense fluid and the flume, the trolley with the instrumentation was placed at a selected measuring station. Then the point gage was lowered until the sensors were about 0.6 cm above the bed. At this time, the calibration curves for the micropropeller and the light probe were supplied to a computer program used for data collection. Usually, a few trial measurements were made to ensure that the instrumentation was working well before starting the run.

3.6.3 The Run

Most of the runs involved the participation of two people, one in charge of the measuring instrumentation, and the other in charge of the data collection.

A typical run was started by delivering the recirculating dense fluid to the flume with the help of butterfly valves. After this operation, the manometer reading was checked and the sluice gate flow rate (Q_o) was readjusted if necessary. The underflow emanating from the sluice gate was allowed to develop until it reached the end tank. At this point, the surface manifold flow discharge was adjusted to provide a small overspill through a "morning glory" weir placed in the end tank ensuring a constant water surface. Immediately after this, the measurements were commenced.

The operator in charge of the trolley with the instruments placed the sensors at different locations above the bed with the help of the point gage. Sampling duration varied from 10 to 20 seconds, and the sampling rate was five samples per second. Once the computer finished with the sampling and the computation of local flow properties (i.e. mean velocity and excess fractional density), the operator moved the sensors to the next measuring point and positioned them with the help of the point gage. This methodology allowed the computer operator to select the spacing of the measuring points depending on the location within the flow (e.g. velocity gradients). Once the measurements at the different locations in the vertical direction were completed, the resulting velocity and excess fractional density profiles were displayed on the computer monitor. This provided a first view of the local structure of the flow and helped uncover any possible errors or irregularities associated with the measurements. After this, the trolley was moved to the next measuring station, and the measuring process started again. The location of the sensors along the centerline of the flume was established by a one–dimensional coordinate system marked on the glass wall of the flume.

The number of stations surveyed during an experiment was directly related to the duration of the run. The main limitation was imposed by the size of the mixing tank. In some cases, the density of the fluid in the tank was doubled and the dense fluid was diluted with city water just before entering the flume in order to maintain a continuous current for a longer period of time. Proper operation of the facility resulted in fairly long runs (30 to 60 minutes), allowing for measurements at up to ten stations along the centerline of the flume.

After the run was completed, the data collected were analyzed to evaluate integral parameters of the flow (e.g, layer–averaged velocity, Richardson number, etc.), at the measured locations.

3.7 Experimental Procedure: Turbidity Currents

3.7.1 Currents Driven by Well–Sorted Sediment

The procedure followed to generate and monitor the turbidity currents was exactly the same as the one for the saline currents. The only differences were that the dense fluid was prepared by mixing sediment and water instead of salt and water, and the light probe was used to measure sediment concentrations instead of density differences. For all of these experiments, the bed of the flume was initially free of sediment.

The turbidity currents had initial conditions similar to those of the saline currents. In these experiments, the fall velocity of the sediment driving the motion was varied by using different sediment materials of relatively uniform size. The sediments used to generate the turbidity flows were novaculite, daper, glass A, and glass B. Their characteristics are summarized in Table 3.1.

After each experiment, the water was kept ponded in the flume to avoid disturbing the bed, and the sediment deposits (model turbidites) were sampled. A plexiglas tube with a diameter of 10 cm was placed on the bed and used to limit the area of the bed to be sampled. A small hose was then used to siphon out the bed sediment surrounded by the plexiglas tube. Bed samples were collected every 100 cm along the centerline of the channel and placed in 1000 ml glass beakers. These samples were saved and later used to determine the amount of sediment deposited per unit area.

3.7.2 Currents Driven by Poorly–Sorted Sediment

The experimental procedure for these experiments was similar to the one followed to generate the turbidity currents driven by uniform sediment. Again, the flume bed was initially free of sediment. An important difference concerns the measurements of suspended sediment, which for these runs was done with the rakes of siphons described in section 3.2.2. Two sampling rakes were used, one along the model canyon and the other one along the model fan. During each experiment, flow in the siphons was started long before the commencement of the current. Once the current had developed, samples were collected in 1000 ml glass beakers. No particular effort was made to sample isokinetically. After finishing with the collection of samples at two stations along the inclined bed and two stations along the horizontal bed, the trolleys holding the rakes of siphons were moved away. Velocity profiles were then measured at these stations.

In these runs, novaculite 200 was used as the model sediment (Table 3.1). The suspended sediment samples collected with the siphons were used to determine volumetric concentration. Some of these samples were also analyzed with the Coulter counter to determine the vertical distribution of sediment particles of different sizes.

As was done in the previous set of experiments, bed samples were collected after the run without emptying the flume to evaluate the amount of sediment deposited along the canyon and fan. These samples were also analyzed with the Coulter counter to evaluate longitudinal sorting of the sediment.

3.8 Experimental Procedure: Eroding Saline Currents

For this special set of experiments, the bed of the flume was modified to provide an erodible bed along a portion of the model canyon (Figure 3.8). The sediment used to model the erodible bed was crushed coal. The characteristics of the two grades used (coal A and coal B) are described in Table 3.1.

These experiments involved the generation of saline currents, as was done in the first set of experiments. In this case, however, the dense fluid was not mixed with any kind of dye, and therefore, the generated currents were practically transparent. The light probe was calibrated to measure suspended sediment concentrations of coal. By running the saline currents over the erodible bed, an attempt was made to isolate the phenomenon of sediment entrainment into suspension.

The measurement of velocity profiles and concentration profiles of resuspended sediment (when present) was done in a way very much like that in the previous sets of experiments. The measuring program took place along the erodible portion of the bed.

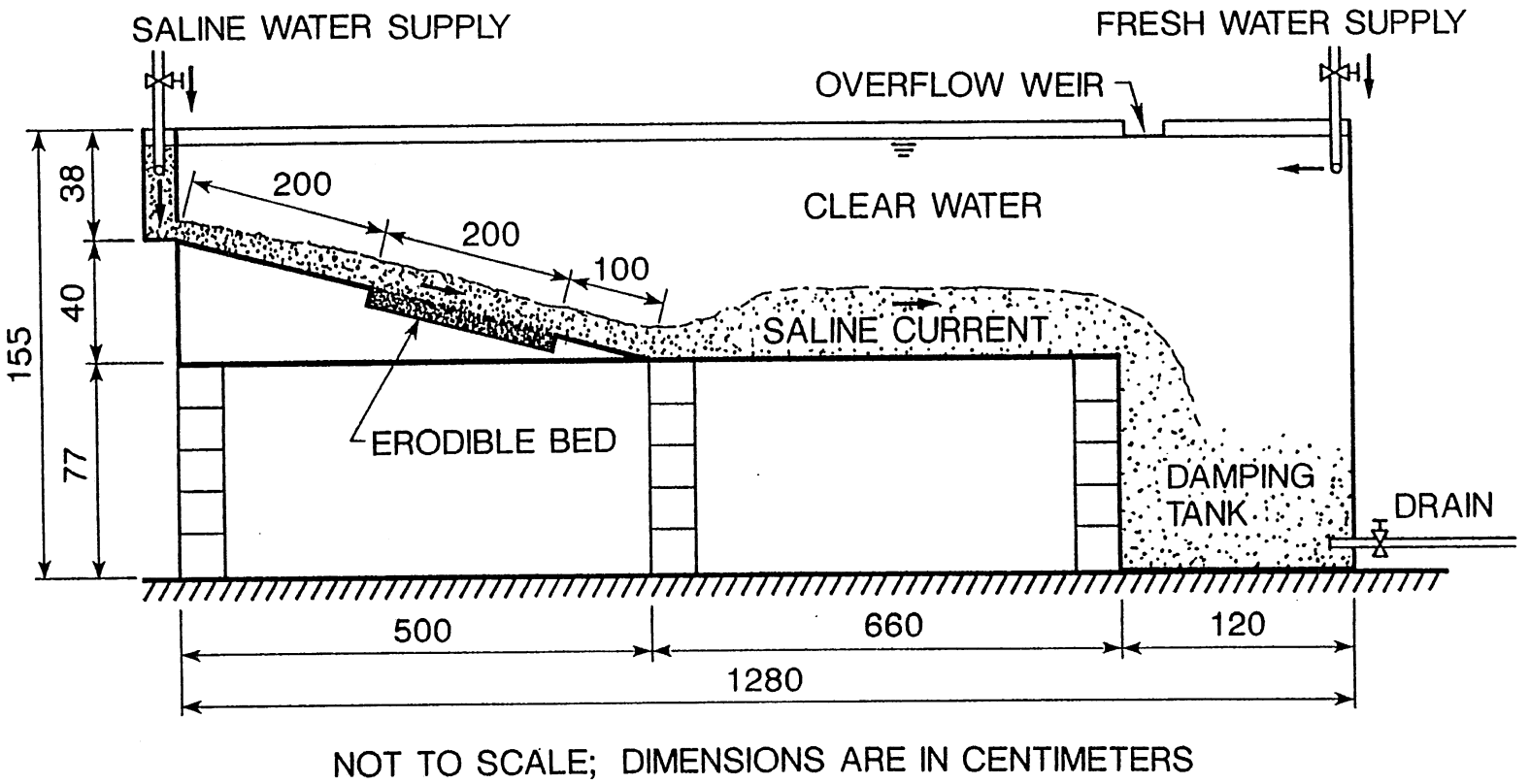

Fig. 3.8 Schematic of the flume with an erodible bed region.

CHAPTER 4

EXPERIMENTAL RESULTS: CONSERVATIVE SALINE CURRENTS

4.1 Purpose of the Experiments

The main purpose of these experiments was to obtain information on the characteristics and behavior of conservative saline currents in the proximity of a break in slope. Such observations would provide both data on density currents driven by sediment with zero fall velocity, and also a benchmark against which to compare the effects of sediment deposition on the flow mechanics.

4.2 Overview of the Experiments

After a number of preliminary tests that were necessary to adjust the experimental facility and measuring technique, approximately thirty experiments were conducted. Considerable emphasis was placed on the ability to reproduce a given flow, so for each set of inlet conditions the experiment was repeated until the quantity and quality of the data were considered acceptable. For all the experiments, the inlet current thickness h_0 was set at 3 cm with the help of a sluice gate. The inlet flow rate per unit width q_0 was set at 33 cm^3/s, thus giving a inlet layer–averaged velocity U_0 ($= q_0/h_0$) of 11 cm/s. The inlet buoyancy discharge per unit width $\Phi_0 = g\Delta_0 q_0$, and the inlet Richardson number $R_{i_0} = \Phi_0/U_0^3$ were varied by changing the inlet fractional density Δ_0 ($=$ RC for sediment) of the current in excess of the uncontaminated water in the flume. The ranges covered for these various parameters were as follows:

$$0.002 < \Delta_0 < 0.015$$

$$68\ cm^3/s^3 < \Phi_0 < 480\ cm^3/s^3$$

$$0.05 < R_{i_0} < 0.36$$

As denoted above, the inlet Richardson numbers R_{i_0} were sufficiently lower than unity to ensure the generation of downslope developing supercritical flows. Since several experiments were conducted for the same initial conditions, for the present analysis only one experiment representative of each set of initial conditions was selected. The inlet conditions of these experiments are shown in table 4.1. Therein, T_{in} denotes the temperature of the salt–water solution in the mixing tank, and T_{fl} denotes the temperature of the uncontaminated water in the flume.

TABLE 4.1 INLET CONDITIONS OF SELECTED EXPERIMENTS

Run	U_0(cm/s)	h_0(cm)	Δ_0	Φ_0(cm^3/s^3)	R_{i_0}	T_{in}(°C)	T_{fl}(°C)
SAL26	11	3	0.0021	68	0.05	26.0	26.3
SAL27	11	3	0.0040	129	0.10	27.0	26.7
SAL28	11	3	0.0080	259	0.19	27.5	28.0
SAL29	11	3	0.0120	388	0.29	27.5	27.9
SAL11	11	3	0.0130	420	0.32	24.0	25.0

In all the experiments the inlet Reynolds numbers $R_{e_0} = U_0 h_0/\nu$ was larger than 3000, ensuring turbulent flow conditions at the inlet. The ratio of the sluice gate opening (h_0 = 3 cm) to the water depth at the inlet (greater than 30 cm) was about 0.1 or less during the experiments, thus avoiding the possibility of significant recirculation due to depth limitation.

4.3 Flow Measurements

In each experiment, as the dense flow entered the sloping region, the leading edge of the current formed a front similar to the one shown in Figure 4.1. The measurements were concentrated on the body of the current; they were started a few minutes after the front had reached the end tank. During each run, several vertical profiles of downstream velocity and excess fractional density were measured along the centerline of the flume. Usually the measurements started along the sloping region, and continued along the horizontal region. In Figure 4.2, local mean velocity u and excess fractional density δ are plotted as functions of distance above the bed at two different locations for a typical run, one upstream and the other downstream of the break in slope. As shown therein, the velocity profiles have a characteristic velocity distribution resembling that of a wall jet. The point along the vertical at which the maximum velocity occurs is seen to move up and away from the bed while going from the model canyon to the model fan, indicating a clear deceleration of the flow.

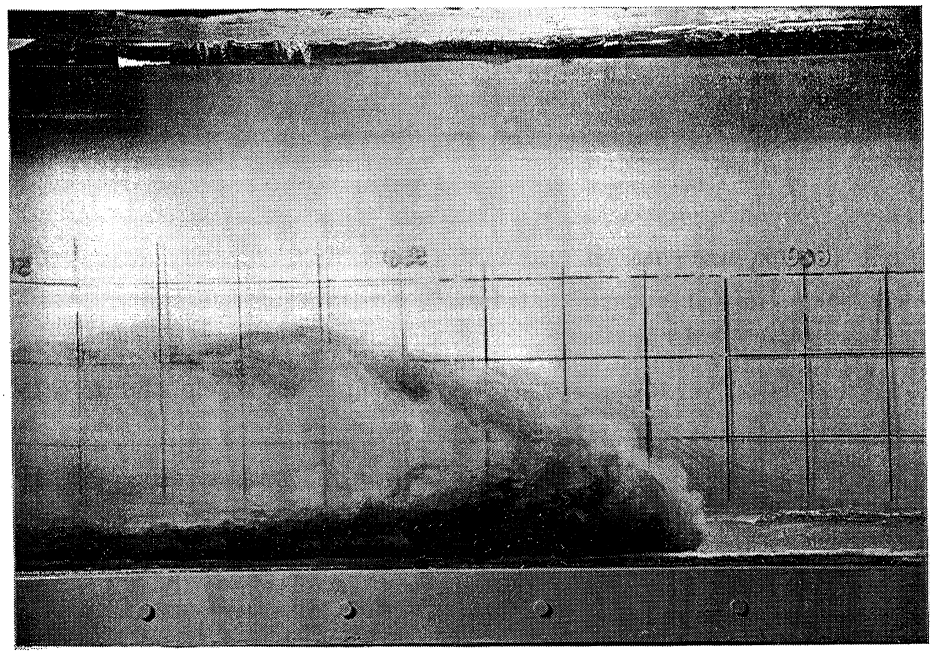

Fig. 4.1 Density current front. The flow is from left to right.

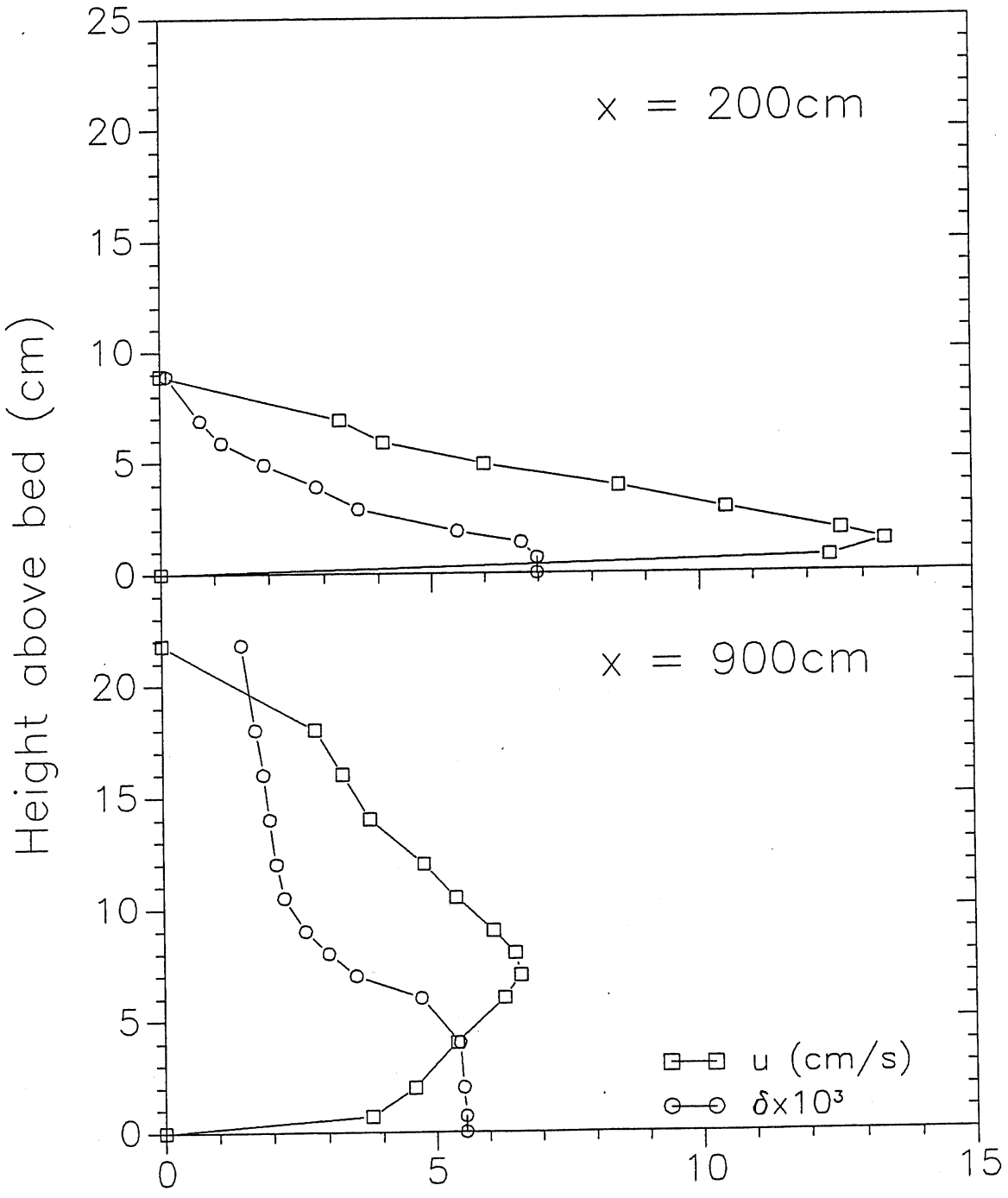

Fig. 4.2 Typical velocity and fractional density profiles at two different locations, one upstream (x = 200 cm) and the other downstream (x = 900) of the break in slope (x = 500 cm).

4.4 Layer–Averaged Flow Parameters

The velocity profiles measured along the centerline of the channel during an experiment were used to determine the current thickness h and the layer–averaged velocity U at each measuring station, with the aid of equations (2.15) and (2.16) as follows

$$U = \frac{\int_0^\infty u^2 \, dz}{\int_0^\infty u \, dz} \tag{4.1}$$

$$h = \frac{\left[\int_0^\infty u \, dz\right]^2}{\int_0^\infty u^2 \, dz} \tag{4.2}$$

In the case of a saline density current the buoyancy discharge Φ is conserved, and the bulk Richardson number of the flow at a given location can be readily obtained if the current velocity is known,

$$R_i = \frac{\Phi_0}{U^3} = \frac{\Phi}{U^3} \tag{4.3}$$

Such a current quickly reaches a normal or equilibrium state at which the current velocity U becomes constant and the current thickness h grows linearly with distance due to water entrainment from above (Ellison and Turner, 1959). The normal Richardson number R_{in} associated with the normal velocity U_n, has a constant value for a given slope and bed roughness. This is illustrated in Figure 4.3, where the layer–averaged velocities computed from the measurements taken at 300 cm from the inlet during the experiments are plotted against the buoyancy discharge Φ. A fit of the data points therein gives a value of $R_{in} = 0.25$. The plot also indicates the range of layer–averaged velocities that can be expected along the model canyon, and illustrates clearly how modestly the current velocity increases as the buoyancy discharge is increased.

4.5 Spatial Development of the Underflows

The supercritical currents generated at the inlet reached equilibrium within the first 150 cm from the inlet. According to equation (2.37), the rate of thickening at equilibrium is given by

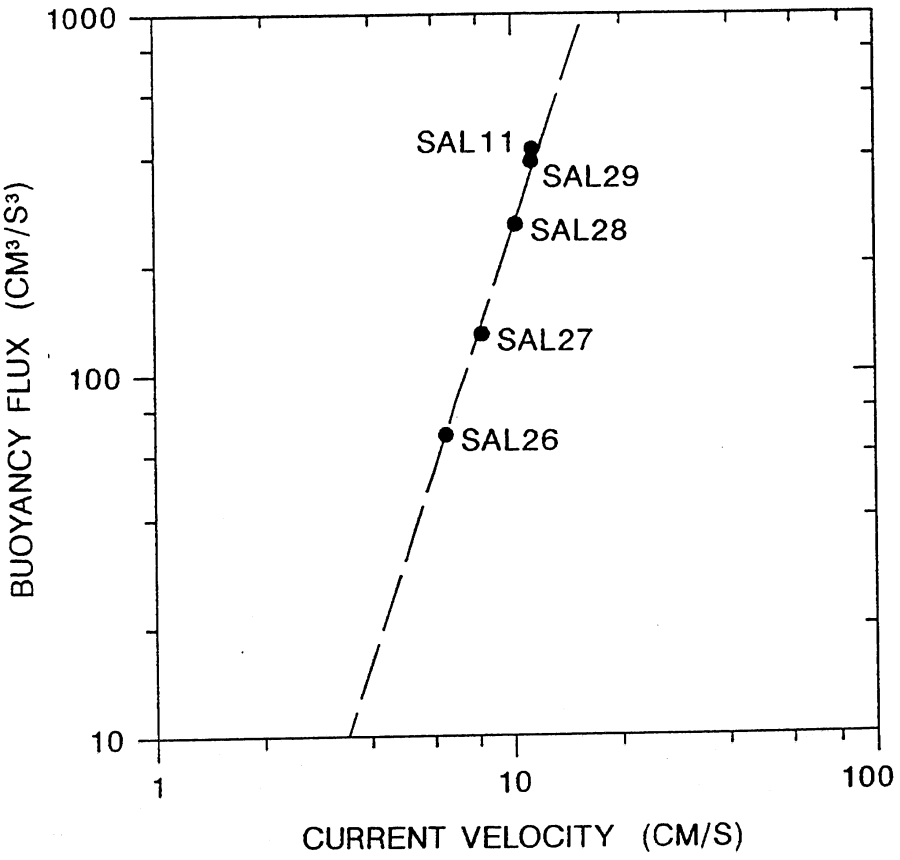

Fig. 4.3 Plot of buoyancy discharge Φ versus layer–averaged velocity U along the sloping bed region.

$$\frac{dh}{dx} = e_w(R_{in}) \tag{4.4}$$

The linear growth displayed by the currents along the sloping portion of the bed is illustrated in Figure 4.4. The fits shown therein indicate values of the water entrainment coefficient e_w ranging from 0.0055 to 0.0092. As implied by (4.4), e_w should in principle be the same for all the currents. The differences might be attributed to the fact that the Reynolds number was not always large and viscous effects could have been important. In spite of these differences, the values of e_w observed herein are in good agreement with the data in the literature on dense bottom currents. This is illustrated in Figure 4.5 where the water entrainment coefficient is plotted as a function of the bulk Richardson number measured in each experiment.

In Figure 4.6, the velocity profiles measured along the centerline of the channel during a typical run are shown. The current thickness h at each location is also denoted in the figure, as well as the visual interface determined with the help of the light probe. The bulk Richardson numbers computed at each station indicate that the underflow is supercritical ($R_i > 1$) along the sloping bed and subcritical ($R_i < 1$) along most of the horizontal bed region, thus showing the existence of a hydraulic jump. The supercritical flow is controlled by the inlet conditions, and the subcritical flow is controlled by the condition imposed by the critical section (i.e. outfall) at the end of the channel. The hydraulic jump is seen to take place at a point very near the slope discontinuity. The underflow thickness h is doubled, and its velocity U is halved, in going through the jump. The measurements also indicate that the specific flow discharge q increases smoothly along the supercritical flow region, but remains fairly constant after the jump, along the subcritical flow region.

4.6 Characteristics of the Hydraulic Jumps

In the Table 4.2, information concerning the characteristics of the observed jumps is provided. The hydraulic jumps are relatively weak, as suggested by the ratio of the current thickness after the jump h_2 to the current thickness before the jump h_1, which is seen to take values between 2.0 and 2.4. In all cases the flow velocity of the current is almost halved after going through the jump.

The degree of stratification of the subcritical portion of the flows, as indicated by the postjump Richardson number R_{i_2}, is seen to increase with the buoyancy discharge. The amount of water entrained by the jumps, quantified by the ratio q_2/q_1 in Table 4.2, is found to be rather small. For

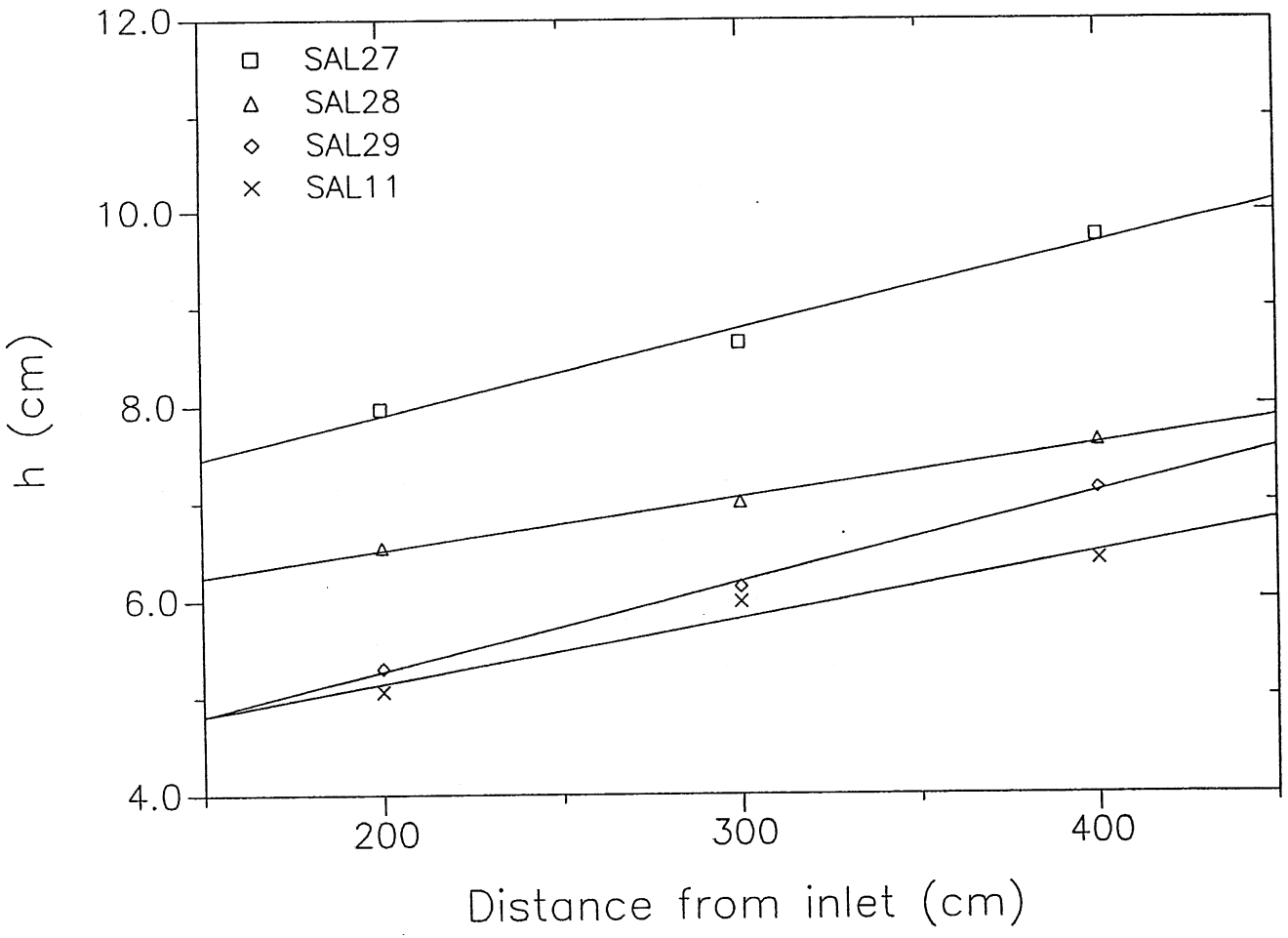

Fig. 4.4 Variation of current thickness along the sloping bed region.

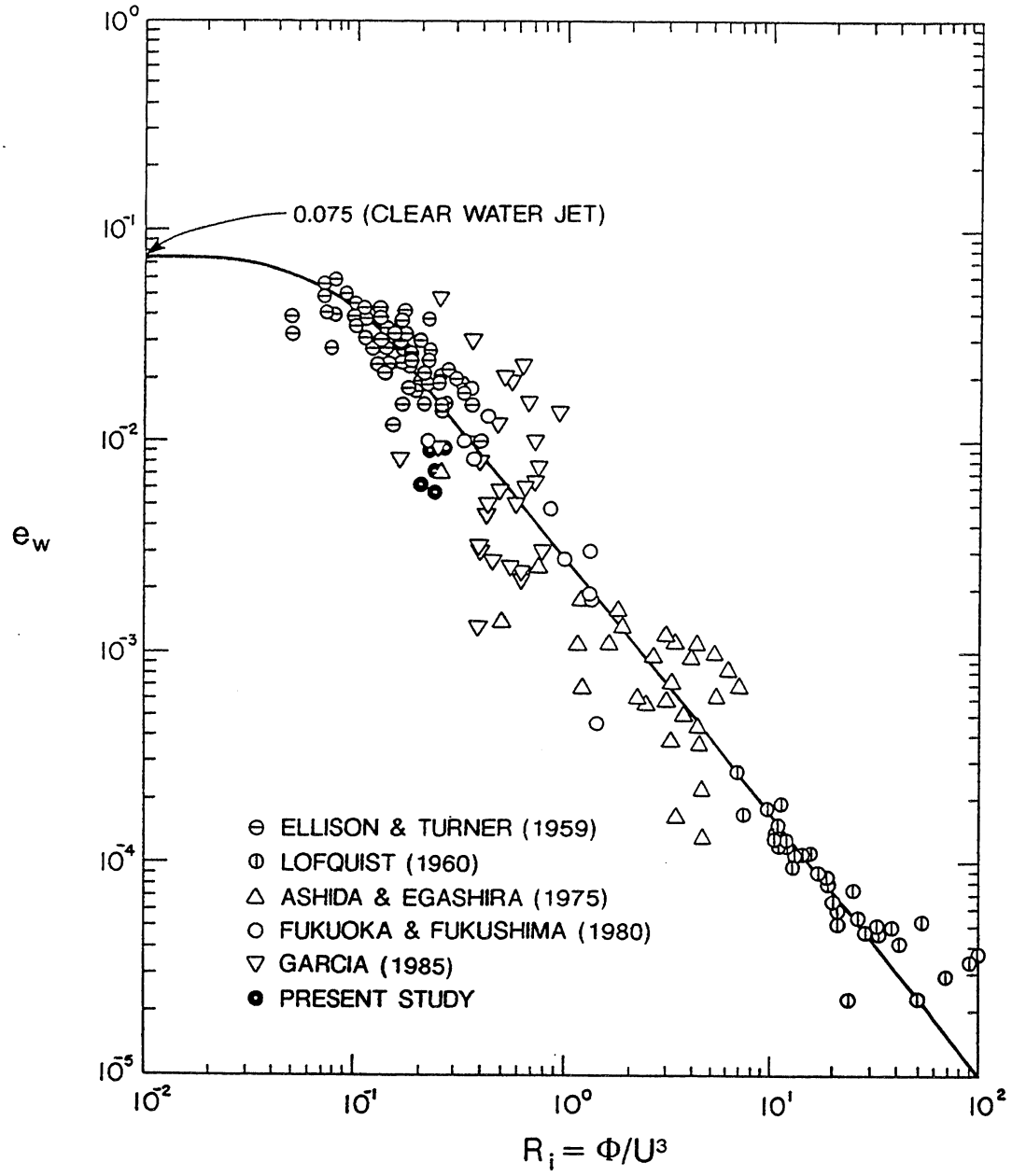

Fig. 4.5 Water entrainment coefficient e_w as a function of the bulk Richardson number R_i. The line is that of equation (2.28) (from Garcia, 1985).

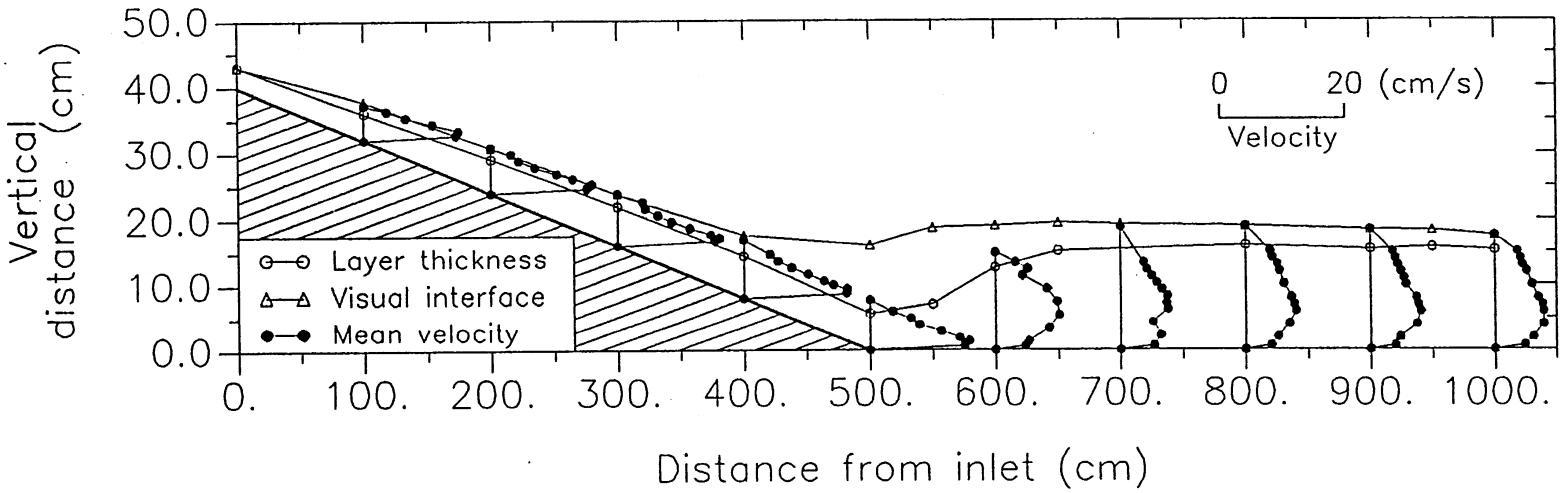

Fig. 4.6 Typical observations for a saline current (run SAL11).

the sake of comparison, the ratio of the current flow rate before the jump q_1 to the inlet flow rate q_0 is included in the table. As shown therein the amount of water entrained by the currents before the jump is on the average seven times larger than the amount of water entrained by the currents while going through the jump.

TABLE 4.2 CHARACTERISTICS OF HYDRAULIC JUMPS

Run	h_1	h_2	U_1	U_2	R_{i_1}	R_{i_2}	h_2/h_1	U_2/U_1	q_2/q_1	q_1/q_0
SAL26	11.1	22.5	6.9	3.9	0.21	1.15	2.00	0.56	1.16	2.30
SAL27	9.7	20.0	8.2	4.6	0.23	1.32	2.05	0.56	1.15	2.43
SAL28	7.6	16.3	10.1	5.9	0.25	1.26	2.14	0.58	1.25	2.34
SAL29	7.1	15.7	11.3	6.4	0.27	1.48	2.20	0.57	1.24	2.45
SAL11	6.4	15.1	11.8	5.9	0.25	2.04	2.36	0.50	1.19	2.28

note: h_1 and h_2 are in centimeters and U_1 and U_2 are in centimeters per second

The observation of the currents through the glass wall of the flume usually indicated that the transition from one regime to another took place very close to the break in slope. This is illustrated in Figure 4.6, where the interface of the current, as detected by the light probe, is seen to jump before the position at which the hydraulic jump is located according to the measurements. An attempt was made to expose the structure of the transition by generating a current colored with green fluorescent dye, and injecting blue dye in the proximity of the bed just before the break in slope. The resulting flow visualization is shown in Figure 4.7. Therein the upper green layer is seen to jump before than the lower blue layer, suggesting that the wall–bounded layer has more momentum than the upper jet–like layer and therefore is able to drive further into the pressure wall imposed by the subcritical portion of the flow. Interestingly, the position at which the wall–bounded blue layer jumps is about where the "nose" of the velocity profiles moves away from the wall.

4.7 Variation of Bed Shear Stress

The bed shear stress τ_b along the centerline of the channel, or its surrogate the bed shear velocity $u_*^2 = \tau_b/\rho$, can be estimated in different ways with the help of the measured profiles. One way is to apply the momentum balance equation (2.24) between two measuring stations. An alternative is to estimate the bed shear velocity using the velocity measurements in the proximity of the bed in conjunction with the logarithmic law

$$\frac{u}{u_*} = \frac{1}{\kappa} \ln(\frac{z}{z_o}) \tag{4.5}$$

in which u denotes the mean flow velocity at a distance z above the bed, u_* denotes the bed shear velocity, κ is Von Karman's constant (=0.4), z_o is the zero–velocity level taken as $0.11(\nu/u_*)+0.033k_s$, and k_s is the equivalent bed roughness (Van Rijn, 1984). Using the velocities below the maximum velocity point of the profiles measured along the supercritical flow region, the value of k_s can be estimated. In Figure 4.8, the variation of the bed shear velocity along the centerline of the channel obtained with the help of (4.5) and measurements from run SAL11, are shown. It is seen that the bed shear stress decreases remarkably after the current has gone through the jump.

4.8 Similarity of Profiles and other Characteristics

In Figure 4.9, velocity profiles for a number of runs are plotted in normalized form with the help of the corresponding current layer–averaged velocity U and the current thickness h. The similarity collapse is quite good for both supercritical and subcritical flows. In the case of supercritical flows, the boundary layer extending up to the maximum velocity point covers a small portion of the current thickness, while the unbounded layer entails approximately 75% of flow. On the other hand, the wall–bounded layer covers a larger portion of the flow in the case of subcritical currents, where the "nose" or maximum velocity point is located farther away from the wall.

In Figures 4.10, excess fractional density profiles are presented in normalized form. The similarity collapse is good for the supercritical flow profiles and fair for the subcritical flows. In the case of supercritical flows, the excess fractional density is seen to decrease monotonically in the vertical direction. A different structure is observed in the case of subcritical flows, which shows a layer of almost constant excess fractional density that extends up to the maximum velocity point followed by a decreasing excess fractional density in the upward direction.

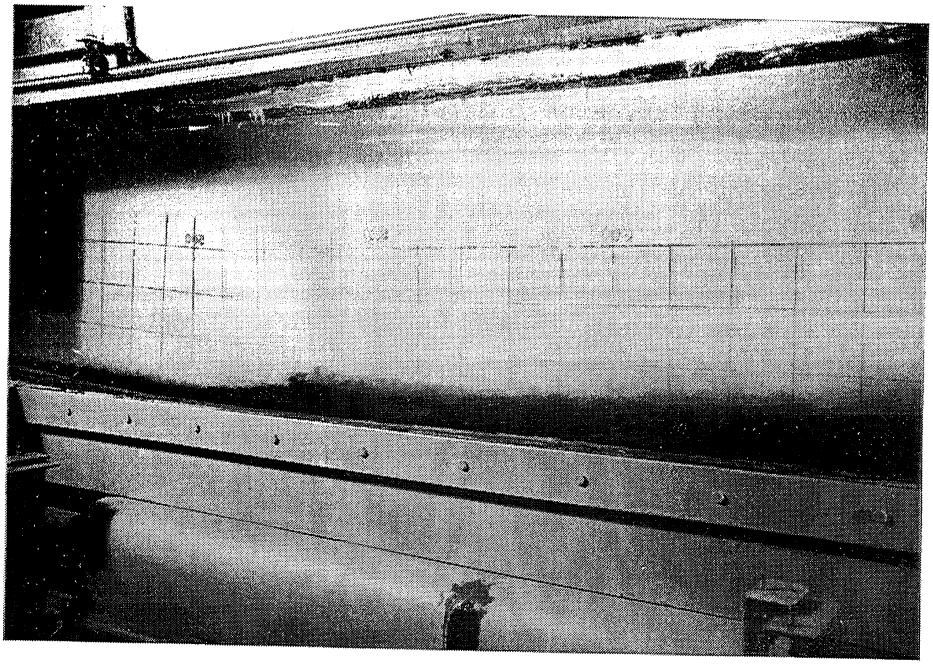

Fig. 4.7 Flow visualization of internal hydraulic jump.

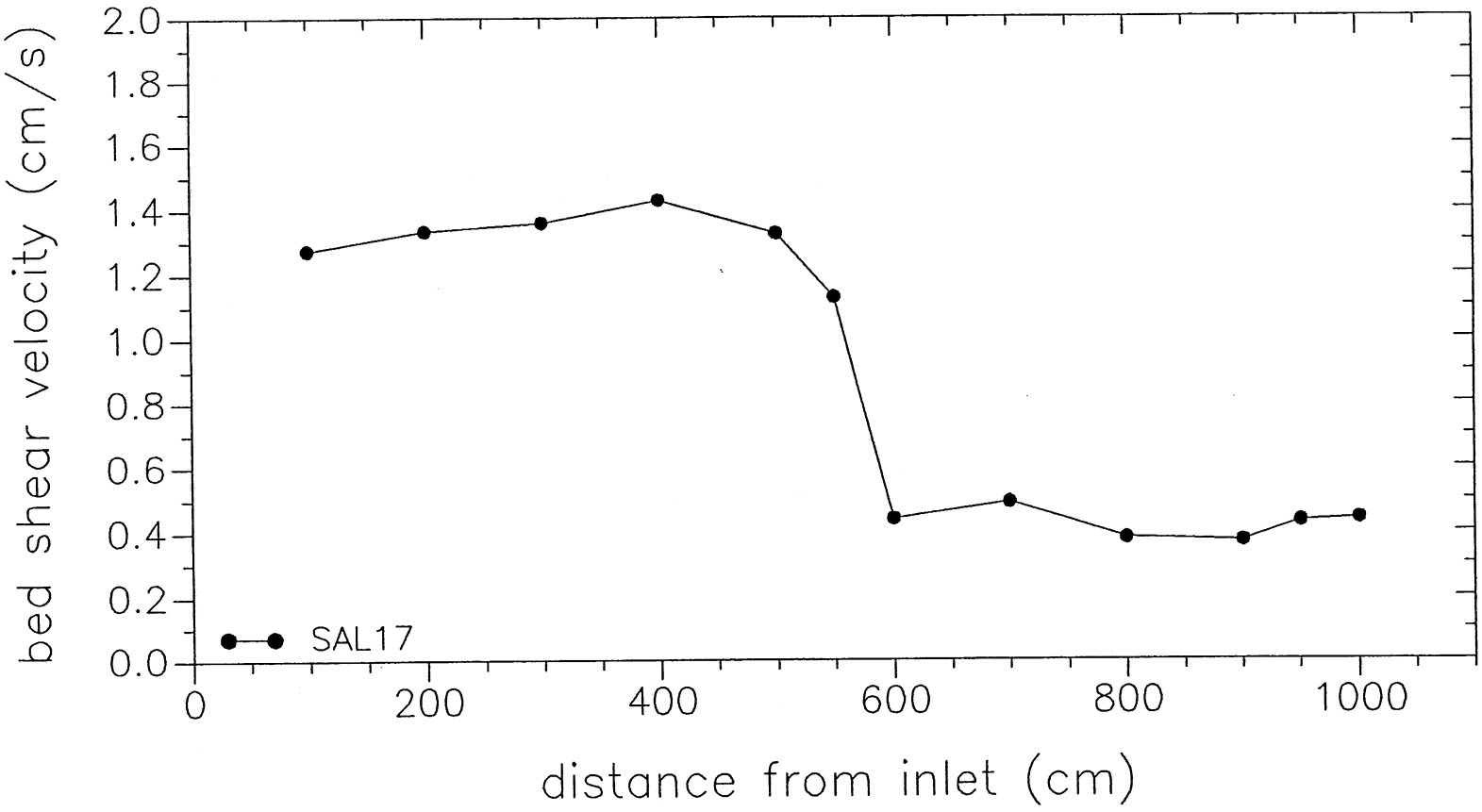

Fig. 4.8 Variation of bed shear velocity along the centerline of the flume.

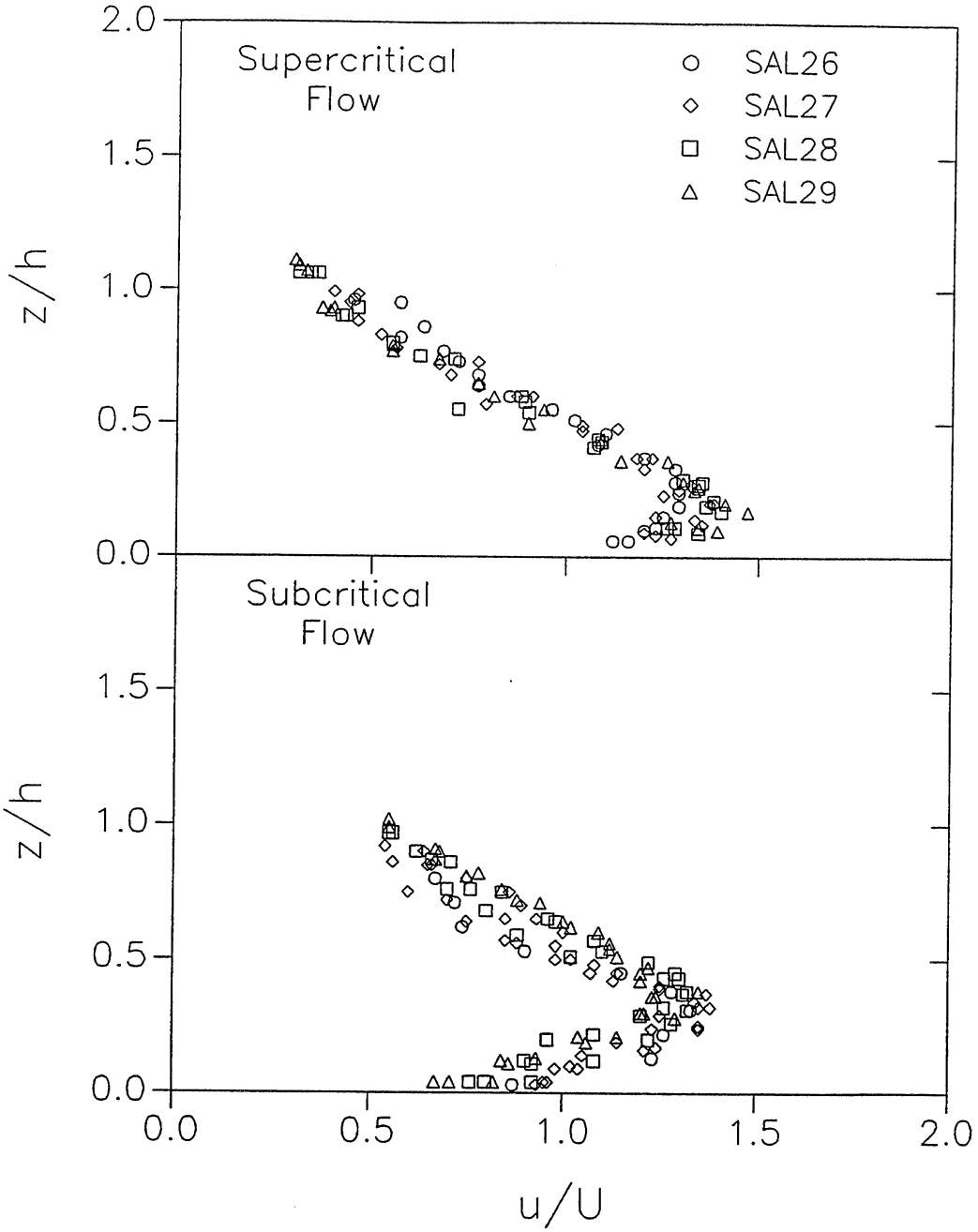

Fig. 4.9 Similarity collapse of velocity profiles for supercritical and subcritical flows.

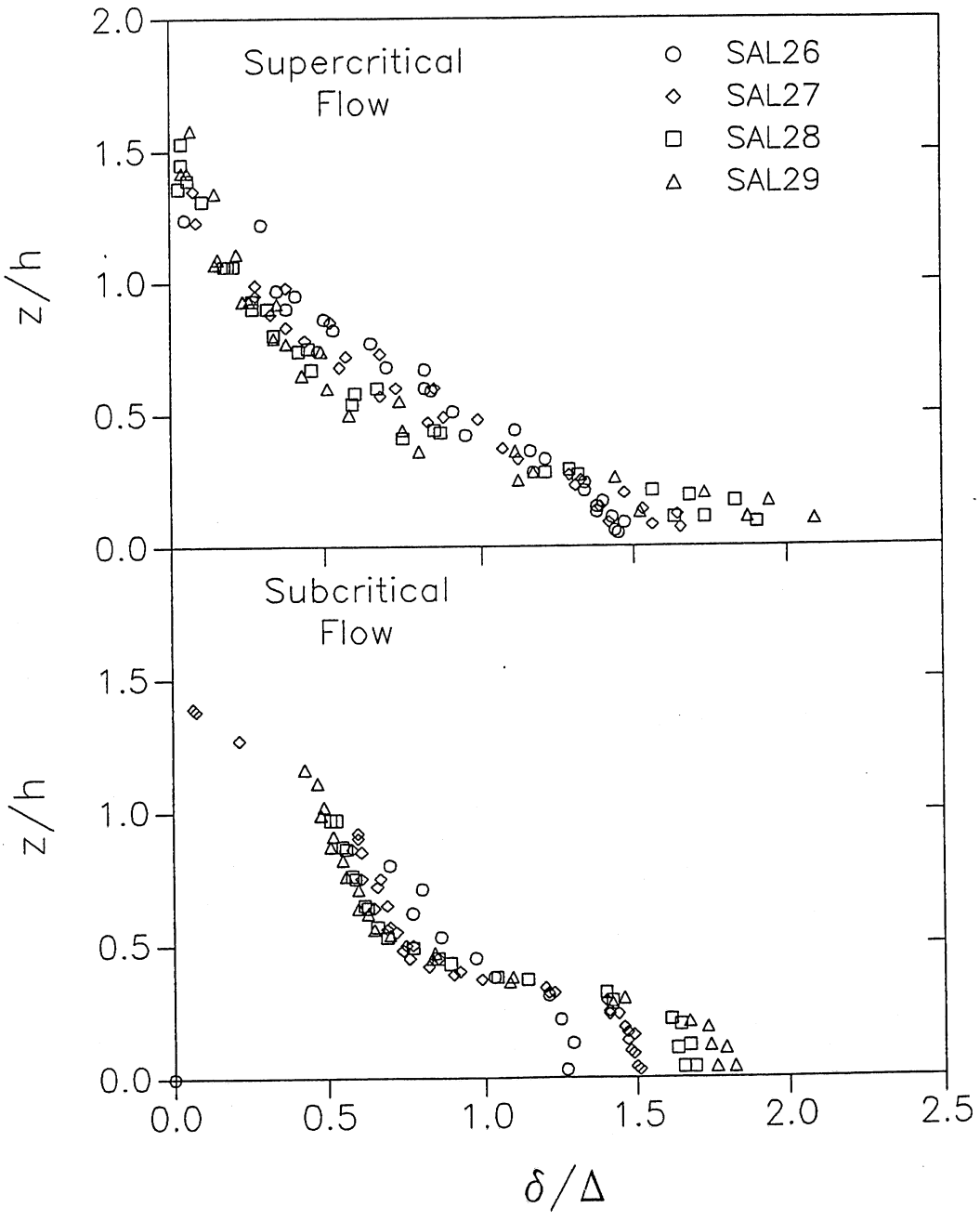

Fig. 4.10 Similarity collapse of excess fractional density profiles for supercritical and subcritical flows.

An important characteristic of the velocity profiles is that they show an almost linear variation above the maximum velocity point. This is consistent with Turner (1973) who states that in the upper region of the flow, where turbulence is locally generated, the only parameters that are of importance in determining the velocity and density gradients are the local velocity scale ΔV and buoyancy scale ΔB at the edge of the plume. Using dimensional analysis Turner obtains the following

$$\frac{du}{dz} = Q_1 \frac{\Delta B}{\Delta U}, \quad -\frac{g}{\rho}\frac{d\rho}{dz} = Q_2 \frac{(\Delta B)^2}{(\Delta U)^2} \tag{4.6}$$

where Q_1 and Q_2 are constants. The above equations predict linear profiles simply because no external length scale is relevant in the upper portion of the flow. The maintenance of the turbulence is usually quantified by a gradient Richardson number (Harleman, 1969)

$$R_i = -\frac{g\ d\rho/dz}{\rho\ (du/dz)^2} \cos\beta \tag{4.7}$$

where β is the bed slope angle (for this study $\cos\beta \approx 1$). For values of $R_i > 0.25$ turbulence can not be maintained (Monin and Yaglom, 1971). Substitution of (4.6) into (4.7), yields

$$R_i = \frac{Q_2}{Q_1} = \text{constant} \tag{4.8}$$

indicating that R_i should be constant above the maximum velocity point. For the profiles measured in the experiments, R_i is seen to take values in the range 0.13 – 0.23, with a mean value of 0.16 for the supercritical flows, while the range is 0.54 – 0.84 with a mean value of 0.64 for the subcritical flows. These values clearly indicate that the subcritical flows were highly stable.

In Figure 4.11, shape factors for a number of excess fractional density profiles measured during the experiments are plotted against the corresponding local bulk Richardson number. These shape factors are equivalent to those defined in Chapter 2, and are defined by

$$\alpha_0 = \int_0^\infty \frac{\delta}{\Delta}\, d\eta \tag{4.8}$$

$$\beta_0 = \int_0^\infty \int_\eta^\infty \frac{\delta}{\Delta}\, d\eta' d\eta \tag{4.9}$$

where $\eta = z/h$. The shape factors for both supercritical and subcritical flows are seen to have in general values close to unity.

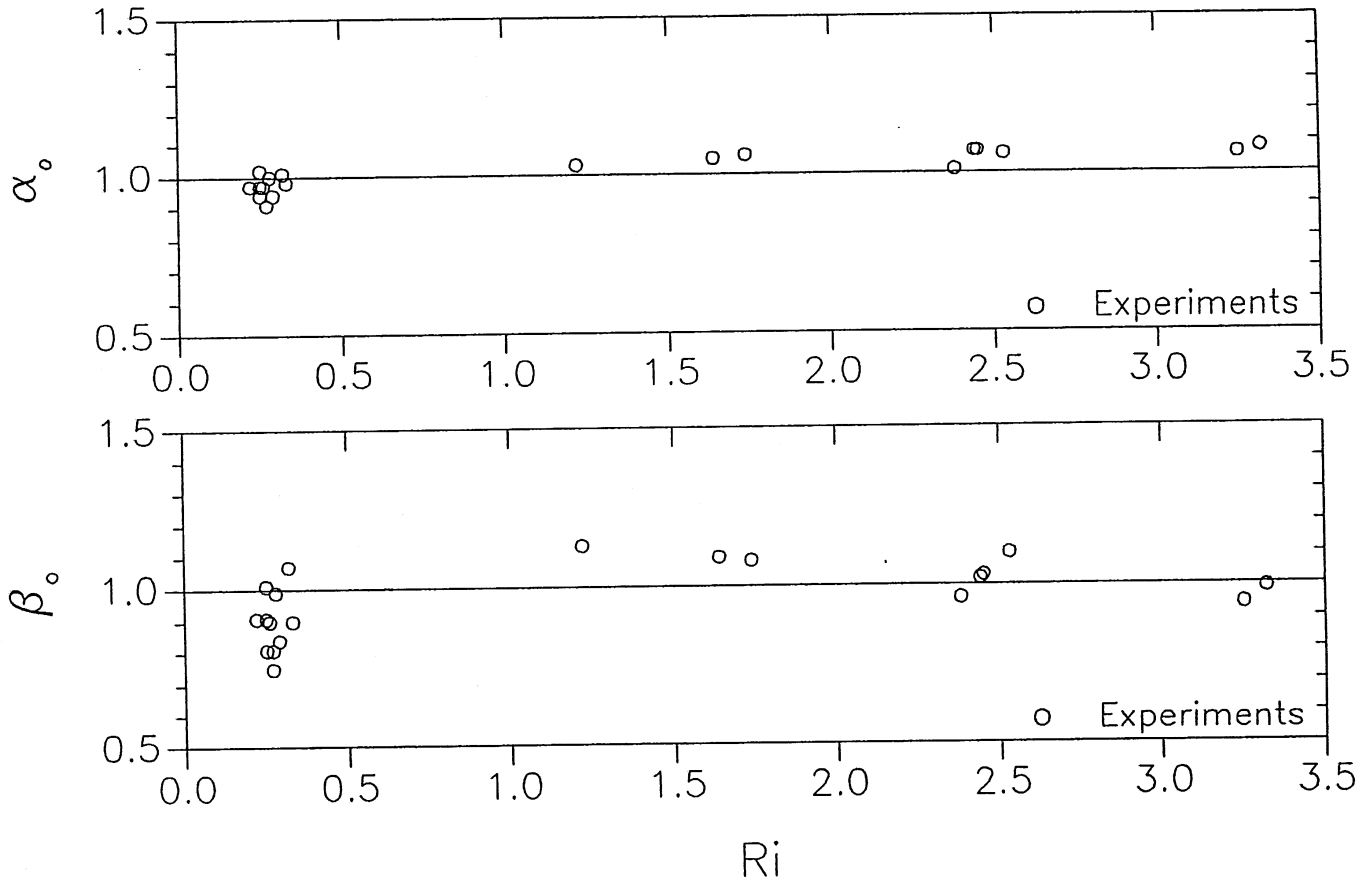

Fig. 4.11 Shape factors for supercritical and subcritical flows.

4.9 Conclusions

The experiments have shown several important characteristics of conservative currents in the proximity of a break in slope.

The observations clearly indicate that water entrainment from above is most important along the supercritical region of the flow, and is almost negligible along the subcritical region of the flow. The water entrainment coefficients estimated along the sloping region are in good agreement with the data in the literature.

The amount of water entrained by a current while going through a jump was found to be rather small, particularly when compared with the amount of water entrained by the current before the jump. Even though the facility did not allow for a wide variation of flow conditions at the break in slope, the observations made seem to be supported by the work of several researchers concerned with the dilution of heated water discharged at relatively low Richardson numbers (i.e. $R_i < 0.05$). These studies indicate that most of the water entrainment occurs in the jet–like region before the jump itself (Wilkinson and Wood, 1971; Stefan and Hayakawa, 1972; Baddour, 1987). The hydraulic jumps associated with plume–like flows ($R_i > 0.1$) can be expected to be rather weak. This was the case for the flows observed herein. For example, equation (2.47) gives for $R_i = 0.25$, which is the normal Richardson number of the sloping region, a thickness ratio $h_2/h_1 = 2.37$. This value is very close to those measured during the experiments as illustrated in Table 4.2.

Probably the most important effect of the transition on the flow characteristics is the marked reduction of bed shear stress downstream of the the hydraulic jump. This suggests that the capacity of a given current to transport sediment should be reduced substantially due to the jump.

The measured velocity and excess fractional density profiles revealed different vertical structures for supercritical and subcritical flows, but for both flow regimes the profiles showed a fair to good similarity collapse.

In the upper portion of the flow, above the maximum velocity point, the velocity profiles showed a linear variation with distance above the bed. This agrees well with the observations made by Turner (1973). In the case of the excess fractional density profiles, an almost linear trend could be discerned but it was no so clear as for the velocity profiles. The computation of the gradient Richardson number for the upper portion of the flows, indicated that the vertical mixing was completely inhibited by the density gradients in the case of subcritical flows. The values of R_i computed for the supercritical flows are found to be in very good agreement with those obtained numerically by Stacey and Bowen (1988).

The computation of shape factors produced values close to unity, suggesting that the top–hat or slab approximation can give reasonable results for both supercritical and subcritical conservative currents.

CHAPTER 5

EXPERIMENTAL RESULTS: DEPOSITIONAL TURBIDITY CURRENTS

5.1 Currents Driven by Well–Sorted Sediment

5.1.1 Purpose of the Experiments

These experiments were conducted to investigate the effect of sediment size on the spatial development and vertical structure of the currents. Of particular interest was the nature of the deposits upstream and downstream of a hydraulic jump, and the conditions under which the slope discontinuity is clearly manifested in the depositional record.

5.1.2 Overview of the Experiments

An effort was made to generate turbidity currents having inlet conditions similar to those set in the experiments with saline currents. The inlet current thickness h_0 was kept at 3 cm, and the inlet flow rate per unit width q_0 was set at 25 cm^2/s for half of the experiments and at 33 cm^2/s for the rest, resulting in inlet layer averaged velocities U_0 of 8.3 cm/s and 11 cm/s, respectively. The inlet buoyancy discharge per unit width $\Phi_0 = gRC_0q_0$, and the inlet Richardson number $R_{i_0} = \Phi_0/U_0^3$ were varied by changing the inlet excess fractional density RC_0. The ranges of inlet values covered were as follows:

$$0.0013 < C_0 < 0.0086$$
$$0.0021 < RC_0 < 0.014$$
$$52.3\ cm^3/s^3 < \Phi_0 < 389.5\ cm^3/s^3$$
$$0.05 < R_{i_0} < 0.6$$

The geometric mean size D_{sg} of the sediment used to generate the underflows was varied between 4 μ and 65 μ, resulting in sediment fall velocities v_s in the range 0.0016 cm/s ~ 0.40 cm/s. As in the case of saline currents, the inlet Richardson numbers were kept bellow unity to ensure the generation of supercritical currents. The inlet Reynolds number were always larger than 2700. In Table 5.1, the inlet conditions and other characteristics of each particular experiment are described.

TABLE 5.1 INLET CONDITIONS AND OTHER CHARACTERISTICS OF THE EXPERIMENTS

Run	U_0 (cm/s)	h_0 (cm)	$C_0 \cdot 10^3$	Φ_0 (cm^3/s^3)	R_{i_0}	D_{sg} (μ)	v_s^1 (cm/s)	T_{in} (°C)	T_{fl} (°C)	Run Time (min)
NOVA1	8.3	3	1.30	52.3	.09	4	.0016	25.5	25.5	40
NOVA2	8.3	3	2.48	99.8	.17	4	.0016	25.0	25.0	40
NOVA3	8.3	3	2.48	99.8	.17	4	.0016	26.0	25.5	38
NOVA4	11.0	3	4.30	229.4	.17	4	.0016	25.0	25.0	27
NOVA7	11.0	3	7.30	389.5	.29	4	.0016	25.5	26.0	22
NOVA8	11.0	3	7.30	389.5	.29	4	.0016	25.0	26.0	28
DAPER1	8.3	3	1.43	57.6	.10	9	.0083	26.0	26.0	40
DAPER2	8.3	3	1.33	53.5	.09	9	.0083	26.0	26.0	40
DAPER4	8.3	3	2.95	118.8	.21	9	.0083	26.5	26.5	33
DAPER5	8.3	3	4.29	172.7	.30	9	.0083	26.5	26.0	36
DAPER6	8.3	3	3.72	149.8	.26	9	.0083	25.5	25.5	40
DAPER7	8.3	3	8.60	346.3	.60	9	.0083	23.0	23.0	30
GLASSA1	8.3	3	1.52	55.6	.10	30	.0840	25.5	25.5	33
GLASSA2	8.3	3	3.39	124.1	.22	30	.0840	26.0	26.0	30
GLASSA4	8.3	3	2.84	104.0	.18	30	.0840	26.0	26.0	30
GLASSA5	8.3	3	3.94	144.2	.25	30	.0840	26.0	26.0	33
GLASSA6	11.0	3	4.49	217.8	.16	30	.0840	25.5	26.0	30
GLASSA7	11.0	3	2.66	129.0	.10	30	.0840	26.0	26.0	30
GLASSA8	11.0	3	5.79	280.9	.21	30	.0840	26.5	26.0	28
GLASSA9	11.0	3	6.62	321.1	.24	30	.0840	26.5	26.5	30
GLASSB1	11.0	3	3.00	145.5	.11	65	.3950	25.0	25.0	28
GLASSB2	11.0	3	6.00	291.1	.22	65	.3950	23.5	23.5	27
GLASSB3	11.0	3	1.50	72.8	.05	65	.3950	23.0	23.0	28

(1) estimated for a temperature of 26°C

5.1.3 Flow Measurements

During each experiment, several vertical profiles of downstream velocity u and volumetric suspended sediment concentration c were measured along the centerline of the channel. The measurements concentrated in the body of the currents. The profiles were then used to compute the current velocity U and thickness h at different locations, with the help of equations (4.1) and (4.2). In the case of turbidity currents, the buoyancy discharge $\Phi = gRCUh$ can change in the downstream direction due to sediment erosion and deposition, and hence the following integral must be evaluated to determine this parameter at different locations

$$\Phi = g\,R \int_0^\infty u\,c\,dz \tag{5.1}$$

The buoyancy discharge can then be used to compute the Richardson number $R_i = \Phi/U^3$ and the layer–averaged concentration C at each location.

5.1.4 Spatial Development of the Currents

The turbidity currents driven by 4 μ sediment showed little tendency to deposit either in the model canyon or on the model fan; their spatial development thus resembled that of the saline currents. In Figure 5.1, the observations made for a typical run are shown. The current thickness calculated from the measurements is also included. Therein the transition from the canyon to the fan is seen to take place through a hydraulic jump. The measurements locate the jump between 550 and 800 cm from the inlet. In Figure 5.2, the flow characteristics before and after the jump are compared for the cases of a saline current and a turbidity current with the same inlet conditions. It is seen that the structure of the saline underflow and the turbidity current laden with 4 μ sediment are almost identical. In particular, the same sharp decrease in bed shear stress can be inferred.

The turbidity currents driven by 9 μ sediment were weakly depositional along the canyon and the fan. The spatial development of these currents thus resulted, as in the case of currents driven by 4μ sediment, in supercritical and subcritical flow regions with an intervening hydraulic jump. This is illustrated in Figure 5.3, where the measurements taken along the centerline of the flume during a typical run are shown. The jump is seen to take place between 600 and 800 cm from the inlet.

The turbidity currents driven by 30 μ material showed a clear tendency to deposit sediment from their very inception. The more dilute currents often dissipated shortly after reaching the fan. Those currents that were dense enough to reach the downstream end of the flume continuously decelerated and thickened after the break in slope. The

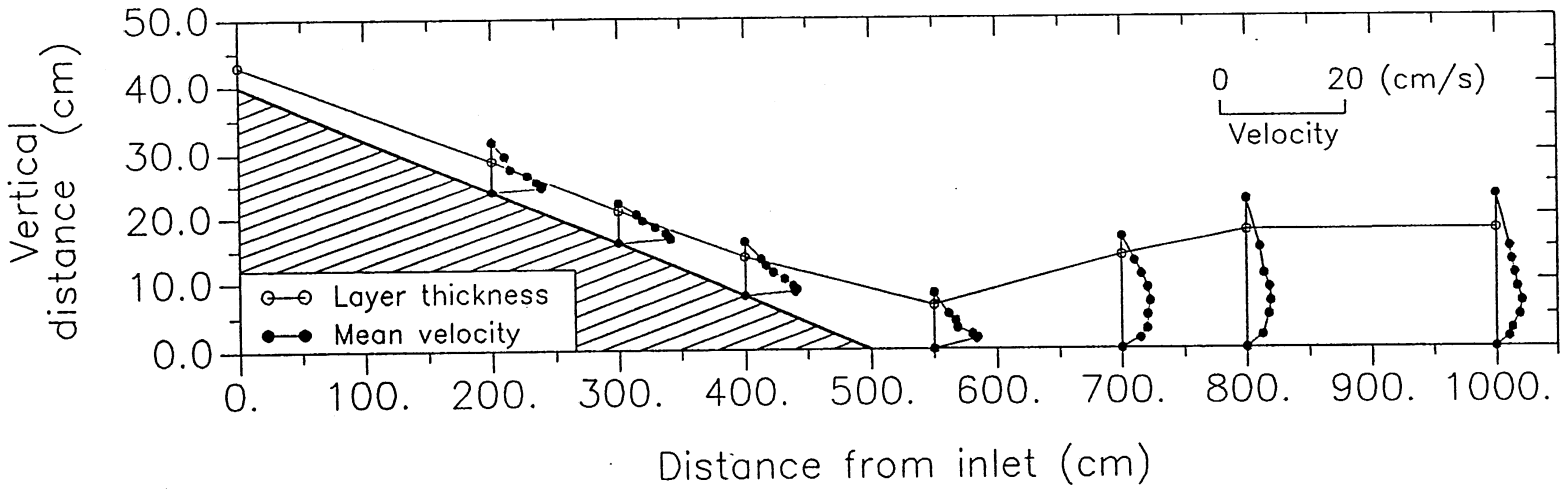

Fig. 5.1 Observations for a turbidity current driven by 4 μ sediment (run NOVA3).

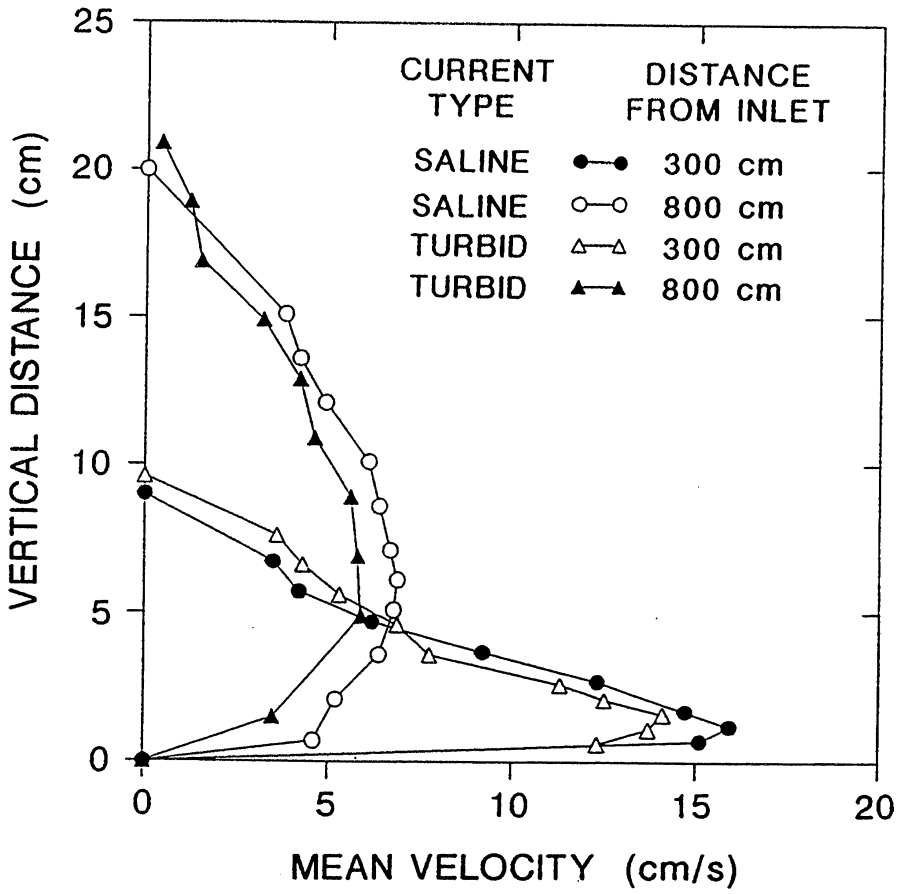

Fig. 5.2 Velocity profiles before and after the jump, for a saline current (SAL29) and a turbidity current driven by 4 μ sediment (NOVA7). Both currents have the same inlet conditions.

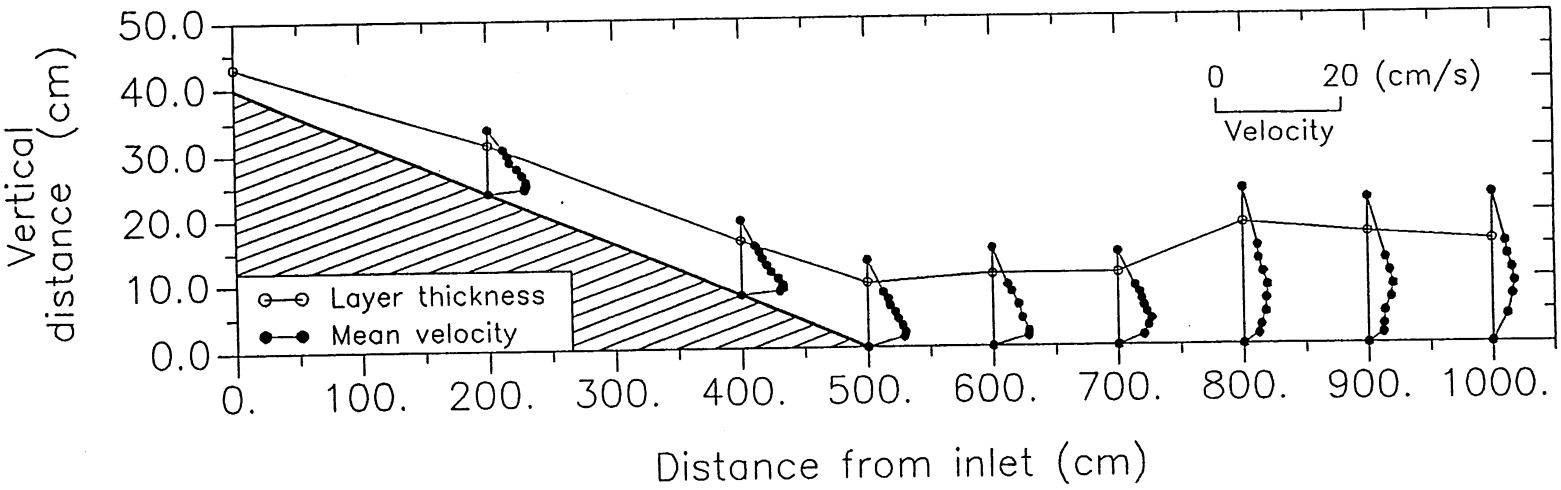

Fig. 5.3 Observations for a turbidity current driven by 9 μ sediment (run DAPER2).

calculated Richardson numbers indicated that the currents reached the end of the flume without going through a jump.

The turbidity currents generated with 65 μ sediment were so strongly depositional that they were not able to preserve their identity; they rapidly disintegrated as they moved downslope. In one of the experiments, sediment deposition in the proximity of the inlet was so strong that the flow conditions in that location were far from being constant.

5.1.5 Characteristics of the Hydraulic Jumps

In Table 5.2, information concerning the characteristics of the jumps is summarized. The jumps are relatively weak, as indicated by the ratio of the current thickness after the jump h_2 to the current thickness before the jump h_1, which is seen to take values between 1.4 and 2.15. The amount of water entrained by the currents while going through the jumps, quantified by the ratio q_2/q_1, is seen to be rather small. In Figure 5.4, the thickness ratio h_2/h_1 is plotted against the pre–jump Richardson number R_{i_1}. The data for saline currents and the relation given by equation (2.47) for non–entraining jumps (i.e. $q_2/q_1 = 1$), are also included. The observations for saline currents and turbidity currents driven by 4 and 9 μ sediment, are seen to agree fairly well with the behavior predicted by equation (2.47).

TABLE 5.2 CHARACTERISTICS OF HYDRAULIC JUMPS

Run	h_1	h_2	U_1	U_2	R_{i_1}	R_{i_2}	h_2/h_1	U_2/U_1	q_2/q_1	q_1/q_0
NOVA1	8.6	14.2	4.3	3.3	0.56	1.45	1.64	0.77	1.24	1.49
NOVA2	6.7	14.2	5.6	3.1	0.31	2.41	2.11	0.55	1.17	1.50
NOVA3	6.5	13.8	5.8	3.6	0.38	2.21	2.12	0.62	1.33	1.51
DAPER1	12.6	18.1	3.9	3.2	0.64	1.45	1.43	0.82	1.16	2.00
DAPER2	10.9	18.4	4.3	3.0	0.51	1.93	1.68	0.70	1.17	1.88
DAPER4	8.7	15.0	5.9	2.8	0.61	3.89	1.72	0.47	1.00	2.07
DAPER5	7.2	11.3	7.9	6.0	0.45	1.22	1.57	0.76	1.19	2.29

note: h_1 and h_2 are in centimeters and U_1 and U_2 are in centimeters per second.

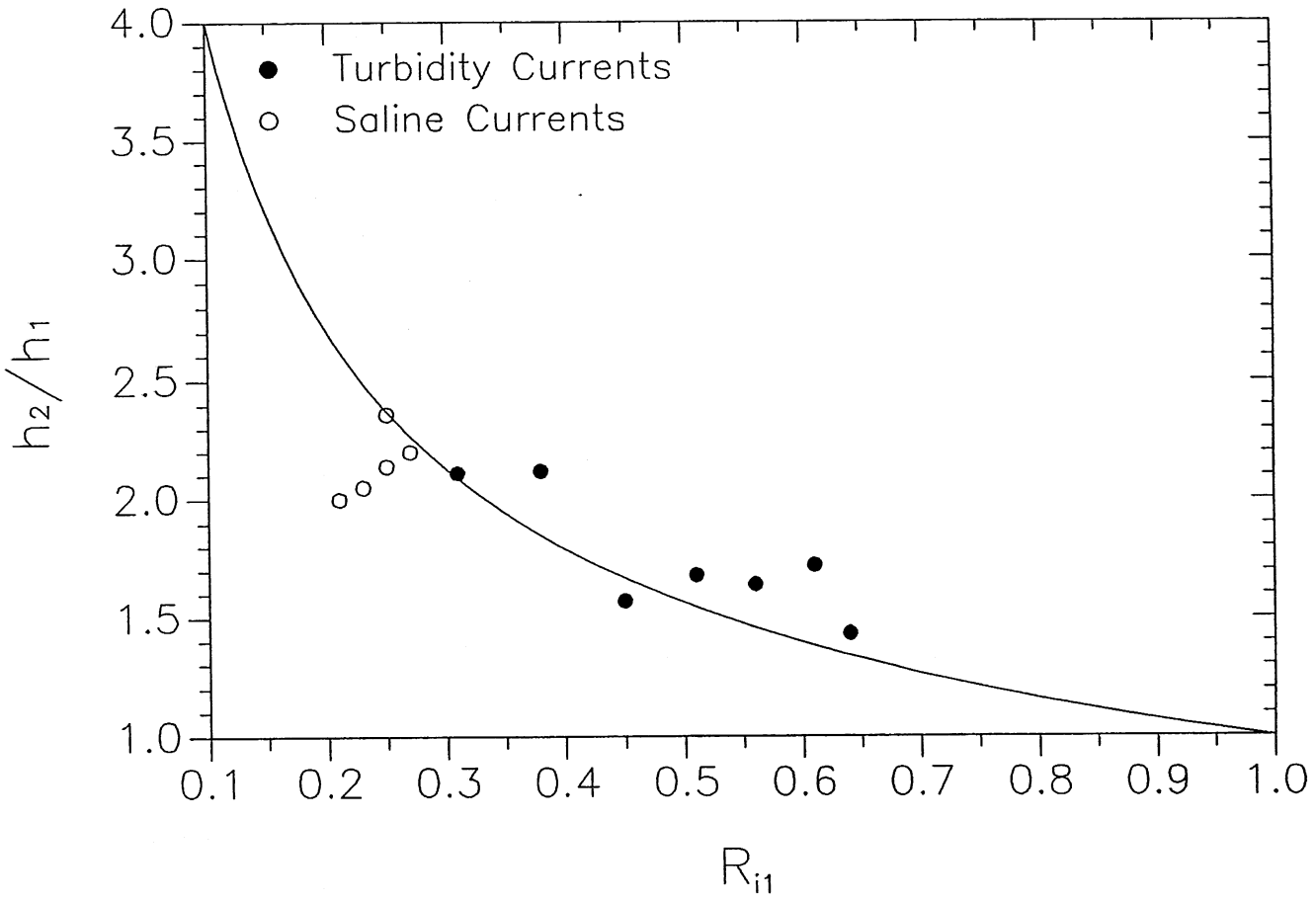

Fig. 5.4 Thickness ratio h_2/h_1 versus the pre–jump Richardson number R_{i_1}. The line is that given by the relationship for non–entraining jumps (2.47).

5.1.6 Vertical Structure of the Currents

As shown in Figure 5.2, the vertical structure of the currents driven by fine–grained sediment is quite similar to that of the saline currents. This is illustrated further in Figures 5.5 and 5.6, where velocity and sediment concentration profiles for currents driven by 4 μ material have been normalized with the corresponding layer–averaged values of velocity and sediment concentration, and current thickness. Similar plots for currents driven by 9 μ and 30 μ sediment are shown in Figures 5.7, 5.8, and 5.9. The supercritical flow profiles were measured at 300 and 400 cm from the inlet, while the subcritical flow profiles correspond to measurements taken at 900 and 1000 cm from the inlet. The similarity collapse is seen to be quite good for supercritical flows. In the case of subcritical flows, where information is available only for currents driven by 4 and 9 μ material, the collapse of the data does not indicate a good similarity of the profiles.

For the case of supercritical flows, an attempt to quantify the effect of sediment size on the vertical structure of the flow can be made by introducing some profile parameters, as denoted in Figure 5.10. They are: the ratio u_m/U of the maximum downstream velocity to the current velocity, the ratio z_m/h of the distance above the bed to the point of maximum velocity to the current thickness; the ratio z_n/h of the distance above the bed at which $u = 0.5\ u_m$ to the current thickness; the ratio c_b/C of the near–bed concentration measured at $z = 0.05$ h to the current layer–averaged concentration; and the ratio z_c/h of the distance above the bed at which $c = 0.5\ c_b$ to the current thickness. Estimates of the above parameters are summarized in Table 5.3. The values therein were obtained by adjusting a line by eye to the normalized profiles in Figures 5.5 ~ 5.9. These values indicate that the grain size does not seem to have any discernible effect on the vertical distribution of velocities. On the other hand, it appears that the grain size has a more noticeable effect on the vertical distribution of suspended sediment. It is seen that as the grain size increases, progressively more of the suspended sediment tends to be located in the lower portion of the flow.

5.1.7 Turbidites Deposited from Suspension

In Figure 5.11, the downstream variation in sediment mass deposited per unit bed area is plotted for turbidity currents driven by sediment of different sizes. The turbidites generated by deposition of 9 μ sediment have an almost uniform thickness along the model canyon and fan. On the other hand, a roughly exponential decrease in turbidite thickness with distance from the inlet can be inferred for the 30 and 65 μ material. The break in slope does not seem to cause any discontinuity in the depositional pattern of the currents driven by 30 μ material.

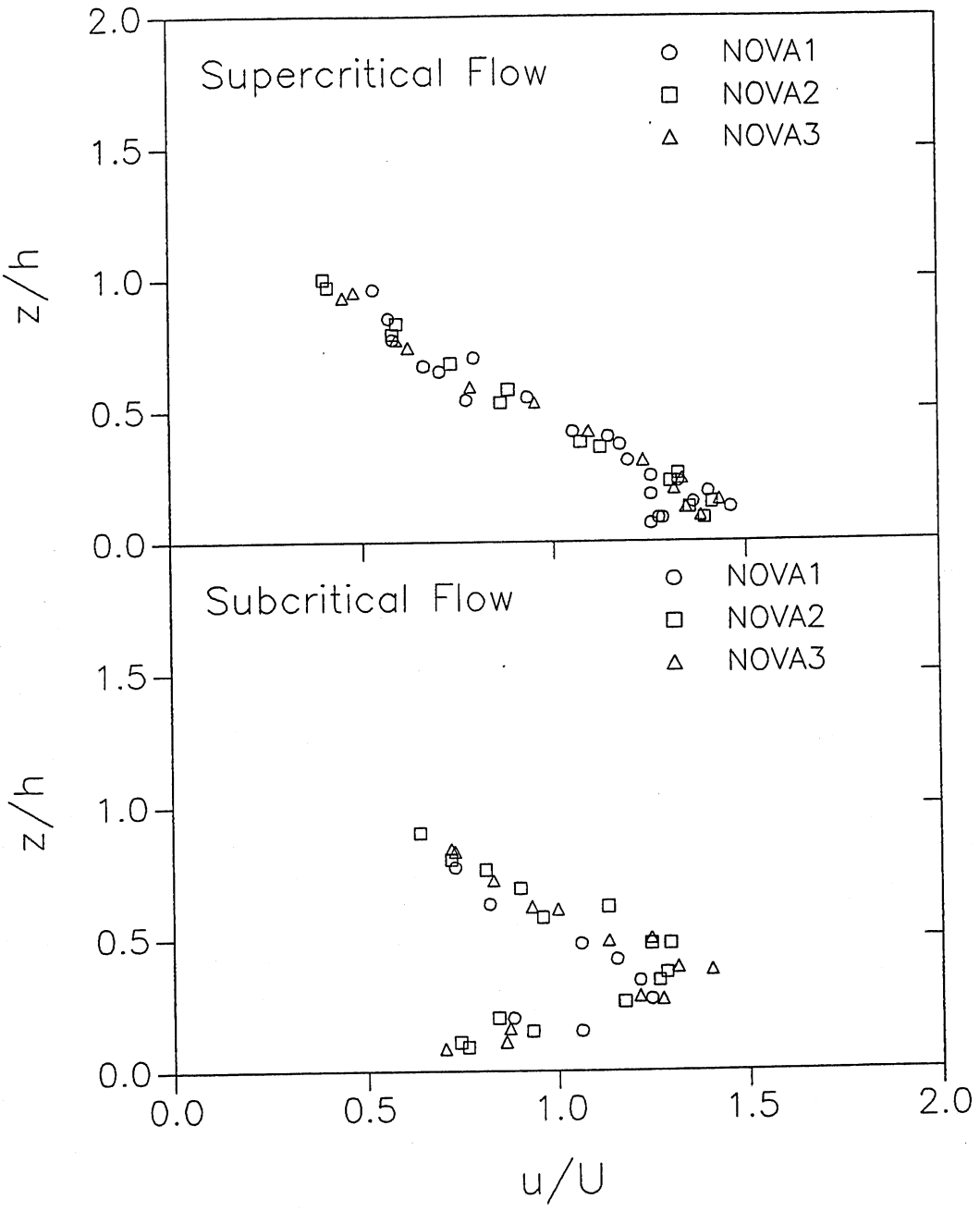

Fig. 5.5 Similarity collapse of velocity profiles for currents driven by 4 μ sediment.

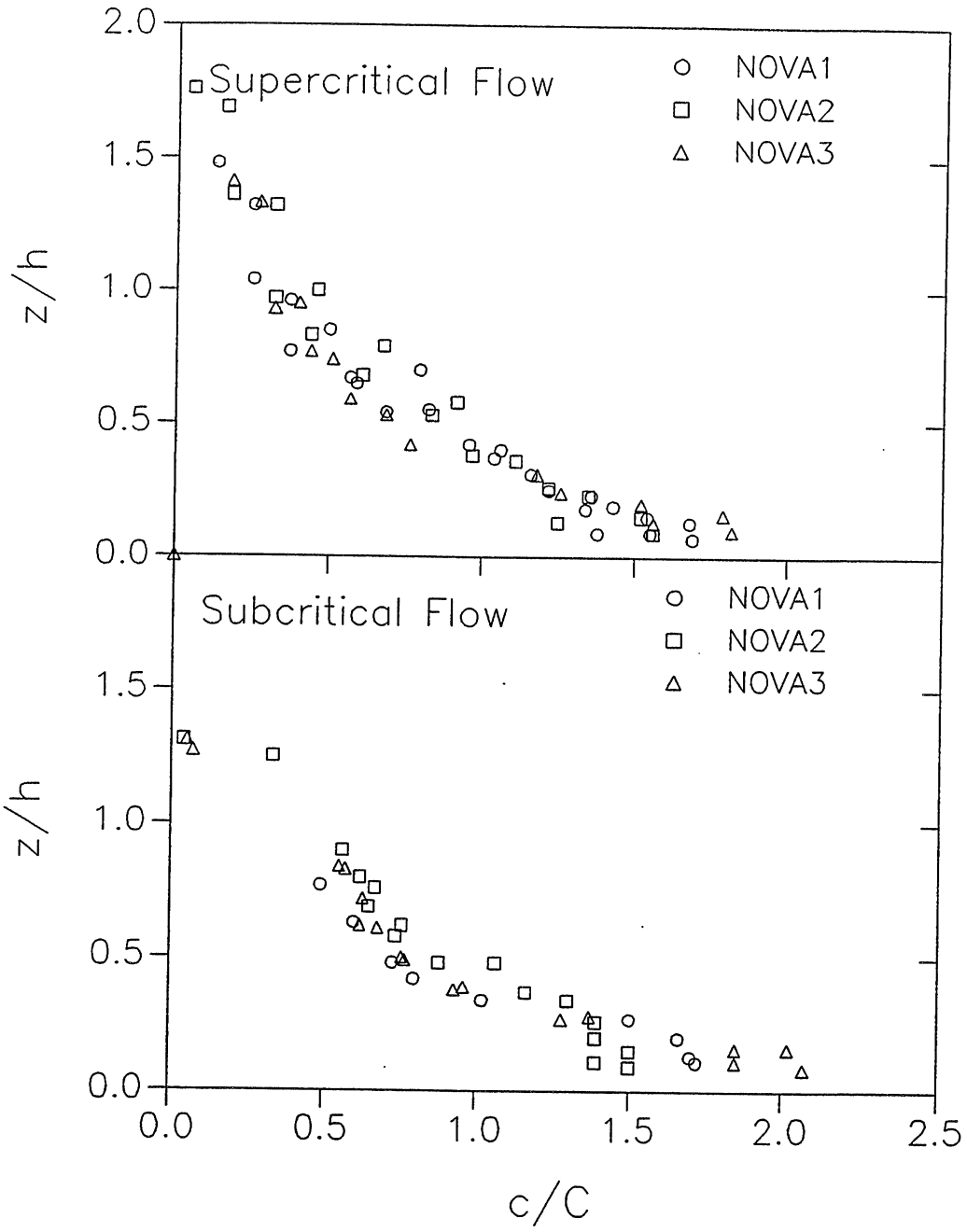

Fig. 5.6 Similarity collapse of sediment concentration profiles for currents driven 4 μ sediment.

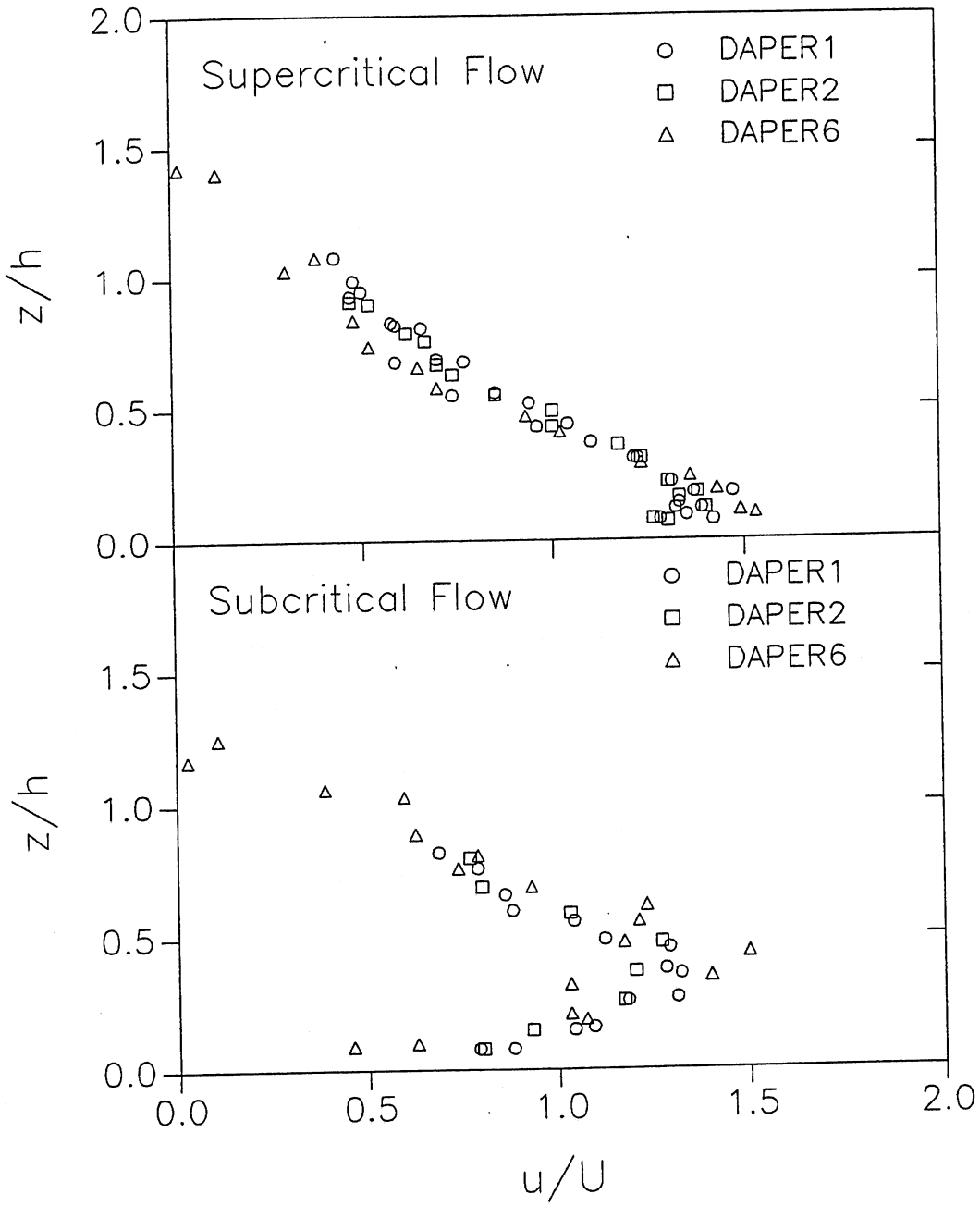

Fig. 5.7 Similarity collapse of velocity profiles for currents driven by 9 μ sediment.

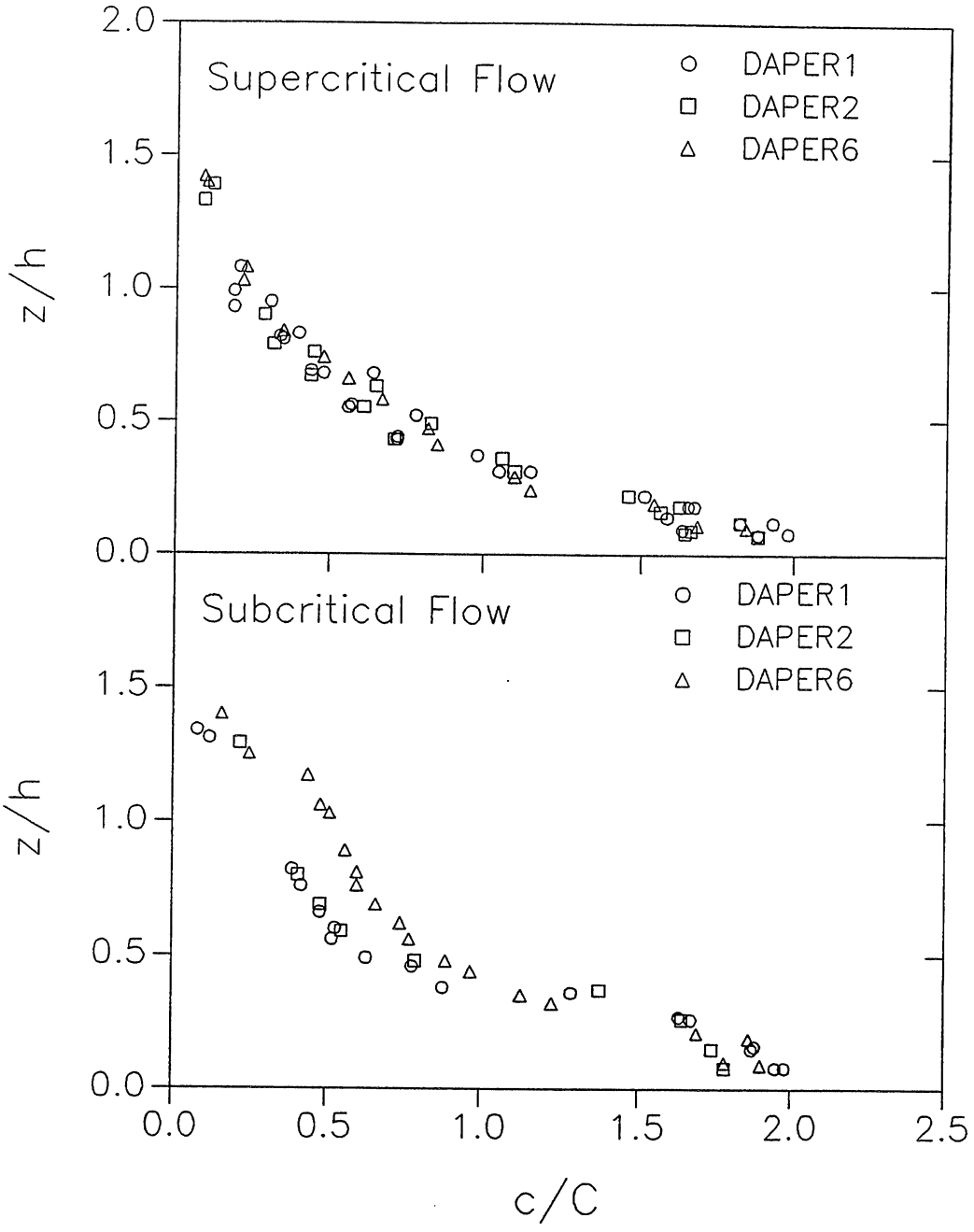

Fig. 5.8 Similarity collapse of sediment concentration profiles for currents driven by 9 μ sediment.

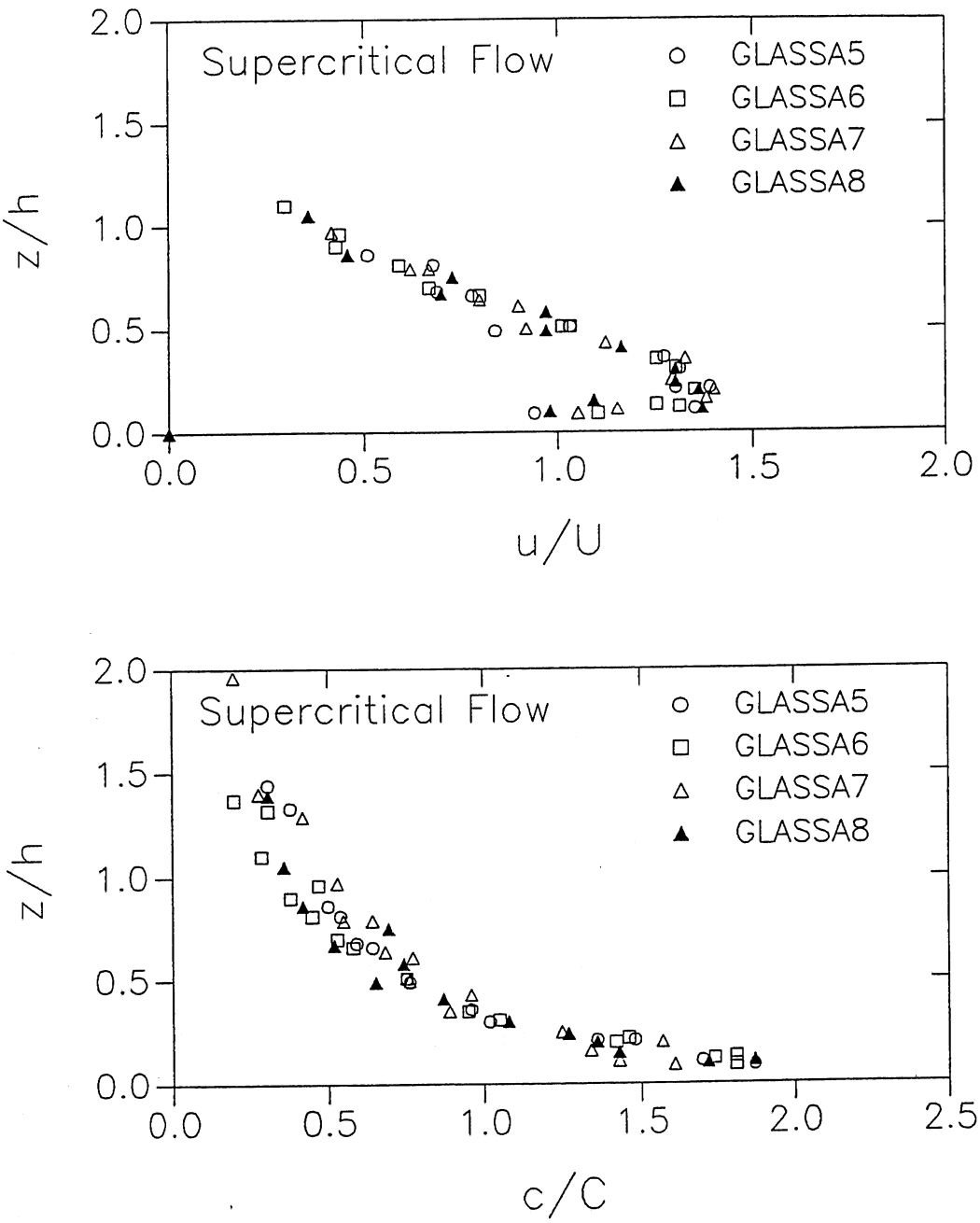

Fig. 5.9 Similarity collapse of velocity and sediment concentration profiles for currents driven by 30 μ sediment.

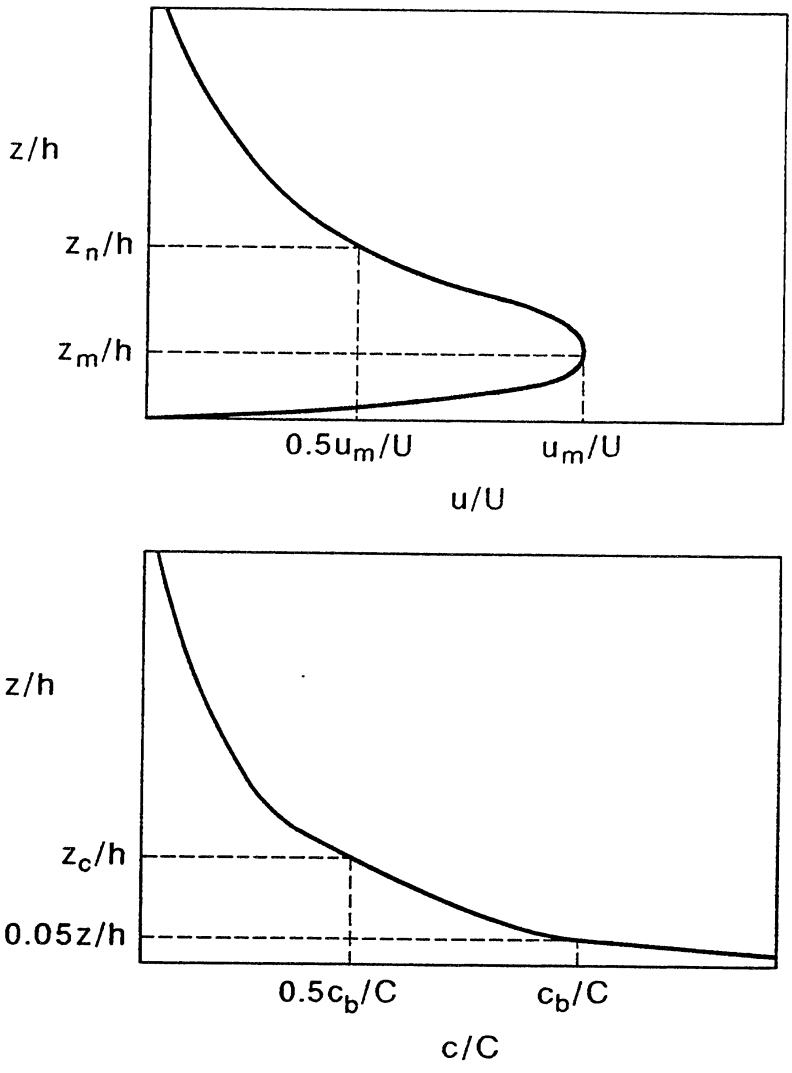

Fig. 5.10 Definition diagram for characteristic current parameters.

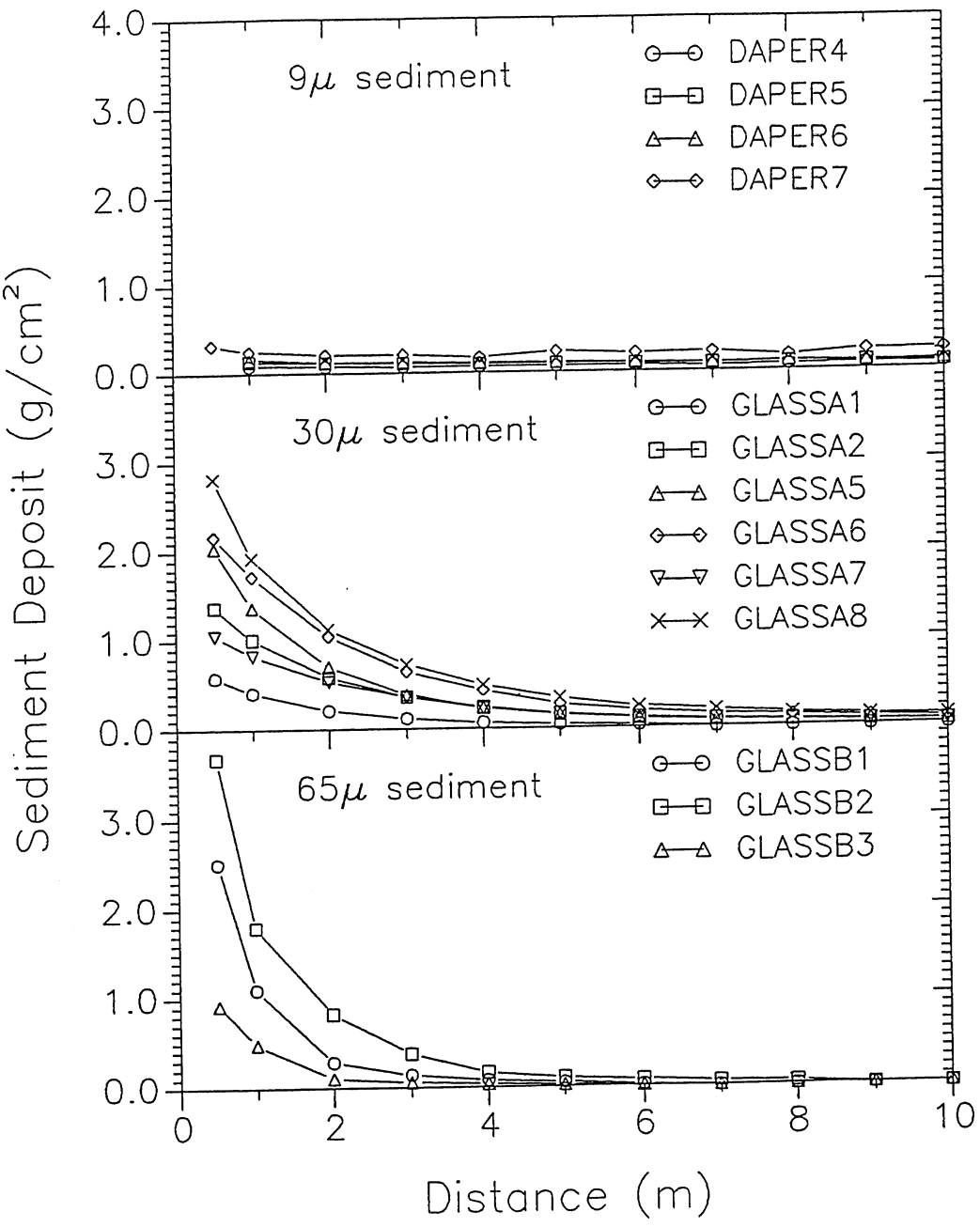

Fig. 5.11 Depositional patterns produced by currents driven by different materials. The break in slope is 5 m from the inlet.

TABLE 5.3 CHARACTERISTICS OF SUPERCRITICAL FLOW PROFILES

$D_{sg}(\mu)$	u_m/U	z_m/h	z_n/h	c_b/C	z_c/h
4	1.40	0.15	0.72	1.78	0.47
9	1.40	0.15	0.70	1.97	0.35
30	1.37	0.15	0.70	2.00	0.30

In the case of currents driven by 4 and 9 μ sediment, for which a jump was clearly observed in all the experiments, no marked change in the rate of deposition or thickness of the deposits was manifested in the vicinity of the jump. It thus follows that a sudden drop in bed shear stress associated with a jump does not necessarily leave a discernible signature in the depositional record immediately downstream. The physical reason for this can be interpreted in terms of the fall velocity v_s of the material available for deposition from suspension. Based on estimates of fall velocities of 0.002 and 0.008 cm/s for 4 and 9 μ material, respectively, and a typical postjump current velocity of 5 cm/s, a particle in suspension would fall between 0.4 and 1.6 mm per meter travelled downstream of the jump. Insofar as the model fan is only 6.6 m in length, it follows that little of the suspended sediment can settle out in response to even markedly reduced shear stress upstream of the end of the flume.

5.1.8 Turbidites Deposited from Bedload

Even though a turbidity current is driven by suspended sediment, it may be easily competent to move rather coarse material as bedload. It is possible that this coarser material would respond more quickly to the reduced shear stress across the jump.

In order to test this idea, the quantitative equivalence between saline and fine–grained turbidity currents illustrated in Figure 5.2 was exploited. In each of several experiments, a saline current colored with green fluorescent dye was generated. Upon establishment of a developed flow, a small but continuous supply of white plastic particles 3 mm in diameter was established at the inlet. These particles had a specific gravity of 1.05 and an estimated fall velocity of 4 cm/s.

The behavior of the plastic particles was clearly visible through the green dye. The particles were transported almost exclusively as bedload down the model canyon, with no tendency to deposit. The case thus modeled up to the jump was that of supply–limited transport of bedload particles. Upon traversing the jump, the particles deposited in quantity. A discontinuous jump in turbidite thickness was thus realized in response to markedly reduced bed shear stress on the downstream side of the jump. The observed sediment deposit is shown in Figure 5.12.

5.1.9 Discussion and Conclusions

Variation of the sediment size used to generate turbidity currents allowed for the observation of different flow behaviors and depositional patterns. The currents driven by fine material (i.e. 4 and 9 μ) behaved very much like conservative currents. A great degree of similarity between the flow structure before and after the hydraulic jump was found. The amount of water entrained by the flows while going through the jump was in general rather small. The strength of the jumps (i.e. h_2/h_1) was seen to take values fairly close to those predicted by the relation for non–entraining jumps (2.47).

An increase in sediment size caused an increase in the tendency of the flow to deposit sediment. The currents driven by 30 μ material decelerated continuously, while depositing sediment along the canyon and fan. On the other hand, the currents generated with 65 μ sediment were so strongly depositional that the flows disintegrated within a rather short distance from the inlet. In both cases, an exponential decrease in turbidite thickness with distance could be discerned. The break in slope did not seem to cause any discontinuity on the depositional pattern of those currents that were capable of reaching the downstream end of the fan.

A good similarity collapse of the velocity and suspended sediment concentration profiles was observed in the case of supercritical flows. The similarity of this profiles was further exploited to quantify the effect of grain size on the vertical structure of the flow. A rather crude analysis using some average profile characteristics showed no apparent effect of the grain size on the vertical distribution of velocities for the sizes ranging from 4 to 30 μ. On the other hand, the profiles of normalized suspended sediment concentration showed, as expected, a tendency for the finer sediment to diffuse farther into the water column than the coarser sediment.

The sharp decrease in bed shear stress experienced by the fine–grained currents after the jump did not cause any change on the rate of deposition from suspension. The following argument can be used to provide a physical explanation for this observation. In a current having a postjump velocity U_2 and thickness h_2, a sediment particle with fall velocity v_s located at a distance 0.5 h_2 above the bed, will reach the bed in a characteristic time t_o given by

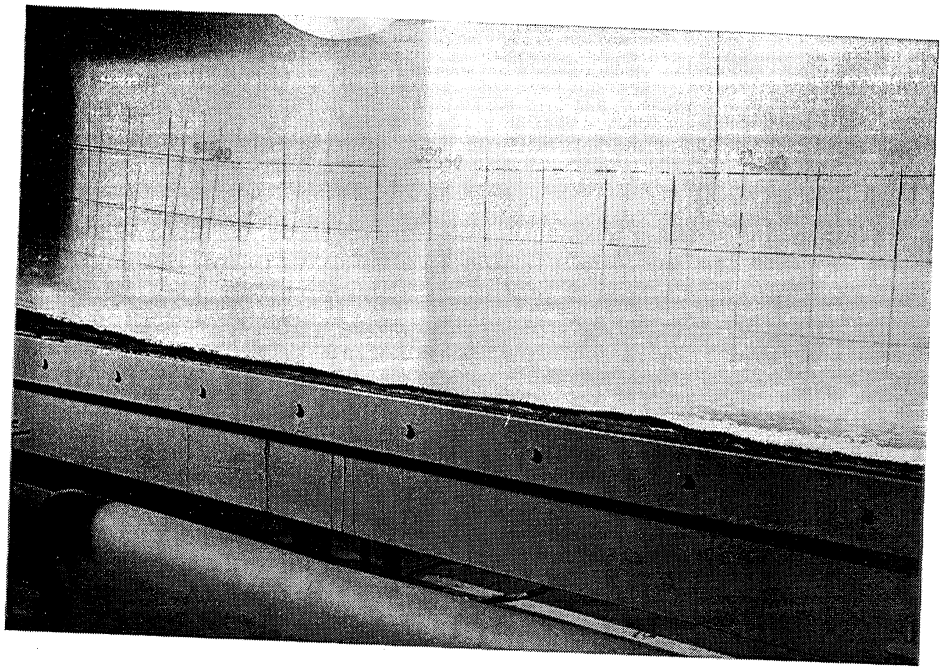

Fig. 5.12 Deposit of plastic particles right after the hydraulic jump undergone by a saline (green) current. The flow is from left to right.

$$\frac{1}{2} h_2 = v_s t_o \tag{5.2}$$

The longitudinal distance ℓ covered by the particle during the depositional process will be

$$\ell = U_2 t_o \tag{5.3}$$

The ratio of (5.3) to (5.2) yields

$$\frac{\ell}{h_2} = \frac{1}{2} \frac{U_2}{v_s} \tag{5.4}$$

which can be rewritten with the help of (2.29) as

$$\frac{\ell}{h_2} = \frac{1}{2} C_D^{-0.5} \frac{u_*}{v_s} \tag{5.5}$$

Smaller values of ℓ imply a tendency for a stronger depositional signature to be left in the depositional record immediately downstream of the jump. The above simple expression indicates that the strength of the signature from the jump tends to increase as the ratio u_*/v_s of the bed shear velocity immediately behind the jump to the particle fall velocity decreases.

The above conclusion is supported by the experimental observations. An inspection of the data indicates that for the currents driven by 4 and 9 μ sediment, the ratio u_*/v_s took values on the order of 200 and 50 respectively. For a typical postjump thickness h_2 = 20 cm and bed friction coefficient C_D = 0.004, equation (5.5) yields settling distances of approximately 32 and 8 m for the 4 and 9 μ material, respectively. This indicates that the model canyon was too short to observe any change in the depositional pattern due to the jump. On the other hand, for the plastic particles that moved as bedload and reacted immediately to the drop in shear stress the ratio u_*/v_s took a value of 0.1. The type of sediment deposit generated with the plastic particles (Fig. 5.12), is in close analogy to that observed in an open–channel flow laden with coarse material downstream of a hydraulic jump (Jopling and Richardson, 1966).

5.2 Currents Driven by Poorly–Sorted Sediment

5.2.1 Purpose of the Experiments

The overall objective of these experiments was to obtain information on the characteristics of turbidity currents driven by poorly–sorted sediment. Of particular interest were the vertical sorting of suspended sediment and the variation of turbidite thickness and grain size with distance from the source.

5.2.2 Overview of the Experiments

The currents generated were in general made to be denser than the turbidity currents driven by well–sorted sediment. This was done in an attempt to generate turbidites that would extend along the whole length of the flume. The material used was novaculite 200. Size distribution is shown in Figure 5.13. As in the previous experiments, the inlet current thickness h_0 was kept at 3 cm. The ranges of inlet values covered were as follows:

$$33 \text{ cm}^2/\text{s} < q_0 < 43.3 \text{ cm}^2/\text{s}$$

$$11 \text{ cm/s} < U_0 < 14.4 \text{ cm/s}$$

$$0.00364 < C_0 < 0.0218$$

$$0.006 < RC_0 < 0.036$$

$$234.8 \text{ cm}^3/\text{s}^3 < \Phi_0 < 1512.2 \text{ cm}^3/\text{s}^3$$

$$0.10 < R_{i_0} < 0.52$$

Here $C_0 = \Sigma C_{i0}$ is the inlet layer–averaged sediment concentration of the sediment mixture, and C_{i0} is the inlet layer–averaged concentration of sediment in the ith size range. The size ranges are defined in Table 5.4.

At the two measuring stations located along the inclined bed, samples of suspended sediment were collected at 0.8, 2.0, 4.5, 7.0, and 9.5 cm above the bed, while at the two stations located along the horizontal region, samples were taken at 1.0, 3.5, 6.5, 11.0, 16.0, and 23.6 cm above the bed. These samples were then used determine the volumetric concentration of suspended sediment **c** at each measuring point, as well as the size distribution.

As in the previous experiments, the inlet Richardson numbers were sufficiently lower than unity to ensure the generation of downstream developing supercritical flows. The inlet Reynolds number $R_{e_0} = U_0 h_0/\nu$ was always larger than 2500. In table 5.5, the inlet conditions and other characteristics of each particular experiment are shown.

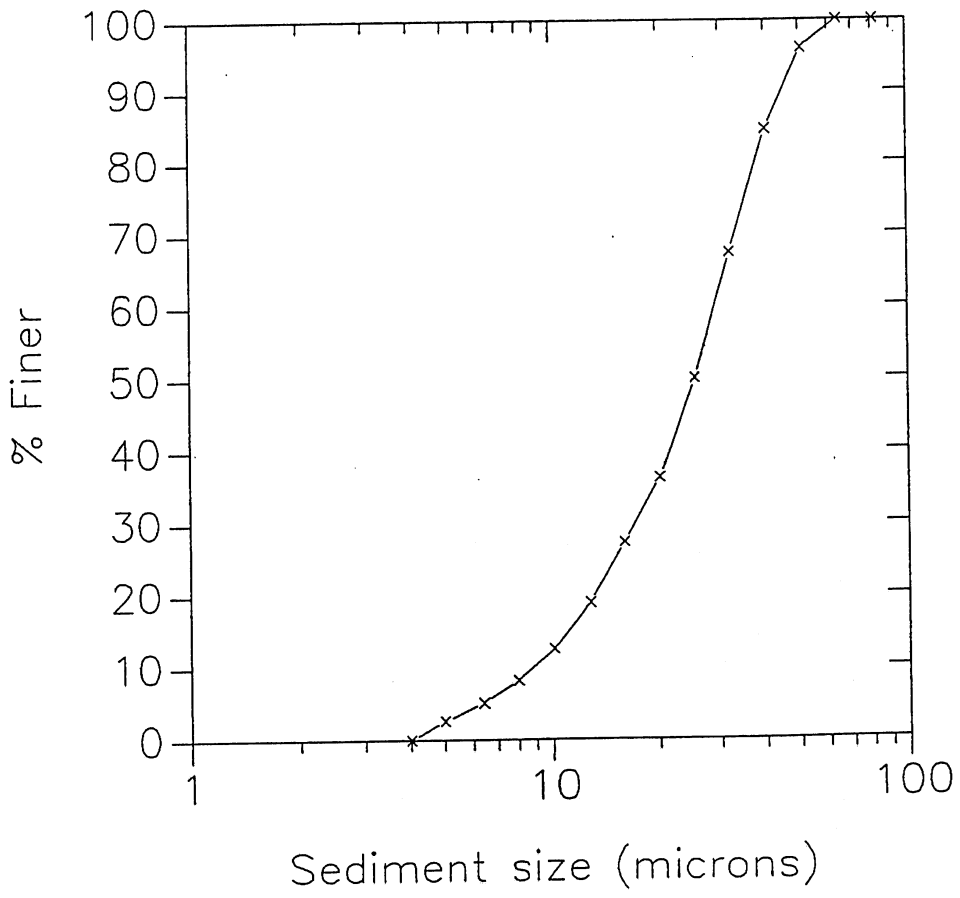

Fig. 5.13 Typical size distribution of the sediment used in the experiments.

TABLE 5.4 SEDIMENT SIZE RANGES

D_{r-1}	D_r	$D_i = (D_{r-1}\, D_r)^{0.5}$
4 μ	– 6.35 μ	5.0 μ
6.35 μ	– 10.08 μ	8.0 μ
10.08 μ	– 16.00 μ	12.7 μ
16.00 μ	– 25.40 μ	20.2 μ
25.40 μ	– 40.30 μ	32.0 μ
40.30 μ	– 64.00 μ	50.8 μ
64.00 μ	– 101.60 μ	80.6 μ

TABLE 5.5 INLET CONDITIONS AND OTHER CHARACTERISTICS OF THE EXPERIMENTS

Run	U_0 (cm/s)	h_0 (cm)	$C_0 \cdot 10^3$	Φ_0 (cm^3/s^3)	R_{i_0}	T_{in} (°C)	T_{fl} (°C)	Run Time (min)
MIX1	13.3	3	3.64	234.8	0.10	17.0	16.5	45
MIX2	13.3	3	7.28	469.7	0.20	4.0	15.0	43
MIX3	13.3	3	7.28	469.7	0.20	7.5	7.5	34
MIX4	11.0	3	6.42	342.6	0.26	6.5	7.0	20
MIX5	11.0	3	7.28	388.5	0.29	6.0	7.0	30
MIX6	11.0	3	10.90	581.6	0.44	4.5	5.0	30
DEP01	13.3	3	3.64	234.8	0.10	6.0	7.0	40
DEP02	14.3	3	21.80	1512.2	0.52	6.8	7.5	24
DEP03	14.3	3	10.90	756.1	0.26	6.0	6.0	24

5.2.3 Flow Characteristics

All the currents were strong enough to reach the downstream end of the flume. In Figure 5.14, the observations made for a typical current are shown. The layer–averaged values obtained from the measurements show that the flow is supercritical at the two stations along the sloping region and subcritical at the two stations along the horizontal region, thus indicating the existence of a hydraulic jump. This flow configuration was observed in most of the runs.

5.2.4 Vertical Sorting of Suspended Sediment

As a current evolves with distance, it can be expected than the suspended sediment will manifest itself within the water column as different vertical distributions for different size ranges. This in turn will determine the characteristics of the turbidite deposited by such a current. In Figure 5.15, the size distribution of suspended sediment samples taken at different locations above the bed are plotted. A clear tendency for the sediment size to decrease in the vertical direction can be discerned.

The product of the sediment size distribution times the total sediment concentration **c** at each measuring point was used to obtain the volumetric concentration c_i for each size range. This information can then be used to construct the vertical distribution of material in the different size ranges. In Figure 5.16, the resulting profiles for a typical measuring station are shown. The data indicate that the finer grains are distributed more uniformly in the vertical direction than the coarser grains. The plot also illustrates clearly the variation in rates of deposition that can be expected for a sediment mixture.

5.2.5 Variation of Turbidite Thickness and Grain Size

All flows showed a tendency to deposit sediment along the model canyon and fan. As illustrated in Figure 5.17, the variation in turbidite thickness with distance from the inlet was roughly exponential in most of the experiments. As was the case with well–sorted sediment, the break in slope did not seem to cause any discontinuity in the depositional pattern.

The mean grain size of the suspended sediment driving a depositional current can be expected to decrease with distance from the inlet due to deposition of the coarser fraction. This suggests that the grain size of the turbidite originated by such a current should decrease in the downstream direction. This is illustrated in Figure 5.18, where the median grain size D_{50} (i.e. the grain size for which 50% of the sediment is finer) of the bed samples collected during several the experiments is plotted as a function of distance from the inlet. Because of the way this samples were collected (i.e. by means of a siphon), the median grain size of each bed sample represents a bulk value of turbidite grain size.

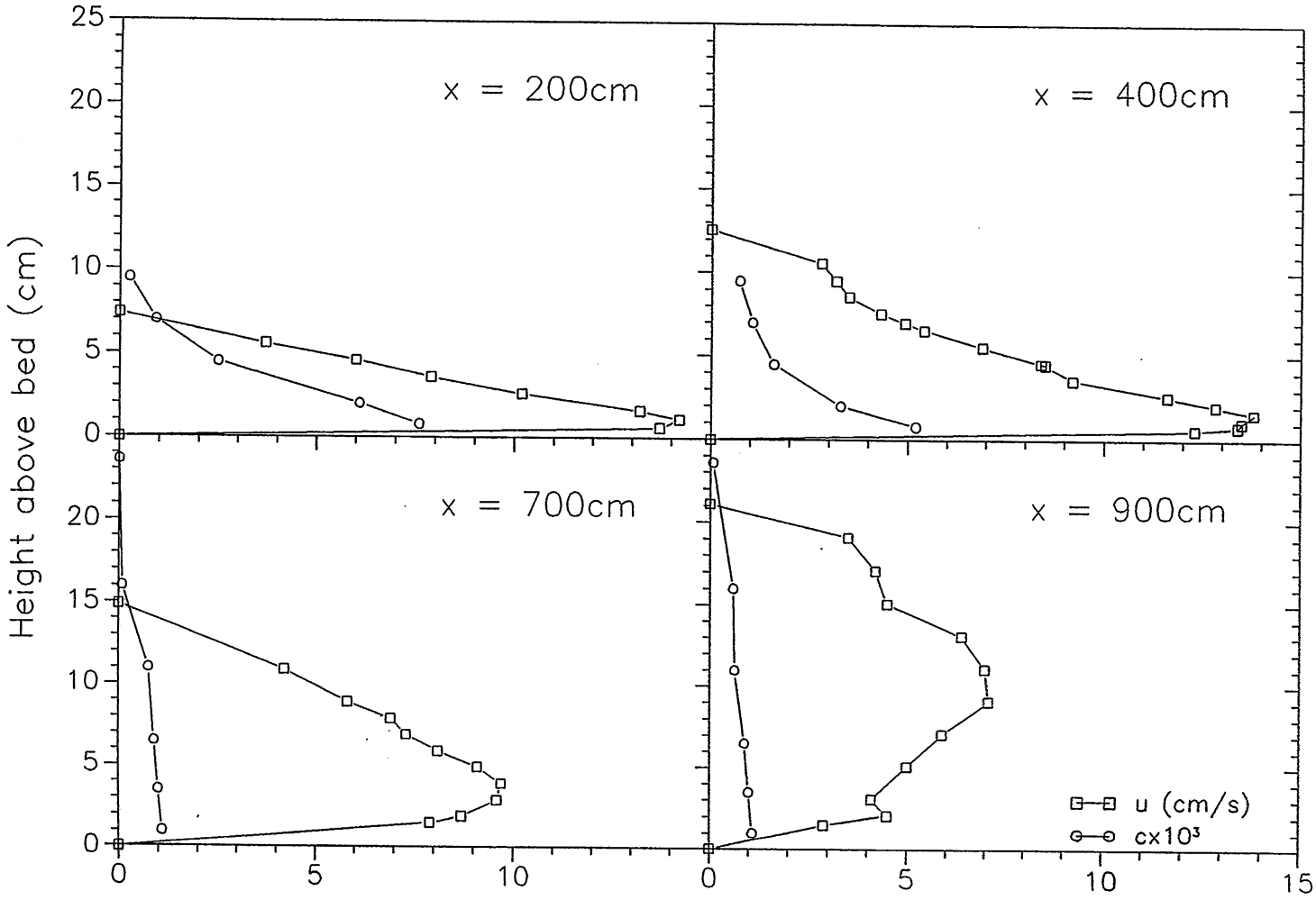

Fig. 5.14 **Observations made for a typical current at two stations along the sloping region and two stations along the horizontal region (run DEPO3).**

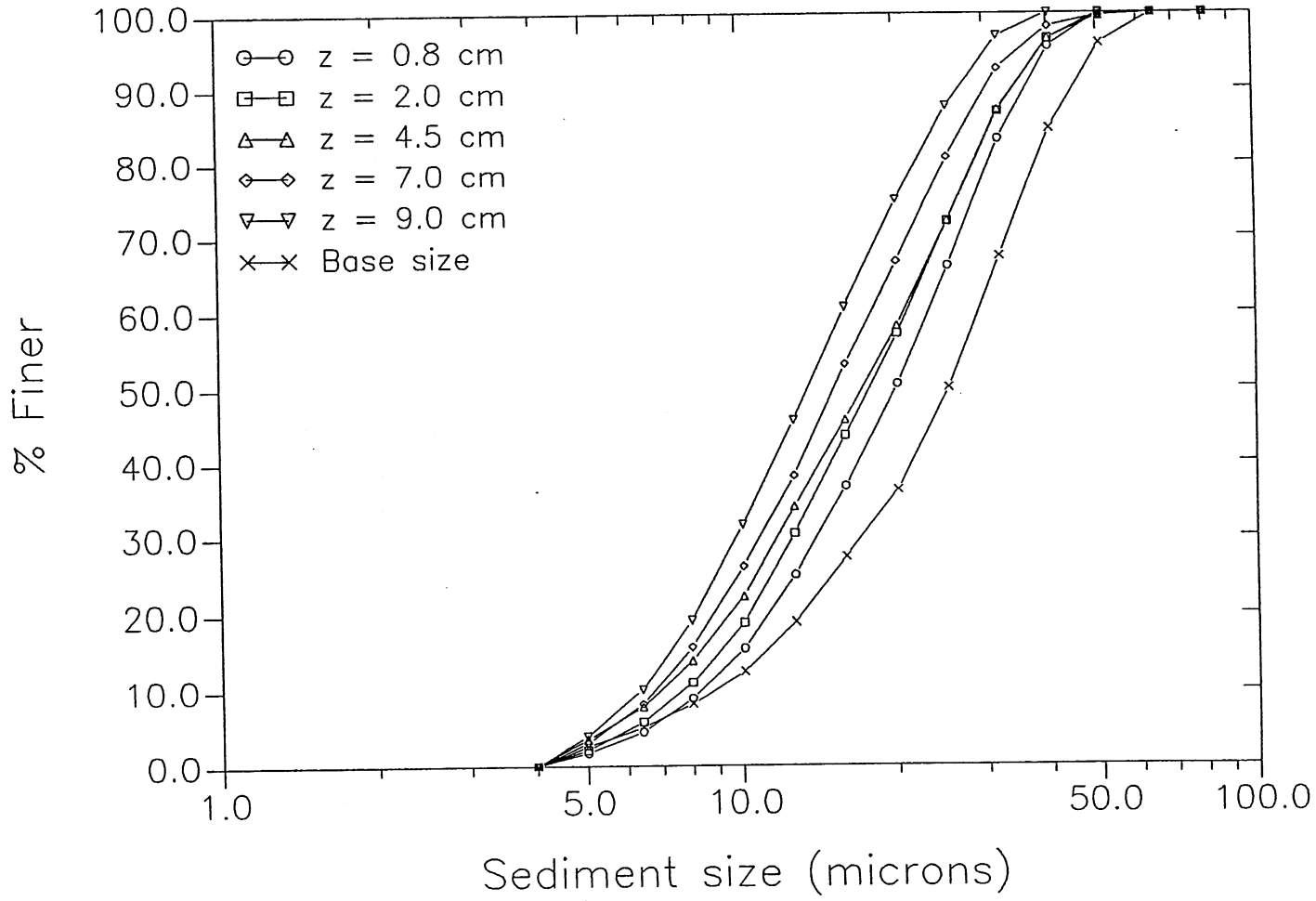

Fig. 5.15 Size distribution of suspended sediment samples taken at different locations above the bed. The size distribution of the suspended sediment at the inlet (base) is also included. The data correspond to the measurements taken at 400 cm from the inlet during run DEPO3.

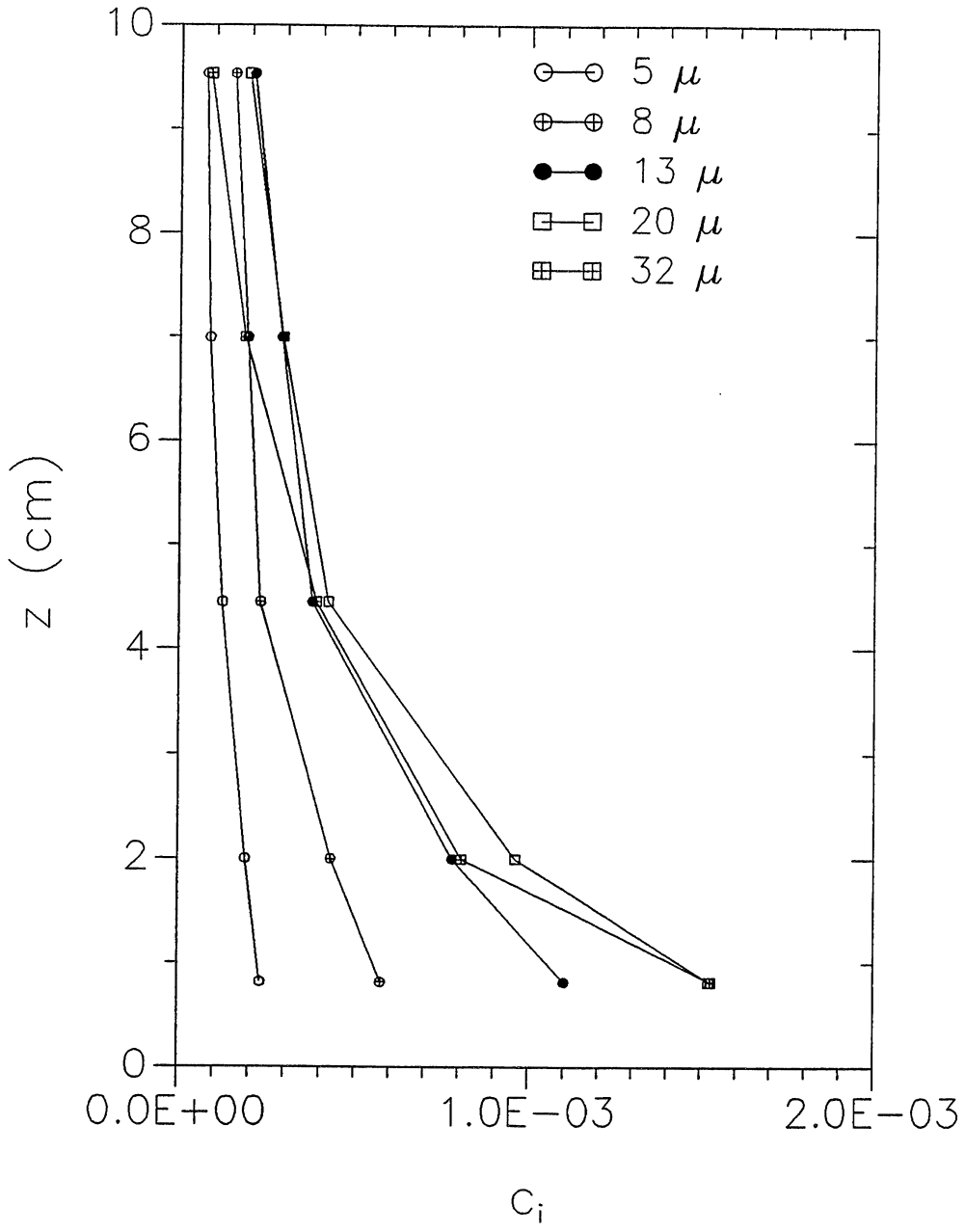

Fig. 5.16 Vertical concentration profiles for different grain sizes. Data from run DEPO3 at x = 400 cm.

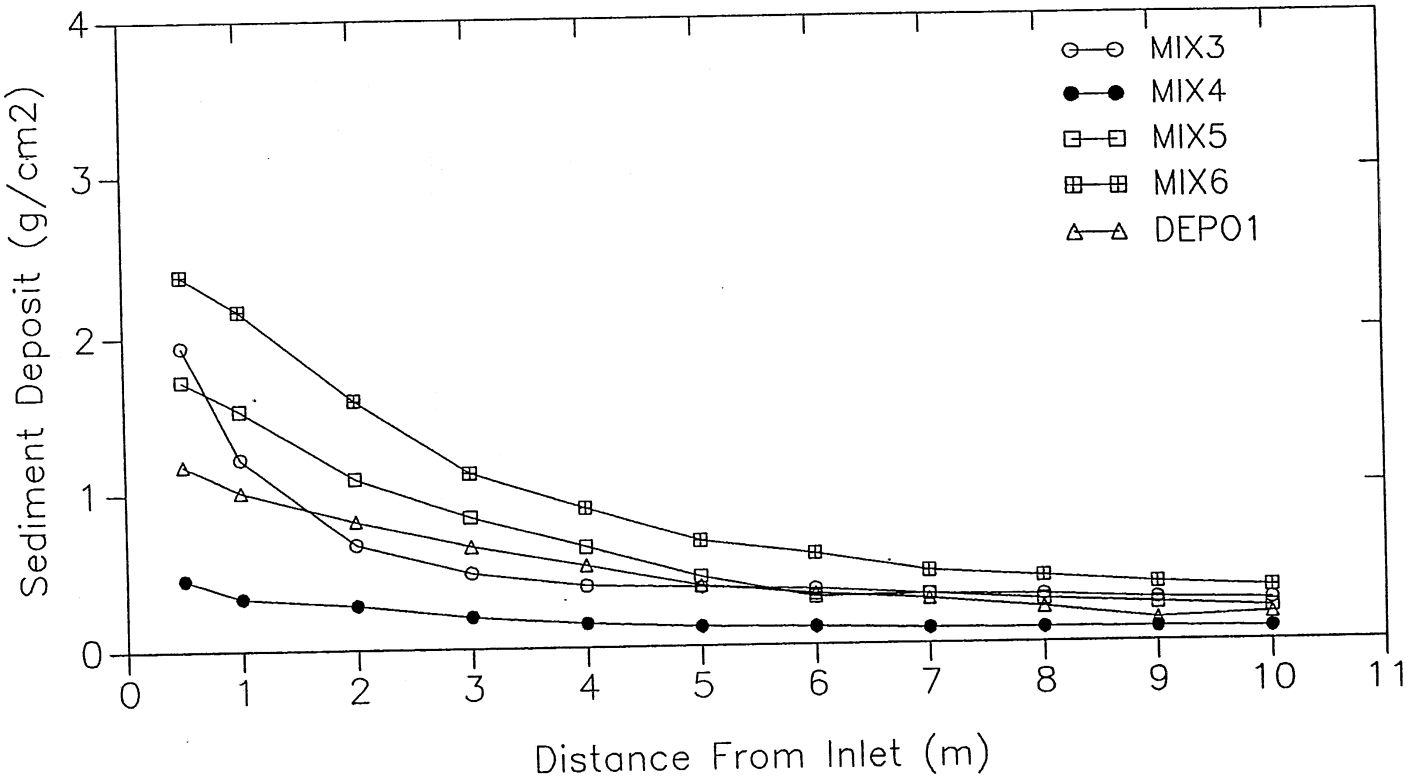

Fig. 5.17 Depositional patterns produced by currents driven by poorly-sorted sediment.

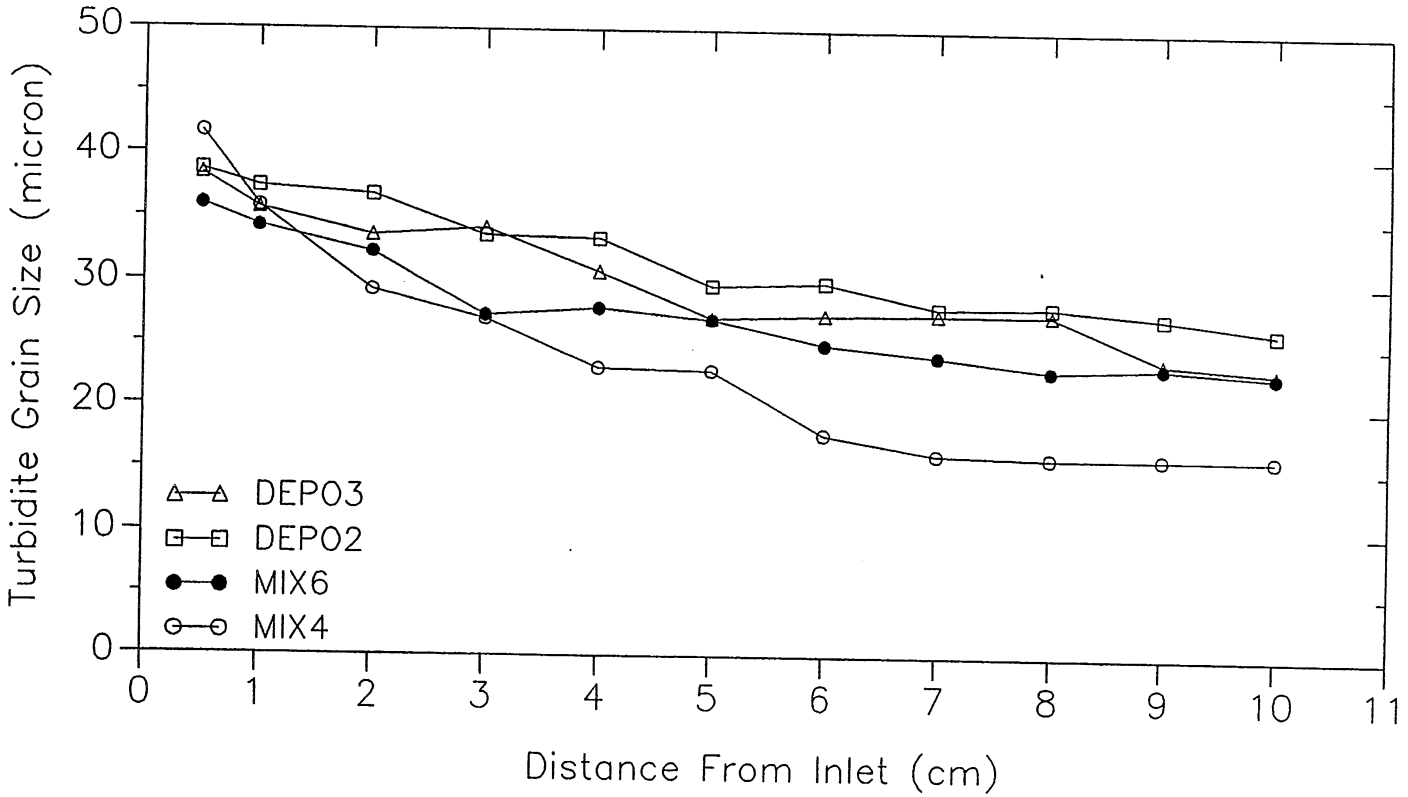

Fig. 5.18 Variation of turbidite median grain size D_{50} with distance from the inlet.

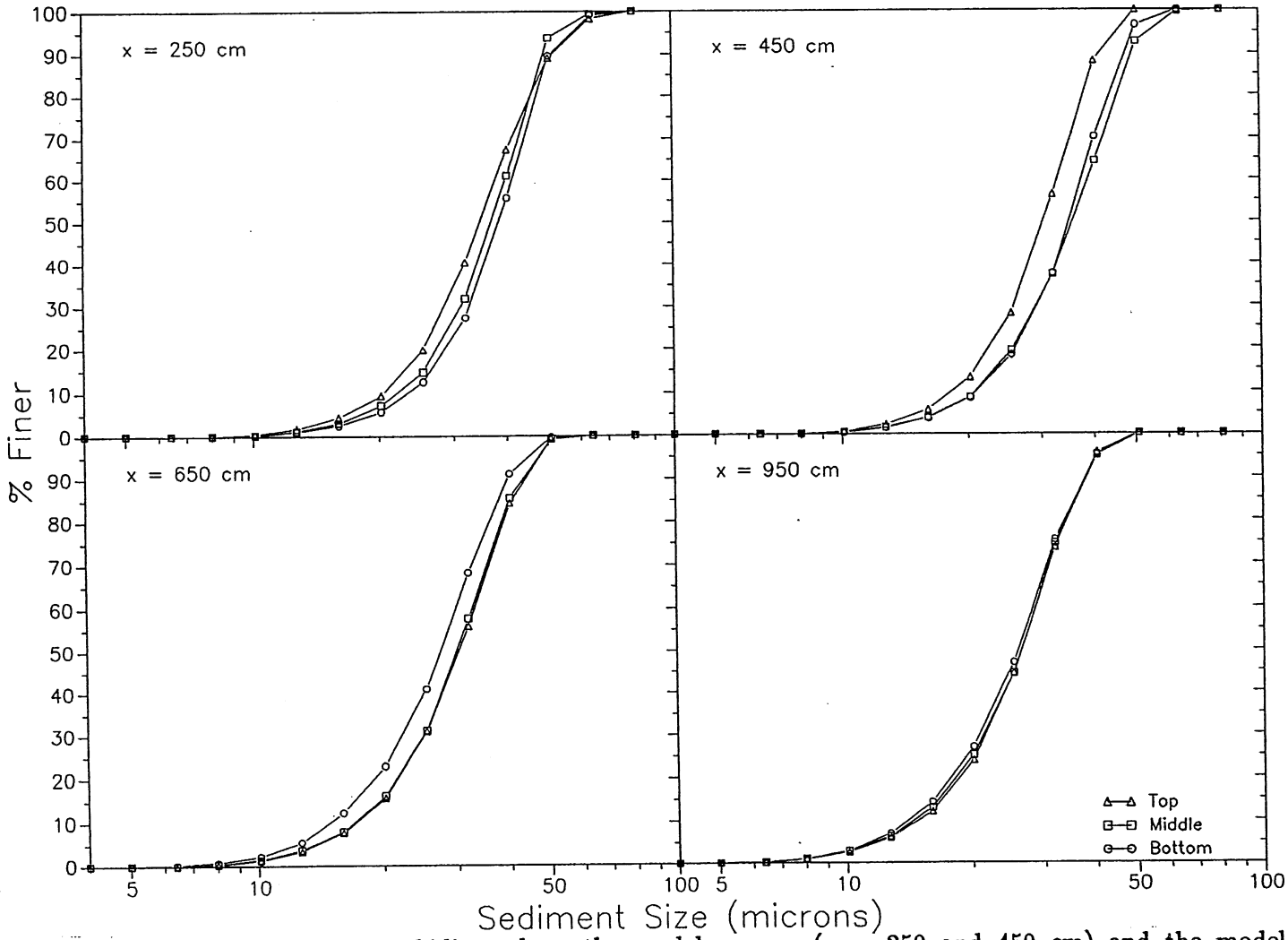

Fig. 5.19 Grain size distribution in turbidites along the model canyon (x = 250 and 450 cm) and the model fan (x = 650 and 950 cm). Data from run DEPO2.

In some of the experiments, the turbidites generated were thick enough to allow for the sampling of sediment at different locations in the vertical direction. The samples were usually taken from the base, the middle, and the top of the deposit. In Figure 5.19, the size distributions obtained from turbidites deposited at two locations along the canyon and two locations along the fan are shown. The two canyon samples show upward fining. One fan sample displays upward coarsening and the other one displays little vertical stratification.

5.2.6 Similarity of Velocity and Sediment Concentration Profiles

The velocity profiles measured during the experiments show a structure very much like that of the currents driven by well-sorted sediment. This is illustrated in Figure 5.20, where a number of velocity profiles measured along the model canyon and fan are plotted in normalized form in terms of the current thickness and layer-averaged velocity. The similarity collapse of the data is quite good for the supercritical region of the flows. On the other hand, the data for the subcritical region of the flows shows a similar shape but with a fair amount of scatter.

The vertical distributions of suspended sediment displayed in Figure 5.16 are plotted in normalized form in Figure 5.21. The volumetric sediment concentrations c_i for each size are normalized with the corresponding layer-averaged concentration C_i. The plot clearly indicates that the finer grains tend to distribute more uniformly in the vertical direction than the coarser grains. In Chapter 2, the parameter c_i was assumed to maintain approximately similar profiles in the vertical direction obeying the following similarity law (2.12)

$$\frac{c_i}{C_i} = \xi_{ci}(\eta, \delta_i) \qquad i=1...N \tag{5.6}$$

where $\eta = z/h$ and $\delta_i = D_i/D_{sg}$. The geometric mean size of the suspended sediment D_{sg} is determined with the layer-averaged concentrations C_i for each size range, according to equation (2.14). A plausible form of the similarity function ξ_{ci} can be obtained with the help the closure relationship given by equation (2.30)

$$c_{b_i} = r_o \, g_o(\delta_i) \, C_i \tag{5.7}$$

and the following similarity relationship

$$\frac{c_i}{c_{b_i}} = f_o\left(\frac{z}{z_{ci}}\right) \tag{5.8}$$

where z_{ci} is the distance above the bed at which $c_i = 0.5 \, c_{b_i}$. Substitution of (5.7) into (5.8) yields

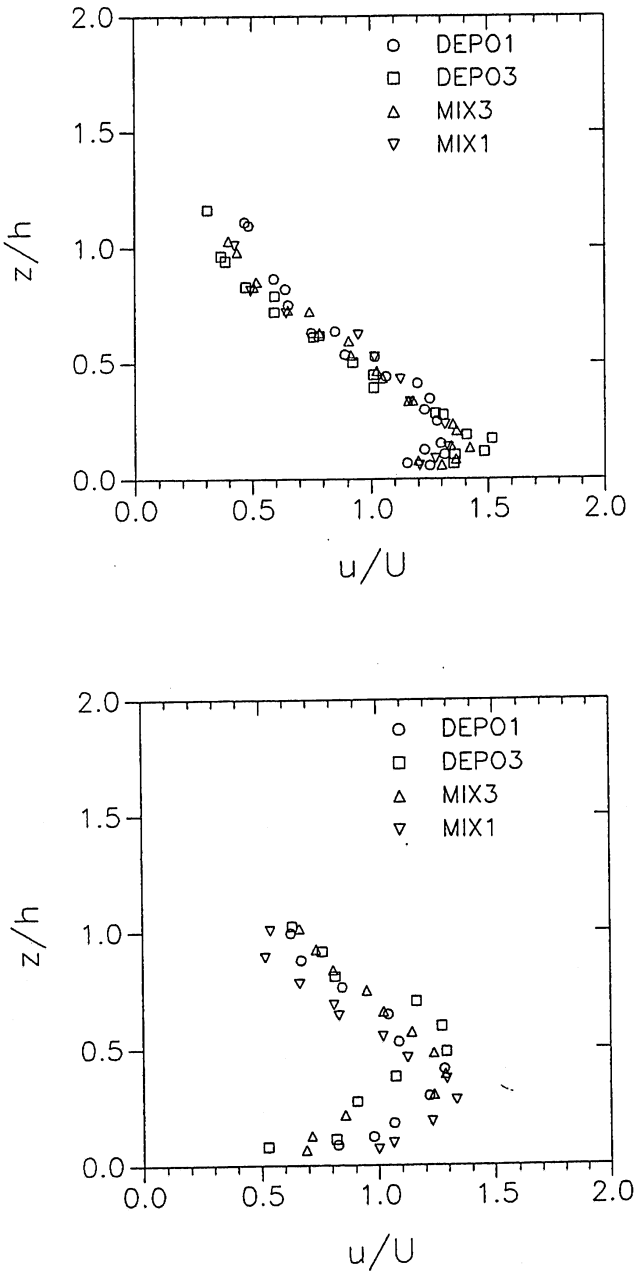

Fig. 5.20 Similarity collapse of velocity profiles measured along the supercritical region of the flows (top) and along the subcritical region of the flows (bottom).

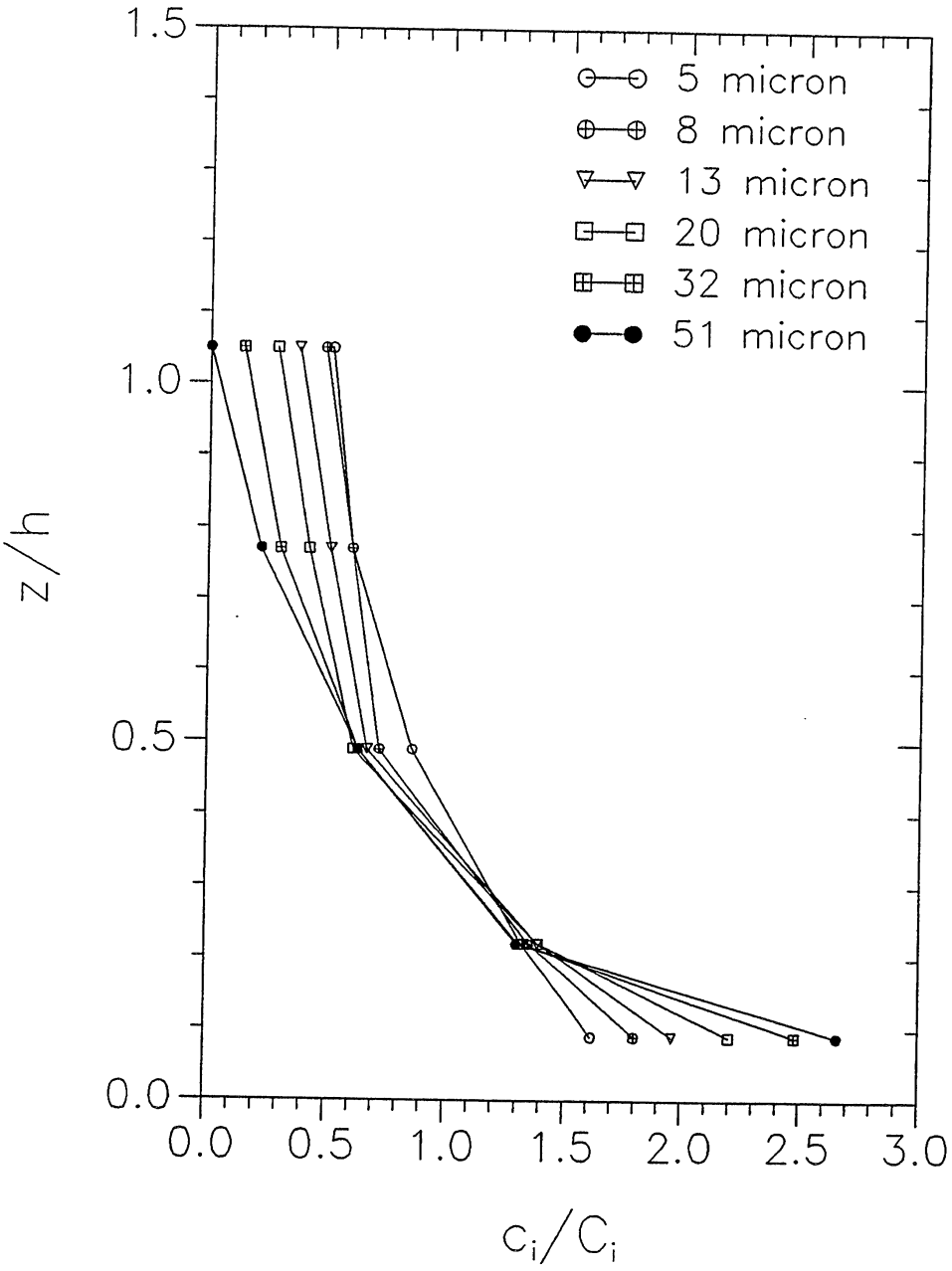

Fig. 5.21 Normalized sediment concentration profiles for different grain sizes. Data from run DEPO3 at x = 400 cm.

$$\frac{c_i}{C_i} = r_o \; g_o(\delta_i) \; f_o(\frac{z}{z_{ci}}) \tag{5.9}$$

A convenient expression for z_{ci} is given by

$$\frac{z_{ci}}{h} = g_*(\delta_i) \tag{5.10}$$

From (5.6), (5.9), and (5.10) the following relationship is obtained

$$\frac{c_i}{C_i} = r_o \; g_o \; f_o(\frac{z}{h} \; g_*^{-1}) \tag{5.11}$$

As illustrated in Figure 5.22, a good similarity collapse is observed when the concentration profiles for the different grain sizes are normalized in terms of the following parameters: the near–bed concentration c_{b_i} measured at $z = 0.05$ h; and the distance z_{ci} above the bed at which $c_i = 0.5 \; c_{b_i}$. This supports the similarity relationship implied by equation (5.8). A fit of the data provides the following expression

$$\frac{c_i}{c_{b_i}} = 1.05 \; e^{-0.68 \; z/z_{ci}} \tag{5.12}$$

The data obtained during the experiments at a station located at 400 cm from the inlet are used to test the relationship implied by (5.10). In Figure 5.23, the values of z_{ci}/h are plotted against the corresponding values of δ_i. The data are seen to collapse into two groups. The lower group indicates an almost constant and low value of z_{ci}/h (= 0.2) for all sediment sizes, while the upper group indicates that z_{ci}/h decreases when δ_i increases. The lack of variation with sediment size shown by the lower group does not seem to be correct. On the other hand , the trend displayed by the upper group is supported by the observations made during the experiments which indicate that the finer grains tend to be more uniformly distributed than the coarser grains. Furthermore, the values of z_{ci}/h in the proximity of $\delta_i = 1$ are seen to fall within the range $0.30 < z_{ci}/h < 0.47$ observed during the experiments with uniform material (Table 5.3). The following expression fits the data reasonably well

$$\frac{z_{ci}}{h} = 0.57 \; e^{-0.43 \; \delta_i} \tag{5.13}$$

The data plotted in Figure 5.21 show that the values of c_{b_i}/C_i increase with sediment size. This is illustrated in Figure 5.24, where the values of c_{b_i}/C_i are plotted against the corresponding values of δ_i. Only the data from those experiments that showed a variation of z_{ci}/h with grain size are

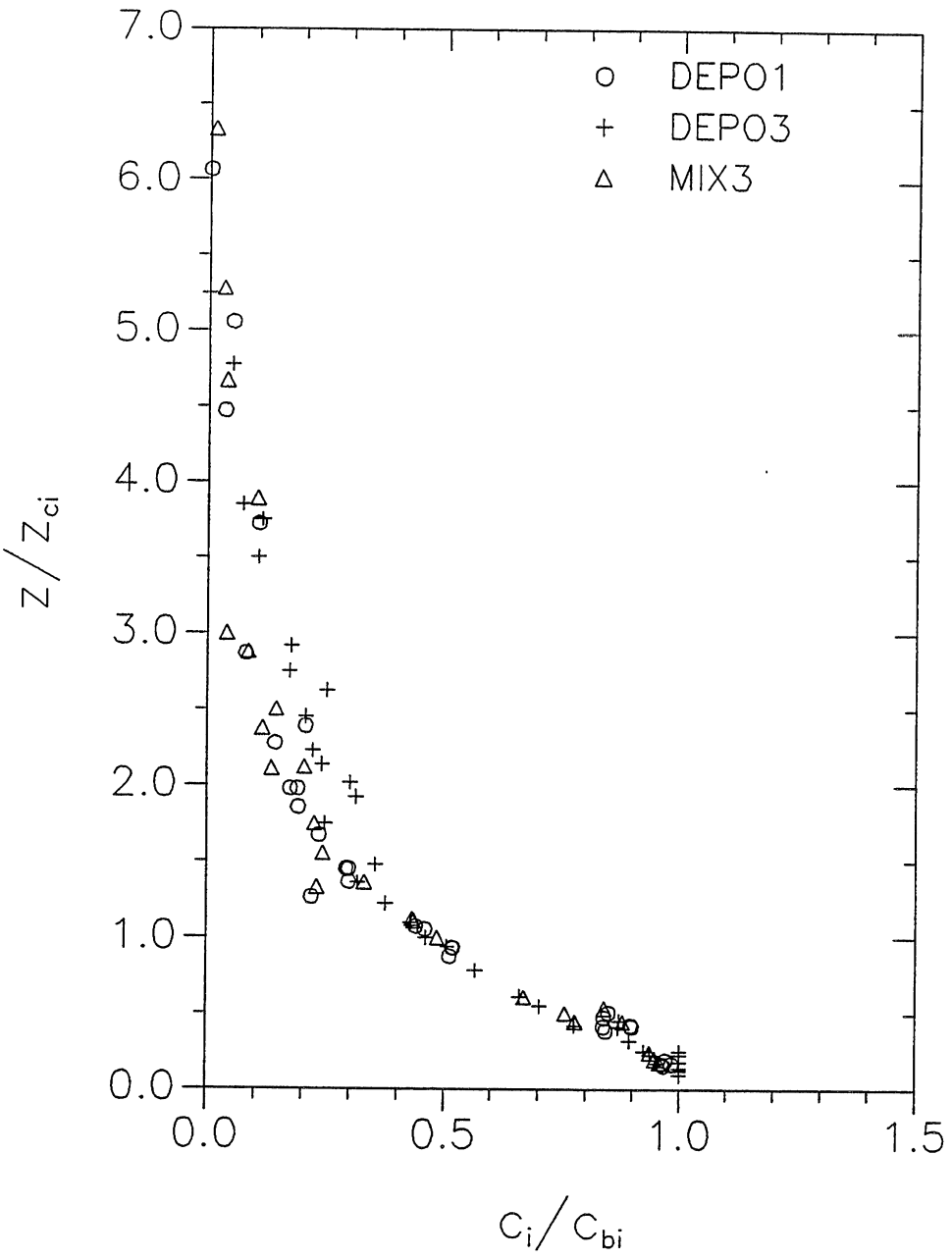

Fig. 5.22 Similarity collapse of concentration profiles for different grain sizes. Data from measurements taken at x = 400 cm during runs DEPO1, DEPO3, and MIX3.

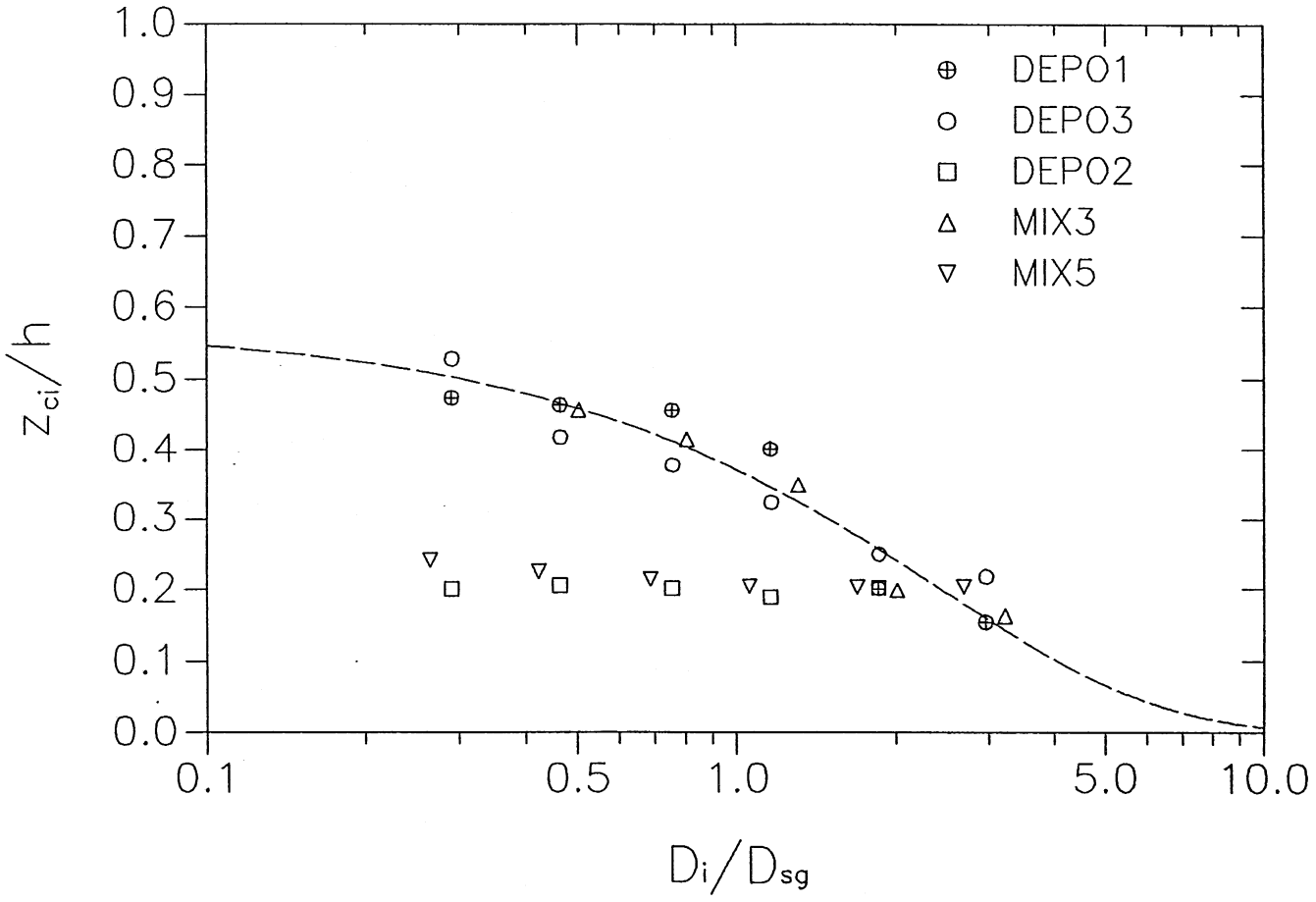

Fig. 5.23 Plot of z_{ci}/h versus the corresponding values of $\delta_i = D_i/D_{sg}$. Data from sediment concentration profiles measured at x = 400 cm.

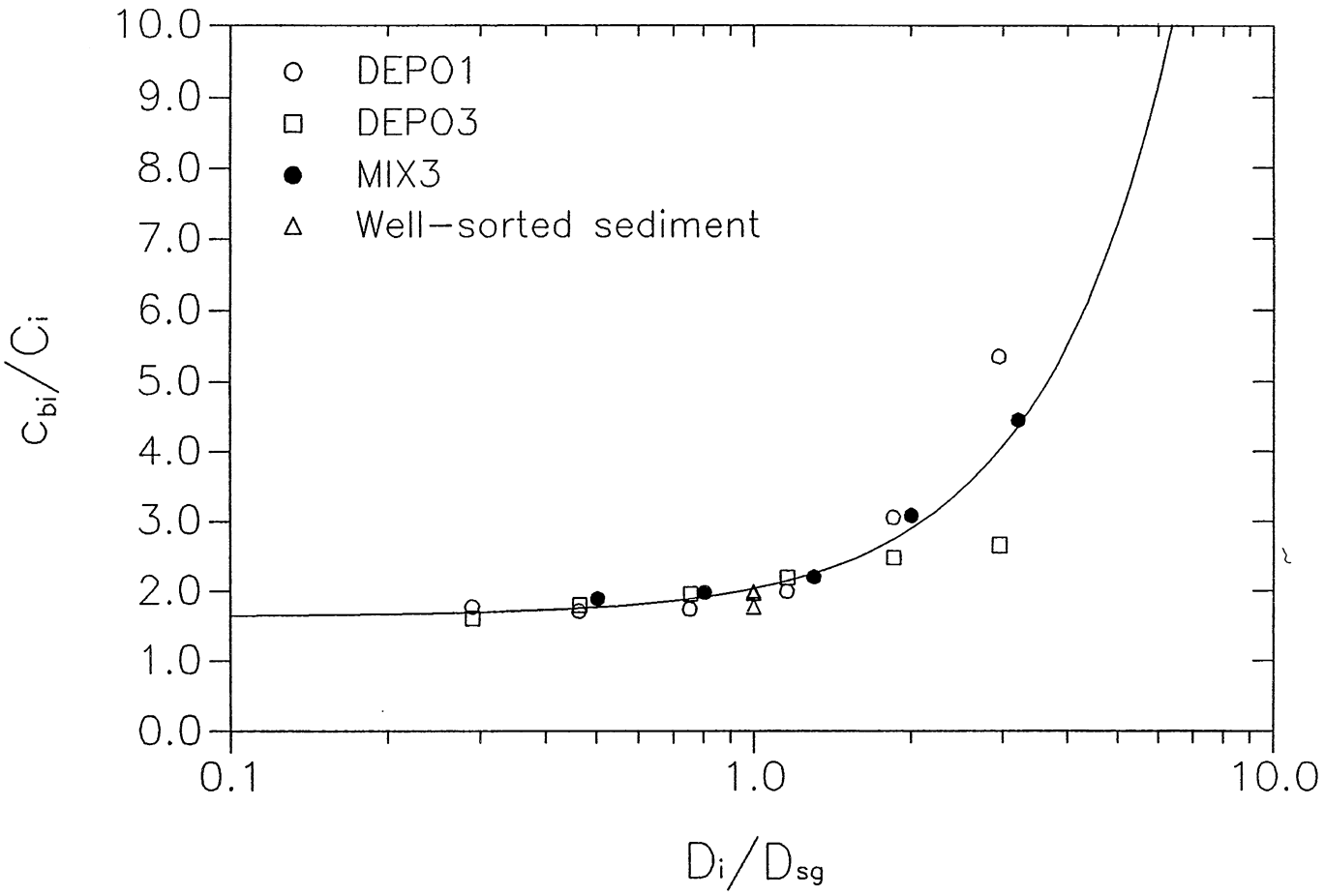

Fig. 5.24 Plot of c_{b_i}/C_i versus the corresponding values of $\delta_i = D_i/D_{sg}$. Data from sediment concentration profiles measured at x = 400 cm.

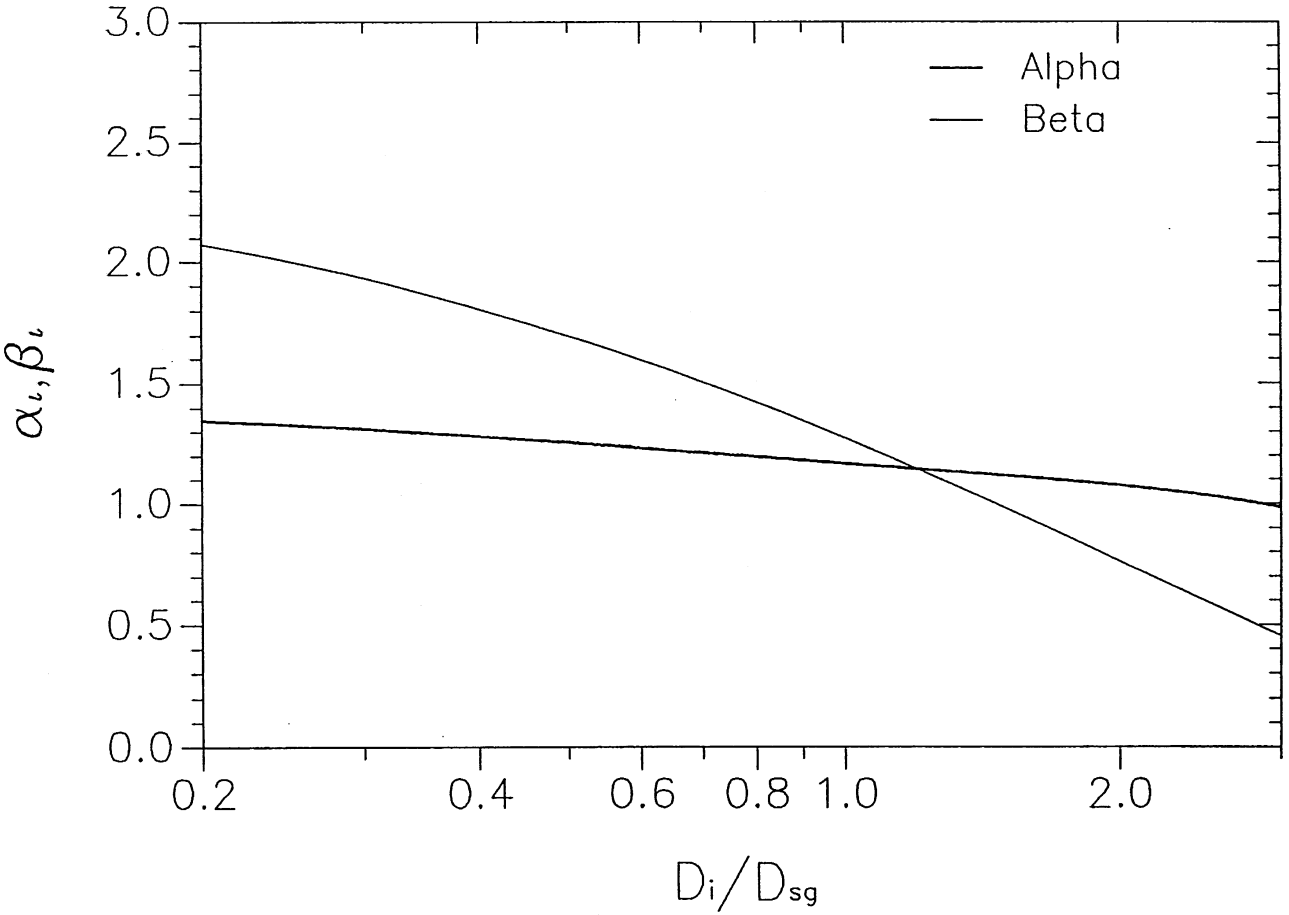

Fig. 5.25 Values of the shape factors α_i and β_i as a function of $\delta_i = D_i/D_{sg}$.

included. For the sake of comparison, the average values of c_b/C observed in the experiments with well–sorted sediment (Table 5.3) are also included in the plot. The data for poorly–sorted sediment is seen to match well the values associated with well–sorted sediment in the proximity of the point $\delta_i = 1$. The following fit approximates the behavior displayed by the data:

$$\frac{c_{b_i}}{C_i} = 0.40\ \delta_i^{1.64} + 1.64 \tag{5.14}$$

Since for uniform sediment $r_o \approx 2$, it follows from (5.7) and (5.14) that following relationship for $g_o(\delta_i)$ can be obtained

$$g_o = 0.20\ \delta_i^{1.64} + 0.82 \tag{5.15}$$

The shape factors α_i and β_i defined by equations (2.21) and (2.22) can be estimated with the help of equation (5.11) and the approximate expressions given by (5.12), (5.13), (5.13), and (5.14). In Figure 5.25, the values of the shape factors are plotted against $\delta_i = D_i/D_{sg}$. The values of α_i are close to unity, while β_i is seen to take values in the range $0.4 \sim 2.1$.

5.2.7 Conclusions

All the underflows were strong enough to traverse the model canyon and fan without losing their identities. In most of the runs, the measurements allowed for the detection of supercritical and subcritical flow regions with an intervening hydraulic jump.

The measurements of suspended sediment indicated a clear tendency for the sediment to decrease in size in the vertical direction. On the other hand, the sediment concentration profiles for grains of different sizes indicated that smaller grain sizes were more uniformly distributed in the vertical. Increased sediment size thus implies an increased depositional rate for the same layer–averaged value C_i.

The thickness and median grain size of the turbidites deposited by the currents were seen to decrease with distance from the inlet. No effect of the hydraulic jump on the rate of deposition and turbidite grain size could be discerned.

When it was possible to analyze the vertical structure of the deposits, the turbidites showed in most cases upward fining along the model canyon. Along the model fan, upward coarsening or no size stratification were typically observed.

The velocity profiles showed a good similarity collapse in the case of supercritical flows and only a fair collapse in the case of subcritical flows. At the same time, the analysis of several profile parameters indicated that the vertical distribution of sediment having different sizes can be expected to be approximately similar as a current evolves in the downslope direction.

The expressions developed to evaluate profile parameters cannot be considered universal. However, the trends displayed by such relationships can be expected to be similar for turbidity currents in natural environments.

The similarity function obtained with the help of the data allowed for a direct evaluation of the shape factors resulting from the vertical integration of the equations of motion. The shape factors have values of the order of unity in the case of α_i, and take values between 0.4 and 2 in the case of β_i. This indicates that the top hat assumption constitutes a crude but reasonable approximation.

CHAPTER 6

EXPERIMENTAL RESULTS: SEDIMENT–ENTRAINING CURRENTS

6.1 Purpose of the Experiments

The direct measurement of the erosion caused by sand–driven turbidity currents constitutes a difficult problem. In the field, the measurements are rendered difficult due to the necessity of working in deep water, and the tendency in some cases for swift currents to destroy measuring instrumentation (Inman et al., 1976). In the laboratory, the amount of bed sediment that can be entrained by a turbidity current is relatively small; thus making the evaluation of the entrainment difficult and inaccurate (Garcia, 1985).

In these experiments, the similarity observed previously between saline currents and turbidity currents driven by fine sediment was exploited. The main objective was to test the ability of saline currents to entrain bed sediment into suspension. The advantage of using salt rather than sediment, is that the occurrence of entrainment can be directly observed and measured. The analogy of relevance consists of the entrainment of sediment into a turbidity current driven by silty clay. However, the results should also be of relevance to the problem of sand entrainment by sand–driven currents.

The flow configuration under consideration is illustrated in Figure 6.1. A saline underflow emerges from a bottom inlet in a basin of fresh water at $x = 0$, and flows down a fixed sloping bed. After some distance, the fixed bed gives way to a bed covered with a layer of fine, loose, non–cohesive sediment. Under appropriate conditions, this sediment can be suspended and entrained into the saline underflow, thus increasing its buoyancy driving.

6.2 Overview of the Experiments

For these experiments, the bed of the flume was modified as described in Figure 3.8. The fixed bed region was 200 cm long. The erodible bed region was 4 cm deep and 200 cm long. The same type of sediment used for the erodible bed was glued to the fixed bed upstream. As in the case of river models, the use of light–weight material was necessary to reproduce suspension at a small scale. Crushed coal with a specific gravity of 1.35 was chosen as the model material. Two grades, with geometric mean sizes of 100 and 180 μ (Table 3.1), were used.

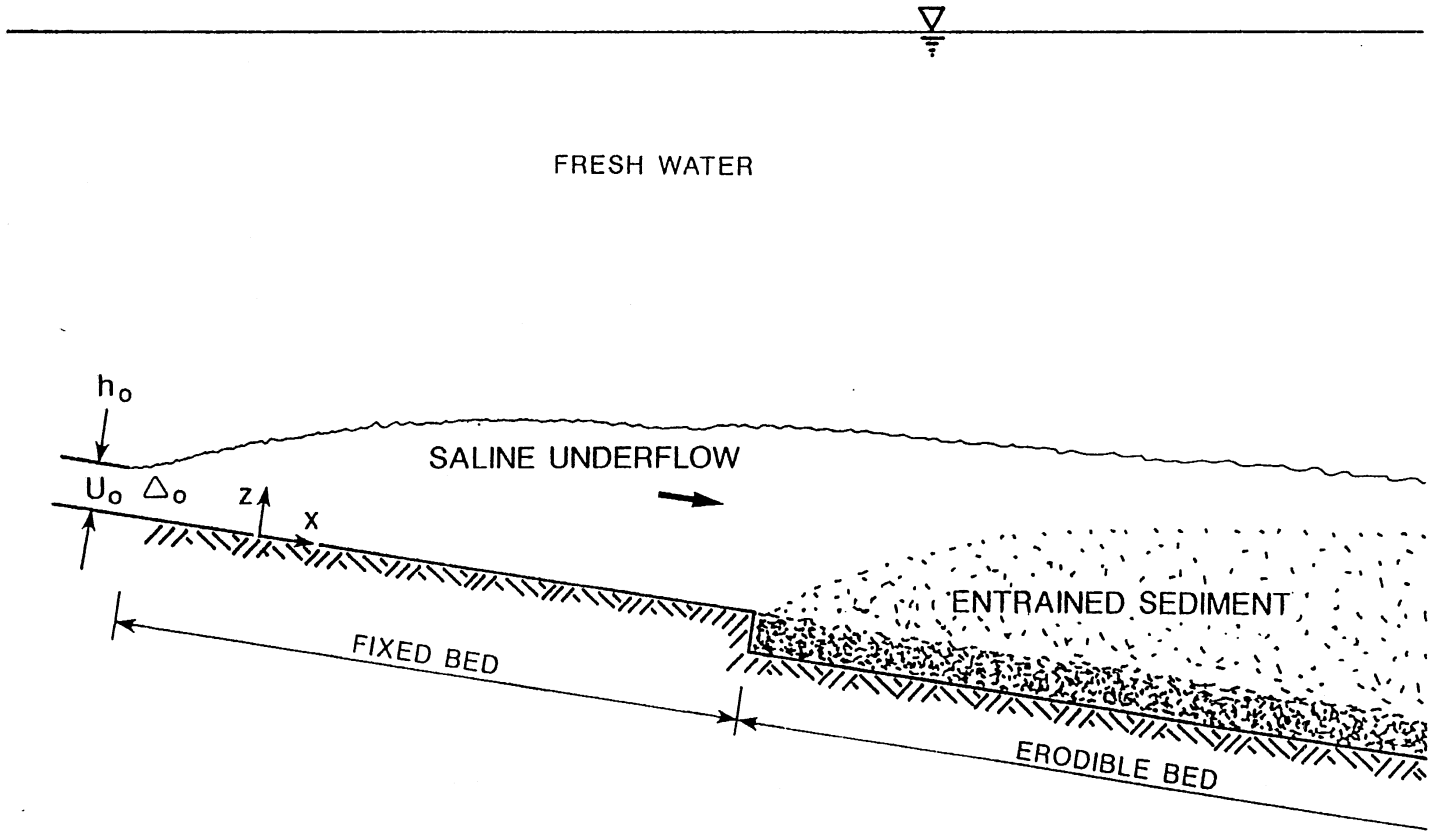

Fig. 6.1 Flow configuration considered in the experiments.

A number of preliminary experiments were conducted to detect the conditions under which sediment erosion could be visible. During this process, the need to generate relatively dense currents in order to observe sediment resuspension became apparent. As in the previous experiments, the inlet current thickness h_0 was fixed at 3 cm. The inlet flow rate per unit width q_0 was set at 33 cm^2/s for all the experiments, except two for which it was set at 40 cm^2/s. The inlet excess fractional density Δ_0 was varied between 0.004 and 0.025, and the buoyancy discharge per unit width ranged from 130 cm^3/s^3 to 809 cm^3/s^3. The inlet Richardson number R_{i_0} varied between 0.10 and 0.61; thus all the generated currents were supercritical at the inlet. For one–half of the experiments, 100 μ material (coal A) was used; 180 μ material (coal B) was used for the rest of the experiments. The current generated in each experiment was sustained for a period of time no shorter than twenty–five minutes. The experimental conditions for the different runs are tabulated in Table 6.1.

TABLE 6.1 EXPERIMENTAL CONDITIONS

Run	U_0(cm/s)	h_0(cm)	Δ_0	$\Phi_0(cm^3/s^3)$	R_{i_0}	$D_{sg}(\mu)$	$T_{in}(^\circ C)$	$T_{fl}(^\circ C)$
T0	11.0	3	0.004	129.4	0.10	100	?	?
T1	11.0	3	0.008	258.8	0.20	100	?	?
T3	11.0	3	0.015	485.1	0.36	100	5.0	5.5
A1	11.0	3	0.015	485.1	0.36	100	5.5	5.5
A2	13.3	3	0.015	586.5	0.25	100	5.0	6.0
A3	13.3	3	0.017	664.7	0.28	100	4.0	6.5
A4	11.0	3	0.025	808.5	0.61	100	3.5	6.5
A6	11.0	3	0.015	485.1	0.36	100	4.0	6.0
B2	11.0	3	0.025	808.5	0.61	180	3.0	6.0
B3	11.0	3	0.021	679.1	0.51	180	3.5	5.5
B4	11.0	3	0.017	550.0	0.41	180	3.5	4.0
B5	11.0	3	0.025	808.5	0.61	180	3.0	5.5
B6	11.0	3	0.021	679.1	0.51	180	2.5	5.0
C1	11.0	3	0.022	711.5	0.53	180	3.5	6.0
C3	11.0	3	0.020	646.8	0.48	180	4.0	6.5
D1	11.0	3	0.017	549.8	0.41	180	4.0	6.0

6.3 Observations of Sediment Entrainment into Suspension

The observations through the glass wall of the channel indicated that for low buoyancy discharge the flows were capable only of moving the sediment as bedload. As the buoyancy discharge was increased, so did the ability of the saline underflows to entrain sediment into suspension. This is illustrated in Figure 6.2, where the volumetric sediment transport rate per unit width UCh evaluated from the measured profiles at the downstream end of the erodible region, is plotted against the buoyancy discharge of the saline underflows. In spite of the scatter, the plot clearly shows that the capacity of the underflow to entrain and to transport sediment increases rapidly with its driving force. The sediment entrained on the two meter reach, increased the buoyancy discharge by as much 10 %.

In Figure 6.3, measurements taken along the erodible bed region during a typical run are shown. It is seen that the current, which initially had no suspended load, is capable of entraining a substantial amount of sediment into suspension while running over the erodible bed. The velocity profiles indicate that the flow tends to decelerate after entering the erodible portion of the channel. This may be due to the fact that in most of the runs where resuspension was clearly evident, well–defined bedforms usually developed. A most interesting feature of the data is the fact that the suspended sediment concentration drops drastically above the point of peak mean velocity. This suggests that suspended sediment is transported only with difficulty from the wall–bounded layer to the free jet–like layer of the underflow.

For some of the runs, only near–bed concentrations c_b were measured at approximately 0.7 cm above the bed. In Figure 6.4, a plot of c_b as a function of distance along the centerline of the channel for two runs having different inlet conditions is shown. In both cases, the tendency of the flow to entrain sediment into suspension is clearly seen. The near–bed concentration first increases very rapidly, but then tends to approach a nearly constant value with distance.

6.4 Evaluation of Sediment Entrainment

Assuming that the erosion process takes place in a quasi–steady state, the sediment mass balance relation given by equation (2.34) should apply. In the case of uniform sediment, equation (2.34) can be written as

$$\frac{dUCh}{dx} = v_s (E_s - c_b) \tag{6.1}$$

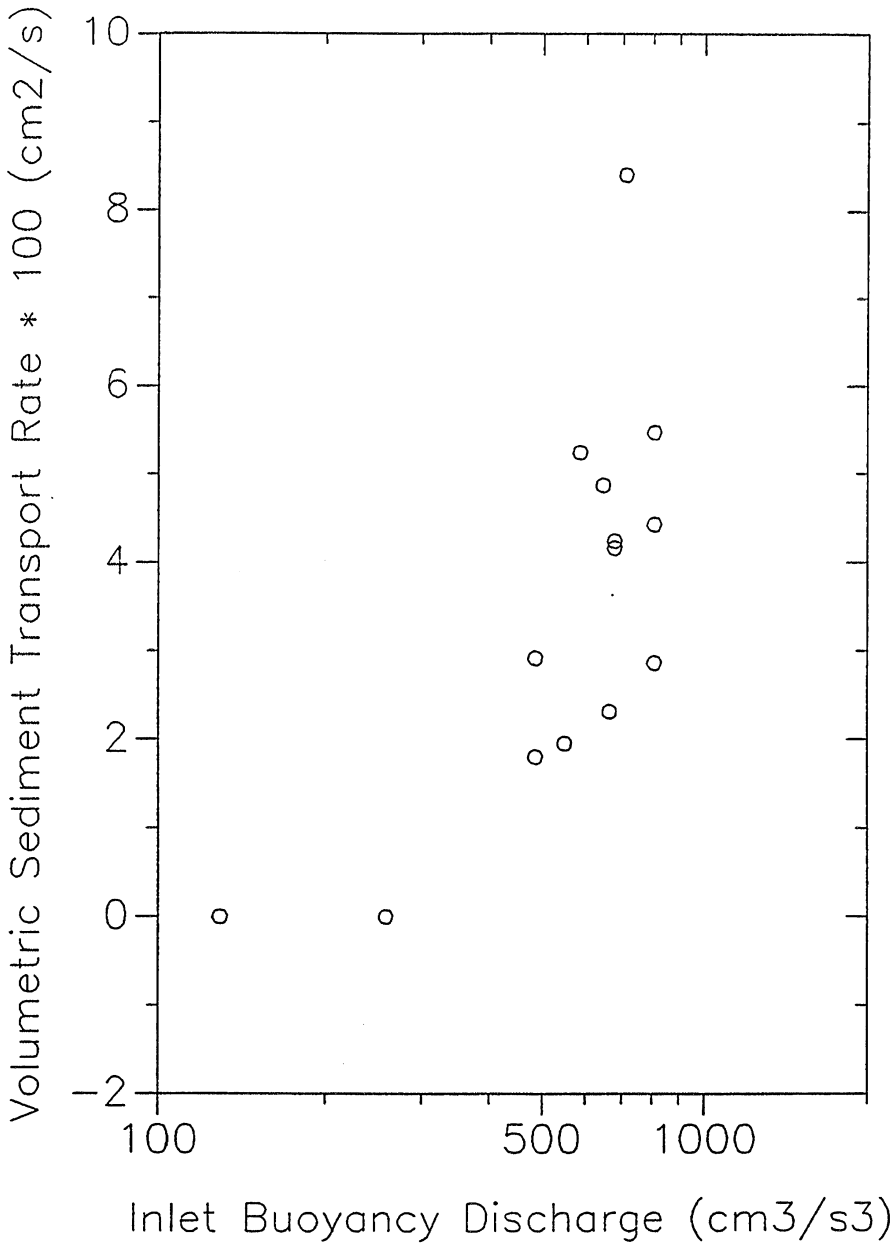

Fig. 6.2 Volumetric sediment transport rate UCh at the farthest downstream measuring station versus saline current buoyancy discharge Φ_0.

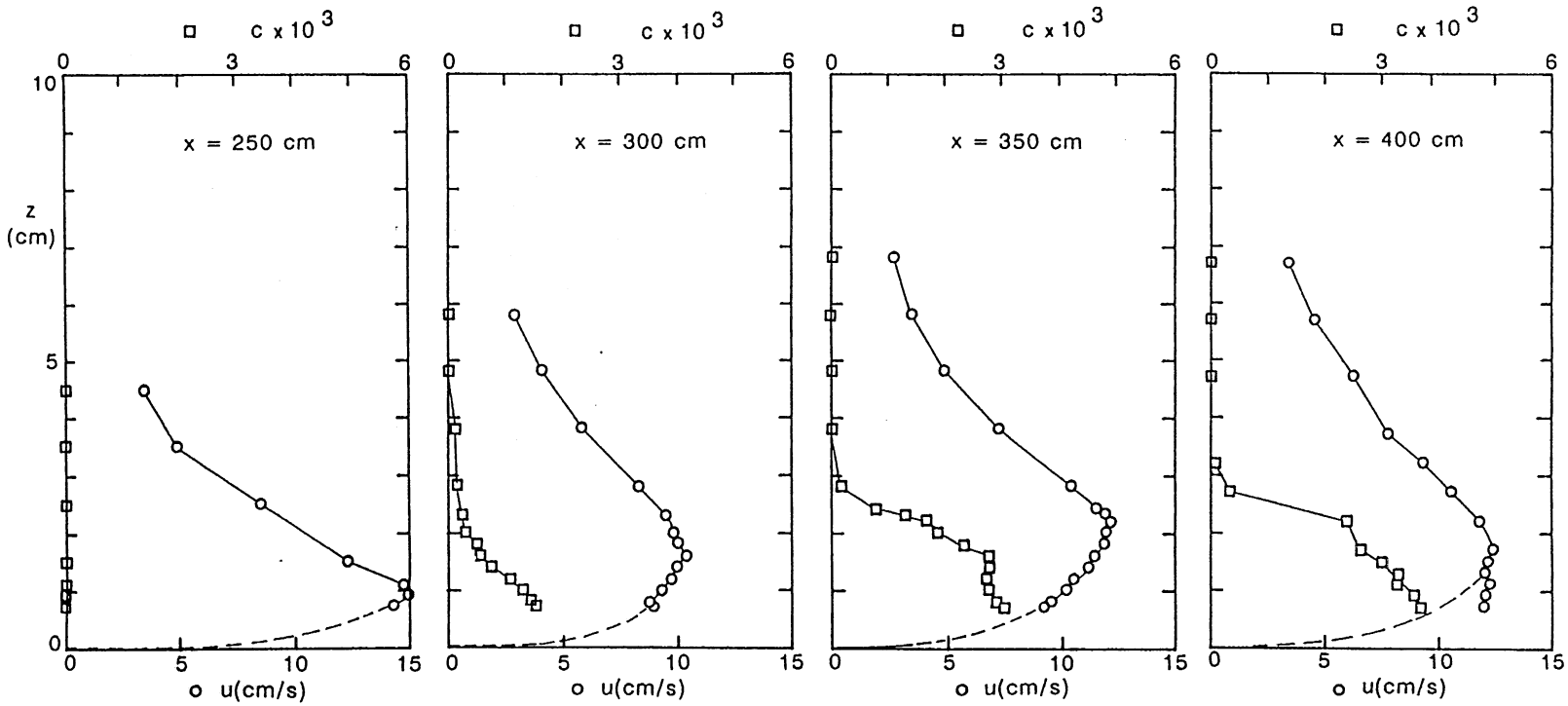

Fig. 6.3 Velocity and sediment (coal) concentration profiles along the centerline of the erodible bed region. Data from run C1.

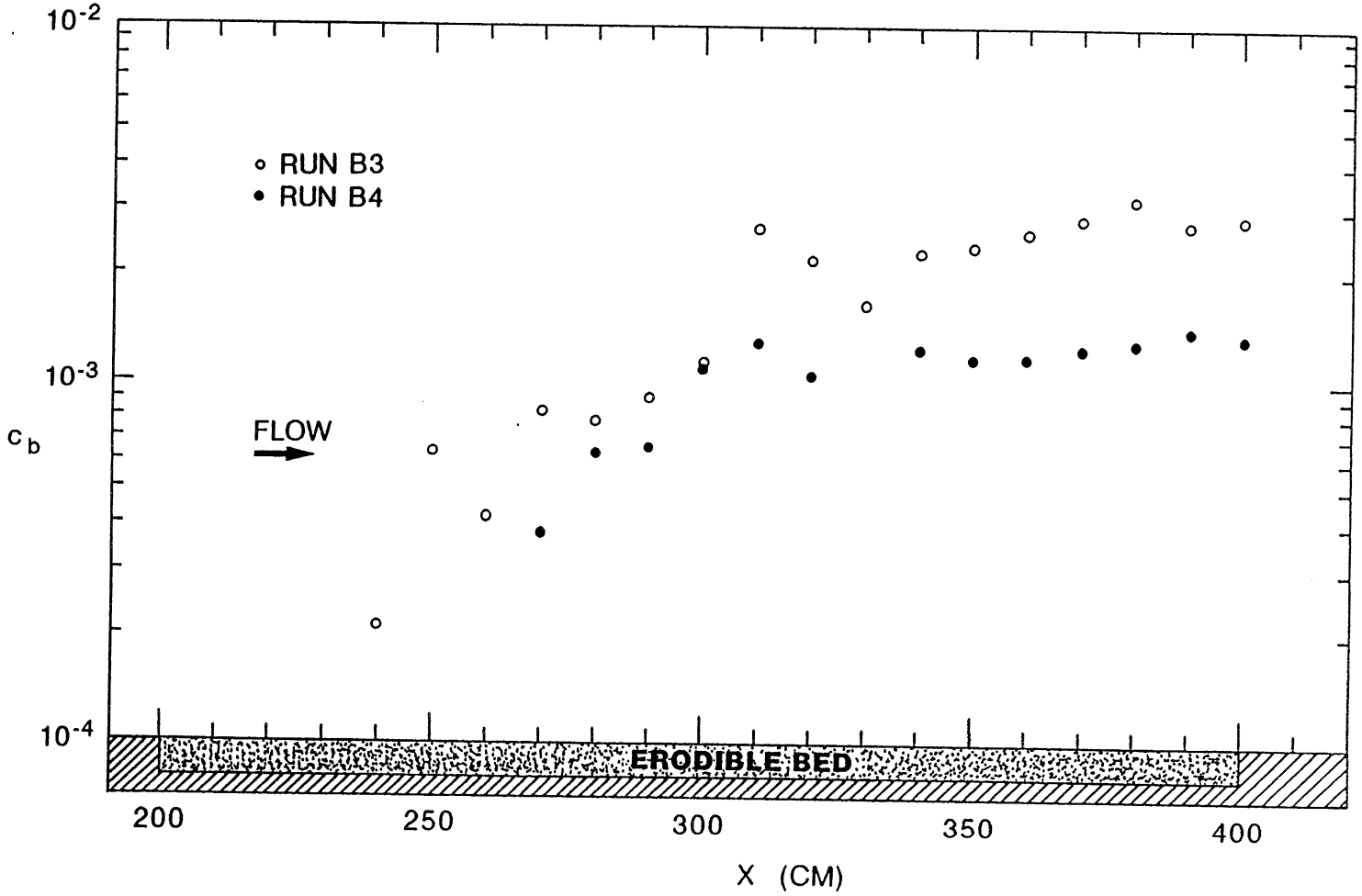

Fig. 6.4 Near–bed concentration along the centerline of the erodible bed region. The horizontal distance x is measured from the inlet.

From the measurements at each station, the layer–averaged values U and C, the current thickness h, and the near–bed concentration c_b, defined as the value of c at z = 0.05h, were evaluated. The sediment entrainment coefficient E_s can then be estimated by writing (6.1) in finite difference form:

$$E_s = \frac{1}{v_s} \frac{UCh|_{i+1} - UCh|_i}{x_{i+1} - x_i} + \frac{1}{2} (c_{b_{i+1}} + c_{b_i}) \qquad (6.2)$$

where the subscript i increases downstream. The range of values of $\Delta x = x_{i+1} - x_i$ varied from 30 to 200 cm. The values of E_s back–calculated from the measurements and the reach (x_1,x_2) considered in each case, are summarized in Table 6.2. They are seen to vary between 0.001 and 0.0043. The rather narrow range of sediment entrainment rates observed is to be expected, since the velocity of the flows changes only slightly for even rather large increments of the buoyancy discharge. On the other hand, the rate of sediment entrainment is found to increase rapidly with the velocity of the saline current. This is illustrated in Figure 6.5, where the values of E_s summarized in Table 6.2 are plotted against the layer–averaged current velocity U just upstream of the erodible region.

6.5 Determination of Bed Shear Stress

The resistance experienced by the underflows while moving over the erodible bed is due to combination of skin friction and form drag. The skin friction is the component responsible for the movement and entrainment of the sediment. The bed shear stress τ_b can then be expressed as

$$\tau_b = \tau_b' + \tau_b'' \qquad (6.3)$$

where τ_b' is the shear stress due to grain (skin) roughness, and τ_b'' is the shear stress due to the form drag associated with the low pressure in the lee of the bedforms. With the help of equation (2.29), the bed shear stress is related to the current velocity by

$$\tau_b/\rho = u_*^2 = C_D\ U^2 \qquad (6.4)$$

Here u_* is the shear velocity, ρ is the density of the uncontaminated water above, and C_D is the bed friction coefficient. Similar expressions can be used for the skin friction and form drag components,

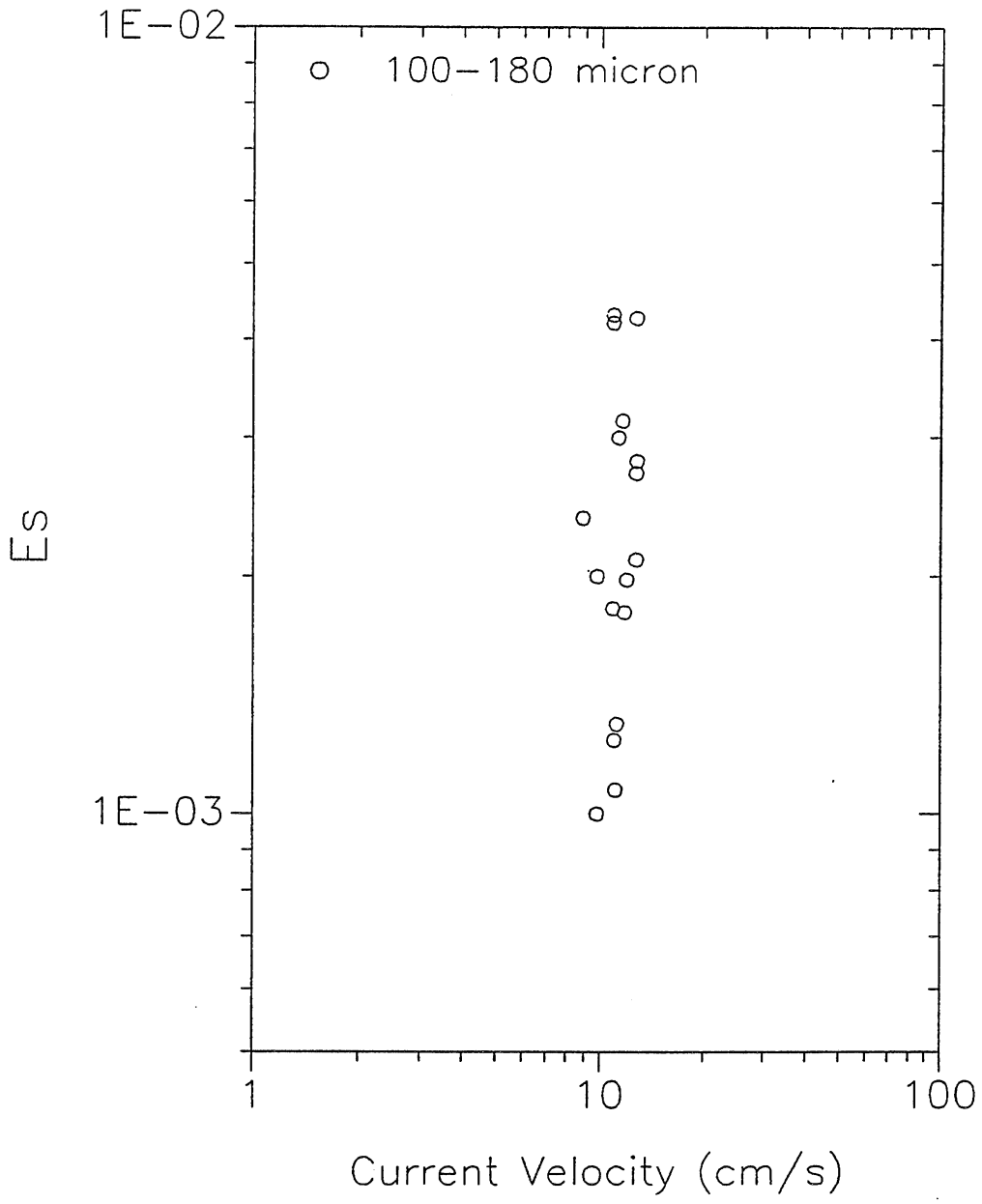

Fig. 6.5 Sediment entrainment coefficient E_s as a function of the current velocity U just upstream of the erodible region.

$$\tau_b'/\rho = u_*'^2 = C_D' U^2 \tag{6.5}$$

$$\tau_b''/\rho = u_*''^2 = C_D'' U^2 \tag{6.6}$$

where u_*' and u_*'' are the grain shear velocity and the bedform shear velocity, respectively, C_D' is a skin friction coefficient, and C_D'' is a bedform drag coefficient.

As in the case of the sediment entrainment coefficient, the measurements are used to back–calculate the bed shear velocity u_*. For this purpose, the momentum equation (2.35) is written in finite difference form as follows:

$$C_D = \frac{u_*^2}{U_a^2} = \frac{\Phi_a}{U_a^3} S - \frac{1}{U_a^2} \frac{1}{(x_{i+1} - x_i)} \left[U^2 h \left(1 + \frac{1}{2} \frac{\Phi}{U^3} \right) \right]_i^{i+1} \tag{6.7}$$

where

$$U_a = \frac{1}{2} (U_{i+1} + U_i) \tag{6.8}$$

$$\Phi_a = \frac{1}{2} (\Phi_{i+1} + \Phi_i) \tag{6.9}$$

and

$$\Phi = g(RC + \Delta)Uh = \Phi_s + \Phi_0 \tag{6.10}$$

In the above equation, $\Phi_s = gRCUh$ is the buoyancy discharge due to the suspended sediment and $\Phi_0 = g\Delta Uh$ is the buoyancy discharge due to the salt. For the computations, the shape factors are set equal to one. The estimated values of u_* and C_D along the erodible region are shown in Table 6.2. It is speculated that the large values of C_D are mostly due to the presence of bedforms. Sidewall effects can be expected to be small since the ratio of current thickness to the channel width was always on the order of 0.15.

An estimate of the skin friction coefficient C_D' can be obtained from the inlet flow conditions ($x = 0$) and the measurements taken just before the erodible region ($x = 200$ cm), since the bed of the channel between those two sections was "painted" with the same material as that used for the erodible bed. An inspection of the computed skin shear velocities u_*'

TABLE 6.2 PARAMETERS IN THE ERODIBLE BED REGION

Run	Reach	U	h	$E_s \cdot 10^3$	C_D	C_D'	C_D''	R_e	u_*	u_*'
	(x_1,x_2)	(cm/s)	(cm)						(cm/s)	(cm/s)
T3	300–360	10.1	5.6	1.1	0.029	0.011	0.018	3757	1.72	1.05
A1	250–300	8.6	4.6	2.0	0.027	0.029	0.000	2635	1.44	1.47
A1	300–390	9.9	5.5	1.0	0.046	0.012	0.034	3663	2.12	1.07
A2	250–300	11.5	6.0	4.3	0.055	0.013	0.042	4584	2.71	1.30
A2	300–400	10.4	6.1	2.7	0.042	0.008	0.034	4250	2.13	0.92
A3	250–300	10.2	5.1	2.8	0.047	0.013	0.034	3512	2.23	1.17
A3	300–350	10.4	5.8	2.1	0.053	0.009	0.044	4014	2.40	0.99
A4	250–400	8.7	5.0	2.4	0.088	0.023	0.065	2871	2.58	1.31
B2	300–350	8.7	5.3	3.0	0.085	0.019	0.066	3068	2.53	1.20
B3	200–400	10.5	5.0	1.3	0.036	0.013	0.023	3531	2.00	1.20
B5	300–400	10.0	5.1	1.8	0.051	0.014	0.036	3400	2.25	1.20
B6	290–390	10.8	5.6	2.0	0.038	0.009	0.029	4013	2.10	1.02
C1	250–300	9.3	4.8	1.8	0.077	0.022	0.056	2942	2.57	1.35
C1	300–350	8.2	5.8	4.2	0.069	0.025	0.044	3149	2.12	1.30
C1	350–400	8.0	6.1	4.3	0.089	0.024	0.065	3274	2.39	1.25
C3	270–300	8.4	5.5	1.8	0.080	0.018	0.061	3108	2.37	1.13
C3	300–340	8.8	5.7	3.2	0.052	0.015	0.038	3351	2.03	1.08
D1	350–400	9.8	6.1	1.2	0.032	0.009	0.023	3978	1.75	0.94

Note: U and h are average values for a given reach. To compute $R_e = Uh/\nu$, a value of $\nu = 0.015$ cm^2/s corresponding to a temperature of 5°C, is used.

shows that turbulent smooth flow conditions (i.e. $u_*' k_s / \nu < 5$, where k_s is the equivalent bed roughness) prevailed in that region. In Figure 6.6, the skin friction coefficient C_D' is plotted as a function of the current Reynolds number $R_e = Uh/\nu$. A clear tendency for C_D' to decrease with R_e can be discerned. A best–fit of the data gives

$$C_D' = 7.24 \cdot 10^7 \, R_e^{-2.75} \tag{6.11}$$

The above relationship and the flow measurements are then used to evaluate the skin friction velocity u_*' within the erodible portion of the bed. The estimated values are presented in Table 6.2.

In Figure 6.7, the values of the sediment entrainment coefficient are plotted against the dimensionless shear velocity u_*'/v_s, where v_s is the sediment fall velocity. The sediment fall velocities used for the 100 μ and 180 μ coal were 0.13 cm/s and 0.42 cm/s, respectively (Dietrich, 1984). A tendency for E_s to increase rapidly with u_*'/v_s can be discerned for the 180 μ material. The data for the 100 μ material seems to follow the similar trend but with a more pronounced scatter. On the other hand, the observed tendency for the values of E_s to be of the same order for both sediment sizes is rather unexpected, since one might presume that the finer material should be entrained with more ease. A plausible explanation for this behavior might be that the viscous sublayer lubricates more effectively the finer material, thus reducing the amount of entrainment. A similar behavior has been observed in the problem of the initiation of motion (Shields diagram), where as the sediment size increases the shear stress necessary to put a particle in motion increases (Vanoni, 1975).

From (6.3), (6.4), (6.5), and (6.6), it follows that the bedform friction coefficient is given by

$$C_D'' = C_D - C_D' \tag{6.12}$$

The values estimated with (6.12) are shown in Table 6.2. It is seen that the friction coefficients associated with the bedforms are in general larger than the corresponding skin friction coefficients. This indicates the importance of removing the effect of the bedforms from the boundary shear stress.

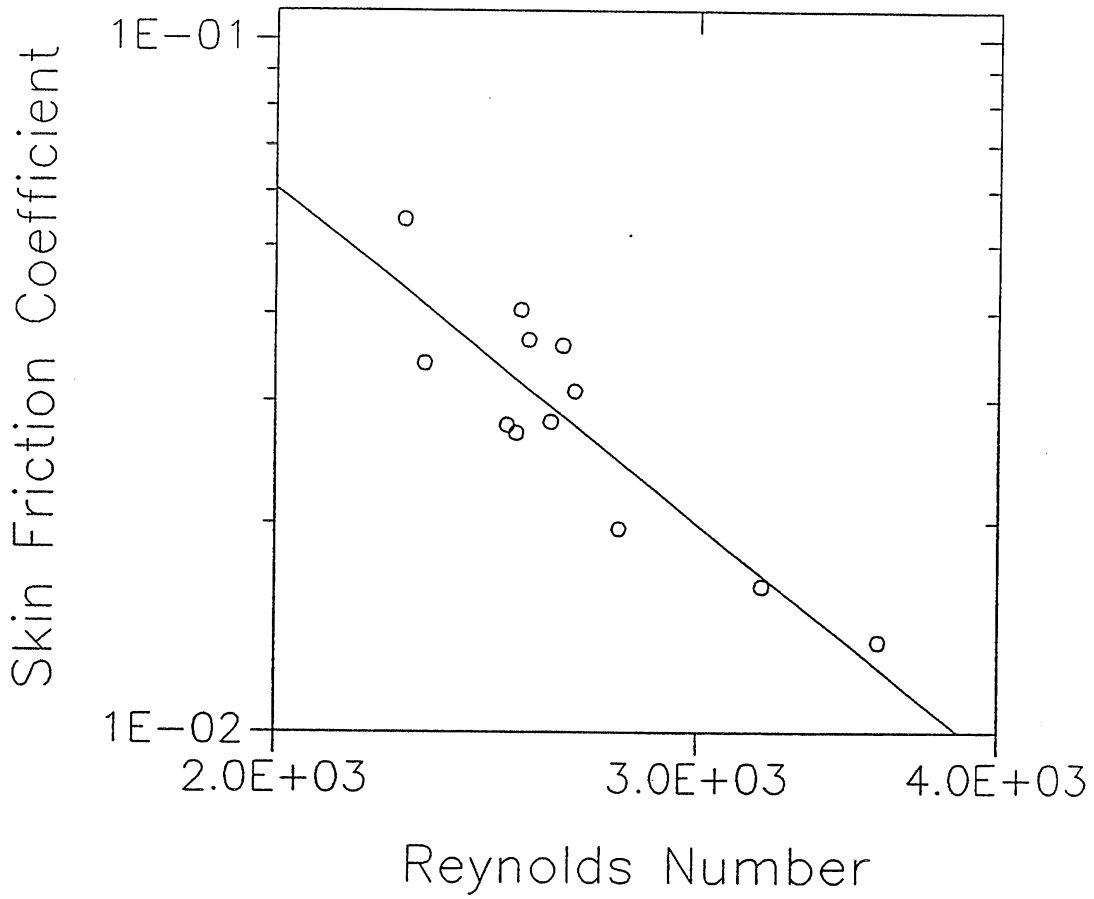

Fig. 6.6 Skin friction coefficient C_D' versus current Reynolds number $R_e = Uh/\nu$. Data from fixed bed region. The line is that of equation (6.11).

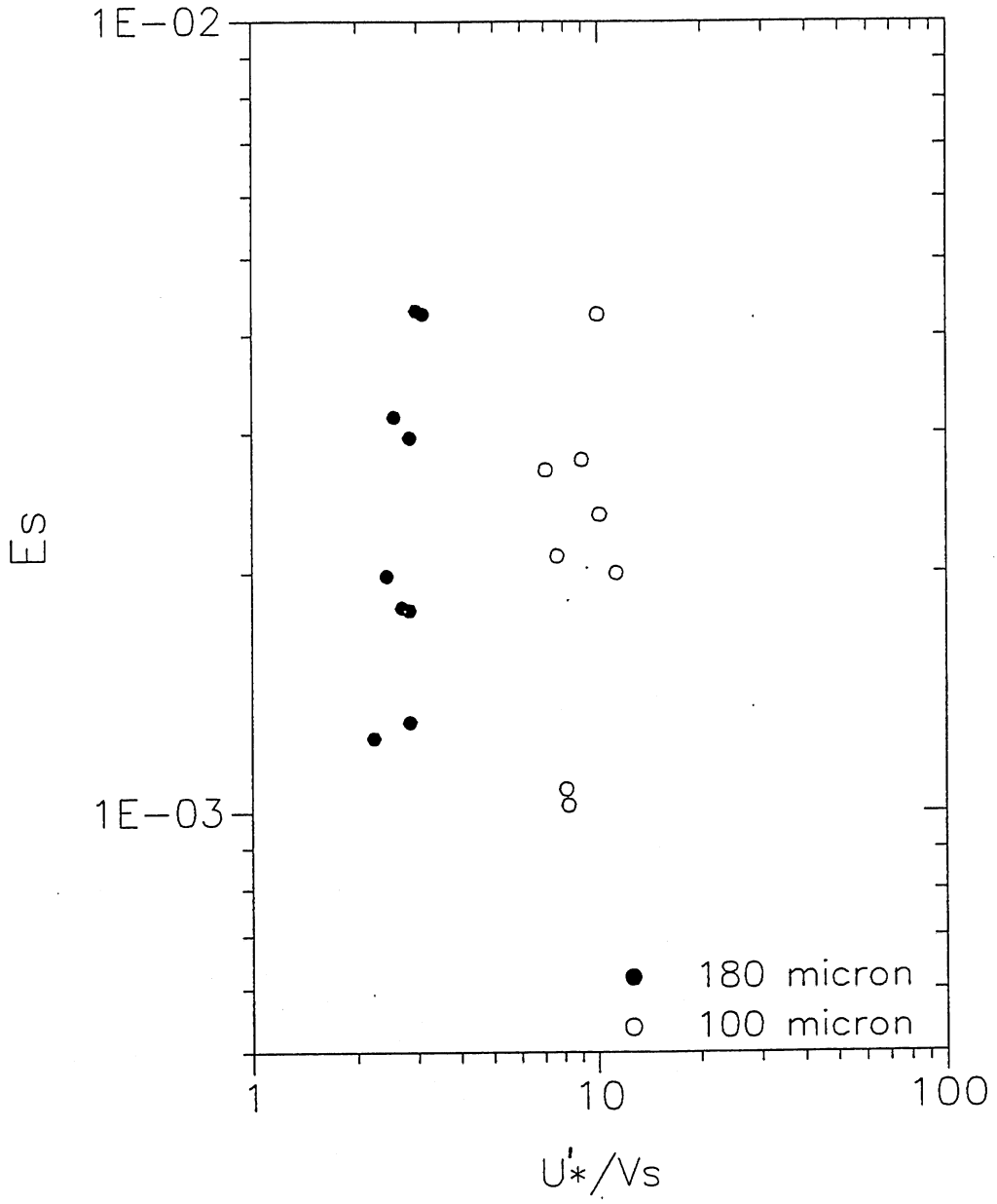

Fig. 6.7 Sediment entrainment coefficient E_s versus dimensionless skin friction velocity u'_*/v_s.

TABLE 6.3 PARAMETERS IN THE FIXED BED REGION

Run	Reach (x_1,x_2)	U (cm/s)	h (cm)	C_D'	u_*' (cm/s)	$u_*'k_s/\nu$	R_e
T3	0–200	11.1	3.8	0.020	1.55	1.03	2777
A1	0–200	10.4	3.3	0.034	1.81	1.21	2301
A2	0–200	11.8	4.0	0.016	1.61	1.07	3192
A3	0–200	13.0	4.1	0.013	1.47	0.98	3562
A4	0–200	9.9	3.4	0.055	2.08	1.39	2255
B2	0–200	11.2	3.4	0.041	2.27	2.72	2527
B3	0–200	11.1	3.4	0.027	1.84	2.21	2516
B5	0–200	11.4	3.4	0.037	2.26	2.71	2546
B6	0–200	11.3	3.5	0.031	2.04	2.45	2659
C1	0–200	10.9	3.6	0.036	2.07	2.48	2628
C3	0–200	11.3	3.5	0.028	1.94	2.33	2599
D1	0–200	11.0	3.4	0.028	1.83	2.20	2493

Note: U and h are the average values for the reach. The roughness height k_s is set equal to the mean geometric diameter of the sediment D_{sg}, and ν = 0.015 cm^2/s.

6.6 Characteristics of Bedforms

The geometry of the bedforms varied from nearly two–dimensional to essentially three–dimensional (Figure 6.8). In most cases, the bedforms were asymmetrical in shape and had a well–defined slip face beyond which the flow separated for a certain length. The height of the bedforms Δ_b was on the order of 1 to 2.5 cm, and the wavelength ℓ_b ranged between 10 and 16 cm (Figure 6.9). The height of the bedforms was relatively large when compared to the thickness of the currents, as indicated by the parameter Δ_b/h which took values between 0.2 and 0.5. The observations through the glass wall indicated that the bedforms migrated in the downstream direction at speeds in the order 1 cm/min. The fact that the flow was supercritical for all the experiments and the prominent size of the bedforms, suggest that the bedforms were most likely antidunes (Vanoni, 1974). Antidunes may migrate either upstream or downstream. In open

channel flows, the potential–flow criterion dividing upstream–migrating antidunes from downstream–migrating antidunes is given by (Engelund, 1970)

$$F_*^2 = \frac{1}{\mathbf{k}\ \tanh(\mathbf{k})} \tag{6.13}$$

where

$$\mathbf{k} = \frac{2\ \pi\ H}{\ell_b} \tag{6.14}$$

Here F_* is a limit Froude number, $\mathbf{k}$ is a wavenumber, and H is the depth of the flow. Values of the Froude number larger than F_* are associated with downstream–migrating antidunes. If the Froude number is substituted by the densimetric Froude number $F = (R_i)^{-0.5}$, and the flow depth H is replaced by the current thickness h, the criterion given by (6.13) can be applied as a crude but reasonable approximation for the present underflows.

The bedforms were measured or photographed during five of the experiments. In Table 6.4, the characteristics of the bedforms observed are summarized. Also shown in the table, are the average current thickness and densimetric Froude number F for a given reach, and the densimetric Froude number F_* estimated with (6.13). In all cases the observed Froude number is larger than the value given by the potential–flow criterion (6.13), indicating that the bedforms were antidunes migrating in the downstream direction.

Downstream migrating antidunes may be an artifact of the small scale of the experiments. The value of the ratio Δ_b/h can be expected to be much smaller in the field, perhaps precluding strong coupling between bedforms and the density interface. In this case the dominant bedform will be expected to be the ripple.

6.7 Removal of Bedform Effect

The formulation proposed by Nelson and Smith (1989) to remove the effect of bedforms in open channel flows was modified to deal with the underflows of the present study. The Nelson–Smith approach builds up on the work of Smith and McLean (1977), and is very similar to the method proposed independently by Kikkawa and Ishikawa (1979).

For a two–dimensional bedform, the bed shear stress due to form drag can be expressed as follows:

$$\tau_b'' = \frac{1}{2}\ \rho\ C_f\ \frac{\Delta_b}{\ell_b}\ U_r^2 \tag{6.15}$$

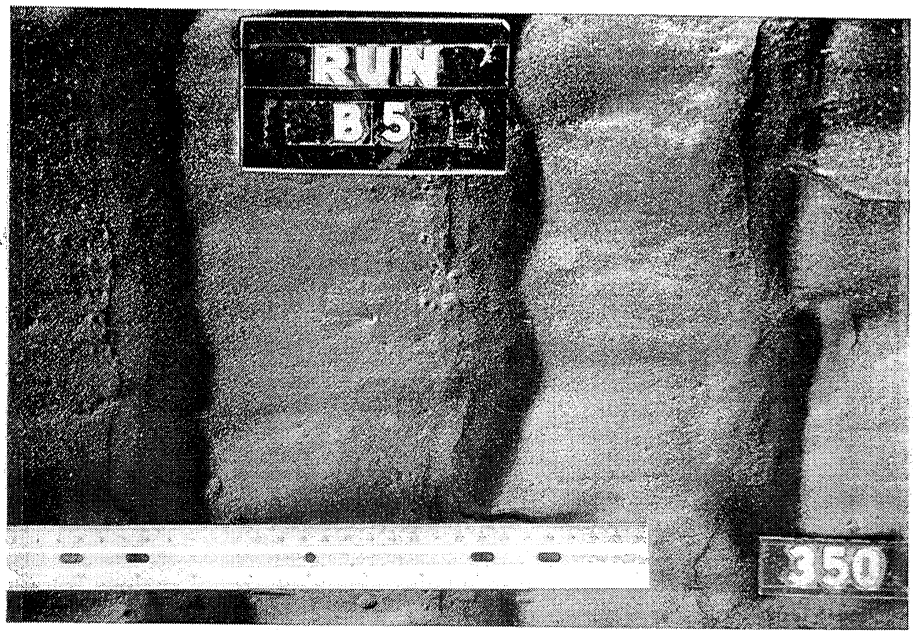

Fig. 6.8 Top view of two–dimensional bedforms originated by the passage of a density current. The flow was from right to left.

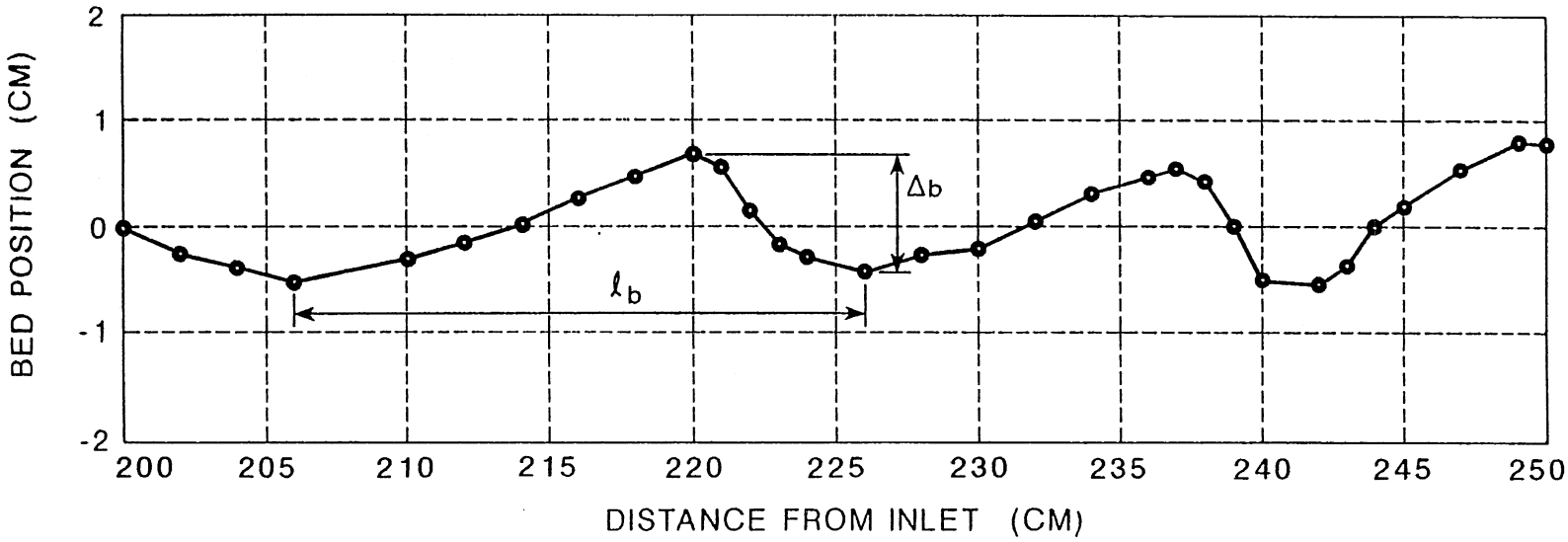

Fig. 6.9 Characteristic dimensions of a typical bedform. The flow was from left to right.

TABLE 6.4 BEDFORM CHARACTERISTICS

Run	Reach	h(cm)	Δ_b(cm)	ℓ_b(cm)	$F^2=1/R_i$	k	$F_*^2=1/(k \tanh(k))$
A3	250–300	5.1	1.5	15.0	1.60	2.14	0.48
A3	300–350	5.8	1.4	14.0	1.69	2.60	0.39
B2	300–350	5.0	2.5	12.0	1.13	2.62	0.39
B3	200–400	5.0	1.5	15.0	1.70	2.10	0.49
B5	300–400	5.1	1.8	13.0	1.24	2.46	0.41

Here C_f is a drag coefficient set equal to 0.21 (Nelson and Smith, 1989), and U_r is an appropriate reference velocity. The reference velocity is defined as the average velocity that would exist if the bedform were not present. For hydraulically smooth flow conditions, the velocity distribution near the bed is given by (Schlichting, 1979)

$$\frac{u}{u_*'} = \frac{1}{\kappa} \ln(9\ u_*'\ z\ /\ \nu) \tag{6.16}$$

Integrating the above equation over the bedform height Δ_b, an expression for the reference velocity can be obtained as follows:

$$U_r = u_*' \frac{1}{\kappa} \left[\ln(9\ u_*'\ \Delta_b\ /\ \nu) - 1\right] \tag{6.17}$$

Substitution of (6.6) and (6.17) into (6.15) yields

$$u_*'^2 = \frac{1}{2} C_f \frac{\Delta_b}{\ell_b} \kappa^{-2} \left[\ln(9\ u_*'\ \Delta_b\ /\ \nu) - 1\right]^2 u_*'^2 \tag{6.18}$$

With the help of (6.5) and (6.6), the above equation can be rewritten as

$$C_D'' = \frac{1}{2} C_f \frac{\Delta_b}{\ell_b} \kappa^{-2} \left[\ln(9\ C_D'^{0.5}\ U\ \Delta_b\ /\ \nu) - 1\right]^2 C_D' \tag{6.19}$$

An expression for the skin friction coefficient can be obtained by substituting (6.19) into (6.12),

$$C_D' = \left[1 + \frac{1}{2} C_f \frac{\Delta_b}{\ell_b} \kappa^{-2} \left[\ln(9\ C_D'^{0.5}\ U\ \Delta_b\ /\nu) - 1\right]^2\right]^{-1} C_D \qquad (6.20)$$

For given values of Δ_b, ℓ_b, U, ν, and C_D, the value of the skin friction coefficient C_D' can be obtained by solving (6.20) iteratively.

In Table 6.5, skin friction coefficients predicted with (6.20) and the information summarized in Tables 6.2 and 6.4, are compared with the values predicted for each reach with the resistance relation given by (6.11). As illustrated in Figure 6.10, the agreement is in general very good.

TABLE 6.5 COMPARISON OF SKIN FRICTION COEFFICIENTS

Run	Reach	C_D' with (6.11)	C_D' with (6.20)	Relative Error
A3	250–300	0.013	0.014	7 %
A3	300–350	0.009	0.016	57 %
B2	300–350	0.019	0.013	38 %
B3	200–400	0.013	0.011	17 %
B5	300–400	0.014	0.014	15 %

6.8 Conclusions

The observations made during the experiments demonstrate conclusively that a conservative current of sufficient strength can entrain substantial amounts of bed sediment. The sediment entrained on a two–meter reach increased the buoyancy discharge by as much 10 %; in a submarine canyon several kilometers in length, much more entrainment could be realized. This suggests that in addition to the purely sand–driven currents analyzed by Fukushima et al. (1985), currents of silty mud could also entrain substantial amounts of sand and carry it to deep water.

Since for a given slope the velocity of a saline current increases modestly with buoyancy discharge, the range of flow velocities covered was rather narrow. However, a clear tendency for the rate of sediment entrainment to increase with flow velocity was indicated by the measurements. A similar tendency was observed, albeit with some scatter, when the skin friction was used as the independent variable. The range of sediment entrainment rates observed was rather small; thus no attempt was

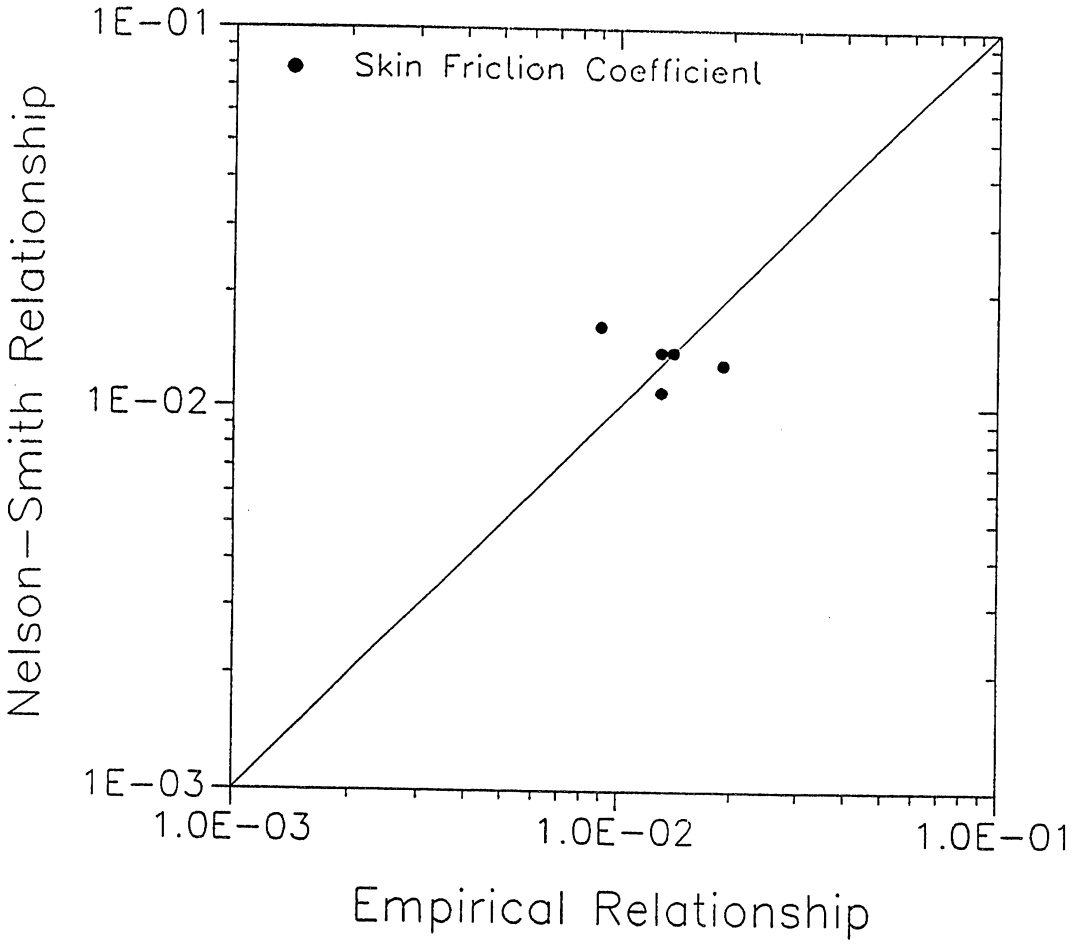

Fig. 6.10 Comparison of skin friction coefficients predicted with the empirical relationship (6.11) versus those predicted with the modified Nelson–Smith formulation (6.20).

made to obtain an empirical sediment entrainment function from the data. The observations are instead compared in the next chapter with data from open channel flows.

The data collected during the experiments allowed for an approximate decomposition of the bed shear stress into components associated with skin friction and form drag. The results indicate the importance of accounting for the presence of bedforms.

An analysis of the bedform characteristics suggested that downstream–migrating antidunes were the predominant bedform during the experiments. It is suspected that the formation of antidunes was due to the small scale of the experiments. In the field, where the flow thickness is likely to be much larger than the height of the bedforms, it is expected that the dominant bedforms will be ripples.

While there are several techniques that allow to remove the effect of bedforms in open channel flows (e.g. Einstein and Barbarossa, 1952; Yalin, 1964; Engelund and Hansen, 1967; Smith and McLean, 1977), no counterpart has been proposed for the case of turbidity currents. The Nelson–Smith formulation modified for smooth flow conditions provided an effective way for removing the boundary shear stress associated with bedforms. It is expected that similar results can be obtained at field scale, provided that some characteristic dimensions of the bedforms are known.

CHAPTER 7

SEDIMENT ENTRAINMENT FUNCTIONS

7.1 Introduction

As observed previously, the phenomenon of sediment entrainment takes place in response to bed shear stresses generated by a given flow. It can be argued that the rate of sediment entrainment associated with a given grain (skin) shear stress should be the same whether the flow is driven by the action of gravity on the fluid phase (i.e. open channel flows) or on the sediment phase (i.e. turbidity currents). Herein data from equilibrium open channel suspensions are used to test the predictive ability of various sediment entrainment functions in the literature. Using the same data set, a new empirical relationship for computing the entrainment of sediment into suspension from a bed covered with uniform material is obtained. Using field data, the empirical relationship is adapted to handle entrainment from a bed covered with poorly–sorted sediment. Finally, the relationship developed for uniform material is tested with the data collected during the experiments with sediment–entraining currents.

7.2 Problem Formulation

For a steady, two–dimensional open channel flow (Figure 7.1), the depth–averaged sediment conservation equation takes the form:

$$\frac{dq_s}{dx} = F_a - v_s c_a \tag{7.1}$$

where q_s is the suspended sediment discharge per unit width; x denotes the downstream direction along the channel; c_a denotes the near–bed sediment concentration, and F_a denotes the near–bed upward normal Reynolds flux of sediment, in both cases evaluated at a small distance "a" above the bed. A dimensionless coefficient of sediment entrainment E_s is defined such that

$$F_a = v_s E_s \tag{7.2}$$

At equilibrium conditions, then the sediment discharge q_s is constant and the sediment entrainment rate equals the sediment deposition rate. Therefore

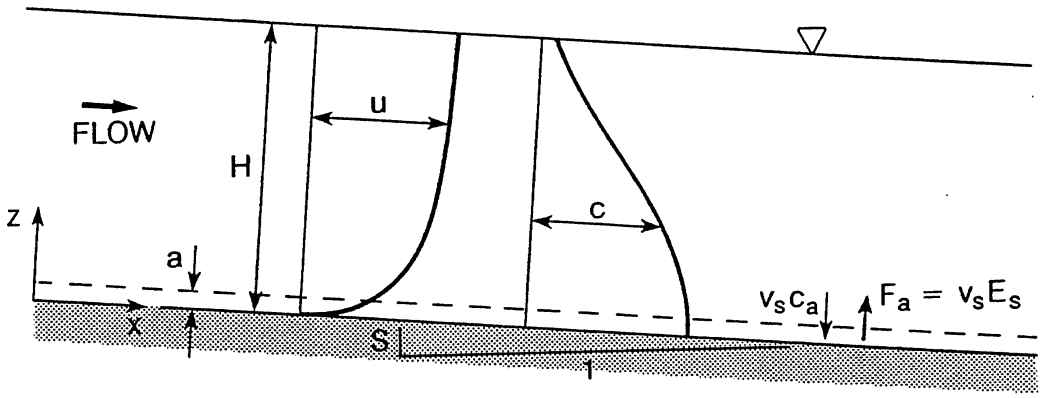

Fig. 7.1 Definition diagram for open channel flow over an erodible bed.

$$E_s = c_{ae} \tag{7.3}$$

where c_{ae} denotes the value of c_a at equilibrium.

This simple equation indicates that E_s can be deduced from experiments and field data approximating equilibrium conditions (Parker, 1978, Ikeda and Nishimura, 1985). A functional relationship obtained in this way can eventually be used to estimate the upward sediment flux F_a in moderate disequilibrium conditions, i.e. cases for which q_s is not constant.

Various formulae can be found in the literature that give the equilibrium near–bed concentration c_{ae} $(= E_s)$, as a function of flow parameters and sediment characteristics. Most of the relationships are of the following type

$$c_{ae} = E_s \sim \tau_b'^{P} \sim u_*'^{2P} \tag{7.4}$$

where τ_b' is the bed shear stress due to grain (skin) friction, and u_*' is the associated shear velocity. The power P takes values between 1 and 15, depending on whose formulation is considered (Figure 7.2). It is clear that estimates of equilibrium near–bed concentration c_{ae} or sediment entrainment E_s can be quite different depending on which relationship is used.

7.3 Previous Functions

7.3.1 Einstein (1950)

The Einstein bed load function relates two parameters, which are the dimensionless bed load transport Φ and the dimensionless bed shear stress θ', both defined below. The form of $\Phi = f(\theta')$ can be found in many sediment transport books (e.g. Graf, 1971). Once the bedload discharge per unit width q_b is obtained, it can be used for the computation of the volumetric suspended sediment concentration c_{ae}, at a distance $a = 2\ D_s$ above the bed, using the following expression:

$$c_{ae} = \frac{1}{11.6}\,\frac{q_b}{2D_s u_*'} = \frac{1}{23.2}\,\frac{\Phi}{\theta'^{0.5}} \tag{7.5}$$

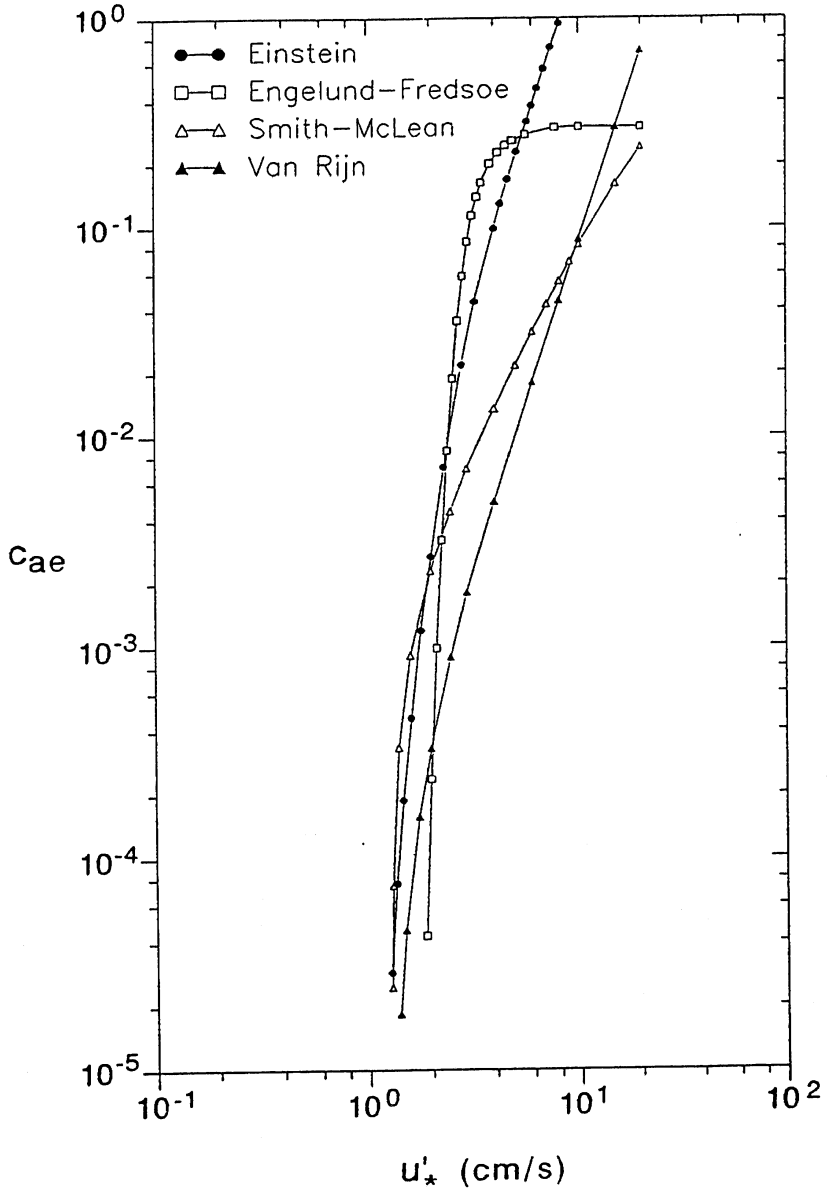

Fig. 7.2 Plot of different formulations for near–bed reference suspended sediment concentration.

where

$$\Theta = q_b / (g\ R\ D_s)^{0.5} \tag{7.6}$$

and

$$\theta' = u_*'^2 / (g\ R\ D_s) \tag{7.7}$$

In the above equations, u_*' is the shear velocity associated with grain (skin) friction, R is the submerged specific gravity of the sediment, g is the acceleration of gravity, and D_s is the mean diameter of the sediment.

7.3.2 Engelund and Fredsoe (1976)

The value of c_{ae} at a distance $a = 2\ D_s$ above the bed is given by

$$c_{ae} = \frac{0.65}{(1 + \lambda_b^{-1})^3} \tag{7.8}$$

where

$$\lambda_b = \left(\frac{\theta' - .06 - \beta\ p\ \pi / 6}{0.027 \quad s \quad \theta'} \right)^{0.5} \tag{7.9}$$

In (7.9), $\theta' = u_*'^2 / (g\ R\ D_s)$, $s = R + 1$ denotes the specific gravity of the sediment, and the quantity p is computed from the relation

$$p = \left[1 + \left(\frac{\beta\ \pi / 6}{\theta' - 0.06} \right)^4 \right]^{-0.25} \tag{7.10}$$

The parameter β was originally set equal to 0.51 (Engelund and Fredsoe, 1976), but later it was modified to 1.0 (Engelund and Fredsoe, 1982).

7.3.3 Smith and McLean (1977)

The near–bed volumetric sediment concentration is given by

$$c_{ae} = 0.65\ \gamma_o\ S_o / (1 + \gamma_o\ S_o) \tag{7.11}$$

where γ_o is a constant equal to 2.4×10^{-3}, and S_o is a normalized shear stress given by

$$S_o = (\theta' - \theta_c) \; / \; \theta_c \tag{7.12}$$

where $\theta_c = u_{*c}^2 \; / \; (g \; R \; D_s)$, and u_{*c} is a critical shear velocity associated with the initiation of sediment motion.

This formulation assigns the sediment concentration computed with (7.11), to a point situated at a distance

$$a = \alpha_o \; (\theta' - \theta_c) \; D_s + k_s \tag{7.13}$$

above the bed, where α_o is equal to 26.3, and k_s is the equivalent roughness height for a fixed sediment bed.

7.3.4 Itakura and Kishi (1980)

The volumetric sediment concentration c_{ae} is evaluated at a distance $a = 0.05$ H, where H is the water depth; it is given by

$$c_{ae} = k_1 \left[k_2 \frac{u_*}{v_s} \frac{\Omega}{\theta} - 1 \right] \tag{7.14}$$

where

$$\Omega = \frac{\theta}{k_3} \left(k_4 + \left[\exp(-A^2) \; / \; \int_A^{\infty} \exp(-\xi^2) \; d\xi \right] \right) - 1$$

and

$$A = \frac{k_3}{\theta} - k_4 \tag{7.15}$$

In the above equations, u_* is the bed shear velocity; $\theta = u_*^2 \; / \; (g \; R \; D_s)$; k_1, k_2, k_3, and k_4 are constants with values of 0.008, 0.14, 0.143, and 2.0, respectively; and v_s is the sediment fall velocity.

7.3.5 Van Rijn (1984)

The sediment concentration at a reference level "a" above the bed, is given by

$$c_{ae} = 0.015 \frac{D_s}{a} \frac{S_o^{1.5}}{D_*^{0.3}} \tag{7.16}$$

where

$$D_* = D_s \left[\frac{g\ R}{\nu^2}\right]^{1/3} \tag{7.17}$$

In the above equation, ν denotes the kinematic viscosity of water. The reference level "a" is assumed to be equal to half the bed–form height Δ_b. If the dimensions of the bedforms are not known, the equivalent roughness height k_s is taken as the reference level. A minimum value for a is 0.01 H , where H is the water depth.

7.3.6 Celik and Rodi (1984)

The mean transport concentration C_m, i.e. suspended sediment flux divided by volume flux, is given by

$$C_m = 0.034 \left[1 - \left[\frac{k_s}{H}\right]^{0.06}\right] \frac{u_*^2}{g\ R\ H} \frac{U_m}{v_s} \tag{7.18}$$

where U_m is the mean flow velocity, and the rest of the parameters are as defined previously. Using (7.18), the sediment concentration at a distance a = 0.05 H from the bed can be obtained with the following relationship

$$c_{ae} = k_o\ C_m\ /\ I \tag{7.19}$$

where

$$I = \int_{.05}^{1} \left[\frac{1-\eta}{\eta} \Big/ \frac{1-\eta_a}{\eta_a}\right]^{\frac{v_s}{0.4\ u_*}} d\eta \tag{7.20}$$

In (7.20), $\eta = z/H$, where z is the vertical distance from the bed, and $\eta_a = 0.05$. In (7.19), k_o is a constant equal to 1.13 which relates the transport concentration C_m to the average concentration obtained by integrating the sediment concentration distribution in the vertical direction and dividing this value by the water depth.

7.3.7 Akiyama and Fukushima (1985)

The sediment entrainment coefficient E_s $(= c_{ae})$ at a distance a = 0.05 H above the bed is determined from the relation

$$E_s = \begin{cases} 0 & \text{for } Z < Z_c \\ 3 \times 10^{-12}\, Z^{10} \left(1 - Z_c/Z\right) & \text{for } Z_c < Z < Z_m \\ 0.3 & \text{for } Z > Z_m \end{cases} \qquad (7.21)$$

where

$$Z = \frac{u_*}{v_s} R_p^{0.5}$$

$$R_p = \frac{(g\ R\ D_s)^{0.5}\ D_s}{\nu} \qquad (7.22)$$

The parameter Z_c denotes a critical value of Z for suspension, and Z_m denotes an upper bound for Z. These parameters are equal to 5 and 13.2, respectively.

7.4 Data Selection

In selecting the data used to check previous relations and develop a new one, emphasis was placed on obtaining experimental observations of suspended sediment distributions associated with equilibrium or near–equilibrium conditions. In those cases where it was not clear that equilibrium had been reached, the data were left out of the analysis (e.g. the excellent set of data for high sediment concentrations collected by Einstein and Chien, 1955). The data selected were those due to Ashida and Michiue, 1964; Ashida and Okabe, 1982; Barton and Lin, 1955; Brooks, 1954; Coleman, 1969, 1981; Ismail, 1951; Kalinske and Pien, 1943; Lyn, 1986; Straub et al., 1958; and Vanoni and Nomicos, 1960.

As seen in the previous section, the different formulations in the literature associate the computed concentration c_{ae} to a certain reference level "a". The methods used to select the length scale "a", can be summarized as follows:

a) Take "a" as a fraction of the flow depth (H) (e.g. Itakura and Kishi, 1980; Celik and Rodi, 1984; Akiyama and Fukushima, 1985).

b) Take "a" as proportional to the sediment grain size (D_s) (e.g. Einstein, 1950; Engelund and Fredsoe, 1976).

c) Take "a" as a fraction of the bedform height (Δ_b) (e.g. Van Rijn, 1984).

d) Take "a" as proportional to the thickness of the saltation layer (e.g. Smith and McLean, 1977).

From a practical point of view, it is very difficult to measure in the proximity of the bed. It would seem that of all the methods proposed to define "a", the alternative of selecting "a" as a fraction of the water depth is the only one that can be subjected to physical verification. An inspection of the observed sediment concentration profiles indicated that in most cases it was possible to obtain the value of the near–bed sediment concentration at a level a = 0.05 H above the bed, either by interpolation or with a minimum of extrapolation. This reference level is close enough to the bed so that equation (7.1) should hold there, and at the same time is sufficiently far from the bed to allow for the neglect of any viscous effect. In light of these considerations, the measured sediment concentration profiles were used to directly obtain the values of c_{ae} at five percent of the water depth.

The values of c_{ae} at a = 0.05 H and the experimental conditions under which they were obtained, are summarized in Appendix A.

7.5 Predictions versus Observations

To compare the predictions made by the different relationships with the observations, an effort is made in each case to use the methodology proposed by the author or authors of the formula. Before using the data to do any computations, the side–wall correction procedure proposed by Vanoni and Brooks (Vanoni, 1975) is used to remove wall effects and to obtain the bed shear velocity $u_* = (g\ R_b\ S)^{0.5}$, where g is the acceleration of gravity, R_b is the hydraulic radius with respect to the bed, and S is the energy slope. Some of the details concerning the application of the different formulae are explained in the following text.

In Figure 7.3, a plot of predicted versus observed values of c_{ae} obtained using Einstein's formula (equation 7.5) is shown. The Einstein–Barbarossa (1952) method is used to obtain the grain shear velocity $u_*' = (g\ R_b'\ S)^{0.5}$, where R_b' is the hydraulic radius with respect to the grains. In this method, the parameter R_b' is obtained by solving the following equation

$$R_b' = \frac{U_m^2}{g\ S}\left[5.75\ \log(12.27\ R_b'\ x\ /\ D_s)\right]^{-2} \tag{7.26}$$

iteratively, where U_m is the mean flow velocity, and x is a correction factor for viscous effects. Herein D_s is taken as the mean sediment diameter. The sediment concentration c_{ae} at $a = 0.05\ H$ is obtained by extrapolating from the computed concentration $\mathbf{c_{ae}}$ at $a = 2\ D_s$, with the help of the Rousean distribution

$$c_{ae} = \mathbf{c_{ae}}\left[\frac{H-.05H}{.05\ H}\ \frac{a}{H-a}\right]^{\frac{v_s}{0.4\ u_*}} \tag{7.27}$$

where $a = 2\ D_s$, and $u_* = (g\ R_b\ S)^{0.5}$.

In Figure 7.4a, a plot of predicted versus observed values of c_{ae} obtained using Engelund and Fredsoe's formula (equation 7.8) is shown. The grain shear velocity $u_*' = (g\ R_b'\ S)^{0.5}$ is computed using the method of Engelund and Hansen (1967). In this method, the parameter R_b' is obtained by solving the following equation

$$R_b' = \frac{U_m^2}{g\ S}\left[6 + 2.5\ \ln(R_b'/k_s)\right]^{-2} \tag{7.28}$$

iteratively, where $k_s = 2\ D_s$ is the hydraulic roughness. The sediment concentration c_{ae} at $a = 0.05\ H$ is obtained by extrapolating from the computed concentration $\mathbf{c_{ae}}$ at $a = 2\ D_s$, with the help of the Rousean distribution as described by equation (7.24). The parameter β in equation (7.8) is set equal to one.

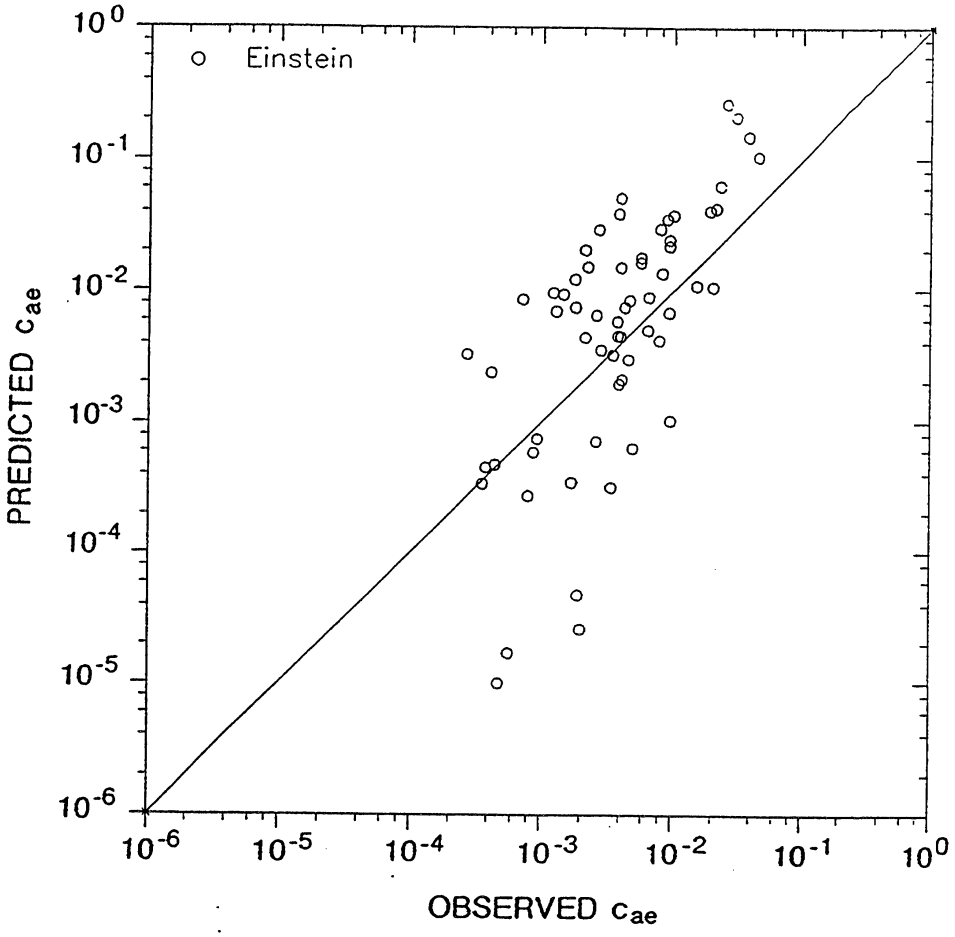

Fig. 7.3 Comparison of predicted and observed values using Einstein's relationship.

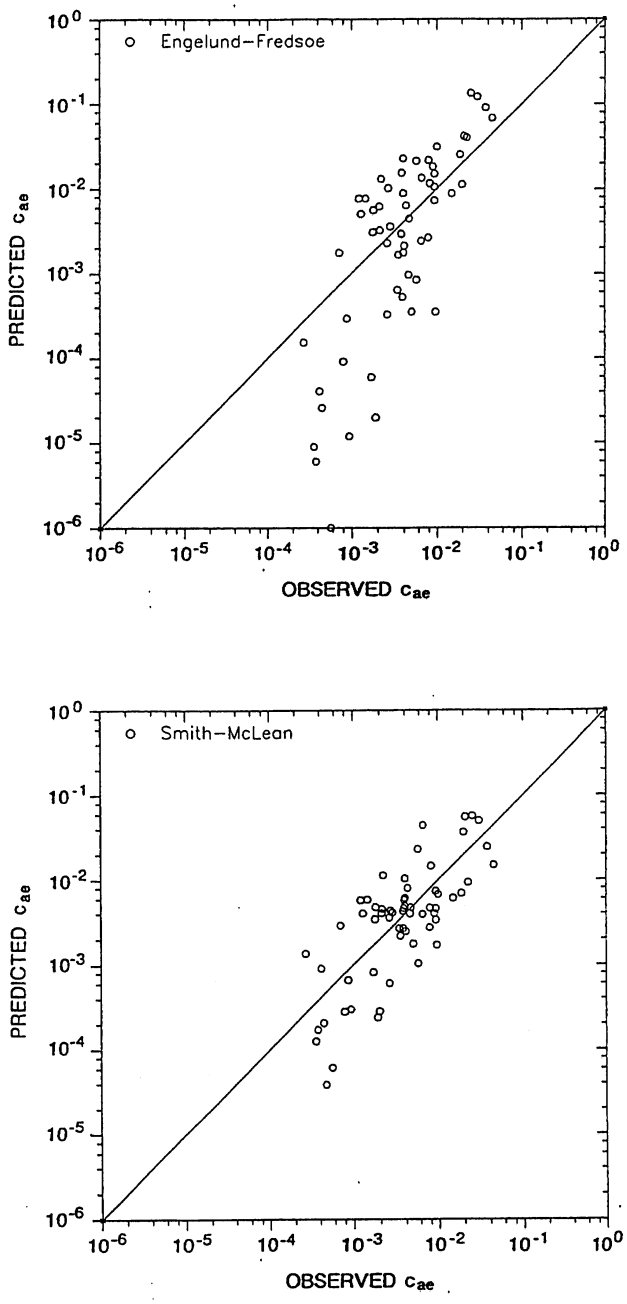

Fig. 7.4a,b Comparison of predicted and observed values using Engelund–Fredsoe's (top) and Smith–McLean's (bottom) relationships.

In Figure 7.4b, a plot of predicted versus observed values of c_{ae} obtained using Smith and McLean's formula (equation 7.11) is shown. Due to the insufficient information about the bedform dimensions in most the experimental data sets, the method proposed by these authors to remove the effect of the bedforms can not be used. Instead, the Engelund–Hansen (1967) method (equation 7.28) is used to compute the grain shear velocity u_*'. The concentration c_{ae} at a = 0.05 H is obtained by extrapolating from the computed concentration c_{ae}, with the help of the following relationship

$$\frac{c_{ae}}{1 - c_{ae}} = \frac{c_{ae}}{1 - c_{ae}} \left[\frac{a}{.05\ H}\right]^{\frac{v_s}{0.4\ u_*}} \tag{7.29}$$

where $a = \alpha_o\ (\theta' - \theta)\ D_s + k_s$, $\alpha_o = 27.3$, $k_s = 2\ D_s$, and $u_* = (g\ R_b\ S)^{0.5}$.

In Figure 7.5a, a plot of predicted versus observed values of c_{ae} obtained using Itakura and Kishi's formula (equation 7.14) is shown. This formulation does not take into account the effect of bedforms, and uses the bed shear velocity $u_* = (g\ R_b\ S)^{0.5}$ as the independent variable.

In Figure 7.5b, a plot of predicted versus observed values of c_{ae} at a = 0.05 H obtained using Van Rijn's formula (equation 7.16) is shown. In this formulation the grain shear velocity u_*' is obtained by means of the following relationships

$$u_*' = \left[g^{0.5} / C'\right] U_m$$

$$C' = 18 \log(12\ R_b / 3\ D_s) \tag{7.30}$$

where g is the acceleration of gravity, and U_m is the mean flow velocity, R_b is the hydraulic radius associated with bed shear stress. Van Rijn uses for D_s the sediment diameter for which ninety percent of the material is finer. Herein, D_s is set equal to the mean diameter, as the material in question is essentially uniform in size distribution.

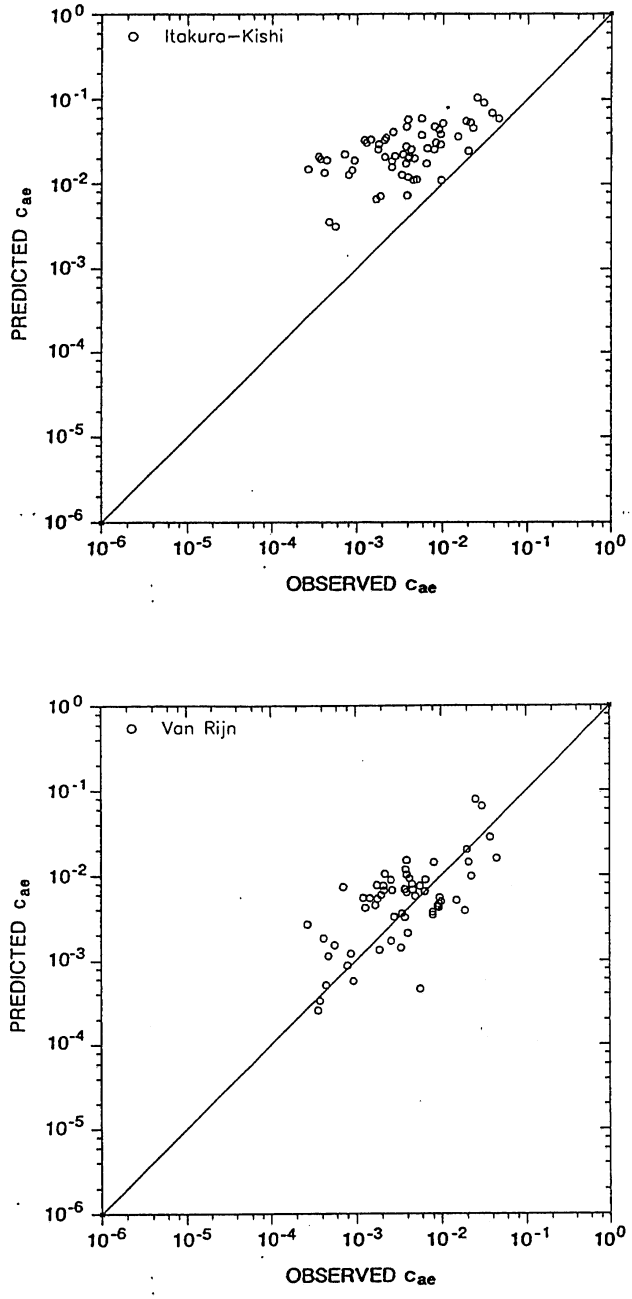

Fig. 7.5a,b Comparison of predicted and observed values using Itakura–Kishi's (top) and Van Rijn's (bottom) relationships.

In Figure 7.6a, a plot of predicted versus observed values of c_{ae} at a = 0.05 H obtained using Celik and Rodi's relationship (equation 7.19) is shown. The constants in this formulation were obtained using data from open channel suspensions without the presence of bedforms, for which $u_* = u_*'$. Therefore, only the data obtained under flat bed conditions are used to test this formula. The roughness height k_s is set equal to two times the mean sediment diameter.

In Figure 7.6b, a plot of predicted versus observed values of c_{ae} obtained using Akiyama and Fukushima's relationship (equation 7.21) is shown. This formulation does not take into account the presence of bedforms and uses the bed shear velocity $u_* = (g\ R_b\ D_s)^{0.5}$ to measure the strength of the flow. Also there is no need to extrapolate since it gives directly the value of c_{ae} at a = 0.05 H.

To quantify the performance of each relationship, two estimators are used. They are the mean of the discrepancy ratio

$$M_e = 10^{b_1} \tag{7.23}$$

where

$$b_1 = \frac{1}{no}\sum_{i=1}^{no} \log(c_{aep}/c_{aeo})$$

and the mean absolute deviation of the discrepancy ratio

$$A_d = 10^{b_2} \tag{7.24}$$

where

$$b_2 = \frac{1}{no}\sum_{i=1}^{no} \left|\log(c_{aep}/c_{aeo}) - b_1\right|$$

Here c_{aep}/c_{aeo} is the discrepancy ratio between predicted and observed values of c_{ae}, and no is the number of data points. It follows that perfect agreement is indicated by $M_e = 1$ and $A_d = 1$. As shown in Table 7.1, the formulations of Smith and McLean (P = 1), and Van Rijn (P = 1.5) predict the observed concentrations quite well.

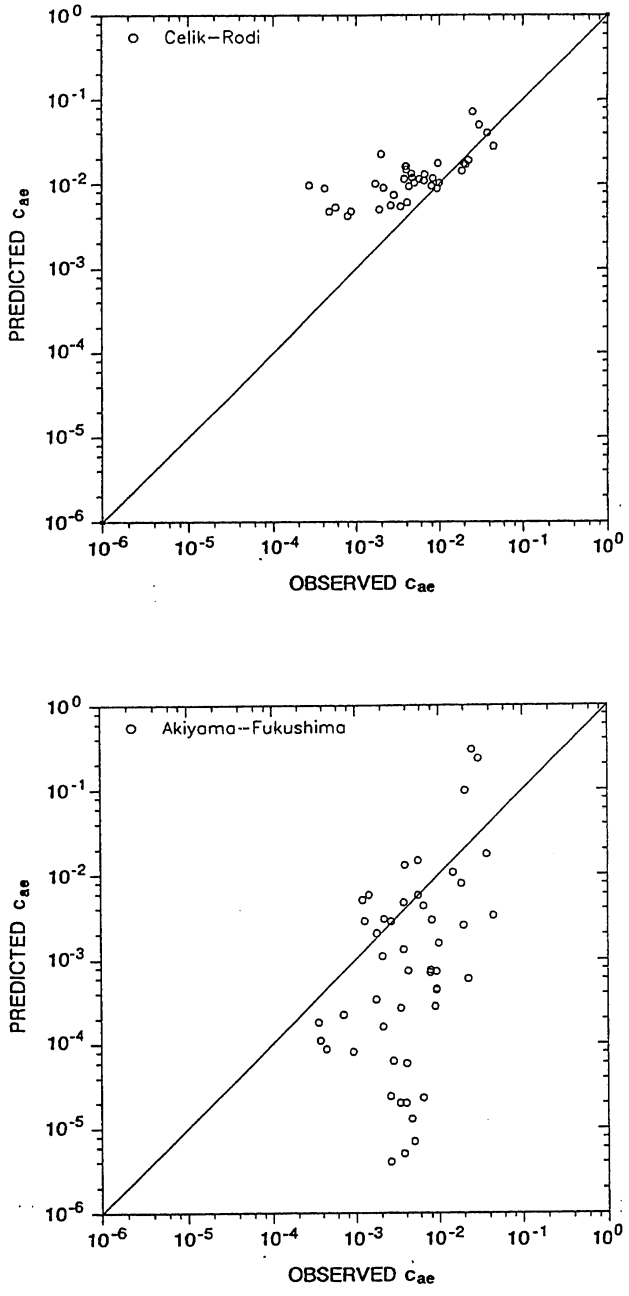

Fig. 7.6a,b Comparison of predicted and observed values using Celik–Rodi's (top) and Akiyama–Fukushima's (bottom) relationships.

TABLE 7.1 PERFORMANCE OF VARIOUS FORMULAE

Formula	M_e	A_d
Einstein (1950)	1.37	3.45
Engelund–Fredsoe (1976)	0.50	5.30
Smith–McLean (1977)	0.88	2.42
Itakura–Kishi (1980)	6.70	2.22
Van Rijn (1984)	1.31	2.19
Celik–Rodi (1984)	2.57	2.03
Akiyama–Fukushima (1985)	0.12	8.15
Present Study	1.00	2.12

7.6 Proposed Entrainment Function for Uniform Sediment

As suggested by the formulations reviewed previously, the dimensionless sediment entrainment rate E_s should be a function of the fluid forces acting on a bed covered with loose sediment and the characteristics of the bed sediment itself. The general dimensional analysis of Parker and Anderson (1977), suggests the following functional relation

$$E_s = f_1\left[\frac{\tau_b'}{\rho R g D_s} , \frac{H}{D_s} , R_p , R \right] \tag{7.31}$$

where τ_b' is the bed shear stress due to grain friction, g is the gravitational acceleration, D_s is the mean sediment diameter, $R = (\rho/\rho_s - 1)$ is the submerged specific gravity of the sediment, ρ is the water density, ρ_s is the sediment density, H is the depth of the flow, $R_p = (g\ R\ D_s)^{0.5}\ D_s\ /\ \nu$ is a particle Reynolds number, and ν is the water kinematic viscosity.

The sediment in most laboratory flumes and in nearly all rivers has a specific gravity of 2.65; thus R can be taken to be a constant equal to 1.65 and equation (7.31) reduces to

$$E_s = f_2\left[\frac{\tau_b'}{\rho R g D_s} , \frac{H}{D_s} , R_p \right] \tag{7.32}$$

or its equivalent form

$$E_s = f_3\left[\frac{u_*'}{v_s} , \frac{H}{D_s} , R_p \right] \tag{7.33}$$

Here $u_*' = (\tau_b'/\rho)^{0.5}$ is the bed shear velocity due to grain friction, and v_s is the sediment fall velocity.

The data summarized in Appendix A are used to obtain the functional relationship implied by equation (7.33). The values of $u_*' = (g R_b' S)^{0.5}$ are computed with the Engelund–Hansen method (equation 7.28). The data selected covers the following ranges of the variables in (7.33):

$$2 \cdot 10^{-4} < E_s = c_{ae} < 6 \cdot 10^{-2}$$
$$0.70 < u_*'/v_s < 7.50$$
$$240 < H/D_s \leq 2400$$
$$3.50 < R_p < 37.00$$

An inspection of the data shows no clear dependence of E_s (= c_{ae}) on the values of the relative roughness H/D_s. On the other hand, a clear correlation between E_s (= c_{ae}) and the dimensionless shear velocity u_*'/v_s is found as shown in Figure 7.7. The scatter of the data in this figure, motivates the search for a similarity variable to collapse the data. Following the lead of Akiyama and Fukushima (1985), the similarity variable is chosen as

$$Z_u = \frac{u_*'}{v_s} R_p^{\,n} \tag{7.34}$$

Plots of E_s against Z_u with the power "n" varying between 0 and 1 show the best collapse of the data for a value of n near 0.6 (Figure 7.8). An inspection of E_s versus Z_u with n = 0.6, indicates that

$$E_s \sim Z_u^5 \tag{7.35}$$

It has been suggested that c_{ae} (= E_s) should not exceed a value of 0.3 for the sediment–water mixture to be a true suspension (Engelund and Fredsoe, 1976). The data used herein do not permit the detection of any particular trend for high sediment concentrations. To account for the likely existence of an upper limit, the following relationship is proposed

$$E_s = A\ Z_u^5\ /\ (1 + \frac{A}{0.3}\ Z_u^5\ ) \qquad (7.36)$$

where the constant A is found by enforcing the condition $M_e = 1$, with M_e as defined by equation (7.23). In Figure 7.9, equation (7.36) with A = $1.3 \cdot 10^{-7}$ is plotted along with the data used in the derivation. For this formulation $A_d = 2.12$. For the sake of comparing with the equivalent plots the previous formulae, predicted versus observed values are plotted in Figure 7.10. The present formulation is seen to perform better than those of Van Rijn and Smith and McLean, but this should be expected since the data used to test the formulation is the same data used for its derivation.

7.7 Entrainment Function for Non–Uniform Sediment

Natural sediment deposited by flows often has a wide size distribution. It would be of interest to extend the formulation obtained in the previous section for uniform sediment to the case of non–uniform sediment.

For the case of a bed covered by a sediment mixture having N size ranges, such that p_i is the fraction of bed material with a mean size D_i contained in the ith size range, equation (7.33) can be generalized to

$$E_{s_i} = f_4\left[\ \frac{u_*'}{v_{s_i}},\ \frac{H}{D_{50}},\ R_{p_i}\ ,\ \frac{D_i}{D_{50}}\ \right] \qquad (7.37)$$

where E_{s_i} denotes the sediment entrainment rate for the ith sediment size range, D_{50} denotes the median grain size of the mixture, v_{s_i} denotes the fall velocity of the sediment having a grain size D_i, and $R_{p_i} = (gRD_i)^{0.5}\ D_i/\ \nu$.

The steady sediment conservation equation for the ith size range of sediment mixture takes the form

$$\frac{dq_{s_i}}{dx} = v_{s_i}\ (p_i\ E_{s_i} - c_{a_i}) \qquad (7.38)$$

where q_{s_i} is the volumetric suspended sediment discharge for the ith size range, and c_{a_i} denotes the value of c_a for the ith size range. The product

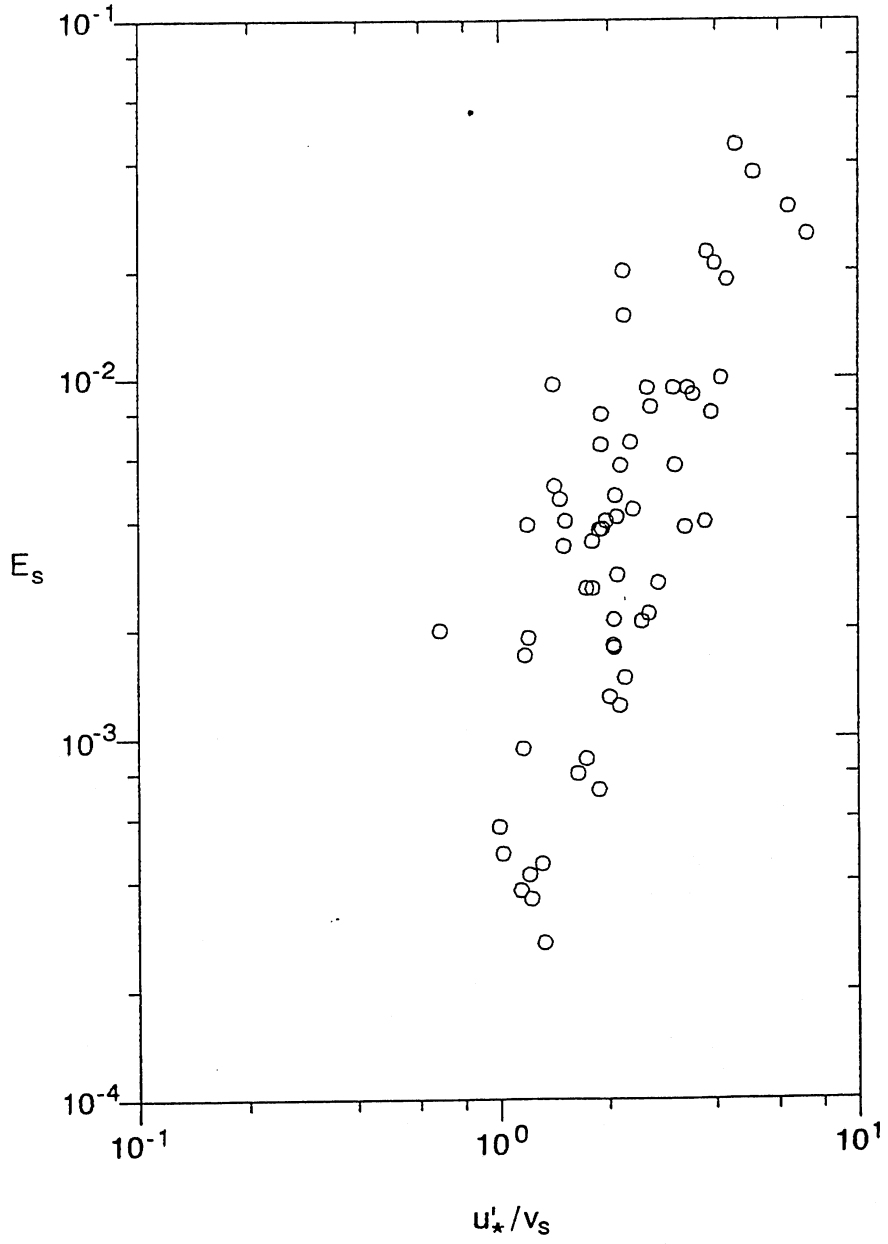

Fig. 7.7 Plot of sediment entrainment coefficient E_s versus dimensionless skin shear velocity u'_*/v_s.

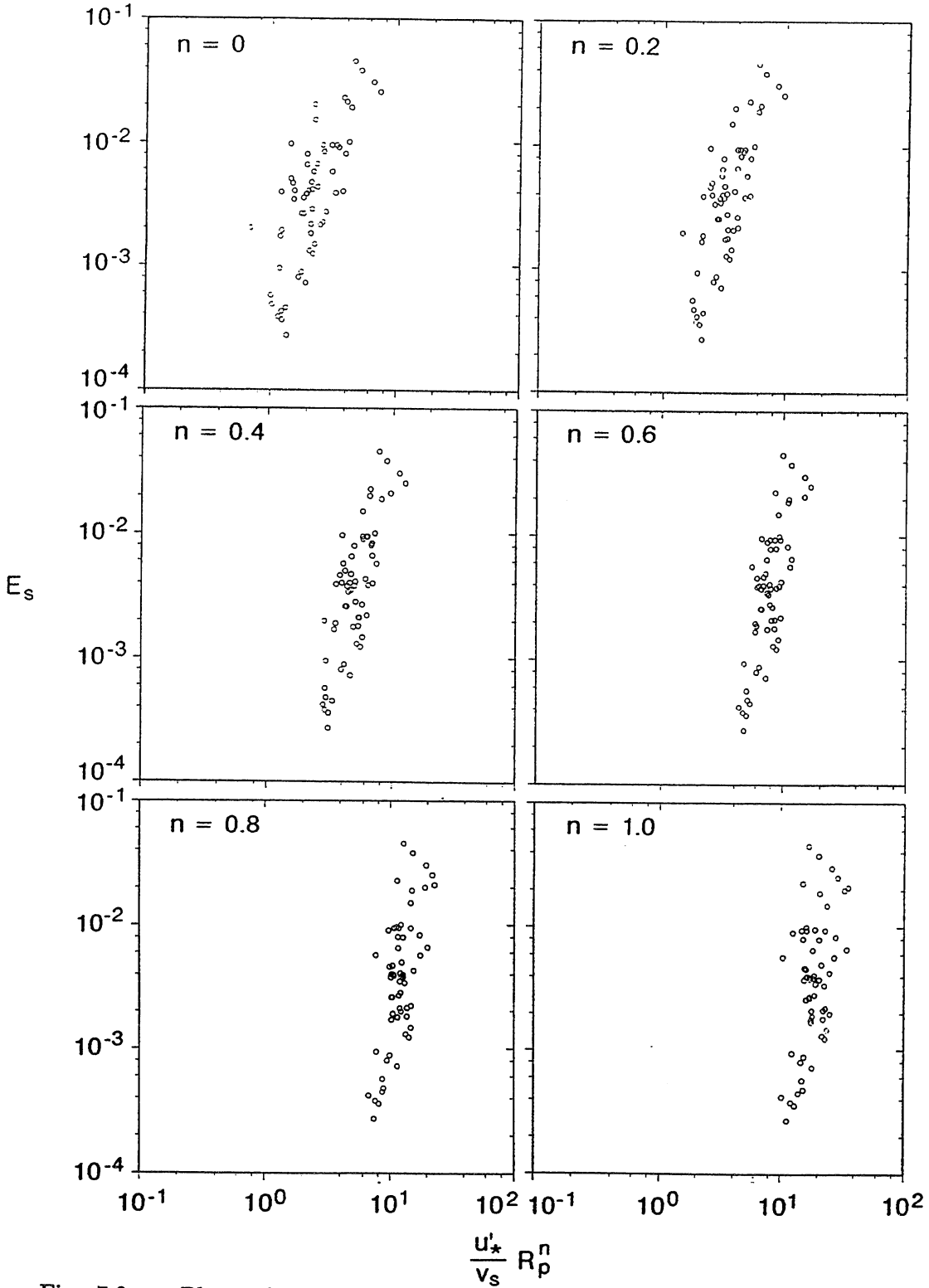

Fig. 7.8 Plot of sediment entrainment coefficient E_s versus similarity variable Z_u for $0 < n < 1$.

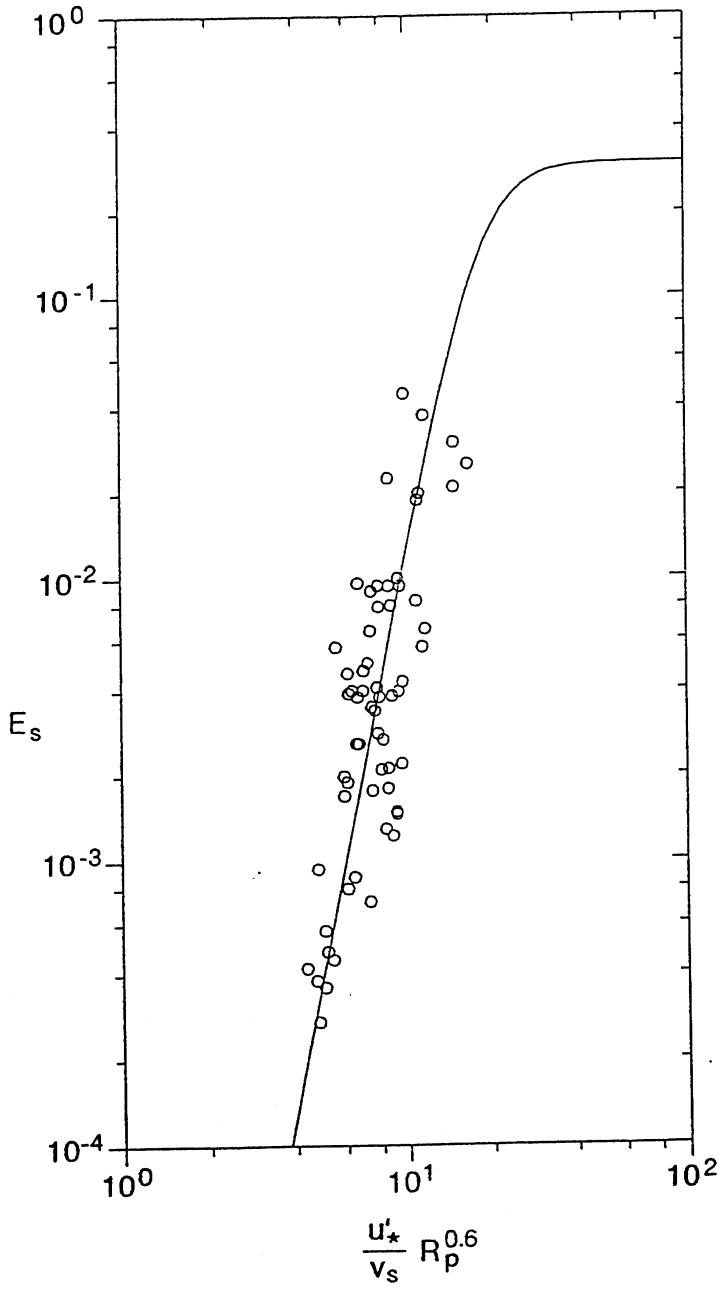

Fig. 7.9 Plot of entrainment relationship for uniform sediment (7.36) and the data used in the derivation.

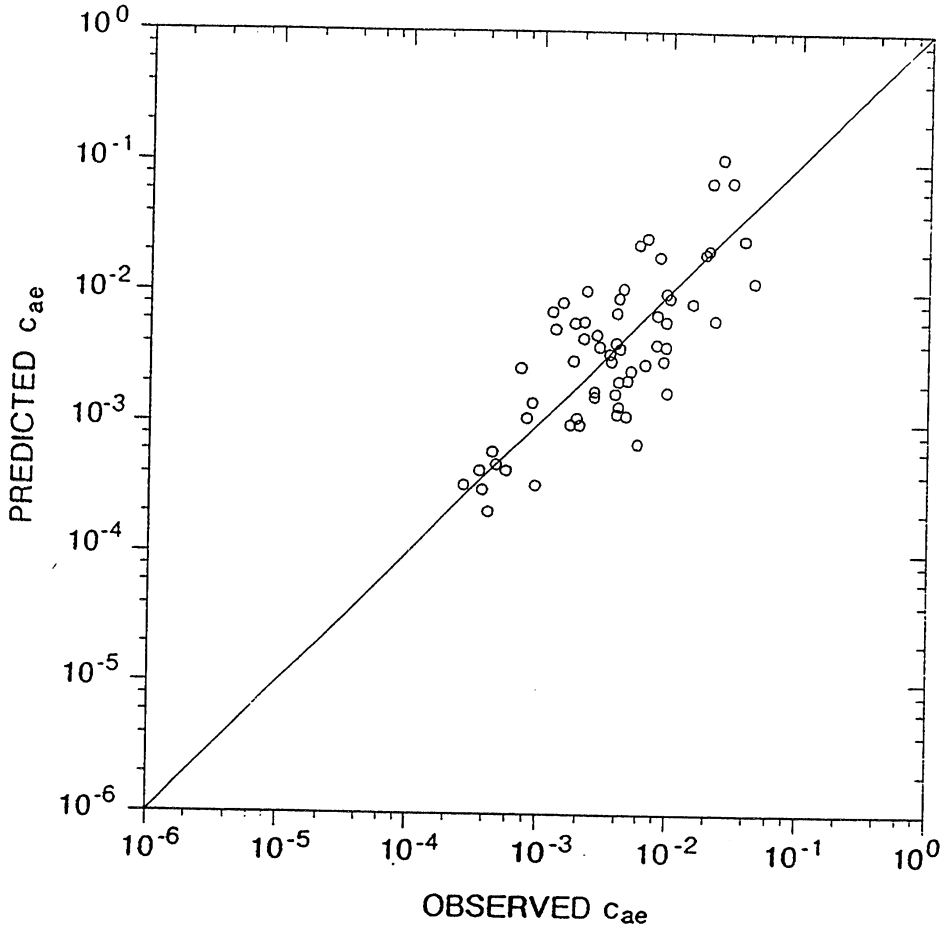

Fig. 7.10 Comparison of predicted and observed values of reference concentration using the present formulation (7.36).

$p_i E_{s_i}$ gives the actual sediment entrainment rate for the sediment in the ith size range, based on the amount available of this sediment size in the bed. For equilibrium conditions, equation (7.38) gives

$$E_{s_i} = \frac{c_{ae_i}}{p_i} \tag{7.39}$$

where c_{ae_i} denotes the equilibrium value of c_{a_i}. As indicated by equation (7.39), to obtain a functional relationship for E_{s_i} it is necessary to have both measured sediment concentration profiles for the different size ranges and the size distribution of the bed material. Herein, field data for two reaches on the Rio Grande (Nordin and Dempster, 1963) are used to obtain a functional relationship for E_{s_i}. Three grain size ranges are used as follows:

Range 1: $0.0625 \text{ mm} < D_s < 0.125 \text{ mm}$, $D_1 = 0.088 \text{ mm}$
Range 2: $0.125 \text{ mm} < D_s < 0.250 \text{ mm}$, $D_2 = 0.180 \text{ mm}$
Range 3: $0.250 \text{ mm} < D_s < 0.500 \text{ mm}$, $D_3 = 0.350 \text{ mm}$

Here D_1, D_2, and D_3 denote the geometric mean of the end points for each grain size range. The values of p_i and D_{50} for the two reaches in question are found to vary from day to day. Averaged values for the two reaches are shown in Table 7.2.

TABLE 7.2 CHARACTERISTICS OF BED SEDIMENT

	Rio Grande: Bernalillo	Rio Grande: Socorro
D_{50}	0.310 mm	0.190 mm
p_1	0.046	0.129
p_2	0.297	0.484
p_3	0.484	0.218

All the data are summarized in Appendix A. As in the case of laboratory suspensions, the Engelund–Hansen method (equation 7.28) is used to compute the values of the grain shear velocity u'_*. The data for the two reaches cover the following ranges of the variables in equation (7.37):

$$1 \cdot 10^{-4} < c_{ae_i}/p_i = E_{s_i} < 0.165$$
$$0.60 < u_*'/v_{s_i} < 12.1$$
$$1000 < H/D_{50} < 3000$$
$$2.7 < R_{p_i} < 32$$
$$0.25 < D_i/D_{50} < 1.40$$

The above values show a good overlap with the data for uniform material.

In Figure 7.11, a plot of E_{s_i} versus the dimensionless grain shear velocity u_*'/v_{s_i} shows a trend similar to the one observed in the equivalent plot for uniform sediment (Figure 7.7). At the same time, the relative roughness H/D_{50} seems to play a secondary role, as was the case for the uniform sediment. The similarity variable used previously is generalized to the case of non–uniform sediment as follows

$$Z_m = \frac{u_*'}{v_{s_i}} R_{p_i}^{0.6} \left[\frac{D_i}{D_{50}}\right]^m \tag{7.40}$$

A remarkable collapse of the data is obtained for $m = 0.2$, as shown in Figure 7.12. It is interesting to see that the data follow a line parallel to the trend given by the relationship developed for uniform sediment. It is clear that any fit of the non–uniform sediment data will give estimates of E_{s_i} smaller than the value one would obtain for the same flow conditions and sediment size with equation (7.36) developed for uniform sediment. To solve this, a parameter λ is used to obtain an effective similarity variable as follows

$$Z_{eff} = \lambda \, Z_m \tag{7.41}$$

The value of λ is obtained by fitting the non–uniform sediment data to the entrainment relationship for uniform sediment (Figure 7.13). The best fits for the Bernalillo and Socorro data, give λ values of 0.847 and 0.775, respectively. The following relationship can then be used to predict sediment entrainment from a bed covered by non–uniform sediment

$$E_{s_i} = 1.3 \; 10^{-7} \; Z_{eff}^5 \; / \; (1 + 4.33 \; 10^{-7} \; Z_{eff}^5) \tag{7.42}$$

This relation reduces to equation (7.36) when the bed sediment is uniform (i.e. $\lambda = 1$).

The value of the straining parameter λ has been evaluated herein in only two specific cases. It can be expected that this parameter characterizes the non–uniformity of the sediment. The standard deviation of the sediment σ_ϕ on the phi–scale can be expressed as

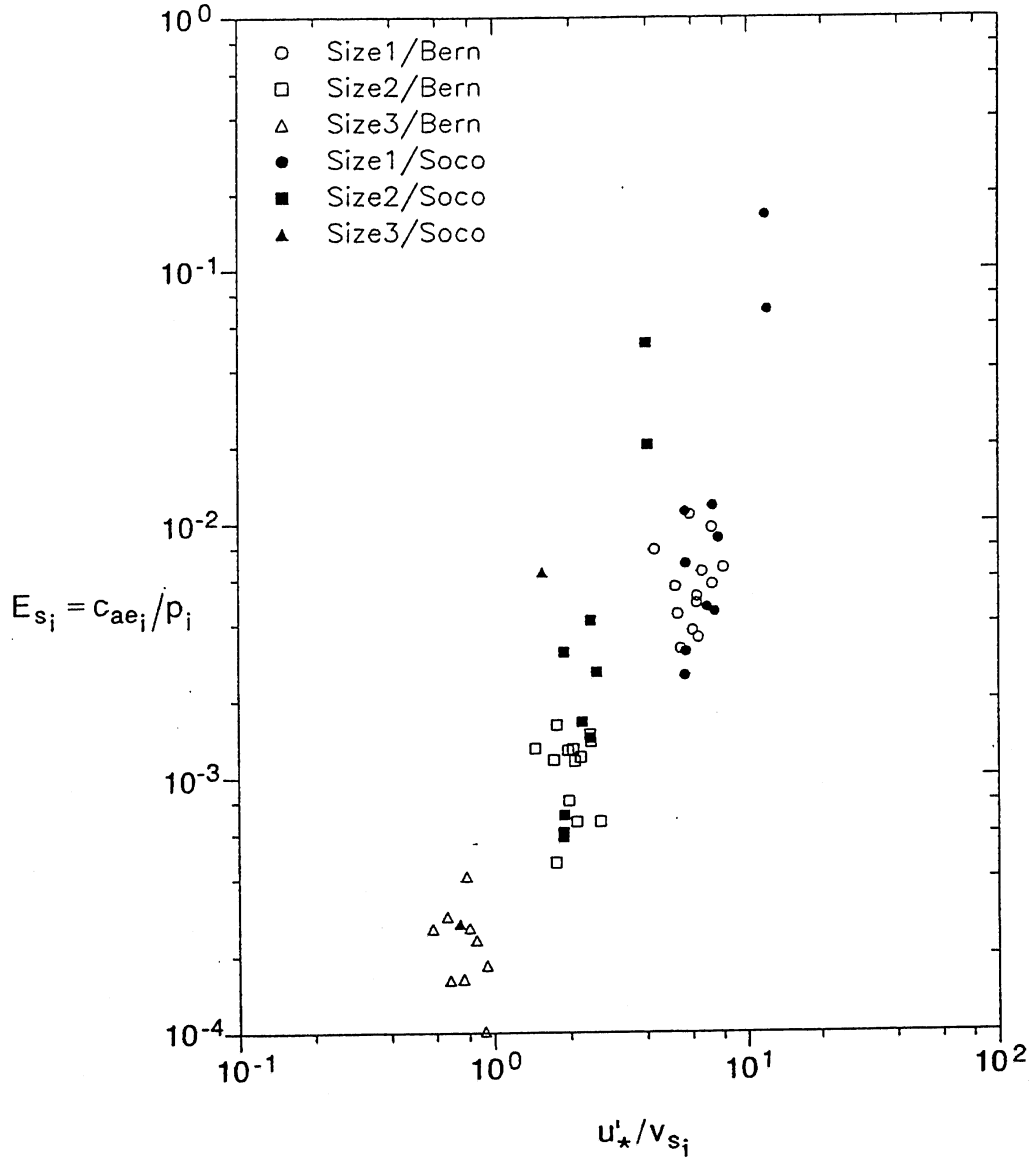

Fig. 7.11 Plot of entrainment coefficient E_{s_i} versus dimensionless skin friction u'_*/v_{s_i}.

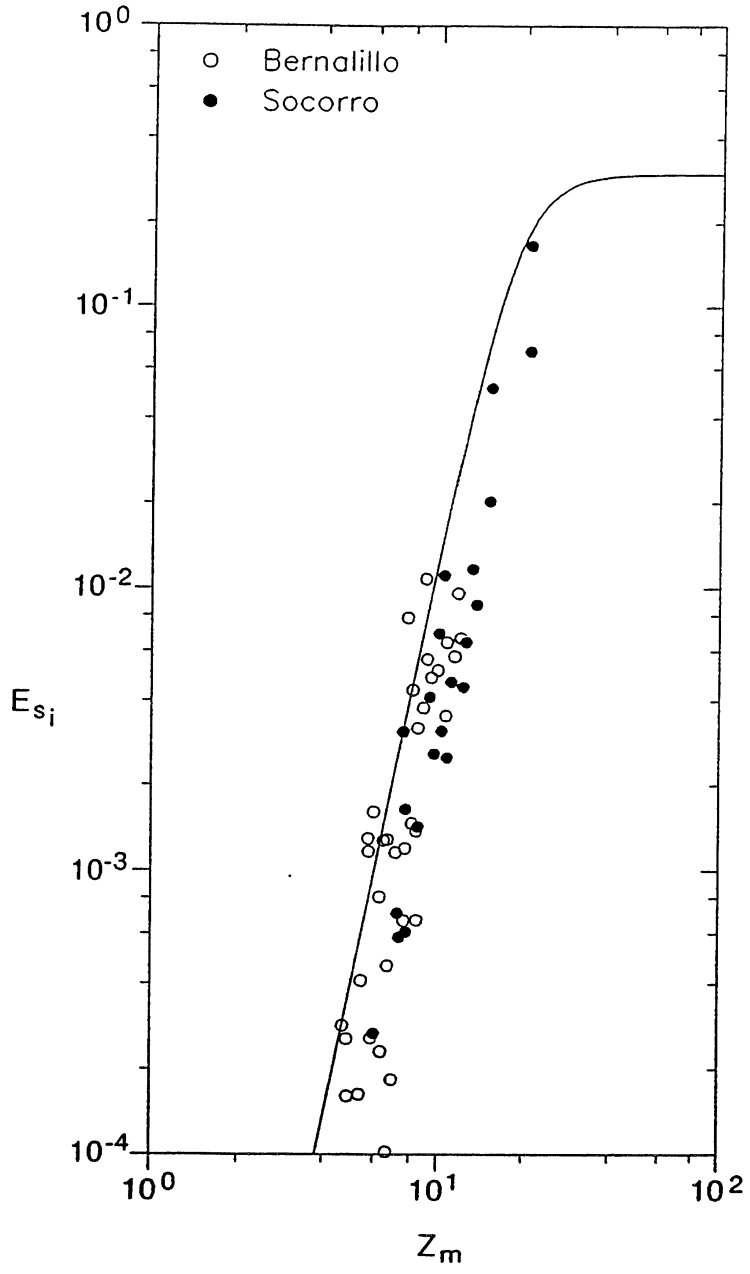

Fig. 7.12 Plot of entrainment coefficient E_{s_i} versus similarity variable Z_m with m = 0.2. The line is that of the proposed formulation for uniform sediment (7.36).

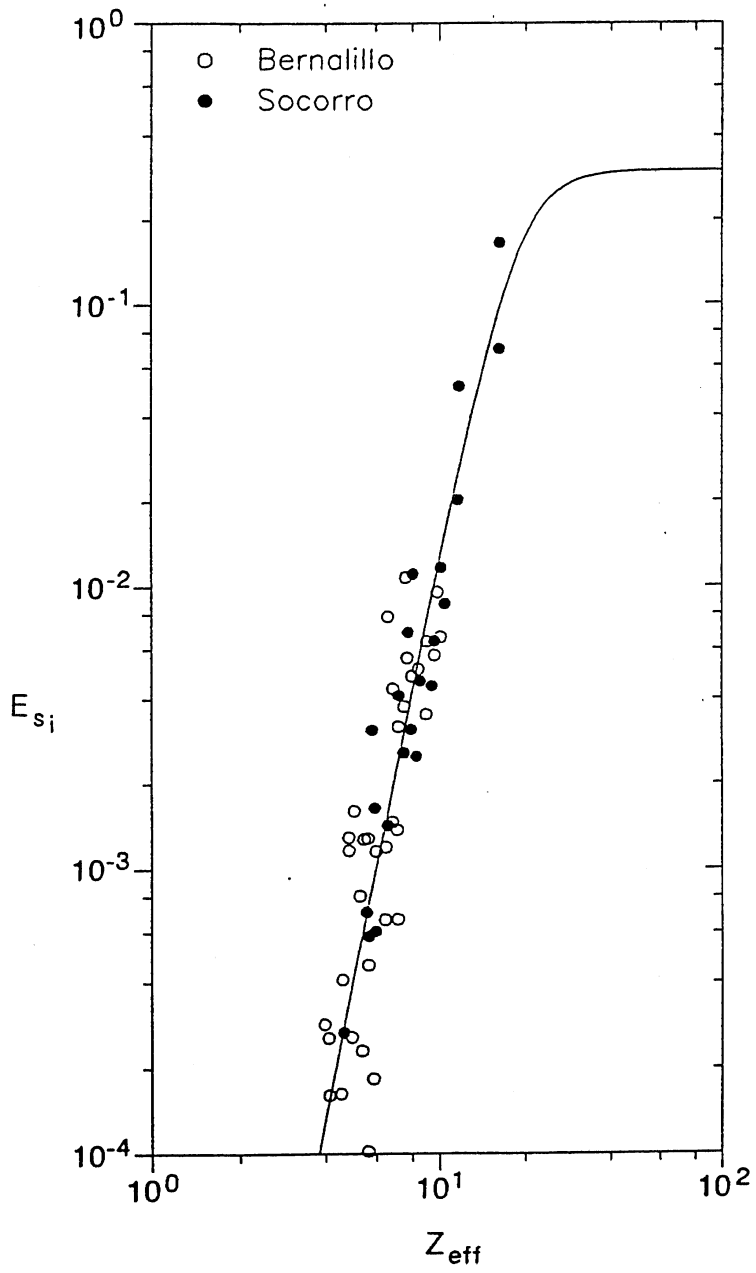

Fig. 7.13 Plot of entrainment coefficient E_{s_i} versus similarity variable $Z_{eff} = \lambda Z_m$.

$$\sigma_\phi^2 = \Sigma\ (\phi - \overline{\phi})^2\ p_i \tag{7.43}$$

where

$$\phi = -\ \ln(D_i)/\ln(2)\ ;\ \overline{\phi} = \Sigma\ \phi\ p_i \tag{7.44}$$

For $\sigma_\phi = 0$ (i.e. uniform sediment), and one would expect $\lambda = 1$. A simple linear relation for λ versus σ_ϕ might look like

$$\lambda = 1 + \frac{\sigma_\phi}{\sigma_{\phi o}}\ (\lambda_o - 1) \tag{7.45}$$

Here λ_o and $\sigma_{\phi o}$ are reference values introduced to normalize the straining parameter λ, so that for $\sigma_\phi = \sigma_{\phi o}$, $\lambda = \lambda_o$. These reference values are computed by taking the average of the values of λ and σ_ϕ obtained for Bernalillo ($\lambda = 0.847$, $\sigma_\phi = 0.731$) and Socorro ($\lambda = 0.775$, $\sigma_\phi = 0.615$), resulting in $\lambda_o = 0.811$ and $\sigma_{\phi o} = 0.673$. Substitution of these values into equation (7.41) yields

$$\lambda = 1 - 0.288\ \sigma_\phi \tag{7.46}$$

To test the ability of the relationship obtained for non–uniform sediment (7.42) an independent source of data from the Niobrara river (Colby and Hembree, 1955) is used. For this data, $\sigma_\phi = 0.686$. Substitution of this value into (7.46) yields $\lambda = 0.802$. In Figure 7.14, a plot of predicted values using (7.42) with $\lambda = 0.0802$ versus observed values is shown. The agreement is found to be fair.

7.8 Comparison with Data From Sediment–Entraining Currents

In Figure 7.15, the sediment entrainment rates back–calculated during the experiments with sediment–entraining density currents are plotted along with the formulation obtained herein for uniform sediment in open channel flows. The values of R_p used for the 100 μ and 180 μ coal, are 1.23 and 3.0, respectively. The trend displayed by the data for density currents is consistent with that given by the sediment entrainment function for open channel flows. However, it is clear that the sediment entrainment data for

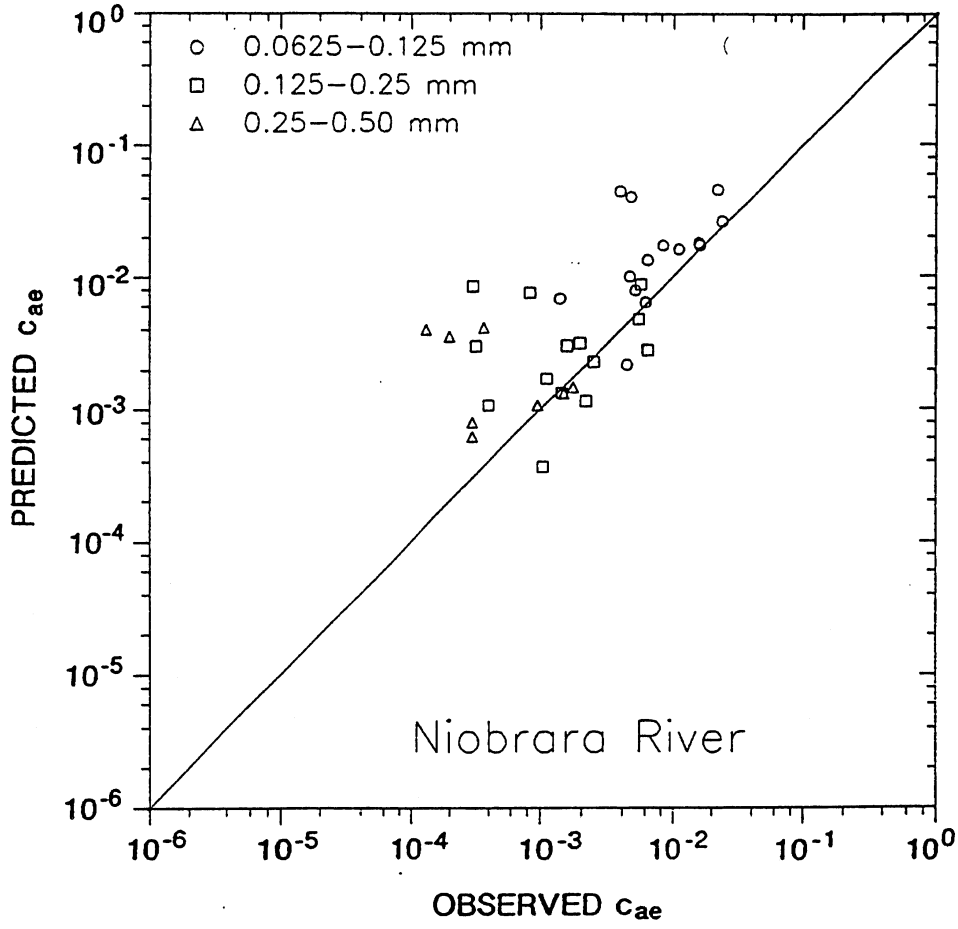

Fig. 7.14 Comparison of observations versus predictions using the formulation for non–uniform sediment (7.42) and data from the Niobrara River.

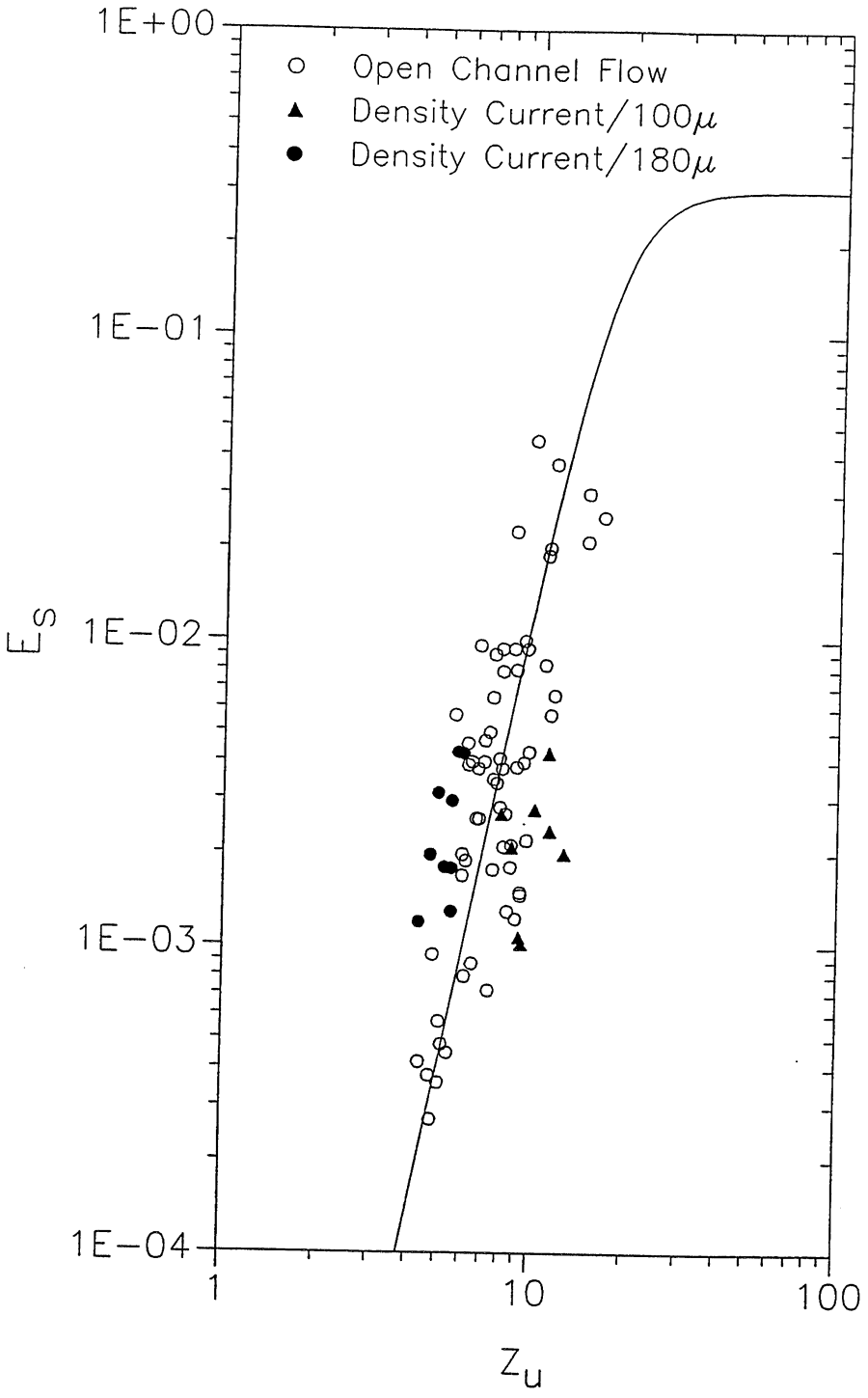

Fig. 7.15 Plot of sediment entrainment rates produced by density currents and the relationship obtained for open channel flows (7.36).

density currents do not collapse when plotted as a function of the similarity variable Z_u. Since the sediment entrainment function for uniform sediment was obtained with data having particle Reynolds numbers R_p (3.5 to 37) larger than those associated with the 100 and 180 μ coal, it is possible that the lack of collapse may be due to a grain size effect. To explore this further, the similarity variable Z_u can be written in a more general form as

$$Z_u = \frac{u_*'}{v_s} f_o(R_p) \tag{7.47}$$

where

$$f_o = \lambda R_p^{0.6} \tag{7.48}$$

Here λ itself could be a function of R_p. For the open channel flow data $\lambda = 1$, and $f_o = R_p^{0.6}$. An inspection of the data in Figure 7.15 indicates that the 100 and 180 μ coal data collapse into the line given by (7.36) for values of λ of 0.68 and 1.23, respectively. In Figure 7.16, these values are used to plot f_o as given by (7.48). Included in the figure is the relation $f_o = R_p^{0.6}$ for the open channel data, plotted over the range of values of R_p covered. Based on the two available points for $R_p < 3$, the plot suggests that f_o decreases more rapidly with sediment size than implied by the relation $f_o = R_p^{0.6}$ in that range. This in turn should result in reduced sediment entrainment rates as the sediment size decreases. This behavior supports the considerations made previously concerning the role of viscous effects as grain size decreases. The implication here is that the open channel formulation is not necessarily wrong; rather, the functionality in R_p may not longer satisfy the relation $f_o = R_p^{0.6}$ for $R_p < 3$.

7.9 Conclusions

Of all the various formulae in the literature, the relationships put forward by Smith and McLean (1977), and Van Rijn (1984), are found to be the best in predicting the observations for uniform sediment. Van Rijn's formulation involves a power of 1.5 of the bed shear stress, while in the case of Smith and McLean the power takes a value of 1.0. This latter result indicates that the rate of sediment entrainment varies almost linearly with the excess grain shear stress $\rho(u_*'^2 - u_{*c}^2)$.

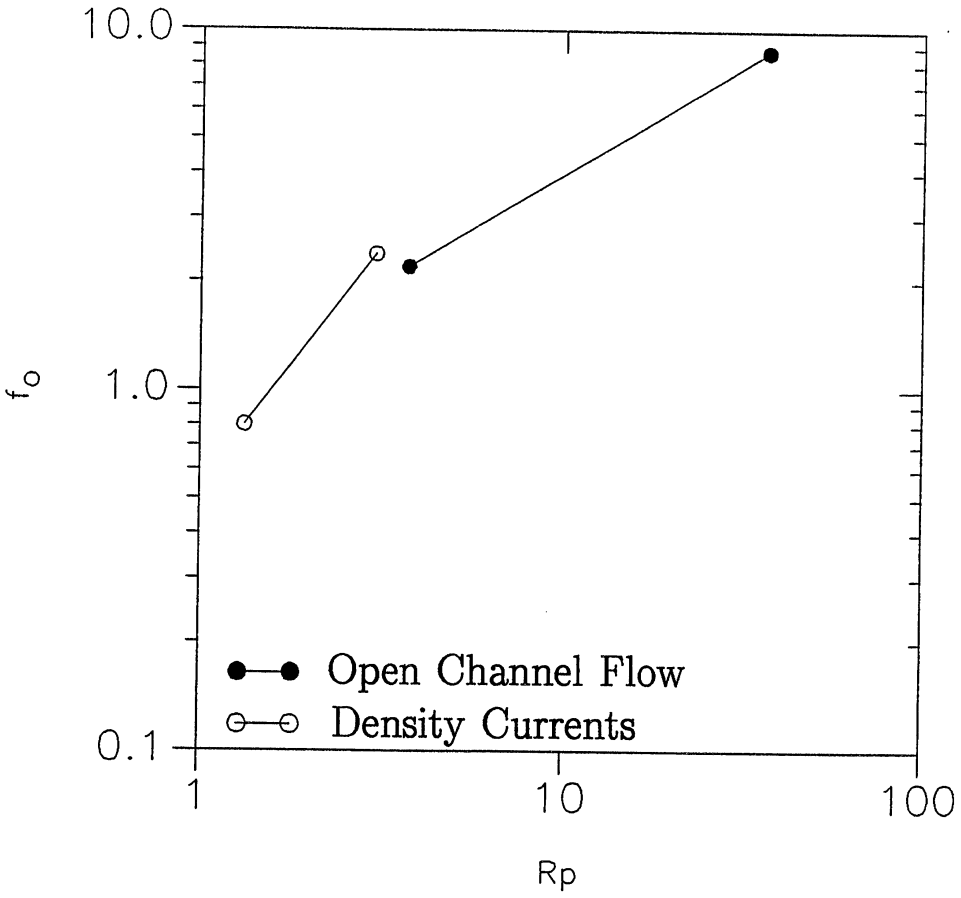

Fig. 7.16 Plot of f_o as a function of particle Reynolds number R_p.

The relationship obtained herein with the help of data employed to test the existing formulations uses the similarity variable $Z_u = u_*'/v_s \, R_p^{0.6}$ to collapse the data; it involves a power of 2.5 of the grain shear stress. The extension of the formulation to handle sediment mixtures also supports the trend displayed by the data for uniform material. Both empirical fits should provide reasonable estimates of the sediment entrainment coefficient for sediment in the size range $95\ \mu < D_s < 450\ \mu$.

The formulation obtained with open channel data was found to show some consistency with observations made in the experiments with sediment–entraining density currents. This consistency should prove useful for the development of predictive relations for sediment entrainment by turbidity currents.

In the absence of better information, the formulations of Smith–McLean, Van Rijn, and the one proposed herein, should provide reasonable estimates of sediment entrainment rates associated with turbidity currents flowing over an erodible bed. Besides being useful in the realm of one–dimensional, integral models, these formulations can eventually be used to compute near–bed boundary conditions in two–dimensional models.

CHAPTER 8

SUMMARY AND CONCLUSIONS

8.1 Summary

An experimental study of continuous turbidity currents was conducted in a laboratory flume modified to simulate a submarine canyon and its associated abyssal fan. The experimental program included the study of conservative saline currents, turbidity currents driven by well–sorted sediment, turbidity currents driven by poorly–sorted sediment, and sediment–entraining saline currents.

An integral model for steady, spatially developing turbidity currents driven by poorly–sorted sediment was developed and used as a basis for the analysis of the experimental results. The model is an extension of the three–equation models proposed by Fukushima, Parker, and Pantin (1985), and Akiyama and Stefan (1985) for turbidity currents driven by well–sorted sediment.

Several existing relationships for computing sediment entrainment rates in open channel flows were tested using data from equilibrium open channel suspensions. The same data were used to obtain a new sediment entrainment function for well–sorted sediment. Using field data, the empirical relationship was adapted to handle entrainment from a bed covered with poorly–sorted sediment.

8.2 Conclusions

8.2.1 Flow Characteristics

The vertical structure of the currents was found to depend on flow regime. Supercritical flows were characterized by a relatively thin boundary layer extending up to the maximum velocity point and an outer jet–like layer that covered most of the current thickness. The boundary layer covered a larger portion of the current thickness in the case of subcritical flows, where the "nose" or maximum velocity point was located farther away from the bed. In both flow regimes, the velocity profiles showed a linear variation above the maximum velocity point.

The vertical structure of saline and fine–grained turbidity currents having similar inlet conditions was found to be approximately the same before and after the hydraulic jump.

Velocity, sediment concentration, and excess fractional density profiles showed a good degree of similarity, in particular for supercritical flows. This has important theoretical implications since the similarity assumption was invoked during the development of the integral model.

The grain size did not affect the vertical distribution of velocities in those currents that were not strongly depositional.

Grain size showed a clear tendency to decrease in the upward direction from the bed. Smaller grains were more uniformly distributed in the vertical. Consequently increased sediment size resulted in increased depositional rates for the same layer–averaged concentration C_i.

The vertical distribution of sediment having different sizes was found to be approximately similar as the current evolved in the downstream direction.

8.2.2 Hydraulic jump

The saline and turbid hydraulic jumps showed similar characteristics. The amount of water entrained by the flows while going through the jump was found to be small. Most of the water entrainment was seen to take place along the supercritical region of the flow extending between the inlet and the jump. The water entrainment from above was negligible along the subcritical region after the jump.

The strength of the jumps, quantified by the ratio of the current thickness after the jump to the current thickness before the jump, was seen to take values fairly close to those predicted by the relation for non–entraining jumps.

Even though the present study was limited to a single canyon slope, the general characteristics of the observed hydraulic jumps are expected to be representative of similar events in the field. This is suggested by the Richardson numbers associated with supercritical turbidity flows which indicate that if the current experiences a hydraulic jump, the jump can be expected to be weak, in agreement with the observations presented herein.

The most important effect of the change in flow regime was a marked reduction of the bed shear stress downstream of the jump.

It was found that the thickness of the sediment deposit left immediately downstream of the jump tends to increase as the ratio u_*/v_s of the bed shear velocity immediately behind the jump to the particle fall velocity decreases.

These observations suggest that a continuous, channelized turbidity current driven by fine material experiencing a hydraulic jump in the proximity of a canyon–fan transition will drop most of its bedload immediately downstream of the jump. The suspended load can be expected to respond more gradually to the change in flow regime, with the resulting deposit spread out over hundreds of meters to kilometers.

8.2.3 Sediment Deposits: Turbidites

A clear correlation between turbidite thickness and grain size of the sediment driving the flow was observed. For similar inlet conditions, the currents laden with coarser sediment generated thicker turbidites. The thickness of the turbidites was seen to decrease roughly exponentially with distance from the inlet.

The median grain size of the turbidites deposited by currents driven by poorly–sorted sediment was found to decrease with distance from the inlet. In those cases when analysis was possible, the vertical structure of the deposits also showed some weak grain size stratification. Upward fining was observed along the model canyon, while upward coarsening or no size stratification was observed along the model fan.

The break in slope did not seem to cause any discontinuity in the pattern of deposition from suspension.

It can be concluded that any sudden increase in the thickness of the deposit associated with a dilute turbidity current near a slope change is not due to the break in slope itself, but rather to the hydraulic jump induced by the break.

The fan deposits generated in the experiments were two–dimensional because the currents were not able to spread laterally. Many turbidite environments do involve significant lateral flow, but there are a number of cases where turbidity flows are fairly two–dimensional over significant distances. For instance, the major channel of the Rhone river fan (Bellaiche et al., 1981) shows significant spillover from the channels to the sides, but the channel has remained in the same place for thousands of years of deposition, being simply displaced vertically.

8.2.4 Sediment Entrainment

The observations indicated conclusively that a conservative current of sufficient strength can entrain substantial amounts of bed sediment into suspension.

The amount of sediment entrained over a two–meter reach increased the buoyancy discharge by a modest amount (not more than 10 %). It can be expected that in a submarine canyon several kilometers in length, much more entrainment could be realized.

The results also suggest that in addition to the purely sand–driven currents analyzed by Fukushima et al. (1985), currents driven by silty mud could also entrain substantial amounts of sand and carry it to deep water.

A clear tendency for the rate of sediment entrainment to increase with flow velocity was observed.

An approximate decomposition of the bed shear stress into skin friction and form drag components indicated the importance of accounting for the presence of bedforms.

Bedforms that developed during the experiments were found to be downstream–migrating antidunes. They are believed to have been induced by the small scale of the experiments. In the field, the ripple is expected to be the dominant bedform.

The method developed by Nelson and Smith (1989) to remove the effect of bedforms on the boundary shear stress in open channel flows was modified to be applied in the present study. A comparison with values obtained using an empirical skin friction relation indicated a remarkable agreement.

8.2.5 Sediment Entrainment Functions

Of all the various formulae in the literature, the empirical relationships proposed by Smith and McLean (1977) and Van Rijn (1984) were found to be the best in predicting reference suspended sediment concentrations of uniform sediment. Probably the most important finding related to this is the fact that sediment entrainment rates are seen to increase roughly linearly with excess (above critical) skin shear stress.

A similarity collapse was used to obtain a new empirical sediment entrainment function for uniform material. Field data were then used to extend the formulation to handle mixtures. A test with data from the Niobrara river showed a fair agreement between observed and predicted values.

The formulation derived from open channel data was found to show some consistency with the results of sediment–entraining density current experiments. The formulation can be expected to provide reasonable estimates of sediment entrainment by turbidity currents.

8.2.6 Modeling Considerations

The observations made during the experiments suggest that the similarity assumption used in the development of the integral model for mixtures is in most cases a good approximation.

The evaluation of shape factors showed that the top–hat or slab assumption is a crude but reasonable approximation, particularly if the size range of the suspended sediment is not too wide. Some indication of the error involved in this approximation is provided by Henderson–Sellers (1981) for the case of a plume.

The analysis of the sediment concentration profiles for different grain sizes produced relationships that cannot be considered universal. They can, however, be expected to be representative of turbidity currents in natural environments.

The one–dimensional model for steady, spatially developing turbidity currents developed herein can be used to predict the downstream variation of flow parameters, suspended grain size, and turbidite thickness. The data collected in the experiments could be used to test and calibrate the model. Once calibrated, the model could be verified at field scale. In Appendix B, the equations and input required to perform such computations are summarized.

REFERENCES

Akiyama, J., and Fukushima, Y. (1985). "Entrainment of noncohesive sediment into suspension." External Memorandum No. 195, St. Anthony Falls Hydraulic Laboratory, University of Minnesota.

Akiyama, J., and Stefan, H. (1985). "Turbidity current with erosion and deposition." *Journal of Hydraulic Engineering, ASCE*, Vol. 111, No. 12, pp. 1473–1496.

Akiyama, J., and Stefan, H. (1988). "Turbidity current simulation in a diverging channel." *Water Resources Research*, Vol. 24, No. 4, pp. 579–587.

Arita, M., Jirka, G., and Tamai, N. (1986). "Classification and mixing of two–dimensional buoyant surface discharges." *Journal of Hydraulic Research*, Vol. 24, No. 5, pp. 333–345.

Ashida, K., and Michiue, M. (1964). "Laboratory study of suspended load discharge in alluvial channels." Kyoto University, Disaster Prevention Research Institute.

Ashida, K., and Egashira, S. (1975). "Basic study of turbidity currents." *Proceedings JSCE*, No. 237, pp. 37–50.

Ashida, K., and Okabe, T. (1982). "On the calculation of method of the concentration of suspended sediment under non–equilibrium condition." *Proceedings 26th Conference on Hydraulics, JSCE*, pp. 153–158, (in Japanese).

Baddour, R. E. (1987). "Hydraulics of shallow and stratified mixing channel." *Journal of Hydraulic Engineering, ASCE*, Vol. 113, No. 5, pp. 630–645.

Bagnold, R. A. (1962). "Auto–suspension of transported sediment, turbidity currents." *Proceedings Royal Society London*, Ser. A, Vol. 205, pp. 315–319.

Barton, J. R., and Lin, P. N. (1955). "A study of the sediment transport in alluvial streams." Civil Engineering Dept., Colorado A & M College, Fort Collins, Colorado.

Bell, H. S. (1942). "Stratified flow in reservoirs and its use in prevention of silting." *Miscellaneous Publication No. 491, United States Department of Agriculture*, 46 p.

Bellaiche, G., *et al.* (1981). *Marine Geology*, Vol. 43, p. 75.

Benjamin, T. B., (1962). "Theory of the vortex breakdown phenomenon." *Journal of Fluid Mechanics*, Vol. 14, pp. 593–629.

Bouma, A. H. (1962). *Sedimentology of Some Flysh Deposits.* Elsevier, Amsterdam, 168 p.

Bouma, A. H., Normark, W. R., and Barnes, N. E., Eds. (1985). *Submarine Fans and Related Turbidite Systems*, Springer–Verlag, New York, pp. 29–34.

Bowen, A. J., Normark, W. R., and Piper, D. J. (1984). *Sedimentology.*

Britter, R. E., and Linden, P. F. (1980). "The motion of the front of a gravity current traveling down an incline." *Journal of Fluid Mechanics*, Vol. 99, pp. 531–543.

Brooks, N. H. (1954). *Laboratory studies of the mechanics of motion of streams flowing over a movable–bed of fine sand.* Ph.D. Thesis, California Institute of Technology, Pasadena.

Bruk, S. (1985). *Methods of Computing Sedimentation in Lakes and Reservoirs*, Unesco, Paris, 224 p.

Buhler, J., and Siegenthaler, C. (1986). "Self–preserving solutions for turbidity currents." *Acta Mechanica*, Vol. 63, pp. 217–233.

Celik, I., and Rodi, W. (1984). "A deposition entrainment model for suspended sediment transport." SFB 210/T/6, November, Universitat Karlsruhe.

Chikita, K. (1980). "Sedimentation by turbidity currents." *Journal of the Faculty of Science*, Hokkaido University, Ser. VII (Geophysics), Vol. VI, No. 2, pp. 255–300.

Chikita, K. (1989). "A field study on turbidity currents initiated from spring runoffs." *Water Resources Research*, Vol. 25, No. 2, pp. 257–271.

Chu, F. H., Pilkey, W. R., and Pilkey, O. H. (1979). "An analytical study of turbidity current steady flow." *Marine Geology*, Vol. 33, pp. 205–220.

Chu, V. H., Jirka, G. (1987). "Surface buoyant jets and plumes." In: *Encyclopedia of Fluid Mechanics*, Nicholas P. Cheremisinoff, Ed., Vol. 6, Chapter 25, pp. 1053–1084.

Colby, B. R., and Hembree, C. H. (1955). "Computations of total sediment discharge Niobrara River near Nebraska." *Water Supply Paper 57*, U. S. Geological Survey, Washington, D. C.

Coleman, N. L. (1969). "A new examination of sediment suspension in open channels." *Journal of Hydraulic Research*, Vol. 7, No. 1, pp. 67–82.

Coleman, N. L. (1981). "Velocity profiles with suspended sediment." *Journal of Hydraulic Research*, Vol. 19, No. 3, pp. 211–229.

Dengler, A. T., Wilde, P., Noda, E. K., and Normark, W. R. (1984). "Turbidity currents generated by Hurricane Iwa." *Geo–Marine Letters*, Vol. 4, pp. 5–11.

Dietrich, E. W. (1982). "Settling velocity of natural particles." *Water Resources Research*, Vol. 18, No. 6, pp. 1626–1982.

Einstein, H. A. (1950). "The bed load function for sediment transportation in open channels." Technical Bulletin 1026, U. S. Department of Agriculture, Soil Conservation Service, Washington, D. C.

Einstein, H. A., and Barbarossa, N. (1952). "River channel roughness." *Transactions, ASCE*, Vol. 117, Paper No. 2528, pp. 1121–1146.

Ellison, T. H., and Turner, J. S. (1959). "Turbulent entrainment in stratified flows." *Journal of Fluid Mechanics*, Vol. 6, pp. 423–448.

El–Robrini, M., Gennesseaux, M., and Mauffret, A. (1985). "Consequences of the El–Asnam Earthquakes: Turbidity currents and slumps an the algerian margin (Western Mediterranean)." *Geo–Marine Letters*, Vol. 5, pp. 171–176.

Engelund, F., and Hansen, E. (1967). "A monograph on sediment transport in alluvial streams." Copenhagen: *Teknisk Vorlang.*

Engelund, F. (1970). "Instability of erodible beds." *Journal of Fluid Mechanics*, Vol. 42, Part 2, pp. 225–244.

Engelund, F., and Fredsoe, J. (1976). "A sediment transport model for straight alluvial channels." *Nordic Hydrology*, Vol. 7, pp. 293–306.

Engelund, F., and Fredsoe, J. (1982). "Hydraulic theory of alluvial rivers." *Advances in Hydroscience*, Vol. 13, pp. 187–215.

Estourgie, A. L. P. (1988). "Theory and practice of water injection dredging." *Terra et Aqua*, No. 38, December, pp. 21–28.

Fan, J. (1985). "Methods of preserving reservoir capacity." In: *Methods of Computing Sedimentation in Lakes and Reservoirs*, S. Bruk, Ed., Unesco, Paris, pp. 65–164.

Fietz, T. R., and Wood, I. R. (1967). "Three dimensional density current." *Journal of the Hydraulic Division*, ASCE, Vol. 93, No. HY6, pp. 1–23.

Forel, F. A. (1885). "Les ravins sous–lacustres des fleuves glaciaires." *Comptes Rendus, Acad. Sci.*, Paris, Vol. 101, pp. 725–728.

Fukuoka, S., and Fukushima, Y. (1980). "Mechanics of gravity currents advancing into a stratified reservoir." *Proceedings*, JSCE, No. 293, pp. 65–77. (in Japanese)

Fukushima, Y., Parker, G., and Pantin, H. (1985). "Prediction of ignitive turbidity currents in Scripps submarine canyon." In press, *Marine Geology.*

Garcia, M. H. (1985). *Experimental study of turbidity currents.* M. S. Thesis, Department of Civil and Mineral Engineering, University of Minnesota, 138 p.

Graf, E. H. (1971). *Hydraulics of sediment transport.* McGraw–Hill Book Co., Inc., New York, 513 p.

Graf, W. H. (1983). "The behavior of silt–laden currents." *Water Power and Dam Construction*, September.

Grover, N. C., and Howard, C. S. (1938). "The passage of turbid water through Lake Mead." *Transactions, ASCE*, Vol. 103, pp. 720–790.

Hakanson, L., and Jansson, M. (1983). *Principles of Lake Sedimentology*, Springer–Verlag, New York, 316 p.

Harleman, D. R. F. (1961). "Stratified flow." In: *Handbook of Fluid Dynamics*, V. L. Streeter, Ed., McGraw–Hill, Chapter 26, pp. 2–21.

Hay, A. E., Burling, R. W., and Murray, J. W. (1982). "Remote acoustic detection of a turbidity current surge." *Science*, Vol. 217, pp. 833–835.

Hay, A. E. (1983). *Journal of Geophysical Research*, Vol. 88, pp. 751–754.

Hay, A. E. (1987a). "Turbidity currents and submarine channel formation in Rupert Inlet, British Columbia, 1. Surge observations." *Journal of Geophysical Research*, Vol. 92, No. C3, pp. 2875–2881.

Hay, A. E. (1987b). "Turbidity currents and submarine channel formation in Rupert Inlet, British Columbia, 2. The roles of continuous and surge–type flow." *Journal of Geophysical Research*, Vol. 92, No. C3, pp. 2883–2900.

Heezen, B. C., and Ewing, M. (1952). "Turbidity currents and submarine slumps and the 1929 Grand Banks earthquake." *American Journal of Science*, Vol. 250, pp. 849–873.

Henderson, F. M. (1966). *Open Channel Flow*, McMillan Co., New York, 522 pp.

Henderson–Sellers, B. (1981). "Shape constants for plume models." *Boundary Layer Meteorology*, Vol. 21, pp. 105–114.

Hinze, J. O. (1960). "On the hydrodynamics of turbidity currents." *Geologie en Mijnbouw*, Vol. 39e, pp. 18–25.

Howard, C. S. (1953). "Density currents in Lake Meed." *Proceedings Minnesota International Hydraulics Convention*, pp. 355–368.

Ikeda, S., and Asaeda, T. (1983). "Sediment suspension with rippled bed." *Proceedings, ASCE*, Vol. 109, No. 3, pp. 409–423.

Ikeda, S., and Nishimura, T. (1985). "Bed topography in bends of sand–silt rivers." *Journal of Hydraulic Engineering, ASCE*, Vol. 111, No. 11, pp. 1397–1411.

Inman, D. L., Nordstrom, C. E., and Flick, R. E. (1976). "Currents in submarine canyons: An air–sea–land interaction." *Annual Review of Fluid Mechanics*, pp. 275–310.

Ismail, H. M. (1951). "Turbulent transfer mechanism and suspended sediments in closed channels." *Proceedings, ASCE*, Vol. 77, Separate No. 56, pp. 1–26.

Itakura, T., and Kishi, T. (1980). "Open channel flow with suspended sediments." *Journal of the Hydraulics Division*, Vol. 106, No. HY8, pp. 1325–1343.

Jenkins, B. S. (1970). "Density currents and turbidity currents in waste disposal in the ocean. A literature review." Report No. 119, Water Research Laboratory, The University of New South Wales, Australia.

Johnson, M. A. (1962). "Physical oceanography: turbidity currents." *Sci. Prog.*, London, Vol. 50, No. 193, pp. 257–273.

Jopling, A. V., and Richardson, E. V. (1966). "Backset bedding developed in shooting flow in laboratory experiments." *Journal of Sedimentary Petrology*, Vol. 36, pp. 821–824.

Kalinske, A. A., and Pien, C. L. (1943). "Experiments on eddy–diffusion and suspended–material transportation in open channels." *Transactions*, AGU, pp. 530–534.

Kikkawa, H., and Ishikawa, T. (1979). "Resistance of flow over dunes and ripples." *Transactions, JSCE*, Vol. 11, pp. 123–125.

Komar, P. D. (1971). "Hydraulic jumps in turbidity currents." *Bulletin Geological Society of America*, Vol. 82, pp. 1477–1488.

Komar, P. D. (1977). "Computer simulation of turbidity current flow and the study of deep–sea channels and fan sedimentation." In: *The Sea: Ideas and Observations on Progress in the Study of the Sea*, E. D. Golbert, Ed., John Wiley and Sons Inc.

Kuenen, P. H., and Migliorini, C. I. (1950). "Turbidity currents as a cause of graded bedding." *Journal of Geology*, Vol. 58, No. 2, pp. 91–127.

Lambert, A. M., Kelts, K. R., and Marshall, N. F. (1976). "Measurements of density underflows from Walensee, Switzerland." *Sedimentology*, Vol. 23, pp. 87–105.

Lambert, A. M. (1982). "Turbidity currents from the Rhine River on the bottom of Lake Constance, Wasserwirtschaft, Vol. 72, No. 4, pp. 1–4.

Lambert, A., and Giovanoli, F. (1987). "Records of channelized turbidity currents in Lake Geneva (Rhone Delta)." IAHR Congress, Lausanne.

Lofquist, K. (1960). "Flow and stress near an interface between stratified liquids." *The Physics of Fluids*. Vol. 3, Number 2, March–April.

Luthi, S. (1980). "Some new aspects of two–dimensional turbidity currents." *Sedimentology*, Vol. 28, pp. 97–105.

Luthi, S. (1981). "Experiments on non–channelized turbidity currents and their deposits." *Marine Geology*, Vol. 40, M 59–68.

Lyn, D. A. (1986). "Turbulence and turbulent transport in sediment–laden open–channel flows." Report No. KH–R–49, W. M. Keck Laboratory of Hydraulics and Water Resources, California Institute of Technology.

Menard, H. W. (1964). *Marine Geology of the Pacific*, McGraw–Hill, New York.

Michon, X., Goddet, J., and Bonnefille, R. (1955). "Etude theorique et experimentale des courants de densite." Tomes I, II. Lab. Natl. Hydraulique, Chatou, France.

Middleton, G. V. (1966a). "Small–scale models of turbidity currents and the criterion for auto–suspension." *Journal of Sedimentary Petrology*, Vol. 36, No. 1, pp. 202–208.

Middleton, G. V. (1966b). "Experiments on density and turbidity currents, I. Motion of the head." *Canadian Journal of Earth Sciences*, Vol. 3, pp. 523–546.

Middleton, G. V. (1966c). "Experiments on density and turbidity currents, II. Uniform flow of density currents." *Canadian Journal of Earth Sciences*, Vol. 3, pp. 627–637.

Middleton, G. V. (1967). "Experiments on density and turbidity currents, III. Deposition of sediment." *Canadian Journal of Earth Sciences*, Vol. 4, pp. 475–505.

Middleton, G. V., and Neal, W. J. (1989). "Experiments on the thickness of beds deposited by turbidity currents." *Journal of Sedimentary Petrology*, Vol. 59, No. 2, pp. 297–307.

Monin, A. S., and Yaglom, A. M. (1971). "Statistical fluid mechanics." *The M.I.T. Press*, Cambridge, Mass.

Mutti, E. (1977). "Distinctive thin–bedded turbidite facies and related depositional environments in the Eocene Hecho Group (South–central Pyrenees, Spain)." *Sedimentology*, Vol. 24, pp. 107–131.

Mutti, E., Nilson, T., and Ricci–Lucci, F. (1978). "Outer fan depositional lobes of the Laga formation (Upper Miocene and Lower Pliocene), east central Italy." In: *Sedimentation in Submarine Canyons, Fans, and Trenches.* Dowden, Hutchinson, and Ross, Inc., pp. 210–223.

Nelson, J. M., and Smith, J. D. (1989). "Flow in meandering channels with natural topography." In: *River Meandering*, S. Ikeda, and G. Parker, Eds., Water Resources Monograph No. 12, AGU, pp. 69–102.

Niedoroda, A. W., Pitman, J. R., and Philpot, T. A. (1985). "OTEC project area survey." *Proceedings 17th Offshore Tech. Conf.*, Houston, Texas, OTC4907, Vol. 2, pp. 87–95.

Nordin, C. F., and Dempster, G. R. (1963). "Vertical distribution of velocity and suspended sediment middle Rio Grande New Mexico." *U. S. Geological Survey*, Professional Paper 462–B.

Normark, W. R. (1970). "Growth patterns of deep–sea fans." *Am. Assoc. Petrol. Geol. Bull.*, Vol. 54, pp. 2170–2195.

Normark, W. R., and Dickson, F. H. (1976). "Man–made turbidity currents in Lake Superior." *Sedimentology*, Vol. 23, pp. 815–831.

Normark, W. R., and Dickson, F. H. (1976). "Sublacustrine fan morphology in Lake Superior." *The American Association of Petroleum Geologists Bulletin*, Vol. 60, No. 7, pp. 1021–1036.

Normark, W. R., Mutti, E., and Bouma, A. H. (1983/1984). "Problems in turbidite research: A need for COMFAN." *Geo–Marine Letters*, Vol. 3, pp. 53–56.

Pallesen, T. R. (1983). "Turbidity currents." Institute of Hydrodynamics and Hydraulic Engineering. Technical University of Denmark. Series Paper 32.

Pantin, H. M. (1979). "Interaction between velocity and effective density in turbidity flow: Phase–plane analysis, with criteria for autosuspension." *Marine Geology*, Vol. 31, pp. 59–99.

Parker, G. (1978). "Self–formed straight rivers with equilibrium banks and mobile bed. Part 1. The sand–silt river." *Journal of Fluid Mechanics*, Vol. 89, Part 1, pp. 109–125.

Parker, G. (1982). "Conditions for the ignition of catastrophically erosive turbidity currents." *Marine Geology*, Vol. 46, pp. 307–327.

Parker, G., Fukushima, Y., and Pantin, H. M. (1986). "Self–accelerating turbidity currents." *Journal of Fluid Mechanics*. Vol. 171, pp. 145–181.

Parker, G., Garcia, M., Fukushima, Y., and Yu, W. (1987). "Experiments on turbidity currents over an erodible bed." *Journal of Hydraulic Research*, Vol. 25, No. 1, pp. 123–147.

Pedersen, F. B. (1977). "The entrainment function for gradually varying two–layered stratified flow." Progress Report No. 44, Technical University of Denmark, pp. 3–12.

Pedersen, F. B. (1980). "A monograph on turbulent entrainment and friction in the two–layer stratified flow." Institute of Hydrodynamics and Hydraulic Engineering. Technical University of Denmark. Series Paper No. 25.

Pettijohn, F. J., Potter, P. E., and Siever, R. (1987). *Sand and Sandstone*, Second Edition, Springer–Verlag, New York, 553 p.

Piper, D. J. W. (1970). "Transport and depositon of holocene sediment on La Jolla deep–sea fan, California." *Marine Geology*, Vol. 8, pp. 211–227.

Plapp, J. E., and Mitchell, J. P. (1960). "A hydrodynamic theory of turbidity currents." *Journal Geophys. Res.*, Vol. 65, No. 3, pp. 983–992.

Prior, D. B., Bornhold, B. D., Wiseman, Jr., W. J., and Lowe, D. R. (1987). "Turbidity current activity in a British Columbia Fjord." *Science*, Vol. 237, pp. 1330–1333.

Rajaratman, N. (1967). "Hydraulic jumps." In: *Advances in Hydroscience*, V. T. Chow, Ed., Vol. 4, pp. 197–280.

Rajaratnam, N. (1976). "Turbulent Jets." Elsevier, Amsterdan, 301 p.

Rajaratman, N., Tovell, D., and Loewen, M. (1988). "Internal jumps in two–layer stratified flows." Technical Report (WRE–88–4), Department of Civil Engineering, University of Alberta, Canada.

Ravenne, C., and Beghin, P. (1983). "Apport des experiences en canal a l'interpretation sedimentologique des depots de cones detritiques sous–marins." *Revue de L'Institut Francais du Petrole*, Vol. 38, No. 3, pp. 279–297.

Schlichting, H. (1979). *Boundary Layer Theory*, Seventh edition, McGraw Hill, New York, 817 p.

Seymour, R. J. (1986). "Nearshore auto–suspending turbidity flows." *Ocean Engineering*, Vol. 13, No. 5, pp. 435–447.

Shanmugam, G., and Moiola, R. J. (1985). "Submarine Fan Models: Problems and Solutions." In: *Submarine Fans and Related Turbidite Systems*, A. H. Bouma, W. R. Normark, N. E. Barnes, Eds., Springer–Verlag, New York, pp. 29–34.

Shepard, F. P., and Dill, R. F. (1966). *Submarine Canyons and Other Sea Valleys*, Rand McNally, Chicago.

Shepard, F. P., Marshall, N. F., and McLoughlin, P. A. (1974). "Currents in submarine canyons." *Deep–sea Research*, Vol. 21, pp. 19–24.

Siegenthaler, C., and Buhler, J. (1985). "The kinematics of turbulent suspension currents (turbidity currents) on inclined boundaries." *Marine Geology*, Vol. 64, pp. 19–40.

Siegenthaler, C., and Buhler, J. (1986). "The reconstruction of the paleo–slope of turbidity currents, based on simple hydromechanical parameters of the deposit." *Acta Mechanica*, Vol. 63, pp. 235–244.

Simpson, J. E., and Britter, R. E. (1979). "The dynamics of the head of a gravity current advancing over a horizontal surface." *Journal Fluid Mechanics*, Vol. 94, pp. 477–495.

Simpson, J. E. (1982). "Gravity currents in the laboratory. atmosphere, and ocean." *Annual Review of Fluid Mechanics*, Vol. 14, pp. 213–234.

Smith, J. D., and McLean, S. R. (1977). "Spatially averaged flow over a wavy surface." *Journal of Geophysical Research*, Vol. 82, No. 12, pp. 1735–1746.

Stacey, M. W., and Bowen, A. J. (1988a). "The vertical structure of density and turbidity currents: Theory and observations." *Journal of Geophysical Research*, Vol. 93, No. C4, pp. 3528–3542.

Stacey, M. W., and Bowen, A. J. (1988b). "The vertical structure of turbidity currents and a necessary condition for self–maintenance." *Journal of Geophysical Research*, Vol. 93, No. C4, pp. 3543–3553.

Stefan, H., and Hayakawa, N. (1972). "Mixing induced by an internal hydraulic jump." *Water Resources Bulletin, AWRA*, Vol. 8, No. 3, pp. 531–545.

Stefan, H. (1973). "High concentration turbidity currents in reservoirs." *Proceedings 15th Conference*, IAHR, Vol. 1, pp. 341–352.

Stow, D. A. V., and Bowen, A. J. (1980). "A physical model for the transport and sorting of fine–grained sediment turbidity currents." *Sedimentology*, Vol. 27, pp. 31–46.

Straub. L. G., Anderson, A. G., and Flammer, G. H. (1958). "Experiments on the influence of the temperature on sediment load." MRD Sediment Series No. 10, St. Anthony Falls Hydraulic Laboratory, Minneapolis, Minnesota.

Tesaker, E. (1969). "Uniform turbidity currents." Thesis in Civil Engineering. The Technical University of Norway, 200 p.

Turner, J. S. (1973). *Buoyancy Effects in Fluids.* Cambridge University Press, Cambridge, U. K., 367 p.

Van Andel, T. H., and Komar, P. D. (1969). "Ponded sediments of the Mid–Atlantic Ridge between 22° and 23° North Latitude." *Geological Society of America Bulletin*, Vol. 80, pp. 1163–1190.

Van Rijn, L. C. (1984). "Sediment transport, Part II: Suspended load transport." *Journal of Hydraulic Engineering*, Vol. 110, No. 11, pp. 1613–1641.

Vanoni, V. A. (1974). "Factors determining bed forms of alluvial streams," ASCE, *Jour. of Hydraulic Engineering*, Vol. 100, No. 3, pp. 363–377.

Vanoni, V. A. (1975). *Sedimentation Engineering*, ASCE, New York, 745 p.

Vanoni, V. A., and Nomicos, G. N. (1960). "Resistance properties of sediment laden streams." *Transactions*, ASCE, Vol. 125, Paper No. 3055, pp. 1140–1175.

Walker, R. G. (1980). *Facies Models*, Geoscience Canada, Reprint Series 1, Geological Association of Canada.

Weirich, F. H. (1984). "Turbidity currents: Monitoring their occurrence and movement with a three–dimensional sensor network." *Science*, Vol. 224, pp. 384–387.

Weirich, F. H. (1986). "The record of density–induced underflows in a glacial lake." *Sedimentology*, Vol. 33, pp. 261–277.

Wilkinson, D. L., and Wood, I. R. (1971). "A rapidly varied flow phenomenon in a two–layer flow." *Journal of Fluid Mechanics*, Vol. 47, Part 2, pp. 241–256.

Wood, I. R. (1967). "Horizontal two–dimensional density current." *Journal of the Hydraulics Division, ASCE*, Vol.93, No. HY2, pp. 35–42.

Wood, I. R., and Simpson, J. E. (1984). "Jumps in layered miscible fluids." *Journal of Fluid Mechanics*, Vol. 140, pp. 329–342.

Wood, W. L., Davis, S. E., Meadows, G. A., Weishar, L. L., and Lesht, B. M. (1984). "High velocity bottom boundary layer flow in the head of a submarine canyon." In preparation.

Yalin, S. (1964). "On the average velocity of flow over a movable bed." *La Houille Blanche*, No. 64, pp. 45–51.

Yih, C. S., and Guha, C. R. (1955). "Hydraulic jump in a fluid system of two layers." *Tellus*, Vol. 7, No. 3, pp. 358–366.

APPENDIX A

In this appendix, the laboratory and field data used in Chapter 7 are presented in tabulated form.

OPEN CHANNEL SUSPENSIONS

Author	Run	H (cm)	U (cm/s)	Slope	Rb (cm)	U* (cm/s)	nU (cm2/s)	Dsg (cm)	Re	Vs (cm/s)	U*' (cm/s)	Ca	U*'/Vs	Zu
Ashida	1	4.20	62.60	0.00400	3.47	3.69	0.01000	0.016	8.14	1.80	3.56	0.00400	1.98	6.96
Michiue	2	7.05	63.80	0.00230	5.21	3.43	0.01000	0.016	8.14	1.80	3.41	0.00377	1.89	6.67
Ashida	7	4.60	40.00	0.00310	3.52	3.27	0.01000	0.017	8.50	1.85	2.46	0.00027	1.33	4.80
Okabe	8	4.10	35.40	0.00310	3.22	3.13	0.01000	0.017	8.50	1.85	2.24	0.00042	1.21	4.37
Barton	28	14.63	42.37	0.00116	13.72	3.95	0.00914	0.018	10.62	2.00	2.33	0.00094	1.17	4.81
Lin	32	22.25	43.28	0.00082	20.36	4.04	0.00914	0.018	10.62	2.00	2.29	0.00038	1.15	4.73
	34	42.06	48.77	0.00065	27.71	4.20	0.00914	0.018	10.62	2.00	2.45	0.00036	1.23	5.06
	33	31.39	53.34	0.00061	26.36	3.97	0.00914	0.018	10.62	2.00	2.62	0.00045	1.31	5.41
	29	18.29	73.46	0.00121	15.82	4.33	0.00914	0.018	10.62	2.00	3.62	0.00350	1.81	7.47
	26	21.03	78.64	0.00125	17.95	4.69	0.00914	0.018	10.62	2.00	3.84	0.00792	1.92	7.92
	25	23.77	79.25	0.00124	20.18	4.95	0.00914	0.018	10.62	2.00	3.86	0.00380	1.93	7.97
	18	21.03	81.69	0.00156	18.29	5.29	0.00914	0.018	10.62	2.00	4.05	0.00130	2.03	8.36
	20	18.59	83.51	0.00166	16.22	5.14	0.00914	0.018	10.62	2.00	4.14	0.00181	2.07	8.54
	23	19.81	86.56	0.00183	17.31	5.57	0.00914	0.018	10.62	2.00	4.31	0.00123	2.16	8.89
	22	23.16	91.13	0.00170	21.28	5.95	0.00914	0.018	10.62	2.00	4.45	0.01500	2.23	9.18
	19	22.86	91.44	0.00167	19.48	5.64	0.00914	0.018	10.62	2.00	4.46	0.00147	2.23	9.20
	35	17.07	98.14	0.00160	14.17	4.71	0.00914	0.018	10.62	2.00	4.70	0.00430	2.35	9.70
	36	16.15	109.73	0.00210	13.65	5.30	0.00914	0.018	10.62	2.00	5.28	0.00830	2.64	10.90
Brooks	7	7.40	62.18	0.00210	5.18	3.26	0.00778	0.015	9.49	1.70	3.26	0.00650	1.92	7.40
	21	7.20	64.00	0.00225	5.06	3.34	0.00893	0.009	3.84	0.80	3.34	0.01000	4.18	9.36
	29	8.50	64.92	0.00185	5.42	3.13	0.00890	0.009	3.86	0.80	3.13	0.00800	3.91	8.80
Coleman	1	12.19	60.65	0.00160	8.84	3.72	0.00836	0.015	8.84	1.75	3.72	0.00283	2.13	7.86
(1968)	2	12.19	78.64	0.00308	9.66	5.40	0.00836	0.015	8.84	1.75	5.40	0.00570	3.09	11.41
	3	12.19	96.01	0.00517	9.66	7.00	0.00836	0.015	8.84	1.75	7.00	0.02100	4.00	14.79
	4	18.29	53.34	0.00085	11.20	3.05	0.00836	0.015	8.84	1.75	3.05	0.00088	1.74	6.44
	5	18.29	62.18	0.00120	11.62	3.70	0.00836	0.015	8.84	1.75	3.70	0.00410	2.11	7.82
	6	18.29	78.64	0.00180	11.55	4.51	0.00836	0.015	8.84	1.75	4.51	0.00940	2.58	9.53
	7	24.38	53.64	0.00067	12.70	2.89	0.00836	0.015	8.84	1.75	2.89	0.00080	1.65	6.11
	8	24.38	64.00	0.00085	12.17	3.18	0.00836	0.015	8.84	1.75	3.18	0.00260	1.82	6.72
	9	12.19	68.88	0.00144	7.73	3.30	0.00820	0.021	14.92	2.80	3.30	0.00170	1.18	5.97
	10	12.19	76.50	0.00420	10.19	6.48	0.00820	0.021	14.92	2.80	6.48	0.00660	2.31	11.71
	11	12.19	97.23	0.00420	9.24	6.18	0.00820	0.021	14.92	2.80	6.18	0.02000	2.21	11.17
	12	18.29	52.12	0.00075	10.67	2.80	0.00820	0.021	14.92	2.80	2.80	0.00057	1.00	5.06
	13	18.29	52.73	0.00135	13.58	4.24	0.00820	0.021	14.92	2.80	4.24	0.00340	1.51	7.66
	14	18.29	80.16	0.00156	10.43	4.00	0.00820	0.021	14.92	2.80	4.00	0.00500	1.43	7.23
	15	24.38	53.34	0.00065	12.85	2.86	0.00820	0.021	14.92	2.80	2.86	0.00048	1.02	5.17
	16	24.38	56.39	0.00082	14.20	3.38	0.00820	0.021	14.92	2.80	3.38	0.00190	1.21	6.11
Coleman	A20	17.00	107.56	0.00200	7.80	3.91	0.00916	0.011	4.72	0.90	3.91	0.01890	4.34	11.02
(1981)	B11	17.20	106.31	0.00200	8.02	3.96	0.00916	0.021	13.36	2.80	3.96	0.00961	1.41	6.70
	C9	17.10	106.93	0.00220	7.84	4.11	0.00940	0.042	36.82	6.00	4.11	0.00199	0.69	5.96
Ismail	73	4.15	51.50	0.00277	3.35	3.02	0.01110	0.010	3.62	0.81	2.80	0.00900	3.46	7.48
	74	3.50	71.90	0.00415	2.74	3.34	0.01020	0.010	3.94	0.88	3.34	0.02260	3.80	8.64
	75	3.41	90.20	0.00591	2.63	3.90	0.01110	0.010	3.62	0.85	3.90	0.04500	4.59	9.93
	76	3.20	108.20	0.00827	2.46	4.47	0.01030	0.010	3.90	0.87	4.47	0.03770	5.14	11.63
	77	3.48	127.40	0.01150	3.11	5.92	0.01000	0.010	4.02	0.92	5.92	0.03020	6.43	14.83
	78	3.66	149.70	0.01487	2.81	6.39	0.01010	0.010	3.98	0.88	6.39	0.02530	7.26	16.63
Kalinske	1	15.85	86.75	0.00150	11.80	4.16	0.00914	0.018	10.62	2.00	4.16	0.00213	2.08	8.58
Pien	2	18.90	99.37	0.00400	8.67	5.83	0.01100	0.018	8.83	2.00	5.20	0.00221	2.60	9.61
Lyn	1565	6.45	62.80	0.00244	4.70	3.35	0.00991	0.015	7.45	1.60	3.35	0.00470	2.09	6.99
	1965	6.51	63.60	0.00251	4.71	3.40	0.00977	0.019	10.78	2.30	3.40	0.00460	1.48	6.16
	2565	6.54	69.20	0.00296	4.77	3.72	0.00970	0.024	15.41	3.10	3.72	0.00390	1.20	6.19
	1957	5.72	64.60	0.00295	4.29	3.52	0.00980	0.019	10.75	2.30	3.52	0.00400	1.53	6.36
Straub	1	7.47	62.20	0.00235	5.65	3.61	0.00880	0.016	9.51	1.60	3.02	0.00072	1.89	7.29
Anderson	2	7.25	64.00	0.00256	5.50	3.71	0.00890	0.016	8.45	1.50	3.12	0.00178	2.08	7.48
Flammer	3	7.07	65.50	0.00282	5.39	3.86	0.01170	0.016	7.15	1.30	3.23	0.00211	2.48	8.09
	4	7.04	65.80	0.00324	5.51	4.18	0.01370	0.016	6.11	1.20	3.32	0.00269	2.77	8.20
	5	6.86	67.70	0.00326	5.26	4.10	0.01600	0.016	5.23	1.04	3.42	0.00384	3.29	8.87
	6	6.80	68.30	0.00362	5.29	4.33	0.01820	0.016	4.60	0.94	3.52	0.00397	3.74	9.36
Vanoni	1	8.66	37.49	0.00250	7.55	4.30	0.00898	0.011	4.82	0.95	2.05	0.00570	2.17	5.57
Nomicos	3	7.44	61.57	0.00200	5.11	3.16	0.00898	0.011	4.82	0.95	2.89	0.00940	3.06	7.86
	5	7.83	68.88	0.00206	4.99	3.17	0.00898	0.011	4.82	0.95	3.16	0.00940	3.34	8.59
	7	7.77	69.49	0.00258	5.41	3.70	0.00898	0.016	9.15	1.89	3.30	0.00260	1.75	6.59

		H (cm)	U (cm/s)	Slope	D50 (cm)	U* (cm/s)	U*' (cm/s)	T (C)	Nu (cm2/s)	Dsg=0.009cm Cae	Cae/p	Rp	Vs (cm/s)	Zm	Dsg=0.018cm Cae	Cae/p	Rp	Vs (cm/s)	Zm	Dsg=0.035cm Cae	Cae/p	Rp	Vs (cm/s)	Zm
Rio Grande (Nordin and Dempster, 1963)																								
Bernalillo																								
6-2-53	A2	78.0	94.8	0.00083	0.032	7.96	4.53	21.7	0.00976	0.000326	0.00959	3.4	0.63	11.7	0.000328	0.00138	9.7	1.87	8.4	0.000108	0.00018	27.5	4.84	7.0
6-4-53	A2	75.6	95.1	0.00083	0.033	7.83	4.55	16.7	0.01102	0.000213	0.00666	3.0	0.57	12.0	0.000204	0.00067	8.6	1.73	8.4	0.000025	0.00000	24.3	4.55	6.9
	A	51.5	89.6	0.00083	0.030	6.46	4.30	18.9	0.01043	0.000287	0.00574	3.2	0.59	11.4	0.000396	0.00147	9.1	1.79	8.1	0.000057	0.00000	25.7	4.68	6.7
	C	71.9	71.0	0.00083	0.042	7.62	3.69	21.7	0.00976	0.000162	0.01080	3.4	0.63	9.0	0.000193	0.00128	9.7	1.87	6.5	0.000067	0.00016	27.5	4.84	5.4
	E	75.3	82.0	0.00083	0.026	7.80	3.94	21.1	0.00989	0.000138	0.00354	3.4	0.62	10.6	0.000262	0.00067	9.6	1.86	7.6	0.000023	0.00000	27.1	4.81	6.3
4-13-54	B	43.3	59.7	0.00082	0.026	6.07	3.08	16.7	0.01102	0.000381	0.00320	3.0	0.57	8.5	0.000536	0.00161	8.6	1.73	6.0	0.000082	0.00016	24.3	4.55	4.9
	C	44.2	66.1	0.00082	0.037	6.16	3.46	17.2	0.01088	0.000196	0.00377	3.1	0.57	8.9	0.000299	0.00081	8.7	1.74	6.3	0.000020	0.00000	24.6	4.58	5.1
	D	46.6	57.6	0.00082	0.029	6.28	3.02	17.2	0.01088	0.000275	0.00437	3.1	0.57	8.1	0.000381	0.00117	8.7	1.74	5.7	0.000128	0.00029	24.6	4.58	4.7
	E	60.4	70.1	0.00083	0.031	7.13	3.55	16.7	0.01102	0.000237	0.00484	3.0	0.57	9.5	0.000382	0.00129	8.6	1.73	6.7	0.000185	0.00041	24.3	4.55	5.4
5-19-54	B	40.5	76.5	0.00086	0.031	5.85	3.81	20.0	0.01016	0.000236	0.00513	3.3	0.61	10.0	0.000338	0.00116	9.3	1.83	7.1	0.000123	0.00026	26.4	4.74	5.9
	C	59.7	57.9	0.00086	0.027	7.10	3.01	27.8	0.00850	0.000283	0.00786	3.9	0.70	7.8	0.000343	0.00130	11.1	2.05	5.7	0.000117	0.00026	31.5	5.19	4.9
	D	45.7	71.6	0.00086	0.031	6.22	3.62	27.8	0.00850	0.000174	0.00561	3.9	0.70	9.1	0.000143	0.00046	11.1	2.05	6.7	0.000021	0.00000	31.5	5.19	5.7
	E	59.4	83.8	0.00086	0.030	7.10	4.09	21.1	0.00989	0.000270	0.00643	3.4	0.62	10.7	0.000381	0.00120	9.6	1.86	7.7	0.000123	0.00023	27.1	4.81	6.4
Socorro																								
4-16-54	A1	46.6	79.2	0.00076	0.017	5.43	3.60	12.8	0.01220	0.000611	0.00466	2.7	0.52	11.1	0.000849	0.00165	7.8	1.61	7.7	0.000000	0.00000	22.0	4.31	6.2
	A2	30.5	88.4	0.00076	0.017	4.76	4.00	14.4	0.01169	0.000702	0.00447	2.9	0.54	12.2	0.000966	0.00143	8.1	1.66	8.5	0.000000	0.00000	22.9	4.41	6.9
	B	20.1	71.9	0.00098	0.016	4.38	3.44	20.0	0.01016	0.000615	0.00312	3.3	0.61	10.3	0.000354	0.00058	9.3	1.83	7.3	0.000000	0.00000	26.4	4.74	6.1
	B1	43.9	73.2	0.00098	0.021	6.49	3.59	22.2	0.00964	0.000574	0.00692	3.5	0.63	10.0	0.000406	0.00071	9.8	1.89	7.2	0.000073	0.00027	27.8	4.87	6.0
5-21-54	A1	35.4	105.2	0.00084	0.019	5.39	4.70	20.6	0.01001	0.001170	0.00873	3.3	0.61	13.5	0.001550	0.00259	9.5	1.84	9.7	0.000000	0.00000	26.7	4.78	8.0
	A2	36.5	97.8	0.00084	0.016	5.52	4.36	19.4	0.01031	0.001960	0.01170	3.2	0.60	13.1	0.002750	0.00413	9.2	1.81	9.3	0.000000	0.00000	26.0	4.71	7.7
	B	32.6	76.2	0.00100	0.015	5.67	3.59	22.8	0.00951	0.000509	0.00251	3.5	0.64	10.7	0.000370	0.00061	10.0	1.91	7.7	0.000000	0.00000	28.2	4.91	6.4
	B1	27.7	76.5	0.00100	0.019	5.21	3.69	23.9	0.00927	0.000996	0.01110	3.6	0.65	10.4	0.002110	0.00311	10.2	1.94	7.6	0.000000	0.00000	28.9	4.97	6.3
8-17-54	A1	70.1	185.0	0.00086	0.024	7.68	7.65	22.2	0.00964	0.005060	0.06930	3.5	0.63	20.8	0.008300	0.02030	9.8	1.89	15.0	0.002640	0.00644	27.8	4.87	12.5
	A2	72.5	194.2	0.00086	0.025	7.80	7.80	24.4	0.00916	0.008410	0.16500	3.6	0.66	20.9	0.020800	0.05120	10.3	1.95	15.1	0.004340	0.00070	29.2	5.00	12.7
Niobrara (Colby and Hembree, 1955)																								
3-3-50	97	45.7	119.8	0.00170	0.029	8.72	5.81	5.0	0.01520	0.000204	0.00510	2.2	0.43	11.3	0.000547	0.00144	6.2	1.38	7.9	0.000102	0.00030	17.6	3.81	6.7
	109	51.8	144.2	0.00170	0.029	9.29	6.75	5.0	0.01520	0.000445	0.01110	2.2	0.43	13.1	0.002410	0.00634	6.2	1.38	9.1	0.000506	0.00149	17.6	3.81	7.8
	120	54.9	137.2	0.00170	0.029	9.56	6.49	5.0	0.01520	0.000252	0.00630	2.2	0.43	12.6	0.000943	0.00248	6.2	1.38	8.8	0.000325	0.00096	17.6	3.81	7.5
	129	67.1	127.4	0.00170	0.029	10.60	6.11	5.0	0.01520	0.000182	0.00460	2.2	0.43	11.8	0.000426	0.00112	6.2	1.38	8.3	0.000102	0.00030	17.6	3.81	7.1
	141	73.2	86.6	0.00170	0.029	11.00	4.48	5.0	0.01520	0.000175	0.00440	2.2	0.43	8.7	0.000396	0.00104	6.2	1.38	6.1	0.000000	0.00000	17.6	3.81	5.2
4-27-51	14	73.2	93.9	0.00168	0.031	11.00	4.80	14.4	0.01170	0.000121	0.00610	2.9	0.54	10.8	0.000128	0.00040	8.1	1.66	7.5	0.000000	0.00000	22.9	4.40	6.5
	25	76.2	123.1	0.00168	0.031	11.20	5.96	14.4	0.01170	0.000317	0.01590	2.9	0.54	13.4	0.000626	0.00196	8.1	1.66	9.4	0.000906	0.00174	22.9	4.40	8.0
	41	64.0	159.1	0.00168	0.031	10.30	7.34	14.4	0.01170	0.000442	0.02210	2.9	0.54	16.5	0.001790	0.00559	8.1	1.66	11.5	0.000192	0.00037	22.9	4.40	9.9
	46	57.9	136.6	0.00168	0.031	9.70	6.48	14.4	0.01170	0.000479	0.02400	2.9	0.54	14.5	0.001730	0.00541	8.1	1.66	10.2	0.000000	0.00000	22.9	4.40	8.7
	59	51.8	121.9	0.00168	0.031	9.20	5.91	14.4	0.01170	0.000324	0.01620	2.9	0.54	13.3	0.000502	0.00157	8.1	1.66	9.3	0.000000	0.00000	22.9	4.40	8.0
6-19-52	12	64.0	118.9	0.00125	0.028	8.90	5.59	16.7	0.01100	0.000083	0.00830	3.0	0.57	13.3	0.000128	0.00032	8.6	1.73	9.3	0.000032	0.00000	24.3	4.55	7.9
	22	67.1	154.2	0.00125	0.028	9.10	6.91	16.7	0.01100	0.000039	0.00390	3.0	0.57	16.4	0.000121	0.00030	8.6	1.73	11.4	0.000066	0.00013	24.3	4.55	9.8
	32	54.9	150.0	0.00125	0.028	8.20	6.75	16.7	0.01100	0.000047	0.00470	3.0	0.57	16.0	0.000336	0.00084	8.6	1.73	11.2	0.000100	0.00020	24.3	4.55	9.6
	45	61.0	93.9	0.00125	0.028	8.60	4.62	16.7	0.01100	0.000015	0.00140	3.0	0.57	10.9	0.000868	0.00217	8.6	1.73	7.6	0.000000	0.00000	24.3	4.55	6.6

APPENDIX B

In this appendix, the equations and input needed to predict the spatial development of supercritical turbidity currents driven by poorly–sorted sediment are summarized.

B.1 Equations

1) Backwater relationships

$$\frac{dh}{dx} = \frac{-R_i S + C_D + e_w \left[2 - \frac{R_i}{2}\right] + \frac{R_i}{2} \Sigma\, r_{o_i} \frac{v_{s_i}}{U} \frac{\psi_i}{\psi} \left[\frac{\psi_{e_i}}{\psi_i} - 1\right]}{(1 - R_i)} \tag{2.36}$$

$$\frac{h}{U} \frac{dU}{dx} = e_w - \frac{dh}{dx} \tag{2.37}$$

$$\frac{h}{\psi} \frac{d\psi}{dx} = \Sigma\, r_{o_i} \frac{v_{s_i}}{U} \frac{\psi_i}{\psi} \left[\frac{\psi_{e_i}}{\psi_i} - 1\right] \tag{2.38}$$

where

$$\psi = \Sigma\, U\, C_i\, h = \Sigma\, \psi_i \tag{2.39}$$

and

$$\psi_{e_i} = \frac{p_i\, E_{s_i}\, U\, h}{r_{o_i}} \tag{2.40}$$

2) Water Entrainment Coefficient (Garcia, 1985)

$$e_w = \frac{0.075}{(1+718\, R_i^{2.4})^{0.5}} \tag{2.28}$$

where

$$R_i = \frac{gRCh}{U^2} \tag{2.27}$$

and

$$C = \Sigma\ C_i \tag{2.25}$$

3) Near–bed volumetric sediment concentration

$$c_{b_i} = r_{o_i}\ C_i \tag{2.30}$$

where

$$r_{o_i} = 0.40\ \delta_i^{1.64} + 1.64 \tag{5.14}$$

and

$$\delta_i = \frac{D_i}{D_{sg}}$$

4) Sediment Entrainment Coefficient

$$E_{s_i} = 1.3\ 10^{-7}\ Z_{eff}^5\ /\ (1 + 4.33\ 10^{-7}\ Z_{eff}^5) \tag{7.42}$$

where

$$Z_{eff} = \lambda\ Z_m \tag{7.41}$$

$$Z_m = \frac{u_*'}{v_{s_i}}\ R_{p_i}^{0.6} \left[\frac{D_i}{D_{50}}\right]^{0.2} \tag{7.40}$$

$$\lambda = 1 + \frac{\sigma_\phi}{\sigma_{\phi o}} (\lambda_o - 1) \tag{7.45}$$

and

$$\lambda_o = 0.81, \quad \sigma_{\phi o} = 0.73$$

5) Bed friction coefficient

$$C_D = u_*^2\ /\ U^2 \tag{2.29}$$

6) Skin Friction Coefficient

$$C_D' = u_*'^2 \; / \; U^2$$

$$= \left[1 + \frac{1}{2} C_f \frac{\Delta_b}{\ell_b} \kappa^{-2} \left[\ln(9 \; C_D'^{0.5} \; U \; \Delta_b \; / \nu) - 1\right]^2\right]^{-1} C_D \qquad (6.20)$$

where Δ_b and ℓ_b are bedform height and wavelength, respectively, and C_f is a drag coefficient equal to 0.21. This formulation is appropriate for turbulent smooth flow conditions. For rough flow conditions the original Nelson–Smith formulation can be used.

7) Geometric Diameter of Suspended Sediment

$$\ln(D_{sg}) = \frac{\Sigma \; C_i \; \ln(D_i)}{\Sigma \; C_i} \qquad (2.14)$$

8) Bed Variation

$$\frac{\partial z_b}{\partial t} = \frac{1}{1 - \lambda} \sum_{i=1}^{n} v_{s_i} \left(c_{b_i} - p_i \; E_{s_i}\right) \qquad (2.49)$$

where λ is the bed porosity.

9) Sediment Fall Velocity (Dietrich, 1984)

$$v_{s_i} = (g \; R \; \nu \; W_*)^{1/3} \qquad (3.4)$$

where

$$\log(W_*) = -3.7617 + 1.92944 \log(D_*) - 0.09815 \; (\log(D_*))^2$$
$$- 0.00575 \; (\log(D_*))^3 + 0.00056 \; (\log(D_*))^4 \qquad (3.5)$$

$$D_* = g \; R \; D_i^3 \; / \; \nu^2 \qquad (3.6)$$

B.2 Input Requirements

1) Upstream values of U, h, and C_i for i = 1...N.
2) Initial bed slope and elevation (S, z_b).
3) Characteristics of suspended (upstream) and bed sediment (D_i, p_i, σ_ϕ, and R).
4) Bed friction coefficient (C_D).
5) Bed porosity (λ).
6) Bedforms characteristics (Δ_b, ℓ_b).
7) Kinematic viscosity of water (ν).

B.3 Numerical Computations

To predict the development of a steady, supercritical turbidity current, equations (2.36)–(2.38) have to be integrated numerically starting at the canyon head and marching stepwise in the downslope direction (Fukushima et al., 1985).

If a turbidity current is sustained long enough, the bed elevation might change substantially due to sediment erosion and deposition thus affecting the flow behavior. The bed variation with time can be computed with the help of equation (2.49). The computational procedure should be as follows:

Step 1: compute flow characteristics along the canyon–fan length.
Step 2: compute bed variation for a given time increment Δt.
Step 3: update bed elevations.
Step 4: go back to step 1.